EPFL

Atomistic modeling of C-S-H: bulk and surface

Ziga CASAR

École
polytechnique
fédérale
de Lausanne

2023

Acknowledgements

One more acknowledgement to Paul, who not only pushed me to be a good computational material scientist, but also made sure that I was in touch with the experimental site, and how to connect both. And while doing all of this he challenged and broadened my horizon of wine knowledge significantly.

Finally, I would like to acknowledge my never-ending curiosity, which is on pair with a 7-year-old child who is left unsupervised in a fully equipped workshop. I would also like to take a moment and complain about the biological need for sleep and useless paperwork. They really slow down everything.

Ziga, Zürich 2023

Abstract

Concrete is the most used man-made material, while cement is the most manufactured product on earth by mass. Due to this colossal amount of cement being produced it accounts for 7-8% of anthropogenic CO_2 emission. The most viable way to reduce the CO_2 impact is to substitute part of cement with supplementary cementitious materials, which results in degradation of early age properties. Concrete is a composite material, which results from mixing water, cement and mineral aggregates. The main hydraulic phases of Portland cement are tricalcium silicate and dicalcium silicate, followed by aluminium- and iron-containing clinker phases, and calcium sulfate. The impure tricalcium silicate phase (alite) makes up 50% to 80% of Portland cement, and its hydration dominates the setting and strength development, forming the main hydration phase calcium silicate hydrate (C-S-H).

The C-S-H structure has been studied for decades. Today the bulk C-S-H structure is reasonably understood. C-S-H can be described as a highly defective tobermorite 14 Å. The structure is composed of stacked calcium-silicate layers which are separated by water and ion holding interlayers. The calcium-silicate layer is a calcium oxide sheet sandwiched between silicate chains. A silicate chain is composed of units which are assembled by interlinked silicates. These units follow the 3n-1 Dreierketten rule, meaning the lowest chain unit is a silicate dimer, the next longest is a pentamer which is composed of two dimers and a bridging silicate which links the dimers. In applied cement systems the silicate chains are mainly composed of dimers, which are linked by Ca^{2+}. The interlayer is filled with water, Ca^{2+} and OH^- ions.

This thesis addresses the yet unresolved C-S-H structural features. These features are the random assembly of different defects and how they give rise to the nanocrystalline nature of C-S-H, the incorporation sites of zinc in C-S-H and the structure of the C-S-H nanofoil, including its basal (001) surface.

A newly developed force field is presented, which is tailored for carrying out molecular dynamics studies of cementitious systems. The force field was validated on tobermorite 14 Å due to its resemblance to C-S-H. The force field predicts a wide variety of properties (structural, energetical, mechanical and vibrational density of states) with good accuracy.

A new Python program for C-S-H structure generation was developed. The program allows for manual generation of structures as well as automated generation. Approximately 200 C-S-H bulk structures with Ca/Si = 1.5 and 1.7 were generated simulated and analyzed. The generated structures were in excellent agreement with experimentally measured C-S-H properties (Ca/Si, mean chain length, Si-OH/Si, Ca-OH/Ca and 2H/Si). The very close similarities of local structural features and defect energies across these 200 structures clarify the nanocrystalline nature of C-S-H, i.e., there are many different arrangements of defects but the local atomistic structures are very similar and have very similar energies (within 0.02 eV at room temperature)

Due to the potential of minor elements as means of controlling the reactivity of cement, the incorporation of zinc in C-S-H was investigated. By combining ^{29}Si NMR, molecular dynamics and density functional theory modeling the incorporation of two sites for zinc were elucidated. The first site corresponds to the newly observed chemical shift at -72 ppm and is attributed to zincate substitution of silicate in the dimer pair. The second incorporation site is zincate substituting the Q^{2b} silicates which interlinks different dimers (bridging site). The $Q^{(2p,Zn)}$ silicate which shares one oxygen with the zincate and one with another silicate in the dimer has a chemical shift of -79 ppm which overlaps with the Q^1 shift.

Finally, the culmination of 10 years of atomistic modeling and experimental progress is reflected in the first ever atomic-level description of the C-S-H nanofoil. A systematic procedure to generate atomistic model C-S-H nanofoils, which precisely match experimentally measured C-S-H properties is shown. Contrary to current beliefs, it is shown that the C-S-H surface is mostly calcium terminated, whereby the surface silanol density decreases with an increase in the Ca/Si ratio, which is an experimentally known characteristic for early age hydration. Further a calcium and hydroxide co-adsorption mechanism is proposed, which is in agreement with the surface charge densities observed in previous experimental and modelling studies. These findings will be of great benefit to the cement community. They will allow for the construction of atomistic modelling studies which are in close resemblance to the experimentally observed systems. With this it will be possible to conduct studies which have an applicability to real world cementitious systems.

Keywords: calcium silicate hydrate, C-S-H, cement chemistry, atomistic modeling

Zusammenfassung

Beton ist das am häufigsten verwendete menschengemachte Material und Zement ist gleichzeitig das, an der Masse gemessen, am meisten Hergestellte Produkt auf der Erde. Aufgrund der enormen Menge an produziertem Zement, entfallen schätzungsweise 7-8 % der anthropogenen CO_2-Emissionen auf dessen Herstellung. Die praktikabelste Möglichkeit zur Verringerung der anfallenden CO_2-Emissionen besteht darin, einen Teil des Zements durch zusätzliche zementartige Materialien zu ersetzen, was aber zu einer Verschlechterung der Eigenschaften im frühen Alter führt. Beton ist ein Verbundwerkstoff, der durch das Mischen von Wasser, Zement und mineralischen Schotter entsteht. Die wichtigsten hydraulischen Phasen von Portlandzement sind Tricalciumsilikat und Dicalciumsilikat, gefolgt von aluminium- und eisenhaltigen Klinkerphasen und Calciumsulfat. Die unreine Tricalciumsilicatphase (Alit) macht 50 bis 80 % des Portlandzements aus, und ihre Hydratation dominiert das Abbinden und die Festigkeitsentwicklung, wobei sie die Haupthydratationsphase Calciumsilicathydrat (C-S-H) bildet.

Die C-S-H Struktur wird bereits seit Jahrzehnten untersucht und die Bulkstruktur ist heutzutage verhältnismäßig gut charakterisiert. C-S-H kann als ein stark defekter Tobermorit 14 Å beschrieben werden. Die C-S-H Struktur besteht aus gestapelten Calcium-Silikat Schichten, welche durch Zwischenschichten getrennt werden. Die Zwischenschichten bestehen aus Wasser und Ionen. Die Calcium-Silikat Schicht ist aufgebaut aus einer Calcium-Oxid Schicht, welche in Silikatketten eingebettet ist. Eine Silikatkette ist aus verknüpften Silikat-Einheiten zusammengesetzt. Der Aufbau dieser Silikat-Einheiten folgt der 3n-1-Dreierketten-Regel, d. h. die kleinste Ketteneinheit ist ein Silikatdimer, die nächstlängste ist ein Pentamer, das aus zwei Dimeren und einem Brückensilikat besteht, das die Dimere verbindet. In reellen Zementsystemen bestehen die Silikatketten hauptsächlich aus Dimeren, die durch Ca^{2+} verbunden sind. Die Zwischenschicht ist mit Wasser, Ca^{2+} und OH^- Ionen besetzt.

Diese Arbeit befasst sich mit den bislang ungelösten Strukturmerkmalen von C-S-H. Es werden dabei die zufällige Anordnung verschiedener Defekte untersucht und wie sie die Nanokristallinität von C-S-H verursachen. Darüber hinaus sind die Einbaustellen von Zink in C-S-H und die Struktur von C-S-H-Nanofoils, einschließlich ihrer Basalt (001)-Oberfläche untersucht.

Diese Arbeit umfasst die Entwicklung eines neuen Kraftfelds welches speziell für Molekulardynamik Simulationen von zementartigen Systemen zugeschnitten ist. Das Kraftfeld wurde an Tobermorit 14 Å getestet, da es dem C-S-H System ähnelt. Das Kraftfeld sagt eine Vielzahl von Eigenschaften (strukturelle, energetische, mechanische und Schwingungszustandsdichte) mit guter Genauigkeit voraus.

Ergänzend zu dem Kraftfeld, wird ein Python Programm zur Erzeugung von C-S-H Struktur Modellen entwickelt. Das Programm ermöglicht sowohl die manuelle als auch die automatische Generierung von Struktur-Modellen. Mithilfe des Programms, wurden 200 C-S-H-Bulk-Strukturen mit Ca/Si = 1,5 und 1, generiert, simuliert und anschließend analysiert. Die Eigenschaften der generierten Strukturen stimmten hervorragend mit experimentell gemessenen C-S-H Eigenschaften (Ca/Si, mittlere Kettenlänge, Si-OH/Si, Ca-OH/Ca und 2H/Si) überein. Die sehr große Ähnlichkeit der lokalen Strukturmerkmale und Defektenergien in diesen 200 Strukturen verdeutlicht die nanokristalline Natur von C-S-H. Das heißt, es gibt viele verschiedene Anordnungen von Defekten, aber die lokalen atomistischen Strukturen sind sehr ähnlich und haben sehr ähnliche Energien (innerhalb von 0.02 eV bei Raumtemperatur).

Aufgrund des Potenzials von Nebenelementen als Mittel zur Steuerung der Reaktivität von Zement wurde die Aufnahme von Zink in C-S-H untersucht. Durch die Kombination von ^{29}Si-NMR Spektroskopie, Molekulardynamik und Dichtefunktionaltheorie-Modellierung wurde die Aufnahme von Zink in zwei Positionen aufgeklärt. Die erste Position entspricht einer neu beobachteten chemischen Verschiebung bei -72 ppm und wird der Zinkat-Substitution von Silikat im Dimerpaar zugeschrieben. Die zweite Einbaustelle ist die Substitution der Q^{2b}-Silikate durch Zinkat, das verschiedene Dimere miteinander verbindet (Brückenstelle). Das $Q^{(2p,Zn)}$-Silikat, das einen Sauerstoff mit dem Zinkat und einen mit einem anderen Silikat im Dimer teilt, hat eine chemische Verschiebung von -79 ppm, die sich mit der Q^1-Verschiebung überlagert.

Das Ergebnis von 10 Jahren atomistischer Modellierung und experimentellem Fortschritt mündet schlussendlich in der ersten Beschreibung des C-S-H-Nanofilms auf atomarer Ebene. Es wird ein systematisches Verfahren zur Erzeugung atomistischer Modelle von C-S-H-Nanofilmen gezeigt, deren simulierte Eigenschaften genau experimentell gemessenen C-S-H-Eigenschaften entsprechen.

Im Gegensatz zu gängigen Annahmen wird gezeigt, dass die C-S-H-Oberfläche größtenteils mit Kalzium terminiert ist, wobei die Oberflächensilanoldichte mit einem Anstieg des Ca/Si-Verhältnisses abnimmt, was ein experimentell bekanntes Merkmal für die Hydratation im frühen Alter ist. Ferner wird ein Mechanismus der Koadsorption von Calcium und Hydroxid vorgeschlagen, der mit den in früheren experimentellen und Modellierungsstudien beobachteten Oberflächenladungsdichten übereinstimmt. Diese Ergebnisse werden für die Zementindustrie von großem Nutzen sein. Sie ermöglichen die Erstellung atomistischer Modelle, die den experimentell beobachteten Systemen sehr ähnlich sind. Damit wird es möglich sein, Studien durchzuführen, die auf reale zementhaltige Systeme anwendbar sind.

Table of Contents

11

List of Figures

14

List of Tables

1 Introduction

1.1   Cement and Concrete

The oldest evidence of what could be called concrete dates from 10 to 20,000 years ago [1]. An early peak in usage was reached in the Roman Empire. After the fall of the empire around 476 CE the technology was somehow forgotten for a millennium. It was in 1414 CE in a Swiss library that a Roman manuscript from 30 BCE written by the architect and engineer Vitruvius was discovered. The manuscript contains information about pozzolan cement [2], which was then used to build the pier of the Pont de Notre Dame in Paris in 1499 [3]. It was later in 1824 that Joseph Aspdin obtained the patent for Portland cement, also called ordinary Portland cement (OPC), which is the most common type of cement in general use on the planet.

Concrete is a composite material, which results from mixing water, cement and mineral aggregates. One third of the total materials extracted from earth are for cement based materials, where cement is the most manufactured product on earth by mass (in 2015 the total production of cement was 4.6 billion tones [4]), while concrete is the second most used material after water. In more recent years, the cement industry has become highly energy efficient and adopted the use of alternative fuels and clinker (technical term used for cement that is produced in high temperature furnaces from a mixture of limestone and clays) substitutions, which has resulted in a significant CO_2 reduction. Nevertheless, due to the colossal amount of cement being produced, this low impact material per kg, still accounts for 7-8% of anthropogenic CO_2 emission, which is the highest industry share of emissions after power production [4].

Most of the CO_2 in cement production ($\approx$ 60%) comes from the breakdown of limestone [4] ($CaCO_3 \rightarrow CaO + CO_2$), which represents 80% of the raw material needed for Portland cement production. This, so called "chemical" CO_2, cannot be reduced with the use of renewable energies in the production process. To reduce the CO_2 impact a different material is needed, which could fully or partially replace Portland cement, although the new material would potentially have different properties and behavior under given conditions, which could present a new challenge.

Since large amounts of cement are required, the limitation already occurs in the availability of raw materials on Earth. Oxygen, silicon, aluminum, iron, sodium, potassium and magnesium

account for 98% of Earth's crust. Portland cement is a hydraulic binder, thus dissolves in water and forms insoluble hydroxides. The incorporated water in those hydroxides increases the solid volume and fills the space previously occupied by mixing water. The elements calcium, silicon and aluminum oxides only are suitable for the base of hydraulic cements. The alkali hydroxides are too soluble, while the iron and magnesium oxides are very poorly soluble in alkaline solutions. The hydraulic phases tricalcium silicate (C_3S) and dicalcium silicate (C_2S) are the basis of Portland cement. The calcium aluminates and calcium sulfo aluminates form the basis of calcium aluminate (CAC) and calcium sulfo aluminate (CSA) cements. The aluminum-based cements are not suitable as "Portland cement" replacement, since their production is limited by the need of raw materials [4], therefore the most realistic way of lowering the CO_2 impact is by replacing part of Portland cement with other materials, so called SCMs, supplementary cementitious materials.

Today's average of substituting the Portland cement with SCMs is at 20%, which is done with slag and fly ash, both byproducts of other industries. The limitation occurs for two reasons, firstly, there is a limitation in supply, and secondly, the degradation of early age properties due to slower reactivity in comparison to Portland cement. The first limitation can be overcome by substituting Portland cement with limestone and calcined clay, which are globally widely available in almost unlimited amounts [5,6]. The second problem could be resolved with the use of minor elements and/or additives, which can drastically increase the amount of reaction in the first day (main hydration peak observed in calorimetric studies) [7,8].

While Portland cement (PC) has been in use for centuries, several aspects of its hydration when mixed with water are still not known. PC is composed of several phases, which are, in decreasing amount, alite (impure tricalcium silicate – C_3S), belite (impure dicalcium silicate – C_2S), aluminate (tricalcium aluminate - C_3A), and ferrite (tetracalcium aluminoferrite – $C_4(A,F)$). Each phase contains up to 5% impurities. Alite accounts for 50-70% of PC and forms the main hydration phase calcium silicate hydrate (C-S-H), which has a complex nanocrystalline structure.

1.1.1 Calcium Silicate Hydrate

A typical hydration curve of PC is shown in Figure 1, where the heat flow from calomietry corresponds to the reaction intensity. The initial reaction occurs very rapidly between C_3S and

water, after which a period of slow reaction occurs, known as the induction period and lasts until the acceleration period.
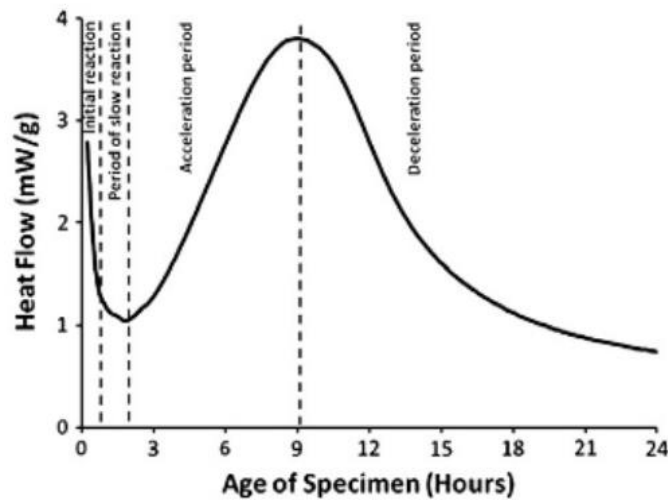
Figure 1-1. Rate of hydration as a function of time given by isothermal calorimetry measurements [9].

The acceleration period is the first half of the main hydration peak. This period is related to nucleation and growth mechanisms, whereby the rate controlling step is related to the nucleation and growth of calcium silicate hydrate (C-S-H) [9]. It was shown that hydration rate of C_3S is proportional to the surface area of C-S-H [10]. C-S-H is the main hydration product of C_3S, forming around 50-60% by volume of hardened cement paste [11], along with smaller quantities of portlandite (CH):

$$C_3S + H_2O \rightarrow C-S-H + CH$$
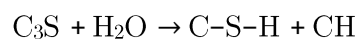
To be able to engineer the reactivity of cement in early stages, a detailed understanding of the mechanisms in the acceleration period is needed. A limitation of doing so is the poor knowledge of the underlying atomistic structure of C-S-H. For example, with X-ray diffraction and selected area diffraction only two weak signals are seen [4], since C-S-H has no long-range 3D order, and consequently the atomic structure cannot be resolved using standard diffraction methods. Despite all these limitations some information about the structural features are known. It has a varying chemical composition inside the sample, where on a distance of 100nm the Ca/Si ratio varies between 1.2 and 2.1, with an average of 1.75 in early age OPC. C-S-H is composed of a dreierketten structure with silicate dimers, which can be linked with bridging silicate tetrahedra, as in the mineral tobermorite. The length of chains follows this dreierketten rule

of 3n-1 (i.e. dimers, pentamers, octamers etc.) [12]. Over recent decades, nuclear magnetic resonance (NMR) techniques became remarkably useful for exploring the nanoscale structure of cementitious materials [11,13–15]. With use of NMR it was discovered that no connectivity larger than 2 can exist between the different silicate tetrahedra, and that the ratio between non-bridging tetrahedra Q^2 and bridging tetrahedra Q^{2b} equals 2:1, which confirms the 3n-1 silicate chain length [16]. Other studies concluded the presence of Ca-OH groups [17], and the decrease of Si-OH groups with increasing Ca/Si ratio [14]. XRD and Raman spectroscopy measurements indicate a resemblance of the C-S-H structure to tobermorite [18,19] All this experimental evidence suggests that C-S-H is composed of defective, nanocrystalline tobermorite with missing bridging silicate tetrahedra, which leads to a decreased silicate chain length and deprotonated silanol groups, the charge of which is compensated by additional calcium ions in the water-interlayer and with additional Ca-OH groups [20].

In previous years many different atomistic models of C-S-H were proposed and were reviewed by Duque-Redondo et al. [21]. When compared with experimental data none of them is entirely satisfactory and several unresolved questions remained regarding the properties and behavior of C-S-H. Kunhi Mohamed et al. [20] has developed the brick model, an atomistic building block description of C-S-H. The model is based on introducing defects to the tobermorite 14Å structure and can construct a variable C-S-H model with a large number of local arrangements, which give rise to the overall C-S-H properties observed experimentally. The construction of the model starts with the unit cell of tobermorite 14Å, in which defects are introduced. Those defects can be deprotonated silanol groups, for which the charge is compensated by additional Ca ions in the interlayer, a missing bridging silicate, where the silanol groups are transferred to the neighboring silicate groups, the missing bridging silicate can be replaced by a calcium [11], which is compensated by a hydroxyl group, or by substituting a silicate dimer by two $Ca(OH)_2$ units, and changing the number of water molecules in the interlayer [19]. With this method it is possible to target a specific Ca/Si ratio, while maintaining a charge neutral unit cell, which was often an issue with previous models. Previous models relied on random generation of defects, while the brick model offers a systematic approach, which allows the control every type of defect and its location. Once different or the same unit cells of C-S-H are constructed, it is possible to unite them and mimic the bulk C-S-H structure. The brick model also allows construction of surfaces, such as the (100) and (001), which is of great interest, since due to the nanosized nature of C-S-H, surfaces are likely to play an important role. Molecular modeling studies on the brick model [20] indicate that defective structures with

deprotonated silanol groups are preferred as first observed in [14], and that protonated silanol groups for higher Ca/Si ratio structures do not seem to be energetically favorable.

1.1.2 Minor Elements

Research on the impact of minor elements on stabilizing different clinker phases and the composition of clinker started in the 70s and 80s [22]. Later in the 90s the focus was on the role of minor elements as potential contaminants [23], concerned over the possible leaching of elements such as Zn, Cr, and Ni out of hydrated cement and the possible contamination of the environment. All these investigations were limited by the lack of adequate analytical methods. It was only in the last two decades that the focus turned to engineering the reactivity of cement with the use of minor elements [24]. The study of minor elements is a complicated task, since different concentrations result in different effects, as seen with zinc, where depending on the concentration, and at which stage of the production process zinc is added, retardation or acceleration can occur [24,25].

One of the first reports of the impact of zinc in solid solution with alite on hydration was from Odler and Abdul-Maula [4], where the focus was mainly on the limits of the solid solution composition and the effect on the C_3S crystal structure. Later the focus shifted to incorporation of zinc into calcium silicate hydrates, as means of storing heavy metals [26,27]. The incorporation of heavy metals into C-S-H was mostly investigated with techniques such as XRD and XPS, while those techniques are not best suited, they still gave some important insights. It was observed that C-S-H can incorporate up to 6 wt.% Zn [26], and that this incorporation does not appear to influence the Ca and Si content [27]. While it was first theorized that zinc replaces calcium in C-S-H [23], it was later concluded that zinc is incorporated into C-S-H in tetrahedral coordination, and according to measured Ca-Zn distances indicates that the zinc tetrahedra substitutes the silicon tetrahedra [28], which was also observed with ^{29}Si NMR [29]. The ^{29}Si NMR suggests a Zn-O-Si linkage, where a Si tetrahedra is linked to Si and Zn tetrahedron. Rose et al. [29] also performed Ab initio simulations on possible zinc sites, where they concluded that zinc is probably in the dimer site and not in the bridging site. However, the initial C-S-H configuration is of questionable origin, and the simulation by itself was heavily simplified, for instance, most of the atoms were fixed in space, therefore without movement.

As mentioned, it was just recently that the focus shifted to the minor elements as a mean of controlling the reactivity of cement. Bazzoni et al. [30] studied the effect of magnesium and zinc ions on the hydration kinetics of C_3S, where they observed that zinc has an accelerating effect from 2 to 10 hours after mixing, where the maximum heat flow is at least twice that of pure C_3S, also the peak is wider. It appears that zinc only plays an important role at the start of hydration, since after 24 hours the reaction rate for doped and undoped samples was the same. The visual examination of the samples showed that the samples containing zinc have a thicker layer of C-S-H around grains and that the length of the C-S-H needles is twice as long.
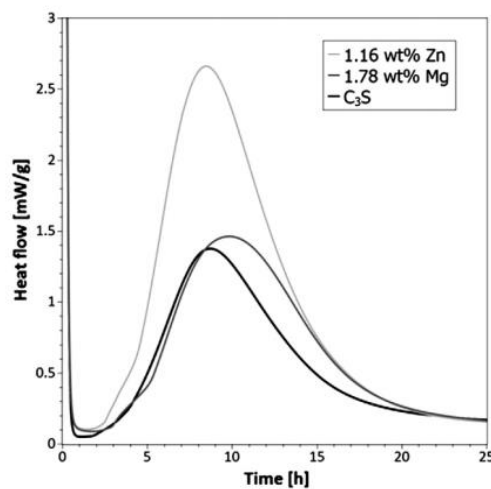
Figure 1-2. Impact of Zn and Mg in alite solid solution on hydration kinetics as measured by isothermal calorimetry [30].

Today's analytical methods, such as STEM-EDX, NMR, SAXS and other characterization techniques, in combination with numerical modeling offer a great combination for resolving the underlying atomic configuration, which would be otherwise unknown, and thus restrict the advances in material design.

1.1.3 Calcium Silicate Hydrate Surface

In contrast to the bulk of C-S-H the surface is poorly understood and barely explored. Transmission electron microscopy (TEM) and scanning transmission electron microscopy (STEM) images (figure 3) show a nanofoil morphology of C-S-H [11,30]. It is known that C-S-H has a high specific surface area, although the exact value is hard to determine, since there is a high inconsistency between surface area measurements, due to different Ca/Si ratios,

water/cement ratios, drying procedures, and/or hydration degrees [31,32], with most values ranging between 200 and 300 m^2/g [31,33,34]. Although not exactly defined, the high specific surface area underlines the importance of the C-S-H surface in the process of cement hydration [35]. The structure of C-S-H surfaces is as of yet not greatly explored.

STEM: Hydrated C$_3$S   **TEM: C-S-H nanofoils, Ca/Si = 2.0**
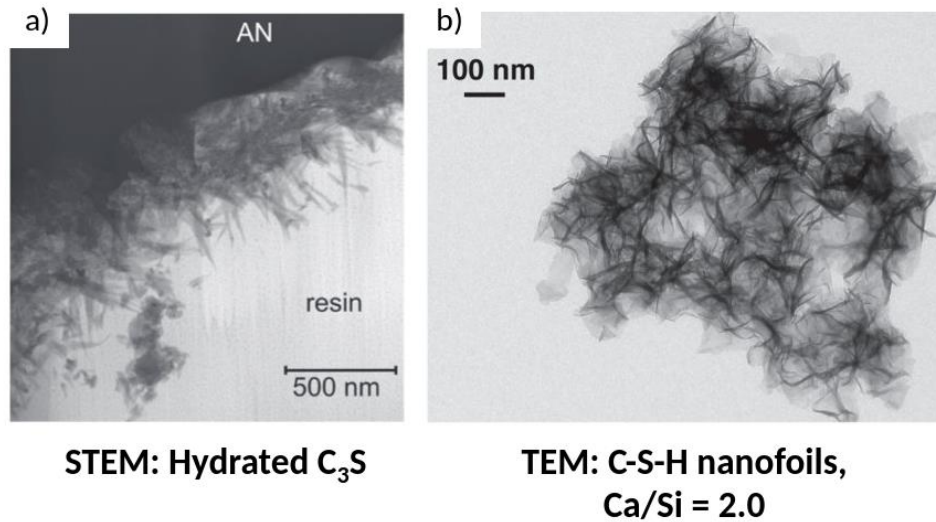
Figure 1-3. STEM (a) image of C-S-H formation around a C$_3$S grain (AN) [30] and TEM image of synthetic phase pure C-S-H [11].

1.2   Methods

The highly defective structure of C-S-H restricts the usage of experimental techniques in the quest of elucidating the atomic-level structure of C-S-H. In the past decade tremendous advances in the fundamental understanding of cementitious materials were achieved due to atomistic modeling [36]. Particularly, the synergy of experimental and modeling techniques contributed significantly to elucidating the local structural features in C-S-H [11] and C-A-S-H [15].

The following simulation methods are used in the thesis to investigate C-S-H. The molecular dynamics part of the work was carried out with the Large-scale Atomic/Molecular Massively Parallel Simulator (LAMMPS) [37], while for the density functional theory calculations Quantum ESPRESSO [38] was used.

Alder and Wainwright introduced the molecular dynamics (MD) method in the 1950s [39]. With advances in computational power the method gained in popularity to study different systems, from ideal gases to complex materials such as proteins and cement phases. With MD one can calculate the time dependent behavior of a molecular system, whereby one evolves the system of interacting atoms with time by solving Newton's law of motion, obtaining position and velocity of each particle in a given time step. The interactions in such a virtual system are described by the force field.

A force field is a collection of empirical equations which describe the interatomic interactions between different and same atomic species. An accurate force field is designed to reproduce molecular geometry and mimic the partial or all properties of a given system [40,41].

While MD considers the atom as the smallest particle in the system, density functional theory (DFT) includes the role of electrons explicitly. To achieve this the wave nature of the electrons is considered, which is outside the realm of classical mechanics. The Schrödinger equation in quantum mechanics is analogous to Newton's law of motion in classical mechanics, and by solving the time-independent Schrödinger equation we obtain the ground state electronic structure [42]. Because of higher computational costs, compared to MD, DFT is only suitable for smaller systems, with shorter simulation times.

For a short review on molecular modeling of cementitious systems the reader is referred to a recently published paper titled Molecular modelling of cementitious materials: current progress and benefits [36].

1.3   Thesis Objective and Structure

The objective of the thesis was to elucidate the atomic structure of C-S-H and the incorporation of minor elements, particularly zinc, into it. The thesis is divided into 8 chapters, including the introduction, conclusions, bibliography and appendix, the other chapters deal with force field development, bulk C-S-H, incorporation of zinc into the bulk C-S-H structure and the atomic-level structure of the C-S-H nanofoil, including the surface termination of its basal (001) surface.

The thesis is written as a series of publications with a brief general introduction and a final summary chapter. Some of the chapters have been published or submitted and the others are all close to submission.

In the second chapter an improved force field is presented. The force field is an improved version of the previously published Erica FF2 [43]. The force field is extended by zinc interactions with which zinc incorporation into C-S-H (chapter 4) can be studied. Further, the Lennard-Jones potential form is adopted for the key ionic species Ca^{2+} and OH^-, which will enable the study of surface phenomena at the C-S-H surface. The force field is validated on a wide range of properties (structural, mechanical, energetical).

The third chapter introduces a new Python code for the automated generation of bulk C-S-H structures which match experimentally measured properties (Ca/Si, 2H/Si, mean chain length, Si-OH/Si and Ca-OH/Ca). The code works on the principles of the brick model [20] and it was used to generate approximately 200 bulk C-S-H structures with Ca/Si of 1.5 and 1.7. The structures were analyzed on their structural features and defect stabilities.

In the fourth chapter the incorporation of zinc into the C-S-H structure is investigated [44]. By combining ^{29}Si NMR and DFT calculation it was possible to elucidate the exact incorporation sites of zinc in C-S-H. Altogether four unique incorporation sites are introduced, from which two appear as a new peak in the 1D NMR spectrum (around –72 ppm), while the remaining two overlap with the Q^1 chemical shift (-79 ppm).

The fifth chapter introduces the structure of the C-S-H nanofoil. It is shown how the brick model [20] can be used to generate representative C-S-H nanofoil structures with the (001) basal surface that match the experimentally measured properties (Ca/Si, mean chain length, Si-OH/Si, Ca-OH/Ca). It is shown that the bulk and surface cannot be separated when investigating C-S-H. The surface termination, and therefore the surface charge, are correlated with the mean chain length. In order to match the model and experimentally measured properties a co-adsorption of Ca^{2+} and OH^- is proposed with which also an excellent agreement with previously reported surface charges is achieved.

The thesis ends with a summary chapter with conclusions and future perspectives and a series of annexes with technical and detailed results sections to supplement each chapter.

References

[1]   P. Jahren, T. Sui, Early concrete history, in: History of Concrete, World Scientific / Chemical Industry Press, 2017: pp. 001–056. https://doi.org/10.1142/9789813145740_0001.

[2]   R. North, How to Invent Everything: A Survival Guide for the Stranded Time Traveler, Riverhead Books, 2018.

[3]   http://concretecontractor.com/concrete-history/, The History of Concrete, Concrete Contractor. (2023).

[4]   K.L. Scrivener, V.M. John, E.M. Gartner, Eco-efficient cements: Potential, economically viable solutions for a low-CO2, cement-based materials industry, Cem Concr Res. 114 (2018) 2–26. https://doi.org/https://doi.org/10.1016/j.cemconres.2018.03.015.

[5]   K.L. Scrivener, Eco-efficient cements: No magic bullet needed, Global Cement Magazine. (2019).

[6]   B. Lothenbach, K. Scrivener, R.D. Hooton, Supplementary Cementitious Materials, Cem Concr Res. 41 (2011) 1244–1256.

[7]   I. Odler, S. Abdul-Maula, Polymorphism and Hydration of Tricalcium Silicate Doped With ZnO, Journal of the American Ceramic Society. 66 (1983) 1–04. https://doi.org/10.1111/j.1151-2916.1983.tb09956.x.

[8]   K. Scrivener, F. Avet, H. Maraghechi, F. Zunino, J. Ston, W. Hanpongpun, A. Favier, Impacting factors and properties of limestone calcined clay cements (LC 3), Green Mater. 7 (2019) 3–14. https://doi.org/10.1680/jgrma.18.00029.

[9]   J.W. Bullard, H.M. Jennings, R.A. Livingston, A. Nonat, G.W. Scherer, J.S. Schweitzer, K.L. Scrivener, J.J. Thomas, Mechanisms of cement hydration, Cem Concr Res. 41 (2011) 1208–1223. https://doi.org/10.1016/j.cemconres.2010.09.011.

[10]   M. Zajac, Étude des relations entre vitesse d'hydratation, texturation des hydrates et résistance méchanique finale des pâtes et micromortiers de ciment portland, Universite de Bourgogne, 2007.

[11]   A. Kumar, B.J. Walder, A. Kunhi Mohamed, A. Hofstetter, B. Srinivasan, A.J. Rossini, K. Scrivener, L. Emsley, P. Bowen, The Atomic-Level Structure of Cementitious Calcium Silicate Hydrate, The Journal of Physical Chemistry C. 121 (2017) 17188–17196. https://doi.org/10.1021/acs.jpcc.7b02439.

[12]   K. Mohan, H.F.W. Taylor, A trimethylsilylation study of tricalcium silicate pastes, Cem Concr Res. 12 (1982) 25–31. https://doi.org/10.1016/0008-8846(82)90095-3.

[13]   J. Francis Young, Investigations of Calcium Silicate Hydrate Structure Using Silicon-29 Nuclear Magnetic Resonance Spectroscopy, Journal of the American Ceramic Society. 71 (1988) C-118-C-120. https://doi.org/10.1111/j.1151-2916.1988.tb05028.x.

[14]   X. Cong, R. James Kirkpatrick, 29Si MAS NMR study of the structure of calcium silicate hydrate, Advanced Cement Based Materials. 3 (1996) 144–156. https://doi.org/10.1016/s1065-7355(96)90046-2.

[15]   A. Kunhi Mohamed, P. Moutzouri, P. Berruyer, B.J. Walder, J. Siramanont, M. Harris, M. Negroni, S.C. Galmarini, S.C. Parker, K.L. Scrivener, L. Emsley, P. Bowen, The Atomic-Level Structure of Cementitious Calcium Aluminate Silicate Hydrate, J Am Chem Soc. 142 (2020) 11060–11071. https://doi.org/10.1021/jacs.0c02988.

[16]   J. Skibsted, C. Hall, Characterization of cement minerals, cements and their reaction products at the atomic and nano scale, Cem Concr Res. 38 (2008) 205–225. https://doi.org/10.1016/j.cemconres.2007.09.010.

[17]   F. Brunet, P. Bertani, T. Charpentier, A. Nonat, J. Virlet, Application of 29Si homonuclear and 1H-29Si heteronuclear NMR correlation to structural studies of calcium silicate hydrates, Journal of Physical Chemistry B. 108 (2004) 15494–15502. https://doi.org/10.1021/jp031174g.

[18] G. Renaudin, J. Russias, F. Leroux, F. Frizon, C. Cau-dit-Coumes, Structural characterization of C-S-H and C-A-S-H samples-Part I: Long-range order investigated by Rietveld analyses, J Solid State Chem. 182 (2009) 3312–3319. https://doi.org/10.1016/j.jssc.2009.09.026.

[19] R.J. Kirkpatrick, J.L. Yarger, P.F. McMillan, P. Yu, X. Cong, Raman spectroscopy of C-S-H, tobermorite, and jennite, Advanced Cement Based Materials. 5 (1997) 93–99. https://doi.org/10.1016/S1065-7355(97)00001-1.

[20] A. Kunhi Mohamed, S.C. Parker, P. Bowen, S. Galmarini, An atomistic building block description of C-S-H - Towards a realistic C-S-H model, Cem Concr Res. 107 (2018) 221–235. https://doi.org/10.1016/j.cemconres.2018.01.007.

[21] E. Duque-Redondo, P.A. Bonnaud, H. Manzano, A comprehensive review of C-S-H empirical and computational models, their applications, and practical aspects, Cem Concr Res. 156 (2022) 106784. https://doi.org/10.1016/j.cemconres.2022.106784.

[22] M. Moranville-Regourd, A.I. Boikova, Chemistry Structure, Properties and Quality of Clinker, in: Keynote Review at 9th International Congress on the Chemistry of Cement, New Delphi, 1992: pp. 3–45.

[23] D. Stephan, H. Haleki, D. Knöfel, B. Eber, R. Härdtl, H. Maleki, D. Knöfel, B. Eber, R. Härdtl, Influence of Cr, Ni, and Zn on the properties of pure clinker phases: Part I. C3S, Cem Concr Res. 29 (1999) 545–552. https://doi.org/10.1016/S0008-8846(99)00009-5.

[24] Q.Y. Chen, C.D. Hills, M. Tyrer, I. Slipper, H.G. Shen, A. Brough, Characterisation of products of tricalcium silicate hydration in the presence of heavy metals, J Hazard Mater. 147 (2017) 817–825.

[25] F.F. Ataie, M.C.G. Juenger, S.C. Taylor-Lange, K.A. Riding, Comparison of the retarding mechanisms of zinc oxide and sucrose on cement hydration and interactions with supplementary cementitious materials, Cem Concr Res. 72 (2015) 128–136.

[26] A. Stumm, K. Garbev, G. Beuchle, L. Black, P. Stemmermann, R. Nüesch, Incorporation of zinc into calcium silicate hydrates, Part I: Formation of C-S-H(I) with

C/S=2/3 and its isochemical counterpart gyrolite, Cem Concr Res. 35 (2005) 1665–1675. https://doi.org/10.1016/j.cemconres.2004.11.007.

[27]   F. Ziegler, R. Gieré, C.A. Johnson, Sorption mechanisms of zinc to calcium silicate hydrate: Sorption and microscopic investigations, Environ Sci Technol. 35 (2001) 4556–4561. https://doi.org/10.1021/es001768m.

[28]   C.E. Tommaseo, M. Kersten, Aqueous solubility diagrams for cementitious waste stabilization systems. 3. Mechanism of zinc immobilizaton by calcium silicate hydrate, Environ Sci Technol. 36 (2002) 2919–2925. https://doi.org/10.1021/es0102484.

[29]   J. Rose, I. Moulin, A. Masion, P.M. Bertsch, M.R. Wiesner, J.Y. Bottero, F. Mosnier, C. Haehnel, X-ray absorption spectroscopy study of immobilization processes for heavy metals in calcium silicate hydrates. 2. Zinc, Langmuir. 17 (2002) 3658–3665. https://doi.org/10.1021/la001302h.

[30]   A. Bazzoni, M. Suhua, Q. Wang, X. Shen, M. Cantoni, K.L. Scrivener, The effect of magnesium and zinc ions on the hydration kinetics of C3S, Journal of the American Ceramic Society. 97 (2014) 3684–3693. https://doi.org/10.1111/jace.13156.

[31]   P.D. Tennis, H.M. Jennings, Model for two types of calcium silicate hydrate in the microstructure of Portland cement pastes, Cem Concr Res. 30 (2000) 855–863. https://doi.org/10.1016/S0008-8846(00)00257-X.

[32]   C. Labbez, B. Jönsson, I. Pochard, A. Nonat, B. Cabane, Surface charge density and electrokinetic potential of highly charged minerals: Experiments and Monte Carlo simulations on calcium silicate hydrate, Journal of Physical Chemistry B. 110 (2006) 9219–9230. https://doi.org/10.1021/jp057096+.

[33]   S. Yoshida, Y. Elakneswaran, T. Nawa, Electrostatic properties of C–S–H and C-A-S-H for predicting calcium and chloride adsorption, Cem Concr Compos. 121 (2021) 104109. https://doi.org/10.1016/j.cemconcomp.2021.104109.

[34]   S. Brunauer, D.L. Kantro, C.H. Weise, The surface energy of tobermorite, Can J Chem. 37 (1958). https://doi.org/https://doi.org/10.1139/v59-097.

[35] K. Scrivener, A. Ouzia, P. Juilland, A. Kunhi Mohamed, Advances in understanding cement hydration mechanisms, Cem Concr Res. 124 (2019) 105823. https://doi.org/10.1016/j.cemconres.2019.105823.

[36] A. Kunhi Mohamed, A. Bouibes, M. Bauchy, Z. Casar, Molecular modelling of cementitious materials: current progress and benefits, RILEM Technical Letters. 7 (2022) 209–219. https://doi.org/10.21809/rilemtechlett.2022.175.

[37] A.P. Thompson, H.M. Aktulga, R. Berger, D.S. Bolintineanu, W.M. Brown, P.S. Crozier, P.J. in 't Veld, A. Kohlmeyer, S.G. Moore, T.D. Nguyen, R. Shan, M.J. Stevens, J. Tranchida, C. Trott, S.J. Plimpton, LAMMPS - a flexible simulation tool for particle-based materials modeling at the atomic, meso, and continuum scales, Comput Phys Commun. 271 (2022) 108171. https://doi.org/10.1016/j.cpc.2021.108171.

[38] P. Giannozzi, S. Baroni, N. Bonini, M. Calandra, R. Car, C. Cavazzoni, D. Ceresoli, G.L. Chiarotti, M. Cococcioni, I. Dabo, A. Dal Corso, S. De Gironcoli, S. Fabris, G. Fratesi, R. Gebauer, U. Gerstmann, C. Gougoussis, A. Kokalj, M. Lazzeri, L. Martin-Samos, N. Marzari, F. Mauri, R. Mazzarello, S. Paolini, A. Pasquarello, L. Paulatto, C. Sbraccia, S. Scandolo, G. Sclauzero, A.P. Seitsonen, A. Smogunov, P. Umari, R.M. Wentzcovitch, QUANTUM ESPRESSO: A modular and open-source software project for quantum simulations of materials, Journal of Physics Condensed Matter. 21 (2009). https://doi.org/10.1088/0953-8984/21/39/395502.

[39] B.J. Alder, T.E. Wainwright, Phase transition for a hard sphere system, J Chem Phys. 27 (1957) 1208–1209. https://doi.org/10.1063/1.1743957.

[40] D. Frenkel, B. Smit, Understanding Molecular Simulations - From Algorithms to Applications, 2002. https://doi.org/https://doi.org/10.1016/B978-0-12-267351-1.X5000-7.

[41] M.H. Müser, S. V. Sukhomlinov, L. Pastewka, Interatomic potentials: achievements and challenges, Adv Phys X. 8 (2023) 2093129. https://doi.org/10.1080/23746149.2022.2093129.

[42] R.O. Jones, Density functional theory: Its origins, rise to prominence, and future, Rev Mod Phys. 87 (2015). https://doi.org/10.1103/RevModPhys.87.897.

2 weFF: Full Atomic Charge Polarizable Force Field for Cementitious Systems: Bulk and Interface

Ziga Casar[1,$], Tecla Bottinelli Montandon[1], Manuel Cordova[2], Paul Bowen[1], Aslam Kunhi Mohamed[3,+], Karen Scrivener[1]

[1] Laboratory of Construction Materials, Institut des Matériaux, Ecole Polytechnique Fédérale de Lausanne (EPFL), CH-1015 Lausanne, Switzerland

[2] Laboratory of Magnetic Resonance, Institut des Sciences et Ingénierie Chimiques, Ecole Polytechnique Fédérale de Lausanne (EPFL), CH-1015 Lausanne, Switzerland

[3] Institute for Building Materials, Department of Civil, Environmental and Geomatic Engineering, ETH Zürich, CH-8093 Zürich, Switzerland

[+] Current address: Department of Civil Engineering, IIT Madras, Chennai-60036, Tamil Nadu, India

Contribution Statement

This chapter comprises the development and validation of a general-purpose force field for cementitious systems, with an emphasis on calcium silicate hydrates. This work will be soon published as a journal paper. The candidate's contributions include development of the zinc interatomic potentials as well as Lennard-Jones potentials, parametrizing the adiabatic core-shell model, running all the molecular dynamics simulations and writing the first draft.

Abstract

A general-purpose formal charge polarizable force field for cementitious systems (weFF) is presented. The force field includes the following atomic species: Ca, Si, O, H, Al, Zn, OH- and H_2O. The force field is validated by comparison of structural features, elastic constants, reaction enthalpies and vibrational density of states to experimental and ab initio values for known crystals. Particular attention is given to the tobermorite 14 Å structure, due to its

similarity to the main hydration phase, calcium silicate hydrate. The results are in excellent agreement with experimental and ab initio data over the entire range of simulated properties.

2.1 Introduction

The cement and concrete industry is responsible for 7-8% of anthropogenic CO_2 emissions [1]. While there are solutions on the horizon, they result in reduced early age strength of concrete [1,2]. The realization of those solutions is limited by the understanding of atomistic scale mechanisms of cement hydration, particularly of hydrated and anhydrous phases and their interactions with the complex high pH solution [3,4]. In the past 10 years considerable effort has been made in furthering our knowledge of the atomic scale structure of cementitious materials, particularly due to the use of molecular modelling techniques [5]. A persisting challenge is the study of the main hydration phase, calcium silicate hydrate (C-S-H). Due to its nanocrystalline structure the studied C-S-H computational models need to be of nanometer size [6], which hinders the use of ab initio methods, such as density functional theory.

The framework of classical molecular dynamics (MD) provides a good approximation of the physical world to explore the bulk [6–9] as well as the surface [3,10] properties of cementitious materials at the molecular level. However, the accuracy of MD simulations is determined by the accuracy of the underlying force field (FF), which is a collection of empirical interatomic potentials that describes the forces between atoms. For a detailed review of interatomic potentials, we refer the reader to the excellent review of Müser et al. [11]. In cementitious systems, several FFs are used, each with its advantages and limitations [12].

No FF is truly versatile, transferable and without limitations. For example, the popular general FFs ClayFF [13] and CSH-FF [14] do not predict the structure of C-S-H accurately (see Results section). Further, due to the lack of bond and angle parameters in silica parametrization the required partial charges are higher, which can lead to unphysically strong electrostatic interaction, consequently overpredicting adsorption phenomena on surfaces [15]. Due to the lack of accuracy in structural prediction the common practice is to use rigid surfaces or frozen bulk structures when investigating interfacial phenomena [16–19] This limits the mobility induced by the vibration of surface atoms, which again influences adsorption phenomena as well as slip along a surface [20,21]. On the other hand, the non-general FFs such as the Interface Force Field (IFF) [22] are precisely fitted to a small set of structures, therefore limited in

transferability. The shared disadvantage of all those FFs is the lack of polarization, which is discussed in section 2.1 below.

Valavi et al. [23] published the Erica FF2, a formally charged polarizable FF, which is developed from the CementFF family, with which portlandite and C-S-H structures were successfully investigated. [6,9,12,24,25]. Erica FF2 predicts the bulk properties of cementitious materials with high accuracy. The main advantage of this force field is the inclusion of the polarization of silicate oxygens, due to which the correct structural properties of the calcium silicate hydrates are achieved. The FF uses mainly the Buckingham interatomic potential, which is appreciated as a more stable function in comparison to the Lennard-Jones potential, due to the exponential-6 term [26]. The disadvantages of the Erica FF2 are the small time-step required due to the adiabatic core-shell (ACS) model for polarization [27], the use of the flexible SPC/Fw water model [28,29] and the Buckingham interatomic potential. Most empirical FFs are of Lennard-Jones format, which allows for the use of mixing rules, therefore allowing good transferability. Since there are no mixing rules between Buckingham and Lennard-Jones potentials, the transferability of Erica FF2 is thus limited.

In this paper we present further development and refinement of Erica FF2 [23], named weFF, to address the previously mentioned shortcomings. We present a systematic procedure to include metals based on potential parameters from Lewis and Catlow [30]. The procedure is demonstrated with the development of zinc interatomic potentials, which are validated on known structures and successfully predict the local atomic environment of zinc incorporated into the C-S-H structure [7]. The adiabatic core-shell model [27] for polarization is refined and results in energetically more stable structures over longer simulation times. In the spirit of transferability, the key interacting ionic species of C-S-H (Ca^{2+} and OH^-) are fitted to the Lennard-Jones potential form, which will enable the use of mixing rules when studying interphase phenomena at the solid-liquid C-S-H interface [Casar2023]. Finally, the TIP4P/2005 water model [31] is adopted as in the original CementFF [9], due to its superior ability to predict bulk solution properties as well as interactions at the surfaces [28,32].

2.2   weFF Parametrization

The predecessors of weFF (the CementFF family) were developed by carefully combining parameters from existing FFs. The calcium hydroxide parametrization was adopted from Freeman et al. [33] while the silica parametrization was previously used by Tilocca et al. [34]

and de Leeuw et al. [35]. Both FFs use the Buckingham potential form ($E_{ij} = A_{ij}e^{-r/\rho_{ij}} - C_{ij}/r^6$) to describe the short-range van der Waals (vdW) interactions between negative-negative and negative-positive ionic species. In addition to the Buckingham potential form Freeman et al. uses the Lennard-Jones 9-6 potential form ($E_{ij} = 4\varepsilon_{ij}\left[(\sigma_{ij}/r)^9 - (\sigma_{ijs}/r)^6\right]$) for the oxygen-hydrogen interactions.

The resulting CementFF FFs combined the above mentioned interatomic potentials and were extended by the addition of different water models [9,23,24], which are parametrized with the Lennard-Jones 12-6 (LJ) potential form ($E_{ij} = 4\varepsilon_{ij}\left[(\sigma_{ij}/r)^{12} - (\sigma_{ijs}/r)^6\right]$), and aluminium interactions of Buckingham potential form. In weFF the latest set of interatomic potentials of the CementFF family was adopted, further developed and validated as described in following. The atomic species included in weFF are listed in table 1.

Table 2-1. List of atomic species in weFF. More details on sources of species parametrization are listed in SI section 1.

Atomic species	Charge	Description
Ca	+2.0	Calcium
Si	+4.0	Silicon
O	+0.84819	Core oxygen
O(S)	-2.84819	Shell oxygen
O$_W$	-1.1128	Water oxygen
H$_W$	+0.5564	Water hydrogen
O$_H$	-1.4	Hydroxide oxygen
H	+0.4	Hydroxide hydrogen
Al	+3.0	Aluminium
Zn	+2.0	Zinc

2.2.1 Polarizability

Polarizability is the tendency of matter to acquire an electric dipole moment [36]. The induced dipole moments arise due to the electric fields emanating from nearby atom clusters. All atoms and molecules are polarizable. When subjected to an electric field the electron cloud of an

atom or molecule is distorted as response. The negatively charged electrons and positively charged atomic nuclei are subjected to opposite forces and undergo charge separation. Polarizability is responsible for a material's dielectric properties.

Typically, the effects of electronic polarizability and screening of electrostatic interactions are implicitly incorporated in the effective charges and other empirical parameters of the FF [37]. Non-polarizable FFs are drastically simplified, but still very successful in modeling many complex molecular systems. However, the incorporation of polarizability is particularly crucial for structures in which highly polarizable atoms or ions, most notably anions, are located in sites that deviate strongly from inversion symmetry. This particularly concerns oxygen in water, as well as in low-temperature tetrahedral network formers like silica [11]. As explained by Müser et al. [11], polarizability is necessary to accurately reproduce bond-angle distributions and the infrared absorption spectra of silica, as well as capturing the α-β transition in quartz. Further, polarizability is essential in obtaining accurate energetics in the vicinity of highly polar moieties, small ions, and anisotropic nonpolar environments. Including polarization in the studied systems can also accommodate the local disruption of hydrogen bond networks by anions, such as chloride, as well as to more accurately reproduce the induced dipole moment of the cation-molecule dimers and describe interfacial systems with better accuracy [38]. Lack of polarizability can result in unreliable results for defects [27], therefore it is crucial to include it when investigating C-S-H, which is a highly defective variation of the tobermorite crystal family.

2.2.1.1   *Adiabatic Core-Shell Model*

Mitchell and Finchman [27] developed the adiabatic core-shell (ACS) model, a simple method for adding polarizability to a system. The model falls under classical Drude oscillator models, where a pair of point charges represents dipoles of finite length [38]. Contrary to the Drude model, where the electronic induction is represented by the displacement of a charge-carrying massless particle attached to a polarizable atom [39], in ACS the mass of the atom is divided between the core and the shell, which are connected by a harmonic spring (bond). It is expected that the shells respond quickly to the changing electric field experienced by the ions and are allowed to freely oscillate around the core. This way the shells are polarized by the field of the surrounding ions and the local environment of each ion affects its charge distribution [34]. Due to the small shell mass (approximately 1% of oxygen mass in Erica FF2 [23]) no energy exchange between core-shell spring and other degrees of freedom should occur as the frequency

of the spring is well above the ionic frequencies [34]. However, a drift in the total energy can occur, if the system is not controlled properly [27,34]. The core and the shell each carry their own charge and the sum of charges equals the formal atomic charge [30] (in Erica FF2 the core has a charge of +0.84819 e, while the shell has -2.84819 e). Short range forces only act on shells. There are no Coulombic interactions between cores and shells.

The parametrization of silicates in weFF and the CementFF family [9,23] was adopted from Tilocca et al. [34] and de Leeuw et al. [35], who used the ACS model to add polarizability to the silicate oxygens for studying pure silica, sodium silicate, and soda-lime silicate glasses. The potentials were validated on experimental and ab initio structural data, such as density, radial and angular atomic distributions, coordination environments, and network connectivity. Their results show that inclusion of polarization effects improves the description of the tetrahedral connectivity and of the local environment surrounding modified Na and Ca cations. With this they obtained an improved Q^n distribution of the sodium silicate glass. Valavi et al. [23] observed that inclusion of polarizable silicate oxygens drastically improves the local environment surrounding Ca cations in the tobermorite 14 Å structure. The pairwise interactions were described by Buckingham potentials. Short-range forces between Si and other cations are excluded, since Si ions are shielded by oxygen atoms surrounding them. In addition to the two-body terms, the three-body forces and harmonic angle terms were included to control the O-Si-O angle. Due to the three-body term, partial covalence effects are approximately accounted for.

2.2.2 Water Model

For water, the predecessor of Erica FF2, namely CementFF3 [9], uses the rigid, 4-point TIP4P/2005 water model [31]. In Erica FF2 the water model was changed to SPC/Fw, which is a flexible 3-point model [29]. The first reason for the change in the water model was due to its good agreement of experimental data on dielectric constant, the relaxation times and thermal properties, as well as good results for transport properties [29,40,41]. The second reason being the much easier implementation of this model in LAMMPS [42,43].

The TIP4P/2005 water model is a rigid 4-point model which consists of three fixed point charges and one Lennard-Jones center [31]. The model was parametrized to fit the temperature of maximum density, the stability of several ice polymorphs and other commonly used target quantities. The model gives an impressive performance for a variety of properties and

thermodynamic conditions, positioning itself as one of the best water models [28,31,32,44,45]. Due to its excellent performance, it became widely popular for the development of FFs describing ions in aqueous solutions [32,46,47]. Further, Döpke et al. [32] compared the transferability of ion parameters from various water models to the TIP4P/2005 model. They showed that many parameters are easily transferable (most notably from the TIP4P/Ew model), which further confirms the wide usefulness of the TIP4P/2005 water model in molecular dynamics simulations. Since cementitious systems have ubiquitous solid-liquid interfaces, where the aqueous solution is composed of a wide variety of ionic species, we decided to re-adopt the TIP4P/2005 water model in weFF.

2.2.3 Lennard-Jones 12-6 Parametrization

The Buckingham potential form is considered more stable than the LJ potential form [26]. However, the LJ 12-6 potential form is the most widely used pair-potential [48]. One of the main reasons for this is that the individual atomic LJ parameters can be directly used without the need to derive the cross-interaction terms, which are obtained from suitable mixing rules are easily obtained from one of the mixing rules . This enables a wide range of well parametrized interatomic potentials which can be easily adapted and used.

In weFF, Ca^{2+} and OH^- ions were fitted to the LJ 12-6 potential form, as described below. These two ionic species are key ionic species in C-S-H and cementitious systems and are expected to play a significant role at the interface between the solid phase and the complex solution(see chapter 5). Further, the LJ 12-6 potential form for Al^{3+} was adopted from the literature [32,49] and is used to model the Al-O_H and Al-O_W interactions. With this, an improved description of the local environment of aluminates was achieved. The Zn^{2+} LJ potential was adopted from literature [50] and is used to model the Zn-O_W interaction.

The Zn-O_H and all interactions with the silicate oxygens O(S) were kept in Buckingham potential form. The Zn-O_H Buckingham potential form predicted the structural features of known crystals with better accuracy than the LJ 12-6 potential form which can be obtained by the mixing rule for Zn^{2+} and $O_H^{1.4-}$. The silicate oxygen interactions were kept in the Buckingham potential form since they would require a completely new reparameterization of the ACS model, pairwise interactions and harmonic angle terms.

2.3   Methods

Force field development can be classified into two categories: top-down and bottom-up [11]. In the bottom-up approach any electronic structure calculation is used to provide analytical results and/or small-scale data, such as forces on individual atoms as a function of the atomic configuration. Interatomic potentials are developed with the goal to replicate this information. In the top-down approach no atomic-scale information is provided. The properties to which the interatomic potentials are fitted are collective, macroscopic properties, such as unit cell parameters and pair distribution functions of known crystal structures, elastic properties, surface energies or phase transitions.

Both approaches are complementary to each other. By using both simultaneously, it is possible to minimize the risk of overfitting [11]. Thus, we employed both approaches. For top-down validation we compare the weFF predictions to structural parameters and elastic properties of known crystals. To validate weFF from the bottom-up approach we compare the calculated vibrational density of states (v-DOS) to the ab initio calculated one. All weFF parameters are listed in SI section 1.

2.3.1   Fitting of Parameters

2.3.1.1   Lennard-Jones 12-6 Potentials

In order to fit a LJ 12-6 potential function to the Buckingham one, a starting point had to be selected. Firstly, the mixing rule must be selected, for which we chose the Lorentz-Berthelot rule ($\varepsilon_{ij} = \sqrt{\varepsilon_i \cdot \varepsilon_j}$ and $\sigma_{ij} = (\sigma_i + \sigma_j)/2$) [51,52]. This rule is widely used in the literature and as long as the σ parameters are similar, the choice of the mixing rule has minimum effect on the result [53]. Afterwards the Ca^{2+} LJ parameter was selected. We chose the parametrization (ε_{Ca} and σ_{Ca}) from Mamatkulov et al. [54], since it predicts the experimental hydration free energy, coordination number, ion-oxygen distance and self-diffusion coefficient of Ca^{2+} in water with good accuracy [32]. At this stage we used the SciPy Python library [55], to fit the LJ potential function (adjustable parameters: ε_{Ca-Oh} and σ_{Ca-Oh}) to the Buckingham potential form (A_{Ca-Oh}, ρ_{Ca-Oh} and C_{Ca-Oh}) from Freeman et al. [33]. The fitting resulted in ε_{Oh} and σ_{Oh}, which were further refined in order to correctly predict the portlandite crystal structure.

With the obtained ε_{Oh} and σ_{Oh} the Al-O$_H$ and O$_W$-O$_H$ were calculated using the Lorentz-Berthelot mixing rule (see SI section 1).

2.3.1.2   *Potentials for Metals*

Lewis and Catlow [30] published a systematic approach for the derivation of empirical potential parameters for binary oxides. For fitting of the potential parameters, they used the top-down approach, where they fit the experimental data to replicate the structural, elastic, dielectric and lattice dynamical crystal properties. In their parametrization, they used the ACS model to add polarizability. While they used it for cations and anions, the cation polarizability is less strongly influenced by the crystal environment. The cation-cation interactions are purely Coulombic since cations are shielded by anions in oxides. The cation-anion interactions are described with the Buckingham potential form.

While the Zn-O(S) Buckingham interaction was adopted from Lewis and Catlow [30], the Zn-O$_W$ Lennard-Jones 12-6 interaction was calculated by the mixing rule, the Zn-O$_H$ Buckingham interaction had to be developed separately. To derive the Zn-O$_H$ Buckingham interaction, we kept the ρ parameter fixed to the value found for in the Zn-O(S) interaction of Lewis and Catlow [30]. The starting A parameter was chosen as $A = A_{Zn-O(S)} \cdot q_{Oh}/q_O$, where q_i is the charge of the respected oxygen species (q_O is the combined charge of the core-shell pair, -2 e). In an iterative process the interatomic potential was used in structure prediction of a reference crystal structure. In each iteration the A parameter was adjusted until the radial distribution function of Zn-O$_H$ agreed with the experimental data. Additionally, a harmonic angle term was considered for the O$_j$-Zn-O$_i$ (where i and j can be O(S) or O$_H$, respectively) connectivity in the zincate tetrahedra. This harmonic angle improved the structural prediction and prevented spontaneous 5-fold coordination of zinc. The parameters for the harmonic angle description were also found by a trial and error iteration.

2.3.2 Molecular Dynamics

All simulations were carried out with LAMMPS [42]. If not otherwise stated in the text the simulation duration was at least 10 ns, whereby the reported results are the average of the last 3 ns, when an equilibrium was reached. The system was considered in equilibrium if the energies and unit cell parameters fluctuated around constant values for 3 ns. All calculations were carried out at constant pressure and temperature (1 atm and 300 K), Noose-Hoover thermostat

and barostat, with flexible angles and simulation cell parameters in the case of solids (anisotropic NPT ensemble) and with constant cell geometry in the case of liquids (isotropic NPT ensemble). The time step was 0.28 fs. The kspace solver was the pppm/tip4p solver with a cutoff of 10 Å and an accuracy of 1e-4, as implemented in LAMMPS.

Simulations of structures which included the ACS model started with a pre-step to equilibrate the core-shells to prevent the drift of total energy, as described in by Mitchel and Fichman [27]. The detailed implementation is given in the LAMMPS documentation [42], is explained by Valavi et al. [23] and can be seen in the provided LAMMPS input files in the SI. The duration of this pre-equilibration can be as short as 1000 steps.

When calculating the enthalpy of the given system a few corrections need to be considered. LAMMPS calculates the enthalpy as $H = E_{Total} + p \cdot V$. In their calculations the contribution of the core-shells is not added, as well as the energy of the hydroxide bond. Therefore, the enthalpy used for the energetical validation is computed as follows:

$$H_{corr} = H + PotEng_{Core-Shell} + N_{Oh} \cdot D \tag{1}$$

where $PotEng_{Core-Shell}$ is the sum of the potential energy which arises due to the bonding of individual core-shell pairs, N_{Oh} is the number of hydroxyls and D is the depth of the potential well in the Morse potential form ($E_{ij} = D\left[1 - e^{-\alpha(r-r_0)}\right]^2$). The last contribution in equation 1 represents the energy correction for each Oh-H bond needed in the LAMMPS implementation of the Morse bond. Historically, the force field was developed in conjunction with the DL Poly molecular simulation package [56]. Since the Morse potential description of DL Poly is slightly different ($E_{ij} = D\left[1 - e^{-\alpha(r-r_0)}\right]^2 - D$), the correction is used to enable the comparison of the force fields.

The elastic constants calculations were carried out at finite temperature as implemented in LAMMPS. First the structures were equilibrated for 10 ns. The final atomic configuration of the equilibration was used as the initial configuration for the elastic constant calculation. For the calculation small deformations in the linear regime to the simulation box in the canonical NVT ensemble are applied. For a detailed description of the simulation protocol, we refer the reader to the Erica FF2 paper of Valavi et al. [23].

The vibrational density of states (v-DOS) was calculated with the TRAVIS software [57,58]. The structures were first equilibrated for 20 ns. Afterwards the trajectories were saved every 0.84 fs over a period of 14 ps, from which the spectra were calculated. The autocorrelation function for the v-DOS calculation was weighted by atomic mass. The frequency shift of the Verlet integrator was not corrected, since with and without the correction gave identical results. Global and projected v-DOS were calculated. To exclude the influence of the time step, the length and saving interval of trajectories, the time step was reduced to 0.15 fs, the trajectories were saved every 0.3 fs and the duration was increased to 30 ps. The input files for TRAVIS are provided as part of SI.

2.3.3 DFT Elastic Constants Calculation

The crystal structures of ε-Zn(OH)$_2$ and clinohedrite were obtained from materials project [59] (ID: mp-625830 and mp-696853, respectively). All computations were carried out using the plane-wave density functional theory (DFT) software Quantum ESPRESSO, version 6.5 [60,61]. All computations were performed at the PBE level of theory [62] using Grimme D2 dispersion correction [63] and projector augmented wave [64] scalar relativistic pseudopotentials obtained from PSlibrary version 1.0.0 [65]. Wavefunction and charge density energy cutoffs were set to 100 Ry and 800 Ry, respectively. 4x3x2 and 3x3x1 Monkhorst-Pack grids of k-points [66] were used for ε-Zn(OH)2 and clinohedrite, respectively.

Elastic constants were obtained using the ElaStic software [67]. The atomic positions and lattice parameters of the initial crystal structures were first optimized while retaining the space group of the crystal structure, then 21 distorted structures with a maximum absolute Lagrangian strain of 0.08 were generated for each deformation type using the ElaStic software. The energy of each distorted structure was obtained after optimization of atomic positions.

For each deformation type, the strain-energy relationship was fitted using 4-th or 6-th order polynomial functions, discarding points deviating from the expected harmonic behavior at large strain values when required, as described in [67]. All energy-strain curves are shown in SI section 6.

2.4 Results

In this section, we summarize the results of weFF validation. First, the improved equilibration of the ACS model is introduced. Second, the newly developed parameters of weFF are validated on known crystal structures. Third, weFF is tested and compared to other FFs in predicting the adsorption of Ca^{2+} at the SiO_2 surface and predicting the tobermorite 14 Å structure, a crystalline calcium silicate hydrate. Finally, weFF is tested on a hypothetical C-S-H structure with incorporated zinc, which was relaxed with density functional theory.

2.4.1 Core-Shell Equilibration

The original parametrization of the silicates in Erica FF2 uses the ACS model for oxygen atoms. The distribution of mass is 15.79 g/mol on the oxygen core and 0.2 g/mol on the oxygen shell. The calculations were carried out for 1 ns, whereby a drift in the total energy was not noticed (sm0.2 in figure 1a). From longer calculation times (20 ns production run in NPT ensemble) it is evident that an increase in the total energy occurs, roughly at 0.75 eV/ns for tobermorite 14 Å. While the kinetic energy of the system remains constant, the potential energy increases which contributes to the increase of the total energy of the system. When monitoring the movement of the cores and shells an increase in the potential energy of the core-shell pairs is observed (figure 1b). This increase can be related to the increase of the kinetic energy (shown as velocity in figure 2), since shells which are oscillating around the cores keep gaining momentum, therefore moving further away from the cores.

While it is possible to regulate the system by adjusting the damping parameters of the thermostat and barostat, this had a minimal effect, and it did not solve the problem of the energy drift (see SI figure S1). The drift in energy is related to the increase of the core-shell potential energy and can be prevented in one of two ways. First, with a lower time step. If the timestep is decreased from 0.2 fs to 0.1 fs the energy drift does not occur. However, due to the already small time-step (in comparison to nonpolarizable force fields) the further decrease in the time step is not desired. The second approach is by adjusting the mass distribution between the core and the shell. The mass of the core was decreased to 15.59 g/mol, while the mass of the shell was increased to 0.4 g/mol. With this, the potential energy of the core-shell pairs and the kinetic energy of the shells remained constant (figure 1b and 2). No structural changes between the different ACS parametrizations in the tobermorite structure were observed (see SI section 3).
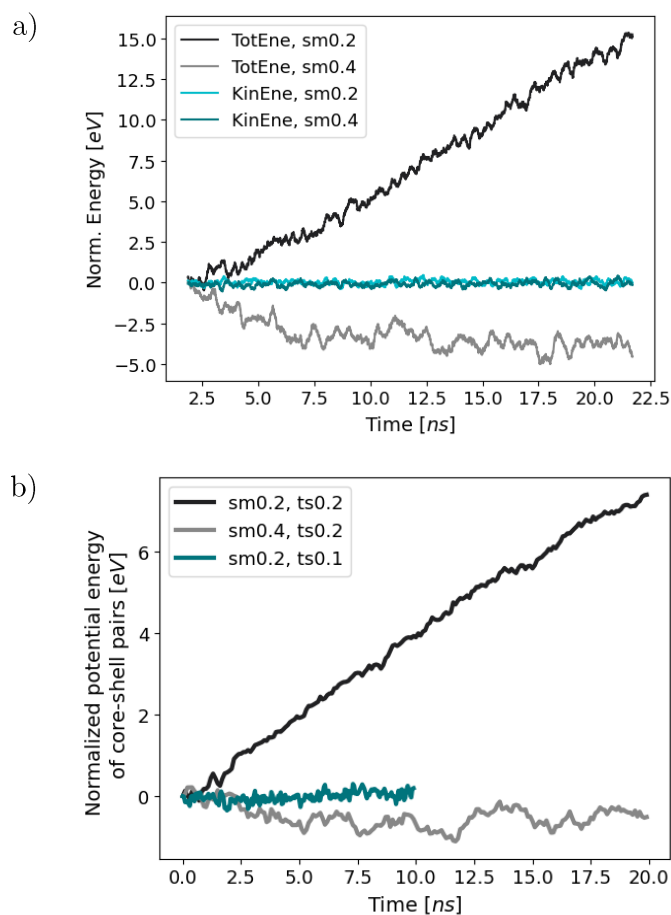
Figure 2-1: a) change of total (TotEne) and kinetic (KinEne) energy of tobermorite 14Å during the 20 ns production run for shell mass 0.2 g/mol (sm0.2) and 0.4 g/mol (sm0.4); b) total potential energy of all core-shell pairs normalized to the initial value during

2.5   Validation

2.5.1   Structural Validation

weFF was used to simulate 12 structures which are relevant for cementitious systems. The structures were chosen based on the local atomic arrangement, which are similar to those in cementitious systems. The deviation in unit cell parameters between the MD predicted structures and experimental references is given in table 2 and the exact values are given in SI section 4. While it is beyond the scope of this manuscript to discuss the structural details of all compounds considered, some of them will be addressed.
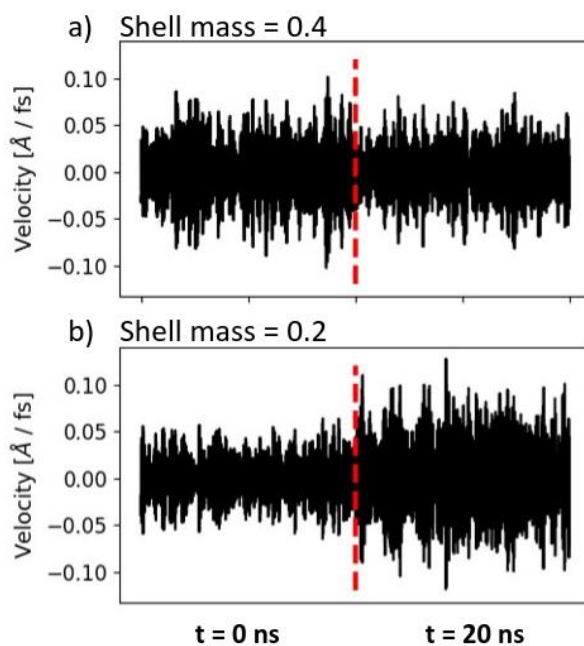
Figure 2-2. The relative velocity of the shell to the core. a) shell mass 0.4 g/mol and b) shell mass 0.2 g/mol. The left side of each graph is the relative velocity of the shell at the start of the equilibration run and on the right side the relative velocity of the shell at the end of the production run.

As seen in table 2, compounds not containing hydroxyl groups are successfully predicted by weFF. Except for $Ca_3Al_2O_6$ which deviates from the experimental reference by roughly 5.5%. This is attributed to the overestimation of the first shell Al-O distance of the aluminium tetrahedra (calculated 2.00 Å versus experimentally determined 1.75 Å). Other distances (Ca-O, Al-Ca) are in good agreement with the experiments (deviation below 2%). However, the octahedral Al polyhedra in Al_2O_3 are accurately modeled (Al-O distance calculated 1.91 Å versus experimental 1.91 Å).

Since the tobermorite structure has a close resemblance to the C-S-H structure it is discussed in a separate section.

2.5.1.1 Hydroxides

The first hydroxide of interest is portlandite ($Ca(OH)_2$), due to its importance in cement hydration. The crystalline structure of portlandite is today very well-known [68]. As seen in table 2, the unit cell expands 2.24% in the a and b-direction, while shrinks by 4.12% in the c-direction. This is comparable to Erica FF2 where the expansion in a and b-direction measured 2.18% and the shrinkage in c-direction 3.85%. The closer examination of the radial distribution

functions (RDF, see SI section 3) reveals an excellent match of the first peaks of Ca-O_H RDF (2.41 Å for MD, and 2.38 Å experimental) and Ca-H RDF (2.98 Å for MD and experiment). The calcium atoms are octahedral coordinated to six oxygen atoms, which is captured by the FF. The structural difference becomes evident after analyzing the O_H-O_H RDF, where the FF predicts the first peak at 3.2 Å, while the experimental O_H-O_H distance is 3.05 Å. This peak corresponds to the smallest distance of two oxygens inside the same calcium octahedra. The structure of portlandite consists of stacked [Ca(OH)$_6$] layers lying in the (001) plane. The layers interact mainly through weak H-mediated dispersive forces [68]. The second peak (3.3 Å) of the experimental O_H-O_H corresponds to the oxygen atoms of neighboring layers and is missing from the computed RDF. This also explains the rather large deviation in the c-direction. While the FF accurately predicts the distances of the first coordination shell, it less accurately describes the interactions between the hydrogen and oxygen atoms. This becomes more evident after analyzing the other hydroxides from table 2.

Table 2-2. Structural validation of weFF. The deviation of unit cell parameters between MD predicted structures and references is given. The exact values are given in table S8.

Structure	a dev	b dev	c dev	α dev	β dev	γ dev
CaO	0.18%	0.19%	0.19%	0.00%	0.00%	0.00%
Ca(OH)$_2$	2.24%	2.24%	-4.12%	0.00%	0.00%	0.00%
Al(OH)$_3$	9.58%	8.38%	10.10%	0.00%	1.34%	0.00%
Ca$_3$Al$_2$O$_{12}$H$_{12}$	7.87%	7.87%	7.87%	0.00%	0.00%	0.00%
SiO$_2$	0.05%	0.05%	2.58%	0.00%	0.00%	0.00%
Ca$_3$Al$_2$O$_6$	5.18%	0.04%	5.47%	-0.08%	-0.10%	0.04%
CaSiZnO$_5$H$_2$	2.06%	0.76%	0.07%	0.00%	1.98%	0.01%
CaZn$_2$Si$_2$O$_7 \cdot$ H$_2$O	2.33%	-1.46%	0.17%	-2.66%	-0.02%	0.50%
Ca$_2$Si$_2$ZnO$_7$	2.50%	2.50%	-0.52%	0.01%	0.00%	0.00%
Zn$_2$SiO$_4$	-1.14%	-1.14%	1.31%	0.00%	0.00%	0.00%
ZnO	-1.00%	-1.00%	-0.89%	0.00%	0.00%	0.01%
ε-Zn(OH)$_2$	9.53%	4.40%	-5.74%	-0.01%	-0.03%	-2.24%
β-Zn(OH)$_2$	1.57%	1.57%	4.42%	0.00%	0.00%	0.00%

Now considering gibbsite ($Al(OH)_3$). The resulting deviation of unit cell parameters is roughly 10%. The predicted structure with the Erica FF2 for gibbsite deviates in the a, b and c-direction by 15%, 19% and 19%. weFF predicts the $Al-O_H$ distance at 2.1 Å, while Erica FF2 predict 1.87 Å. The experimentally measured distance of $Al-O_H$ of the aluminium octahedral is 1.93 Å. While Erica FF2's first shell distance is more accurately described, it predicts a 4-fold aluminium oxygen coordination. Gibbsite's aluminium atoms are 6-fold coordinated, which is captured by the Lennard-Jones potential form of weFF.

There are two different zinc hydroxide ($Zn(OH)_2$) crystals. First is the ε-$Zn(OH)_2$ where zinc is tetrahedrally coordinated to four oxygens, and second is the β-$Zn(OH)_2$, where zinc is in octahedral coordination with six oxygens. Similarly, as for gibbsite weFF predicts the ε-$Zn(OH)_2$ structure with relatively large deviations (9.53%) in the unit cell parameters. However, weFF accurately predicts a 4-fold coordination with an average first shell $Zn-O_H$ distance deviation of 5%. The structural ordering of the zinc tetrahedra comes from hydrogen bonds between the hydroxyl groups of neighboring tetrahedra. Today it is known that the origin of the hydrogen bond arises from quantum mechanics and that the classical type (exchange free) London dispersion and electrostatic 'dipole-dipole' forces play only a secondary role [69]. Therefore, it is of no surprise that classical empirical force fields have limited capabilities in correctly describing structures, which strongly depend on hydrogen bonding. weFF successfully predicts the β-$Zn(OH)_2$ with 6-fold coordinated zinc. The deviation of the Zn-Oh first shell distance is 2.5%.

2.5.1.2   *Energetical Validation*

A unique but an essential validation that is carried out for CementFF family of FFs is the energetical validation on certain relevant chemical reactions for cementitious systems [23]. This not only gives us a way to estimate the error associated with weFF in calculating energies but also ensures the transferability of weFF to a wide range of systems. As classical FFs cannot simulate bond breakage, a correction has to be added for any reactions involving the conversion of water and oxide ions into hydroxyl ions or vice versa. This correction is calculated using the reactions listed in table 3. The average correction for each reaction per water molecule is taken as the correction factor for water splitting and is equal to -2.82 eV/H_2O. All the reactions we have selected for the energetic validation are listed in table 4. The error estimation for these reactions are according to the methodology developed for CementFF1 [70].

Table 2-3. Reaction for calculated water splitting correction. All values are in eV.

Reaction	H_{sim}	H_{exp} [71]	H_{corr}
$Ca(OH)_2 \rightarrow CaO + H_2O$	5.54	0.66	-4.88
$[Si(OH)_4]_{aq} \rightarrow SiO_2 + 2H_2O$	-3.05	-6.27	-1.61
$AlOOH + H_2O \rightarrow Al(OH)_3$	-4.05	-0.11	-3.94
$Al_2O_3 + 3H_2O \rightarrow 2Al(OH)_3$	-3.08	-0.46	-0.87

The reaction enthalpies are calculated as $\Delta H_{MD} = \sum S_i^P H_i^P - \sum S_i^R H_i^R$, where S_i is the stoichiometry coefficient, H_i is the enthalpy and the superscripts P and R represent products and reactants, respectively. In the case of aqueous species, the energy of the aqueous species is estimated based on the energy difference between two boxes of water with the same number of water molecules but with and without the aqueous species.

As seen in table 4 the calculated reactions enthalpies are within the error estimation for non-hydroxides. The reactions 3, 4, 8, 9, 10 and 11 are outside the error estimation. Those reactions are the ones which indicate a transition from a hydroxide to an oxide. As already explained in the structural validation section, pure hydroxides are very difficult to simulate correctly, due to the limitation of modeling hydrogen bonding with empirical interatomic potentials.

2.5.1.3 Mechanical Validation

Elastic properties are among the most important properties of solids [72]. Therefore, any potential should be tested for its ability to reproduce the elastic tensor of crystalline references. The individual components of the elastic tensor (c_{ij}) give a good estimation of the accuracy of weFF then the bulk properties and can be used for further development of the FF [73]. However, elastic constants are not uniquely defined, except at zero stress and zero temperature. Different definitions lead to deviations of the external stress order [11]. Further, the discrepancy between experimentally determined elastic constants can be higher than 100% [74].

The potential parameter from Lewis and Catlow [30], which is used to describe the Zn-O(S) interaction was constructed by fitting the elastic constants of the calculated structures to the experimental ones. This is seen in the excellent agreement between the MD calculated

individual components of the elastic tensor with experimental and DFT reported values for Hardystonite ($Ca_2ZnSi_2O_7$), Zincite (ZnO) and Clinohedrite ($CaZnSiO_4 \cdot H_2O$) (see table 5).

Table 2-4. Reactions for energetic validation. Errest is the estimated error as defined by Galmarini et al. [70]. All values are in eV.

#	Reaction	ΔH_{MD}	ΔH_{EXP} [71]	Err_{est}
1	$Ca(OH)_2 \rightarrow (Ca^{2+})_{aq} + 2(OH^-)_{aq}$	-0.86	-0.19	0.61
2	$2H_2O + SiO_2 \rightarrow (Si(OH)_4)_{aq}$	8.70	6.27	2.30
3	$Ca(OH)_2 + SiO_2 \rightarrow (CaSiO_4H_2)_{aq}$	-2.95	2.44	0.56
4	$(Ca^{2+} + 2OH^-)_{aq} + (Si(OH)_4)_{aq} \rightarrow (CaSiO4H2)_{aq} + 2H_2O$	-12.51	-3.62	3.12
5	$AlOOH + H_2O \rightarrow Al(OH)_3$	-1.22	-0.11	1.16
6	$3Ca(OH)_2 + 2Al(OH)_3 \rightarrow Ca_3Al_2(OH)_{12}$	1.88	-0.42	3.98
7	$3CaO + Al_2O_3 + 6H_2O \rightarrow Ca_3Al_2(OH)_{12}$	-0.88	-2.50	3.90
8	$3CaO + 2Al(OH)_3 + 3H_2O \rightarrow Ca_3Al_2(OH)_{12}$	-6.28	-5.00	0.90
9	$Al_2O_3 + 3H_2O \rightarrow 2Al(OH)_3$	5.40	-0.46	2.56
10	$Ca(OH)_2 \rightarrow CaO + H_2O$	2.72	0.66	0.72
11	$2Ca(OH)_2 + SiO_2 \rightarrow 2CaO + (Si(OH)_4)_{aq}$	14.14	7.6	3.66

Next, we examine the elastic constants of portlandite. First, the calculated bulk modulus (K) with the new Lennard-Jones potential form for Ca-O_H of weFF is closer to experimental measurements than Erica FF2. Portlandite exhibits a large elastic anisotropy in compressional (c_{11} and c_{33}) and shear elastic coefficients (c_{66} and c_{44}). This corresponds to a larger stiffness and rigidity in the basal plane with respect to the axial direction [74]. As seen in table 5, the shear elastic coefficients are in better agreement with the experimental data than the compressional coefficients. The overestimation of the compressional coefficients can be related to the previously reported structural characteristics of portlandite (see section Structural validation). The shrinkage in the c direction hints to a stronger interaction between the basal [Ca(OH)$_6$] layers, resulting in higher compressional coefficients.

Table 2-5. Elastic constants c_{ij} in Voigt notation. All constants are in GPa. For hardystonite average c is reported in brackets, calculated as $c = (c_{11} + c_{12} + c_{13} + c_{33} + c_{44} + c_{66})/6$. K is the bulk modulus and G is the shear modulus. Zincite DFT calculated values are from The Materials Project entry mp-2133 [59].

	c_{11}	c_{12}	c_{13}	c_{22}	c_{33}	c_{44}	c_{66}	G_1	G_2	K
Hardystonite	164.4	77.6	54.0		168.7	16.0	63.0	40.1	51.5	98.3 (90.3)
Exp [75]	163.3	81.0	55.3	-	159.9	29.9	57.3	-	-	- (88.4)
Zincite	221.5	88.9	88.0	224.3	193.4	71.6	67.4	63.1	71.3	128.9
Exp [76]	209.7	121.1	105.1	-	210.9	41.5	44.3	-	-	-
DFT [59]	188.0	109.0	92.0	188.0	205.0	37.0	39.0	42.0	-	130
Clinohedrite	187.4	60.4	79.4	131.1	172.1	55.8	59.9	56.6	45.8	102.4
DFT	142.6	64.7	58.5	183.4	122.6	49.7	38.0	-	45.5	93.2
Portlandite	168.2	44.9	8.1	165.5	32.0	16.5	56.5	29.3	49.0	56.6
Erica FF2	159.4	81.2	20.2	156.9	32.8	3.8	42.0	18.4	37.3	66.5
Exp [77]	99.3	36.2	29.7		32.6	9.9	31.6			46.9
Exp [74]	102.0	32.0	8.4		33.6	12.0	34.3			36.4
Tobermorite	111.2	38.4	20.3	112.7	66.3	2.4	44.4	20.2	35.3	49.7
Erica FF2 [23]	99.4	46.4	19.0	130.7	60.6	26.2	39.4	24.0	35.2	49.9
DFT [9]	-	-	-	-	-	-	-	-	-	49.0
Exp [78]	-	-	-	-	-	-	-	-	-	47 ± 4

2.5.2 Ion-Surface Interaction

In order to evaluate the adsorption of Ca^{2+} weFF is compared to another FF. The reference FF is the one used by Bischoff et al. [79]. In this study they successfully combined molecular dynamics and polarimetric angle-resolved second harmonic scattering to explore ion-specific adsorption effects at the SiO_2 surface. The used FF is a classical FF which uses the Lennard-Jones potential form and employs partial charges.

The used simulation box (see figure S4) was of size 5.5, 3.9 and 8.0 nm in the x, y and z-axis directions. In the middle of the simulation box was the solution slab (3762 water molecules, 24 Ca^{2+} and 16 Cl^- ions), which was enclosed on each side, in the z-axis direction, with 4 layers of crystalline SiO_2. While the simulation box had periodic boundary conditions in the x and y-axis direction, it had a fixed wall boundary condition in z-axis. The fixed wall was used to prevent artificial polarization due to periodicity effects in the treatment of electrostatic interactions [21]. On each surface 12.5% (16 out of 128 per surface) of the silanol groups were deprotonated. Except for the surface silicate layer, the bulk SiO_2 structure was frozen. Identical initial structures were used for both FFs. The simulations were 50 ns long, whereby the results were averaged over the last 4 ns. The plotted density profiles were averaged over each half of the simulation box. The simulation was carried out in the canonical (NVT) ensemble.

Table 2-6. Percentage of adsorbed Ca^{2+} by type of adsorption.

	Inner-sphere	Outer-sphere	Diffuse layer	Bulk solution
weFF	22.4 %	17.7 %	41.4 %	18.5 %
Bischoff et al. [79]	23.0 %	13.3 %	18.2 %	45.5 %

To compare the results the distribution of Ca^{2+} between inner-sphere, outer-sphere, diffuse layer and bulk solution was examined. The results are shown in table 6. Inner-sphere adsorption is considered if a Ca^{2+} is closer than 3.15 Å to a silicate oxygen (below 2 Å in figure 3), outer-sphere if closer than 5.15 Å (between 2 and 4 Å in figure 3). Ions are counted as being in the diffuse layer if they're not inner or outer-sphere adsorbed but less than 15 Å from the surface [79]. All remaining ions are considered as part of the bulk of solution. The amount of inner and outer-sphere adsorbed Ca^{2+} predicted by both FFs is comparable. A difference is observed in the structuring of the diffuse layer and bulk solution, where the FF from Bischoff et al. favors Ca^{2+} in the bulk of solution over the diffuse layer. The difference could be partially attributed to weFF's tendency to adsorb a small amount of Cl^- ions close to the SiO_2 surface, as seen in figure 4. Adsorption of Cl^- due to the attraction to positively charged hydrogens of silanol groups increases the negative charge close to the surface, which would attract more Ca^{2+}.

2.6 Calcium Silicate Hydrates

2.6.1 Tobermorite 14 Å

FFs which are meant to study the main cement hydration phase C-S-H should always be compared with respect to the structures of the tobermorite crystal family. In particular to tobermorite 14 Å, due to its resemblance with the C-S-H structure [6,8]. All calculations were carried out on a tobermorite 14 Å super cell of 4x4x1 crystalline unit cells [80]. The simulation details are given in the Methods section.

Table 7 reports the unit cell parameters for three FFs: the widely used non-polarizable CSH-FF [14], Erica FF2 [23] and weFF. As seen CSH-FF fails to replicate the unit cell of tobermorite, particularly the c direction, where an expansion of the interlayers occurs. Erica FF2 replicates the unit cell with satisfactory accuracy, with a 4% deviation in the β angle. weFF differentiates from Erica FF2 in the use of the TIP4P/2005 water model, as well as calcium-hydroxide, calcium-water and hydroxide-water interactions. The change of those parameters improved the prediction of the unit cell.
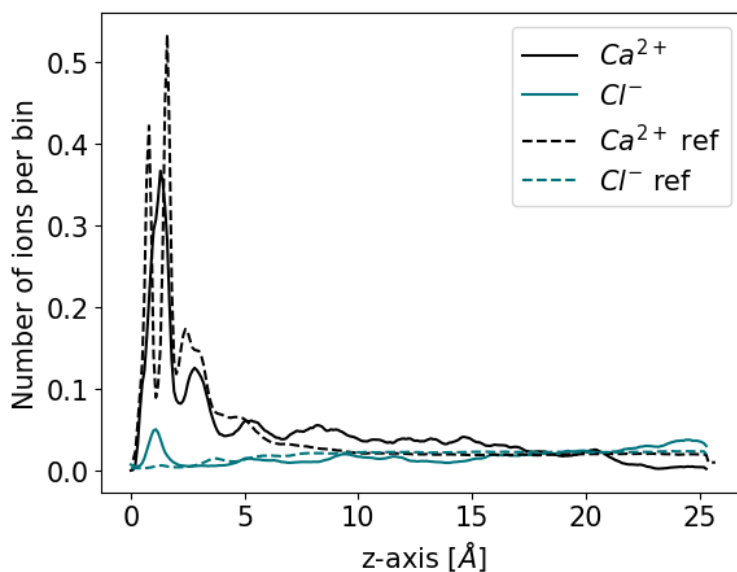
Figure 2-3. Ion distribution through the solution slab. The reference results correspond to the FF used by Bischoff et al. [79].

The calculated pair distribution function (PDF) (figure 4) shows an excellent agreement of Erica FF2 and weFF with the experimentally reported distances. CSH-FF already fails to

correctly describe the calcium-silicate main layers. This is a consequence of a poor description of the silicate tetrahedra (without polarizability) and the Ca-O interactions, which is reflected in the under-coordination of calcium (figure S5).

Table 2-7. Comparison of unit cell parameters as predicted by different force fields.

Force Field	a dev	b dev	c dev	α dev	β dev	γ dev
CSH-FF	8.98%	8.41%	17.03%	-1.62%	-3.15%	0.58%
Erica FF2	-0.05%	0.55%	1.51%	-0.59%	4.01%	0.31%
weFF	-0.15%	0.38%	1.61%	-0.27%	-0.12%	0.26%

Further confidence in the predicted tobermorite 14 Å structures comes from the calculated elastic tensor (table 5). Both Erica FF2 and weFF predict the bulk modulus (K) with very good accuracy. However, to our knowledge there are no individual components of the elastic tensor reported in the literature, and therefore a detailed comparison of the two force fields is not possible.
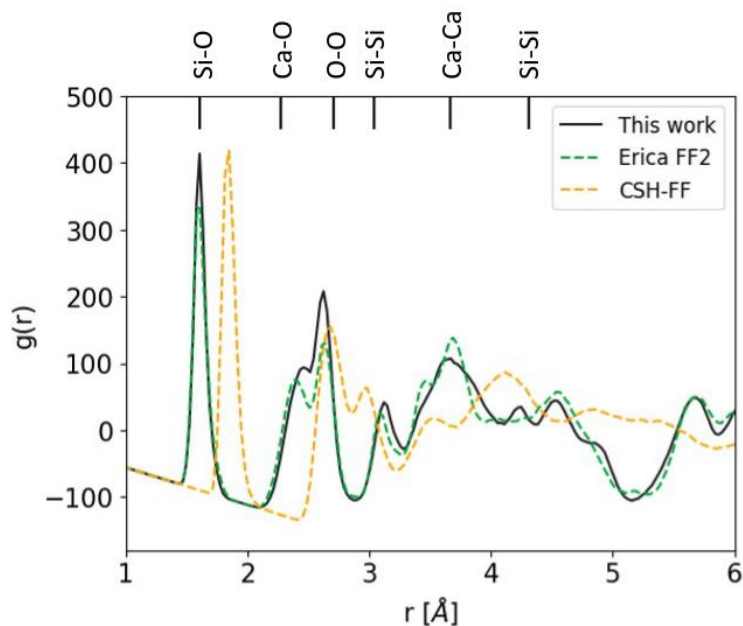
Figure 2-4. Pair distribution function calculated for the tobermorite 14 Å structure, as predicted by different FFs. The top lines correspond to the typical distances between atomic species as reported by Bonacorsi et al. [80]

2.6.1.1   *Vibrational density of states (v-DOS)*

Power spectra, also known as v-DOS, are obtained from the Fourier transform of the velocity autocorrelation function. v-DOS is not based on selection rules but contains all motions of a system [58]. The calculated spectra are a sum of the infrared (IR) spectrum, the Raman spectrum and all motions that are neither IR nor Raman active [57]. The calculated spectrum reflects the force constants for bond stretching and angle bending in the FF [81]. Since the experimentally obtained spectra hold detailed information on molecular structure and dynamics, with enough precision to analyze the hydrogen bonding patterns, they can be used to test the quality of the FF [82]. The comparison to experimental data not only provides information on the correctness but also the relevance of dipolar polarizability [11].

The MD calculated v-DOS of tobermorite 14Å is compared to the first-principles calculation from Vidmer et al. which is in excellent agreement with experiments (see table S9) [83]. Figure 5 shows the comparison of the total v-DOS, while the projected v-DOS for each atomic species are given in SI (figure S6).
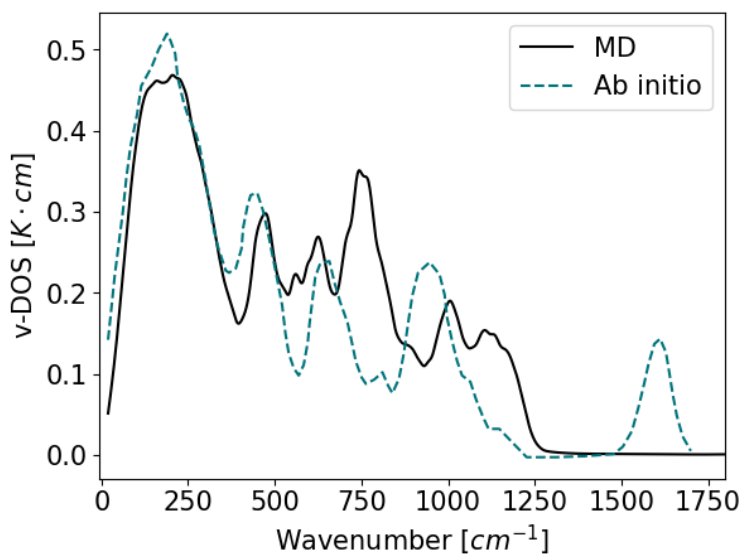
Figure 2-5. Total vibrational density of states (v-DOS) for the tobermorite 14Å structure as predicted by weFF (MD) and first-principles calculation (Ab initio) [83]. The projected v-DOS for each atomic species are shown in figure S6.

Our full charge polarizable force field replicates the ab initio v-DOS with good accuracy. The first half of the first peak (100-200 cm^{-1}) in figure 5 corresponds to the deformation of Si tetrahedra and Ca polyhedral, while the second half (200-350 cm^{-1}) corresponds to the

deformation of Ca polyhedral only. The second peak (370-520 cm^{-1}) corresponds to the deformation of Si tetrahedra. H_2O vibrations are observed around 510, 650 and 705 cm^{-1}. The vibrational band at 650 cm^{-1} is also assigned to the O-Si-O bending, as seen in the projected v-DOS (SI section 5). The vibrational bands between 815 and 1120 cm^{-1} are due to Si-O stretching. The final peak in the MD v-DOS (around 1200 cm^{-1}) is due to water interaction with O-Si, as indicated by the Si, O and H projected v-DOS. The Ab initio predicted band at 1610 cm^{-1} is absent for our force field, since it is assigned to water bending and the used TIP4P/2005 water model is a rigid model.

In conclusion, we showed that weFF yield energetically stable calculations over long simulation times. weFF also replicates the structural, mechanical and vibrational properties of the tobermorite 14 Å structure with very good agreement with experimental and ab initio data reported in the literature.

2.6.2 Zn-C-S-H

Finally, we compare weFF with a density functional theory (DFT) calculated C-S-H structure. The chosen structure is taken from Morales et al. [84], who investigated the incorporation of zinc into the C-S-H structure. The structure is a C-S-H defective unit cell with a zinc tetrahedra replacing the Q^{2b} silicate. This was shown to be the most common incorporation site of zinc in C-S-H[84]. The tetrahedral coordination of the zinc atom is achieved with two oxygens which are shared with neighboring $Q^{2p,Zn}$ silicates and with two hydroxyl groups, which are pointing into the interlayer. The C-S-H defective unit cell was multiplied in all axis direction to create a super cell of dimensions 4x4x3 defective unit cells. The simulation was carried out as stated in the methods section.

Tables 8 and 9 summarize the comparison of the MD predicted structure with the DFT relaxed structure from Morales et al. [84]. The unit cell parameters are well replicated, with the biggest deviation in the c unit direction (5.3%). The first peak of the RDFs show a very good match between the MD and DFT results. The biggest deviation occurs for the Zn-O distance, which is underpredicted by 4.6%. However, the DFT results are at 0 K, while the MD simulation was carried out at 298.15 K.

Table 2-8. Calculated unit cell parameters for Zn-C-S-H. DFT results are from Morales et al. [84]

	MD	DFT	Dev %
a	6.67 Å	6.62 Å	0.8%
b	7.44 Å	7.46 Å	-0.3%
c	14.59 Å	13.86 Å	5.3%
α	106.00 °	106.34 °	-0.3%
β	95.28 °	95.79 °	-0.5%
γ	124.53 °	123.01 °	1.2%

Conclusions

The present paper describes the further development and validation of a general purpose full charge polarizable force field for cementitious systems (weFF). While inclusion of polarizability is needed for the correct structural description of calcium silicate hydrates, it is shown that care must be taken when equilibrating the systems to prevent a drift of total energy. A methodology for the inclusion of transition metals into the force field is presented and validated with respect to experimental measurements and DFT predictions. While the force field correctly predicts the first bond distances of hydroxides, it fails to replicate the long ranger ordering. This is due to the challenge of predicting hydrogen bonding with classical empirical force fields. The key ionic species of C-S-H (namely Ca^{2+} and OH^-) are fitted to the Lennard-Jones potential form, which will enable the use of mixing rules for studying surface phenomena. The Ca^{2+} adsorption on quartz surfaces gave comparable results to an established force field from the literature.

Table 2-9. Comparison of first peak reported radial distribution functions for Zn-C-S-H. DFT results are from Morales et al. [84]

	MD [Å]	DFT [Å]
Zn-O	1.88	1.95
Zn-Oh	1.85-2.2	2.0
Si-O	1.63	1.65
Ca-O	2.35	2.35
Ca-Oh	2.57	2.42-2.58

Finally, the force field is validated on the tobermorite 14 Å structure due to its similarity to the calcium silicate hydrate structure. Unit cell parameters as well as atomic distances are in excellent agreement with experimentally reported values. Elastic constants, which are one of the most important properties of materials, are also in excellent agreement with experimental values. To access the correctness of the force field at the atomic level the vibrational density of states is calculated and compared to an ab-initio calculated one. Again, the force field performs very well. All key vibrational modes of silicates and calcium are captured. These findings demonstrate that cementitious systems (bulk and surfaces) can be explored using this force field with sufficient accuracy to obtain reliable results.

References

[1]   K.L. Scrivener, V.M. John, E.M. Gartner, Eco-efficient cements: Potential, economically viable solutions for a low-CO2, cement-based materials industry, Cem Concr Res. 114 (2018) 2–26. https://doi.org/https://doi.org/10.1016/j.cemconres.2018.03.015.

[2]   B. Lothenbach, K. Scrivener, R.D. Hooton, Supplementary Cementitious Materials, Cem Concr Res. 41 (2011) 1244–1256.

[3]   O. Heinz, H. Heinz, Cement Interfaces: Current Understanding, Challenges, and Opportunities, Langmuir. 37 (2021) 6347–6356. https://doi.org/10.1021/acs.langmuir.1c00617.

[4]   E. Duque-redondo, P.A. Bonnaud, A comprehensive review of C-S-H empirical and computational models , their applications , and practical aspects, (n.d.).

[5]   A. Kunhi Mohamed, A. Bouibes, M. Bauchy, Z. Casar, Molecular modelling of cementitious materials: current progress and benefits, RILEM Technical Letters. 7 (2022) 209–219. https://doi.org/10.21809/rilemtechlett.2022.175.

[6]   A. Kunhi Mohamed, S.C. Parker, P. Bowen, S. Galmarini, An atomistic building block description of C-S-H - Towards a realistic C-S-H model, Cem Concr Res. 107 (2018) 221–235. https://doi.org/10.1016/j.cemconres.2018.01.007.

[7]   A. Morales-Melgares, Z. Casar, P. Moutzouri, A. Venkatesh, M. Cordova, A. Kunhi Mohamed, K. L. Scrivener, P. Bowen, L. Emsley, Atomic-Level Structure of Zinc-Modified

Cementitious Calcium Silicate Hydrate, J Am Chem Soc. 144 (2022) 22915–22924. https://doi.org/10.1021/jacs.2c06749.

[8]   A. Kumar, B.J. Walder, A. Kunhi Mohamed, A. Hofstetter, B. Srinivasan, A.J. Rossini, K. Scrivener, L. Emsley, P. Bowen, The Atomic-Level Structure of Cementitious Calcium Silicate Hydrate, The Journal of Physical Chemistry C. 121 (2017) 17188–17196. https://doi.org/10.1021/acs.jpcc.7b02439.

[9]   A. Kunhi Mohamed, P. Moutzouri, P. Berruyer, B.J. Walder, J. Siramanont, M. Harris, M. Negroni, S.C. Galmarini, S.C. Parker, K.L. Scrivener, L. Emsley, P. Bowen, The Atomic-Level Structure of Cementitious Calcium Aluminate Silicate Hydrate, J Am Chem Soc. 142 (2020) 11060–11071. https://doi.org/10.1021/jacs.0c02988.

[10]   A. Kunhi Mohamed, S.A. Weckwerth, R.K. Mishra, H. Heinz, R.J. Flatt, Molecular modeling of chemical admixtures; opportunities and challenges, Cem Concr Res. 156 (2022) 106783. https://doi.org/10.1016/j.cemconres.2022.106783.

[11]   M.H. Müser, S. V. Sukhomlinov, L. Pastewka, Interatomic potentials: achievements and challenges, Adv Phys X. 8 (2023) 2093129. https://doi.org/10.1080/23746149.2022.2093129.

[12]   R.K. Mishra, A.K. Mohamed, D. Geissbühler, H. Manzano, T. Jamil, R. Shahsavari, A.G. Kalinichev, S. Galmarini, L. Tao, H. Heinz, R. Pellenq, A.C.T. van Duin, S.C. Parker, R.J. Flatt, P. Bowen, cemff: A force field database for cementitious materials including validations, applications and opportunities, Cem Concr Res. 102 (2017) 68–89. https://doi.org/10.1016/j.cemconres.2017.09.003.

[13]   R.T. Cygan, J.J. Liang, A.G. Kalinichev, Molecular models of hydroxide, oxyhydroxide, and clay phases and the development of a general force field, J Phys Chem B. 108 (2004) 1255–1266. https://doi.org/10.1021/jp0363287.

[14]   R. Shahsavari, R.J.M. Pellenq, F.J. Ulm, Empirical force fields for complex hydrated calcio-silicate layered materials, Physical Chemistry Chemical Physics. 13 (2011) 1002–1011. https://doi.org/10.1039/c0cp00516a.

[15]   M. F. Döpke, J. Lützenkirchen, O. A. Moultos, B. Siboulet, J.-F. Dufrêche, J. T. Padding, R. Hartkamp, Preferential Adsorption in Mixed Electrolytes Confined by Charged Amorphous Silica, The Journal of Physical Chemistry C. 123 (2019) 16711–16720. https://doi.org/10.1021/acs.jpcc.9b02975.

[16]   Y. Zhou, D. Hou, J. Jiang, P. Wang, Chloride ions transport and adsorption in the nano-pores of silicate calcium hydrate: Experimental and molecular dynamics studies, Constr Build Mater. 126 (2016) 991–1001. https://doi.org/10.1016/j.conbuildmat.2016.09.110.

[17]   D. Hou, T. Li, P. Wang, Molecular Dynamics Study on the Structure and Dynamics of NaCl Solution Transport in the Nanometer Channel of CASH Gel, ACS Sustain Chem Eng. 6 (2018) 9498–9509. https://doi.org/10.1021/acssuschemeng.8b02126.

[18]   I. Androniuk, A.G. Kalinichev, Molecular dynamics simulation of the interaction of uranium (VI) with the C–S–H phase of cement in the presence of gluconate, Applied Geochemistry. 113 (2020) 104496. https://doi.org/10.1016/j.apgeochem.2019.104496.

[19]   I. Androniuk, C. Landesman, P. Henocq, A.G. Kalinichev, Adsorption of gluconate and uranyl on C-S-H phases: Combination of wet chemistry experiments and molecular dynamics simulations for the binary systems, Physics and Chemistry of the Earth. 99 (2017) 194–203. https://doi.org/10.1016/j.pce.2017.05.005.

[20]   A. Sam, S.K. Kannam, R. Hartkamp, S.P. Sathian, Water flow in carbon nanotubes: The effect of tube flexibility and thermostat, Journal of Chemical Physics. 146 (2017). https://doi.org/10.1063/1.4985252.

[21]   E. Galicia-Andrés, D. Petrov, M. H. Gerzabek, C. Oostenbrink, D. Tunega, Polarization Effects in Simulations of Kaolinite–Water Interfaces, Langmuir. 35 (2019) 15086–15099. https://doi.org/10.1021/acs.langmuir.9b02945.

[22]   H. Heinz, T.J. Lin, R. Kishore Mishra, F.S. Emami, Thermodynamically consistent force fields for the assembly of inorganic, organic, and biological nanostructures: The INTERFACE force field, Langmuir. 29 (2013) 1754–1765. https://doi.org/10.1021/la3038846.

[23]   M. Valavi, Z. Casar, A. Kunhi, P. Bowen, S. Galmarini, Molecular dynamic simulations of cementitious systems using a newly developed force field suite ERICA FF, Cem Concr Res. 154 (2022) 106712. https://doi.org/10.1016/j.cemconres.2022.106712.

[24]   S. Galmarini, P. Bowen, Atomistic simulation of the adsorption of calcium and hydroxyl ions onto portlandite surfaces - Towards crystal growth mechanisms, Cem Concr Res. 81 (2016) 16–23. https://doi.org/10.1016/j.cemconres.2015.11.008.

[25]   S. Galmarini, A. Kunhi Mohamed, P. Bowen, Atomistic simulations of silicate species interaction with portlandite surfaces, Journal of Physical Chemistry C. 120 (2016) 22407–22413. https://doi.org/10.1021/acs.jpcc.6b07044.

[26]   T.-C. Lim, Alignment of Buckingham Parameters to Generalized Lennard-Jones Potential Functions, Z. Naturforsch. 64a (2009) 200–204.

[27]   P.J. Mitchell, D. Fincham, Shell model simulations by adiabatic dynamics, Journal of Physics: Condensed Matter. 5 (1993) 1031–1038. https://doi.org/10.1088/0953-8984/5/8/006.

[28]   M. Předota, D. Biriukov, Electronic continuum correction without scaled charges, J Mol Liq. 314 (2020). https://doi.org/10.1016/j.molliq.2020.113571.

[29]   Y. Wu, H.L. Tepper, G.A. Voth, Flexible simple point-charge water model with improved liquid-state properties, Journal of Chemical Physics. 124 (2006). https://doi.org/10.1063/1.2136877.

[30]   G. V. Lewis, C.R. A Catlow, W.C. Mackrodt, R.F. Stewart, W.C. Mackrodt, R.F. Stewart, C.R.A. Catlow, A.M. Stoneham, Potential models for ionic oxides, Journal of Physics C: Solid State Physics. 18 (1985) 1149–1161. https://doi.org/10.1088/0022-3719/18/6/010.

[31]   J.L.F. Abascal, C. Vega, A general purpose model for the condensed phases of water: TIP4P/2005, Journal of Chemical Physics. 123 (2005). https://doi.org/10.1063/1.2121687.

[32]   M.F. Döpke, O.A. Moultos, R. Hartkamp, On the transferability of ion parameters to the TIP4P/2005 water model using molecular dynamics simulations, Journal of Chemical Physics. 152 (2020). https://doi.org/10.1063/1.5124448.

[33]   C.L. Freeman, J.H. Harding, D.J. Cooke, J.A. Elliott, J.S. Lardge, D.M. Duffy, New forcefields for modeling biomineralization processes, Journal of Physical Chemistry C. 111 (2007) 11943–11951. https://doi.org/10.1021/jp071887p.

[34]   A. Tilocca, N.H. De Leeuw, A.N. Cormack, Shell-model molecular dynamics calculations of modified silicate glasses, Phys Rev B. 73 (2006) 104209. https://doi.org/10.1103/PhysRevB.73.104209.

[35]   N.H. de Leeuw, F.M. Higgins, S.C. Parker, Modeling the Surface Structure and Stability of α-Quartz, J Phys Chem B. 103 (1999) 1270–1277. https://doi.org/10.1021/jp983239z.

[36]   J.N. Israelachvili, Intermolecular and Surface Forces, 3rd ed., Academic Press, 2011.

[37]   I. Leontyev, A. Stuchebrukhov, Accounting for electronic polarization in non-polarizable force fields, Physical Chemistry Chemical Physics. 13 (2011) 2613–2626. https://doi.org/10.1039/c0cp01971b.

[38]   P.E.M. Lopes, B. Roux, A.D. MacKerell, Molecular modeling and dynamics studies with explicit inclusion of electronic polarizability: Theory and applications, Theor Chem Acc. 124 (2009) 11–28. https://doi.org/10.1007/s00214-009-0617-x.

[39]   G. Lamoureux, B. Roux, Modeling induced polarization with classical Drude oscillators: Theory and molecular dynamics simulation algorithm, Journal of Chemical Physics. 119 (2003) 3025–3039. https://doi.org/10.1063/1.1589749.

[40]   W.L. Jorgensen, J. Chandrasekhar, J.D. Madura, R.W. Impey, M.L. Klein, Comparison of simple potential functions for simulating liquid water, J Chem Phys. 79 (1983) 926–935. https://doi.org/10.1063/1.445869.

[41]   P. Mark, L. Nilsson, Structure and dynamics of the TIP3P, SPC, and SPC/E water models at 298 K, Journal of Physical Chemistry A. 105 (2001) 9954–9960. https://doi.org/10.1021/jp003020w.

[42]   A.P. Thompson, H.M. Aktulga, R. Berger, D.S. Bolintineanu, W.M. Brown, P.S. Crozier, P.J. in 't Veld, A. Kohlmeyer, S.G. Moore, T.D. Nguyen, R. Shan, M.J. Stevens, J. Tranchida, C. Trott, S.J. Plimpton, LAMMPS - a flexible simulation tool for particle-based materials modeling at the atomic, meso, and continuum scales, Comput Phys Commun. 271 (2022) 108171. https://doi.org/10.1016/j.cpc.2021.108171.

[43]   S. Plimpton, Fast Parallel Algorithms for Short-Range Molecular Dynamics, J Comput Phys. 117 (1997) 1–42. https://doi.org/10.1006/jcph.1995.1039.

[44]   C. Vega, J.L.F. Abascal, Simulating water with rigid non-polarizable models: A general perspective, Physical Chemistry Chemical Physics. 13 (2011) 19663–19688. https://doi.org/10.1039/c1cp22168j.

[45]   C. Vega, E. De Miguel, Surface tension of the most popular models of water by using the test-area simulation method, Journal of Chemical Physics. 126 (2007). https://doi.org/10.1063/1.2715577.

[46]   T.R. Underwood, H.C. Greenwell, The Water-Alkane Interface at Various NaCl Salt Concentrations: A Molecular Dynamics Study of the Readily Available Force Fields, Sci Rep. 8 (2018). https://doi.org/10.1038/s41598-017-18633-y.

[47]   I.M. Zeron, J.L.F. Abascal, C. Vega, A force field of Li+, Na+, K+, Mg2+, Ca2+, Cl-, and S O 4 2 - In aqueous solution based on the TIP4P/2005 water model and scaled charges for the ions, Journal of Chemical Physics. 151 (2019). https://doi.org/10.1063/1.5121392.

[48]   X. Wang, S. Ramírez-Hinestrosa, J. Dobnikar, D. Frenkel, The Lennard-Jones potential: When (not) to use it, Physical Chemistry Chemical Physics. 22 (2020) 10624–10633. https://doi.org/10.1039/c9cp05445f.

[49]   P. Li, L.F. Song, K.M. Merz, Parameterization of highly charged metal ions using the 12-6-4 LJ-type nonbonded model in explicit water, Journal of Physical Chemistry B. 119 (2015) 883–895. https://doi.org/10.1021/jp505875v.

[50]   M. Arab, D. Bougeard, K.S. Smirnov, Molecular dynamics study of the structure and dynamics of Zn2+ ion in water, Chem Phys Lett. 379 (2003) 268–276. https://doi.org/10.1016/S0009-2614(03)01252-1.

[51]   D. Berthelot, Sur le melange des gaz, C R Hebd Seances Acad Sci. 126 (1898) 1703–1855.

[52]   H.A. Lorentz, Ueber die Anwendung des Satzes vom Virial in der kinetischen Theorie der Gase, Ann Phys. 248 (1881) 127–136. https://doi.org/10.1002/andp.18812480110.

[53]   J. Delhommelle, P. Millié, Inadequacy of the Lorentz-Berthelot combining rules for accurate predictions of equilibrium properties by molecular simulation, Mol Phys. 99 (2001) 619–625. https://doi.org/10.1080/00268970010020041.

[54]   S. Mamatkulov, M. Fyta, R.R. Netz, Force fields for divalent cations based on single-ion and ion-pair properties, J Chem Phys. 138 (2013) 024505. https://doi.org/10.1063/1.4772808.

[55]   P. Virtanen, R. Gommers, T.E. Oliphant, M. Haberland, T. Reddy, D. Cournapeau, E. Burovski, P. Peterson, W. Weckesser, J. Bright, et al, SciPy 1.0: fundamental algorithms for scientific computing in Python, Nat Methods. 17 (2020) 261–272. https://doi.org/10.1038/s41592-019-0686-2.

[56]   W. Smith, I.T. Todorov, A short description of DL_POLY, Mol Simul. 32 (2006) 935–943. https://doi.org/10.1080/08927020600939830.

[57]   M. Brehm, B. Kirchner, TRAVIS - A free analyzer and visualizer for monte carlo and molecular dynamics trajectories, J Chem Inf Model. 51 (2011) 2007–2023. https://doi.org/10.1021/ci200217w.

[58]   M. Brehm, M. Thomas, S. Gehrke, B. Kirchner, TRAVIS—A free analyzer for trajectories from molecular simulation, Journal of Chemical Physics. 152 (2020). https://doi.org/10.1063/5.0005078.

[59]   A. Jain, S.P. Ong, G. Hautier, W. Chen, W.D. Richards, S. Dacek, S. Cholia, D. Gunter, D. Skinner, G. Ceder, K.A. Persson, Commentary: The materials project: A materials genome approach to accelerating materials innovation, APL Mater. 1 (2013). https://doi.org/10.1063/1.4812323.

[60]   P. Giannozzi, O. Baseggio, P. Bonfà, D. Brunato, R. Car, I. Carnimeo, C. Cavazzoni, S. De Gironcoli, P. Delugas, F. Ferrari Ruffino, A. Ferretti, N. Marzari, I. Timrov, A. Urru, S. Baroni, Quantum ESPRESSO toward the exascale, Journal of Chemical Physics. 152 (2020). https://doi.org/10.1063/5.0005082.

[61]   P. Giannozzi, S. Baroni, N. Bonini, M. Calandra, R. Car, C. Cavazzoni, D. Ceresoli, G.L. Chiarotti, M. Cococcioni, I. Dabo, et al, QUANTUM ESPRESSO: A modular and open-source software project for quantum simulations of materials, Journal of Physics Condensed Matter. 21 (2009). https://doi.org/10.1088/0953-8984/21/39/395502.

[62]   J.P. Perdew, K. Burke, M. Ernzerhof, Generalized Gradient Approximation Made Simple, Phys Rev Lett. 77 (1996) 3865–3868. https://doi.org/10.1103/PhysRevLett.77.3865.

[63]   S. Grimme, Semiempirical GGA-type density functional constructed with a long-range dispersion correction, J Comput Chem. 27 (2006) 1787–1799. https://doi.org/10.1002/jcc.20495.

[64]   G. Kresse, D. Joubert, From ultrasoft pseudopotentials to the projector augmented-wave method, Phys Rev B. 59 (1999) 1758–1775. https://doi.org/10.1103/PhysRevB.59.1758.

[65]   A. Dal Corso, Pseudopotentials periodic table: From H to Pu, Comput Mater Sci. 95 (2014) 337–350. https://doi.org/10.1016/j.commatsci.2014.07.043.

[66]   H.J. Monkhorst, J.D. Pack, Special points for Brillouin-zone integrations, Phys Rev B. 13 (1976) 5188–5192. https://doi.org/10.1103/PhysRevB.13.5188.

[67]   R. Golesorkhtabar, P. Pavone, J. Spitaler, P. Puschnig, C. Draxl, ElaStic: A tool for calculating second-order elastic constants from first principles, Comput Phys Commun. 184 (2013) 1861–1873. https://doi.org/10.1016/j.cpc.2013.03.010.

[68]   S. Hajilar, B. Shafei, Assessment of structural, thermal, and mechanical properties of portlandite through molecular dynamics simulations, J Solid State Chem. 244 (2016) 164–174. https://doi.org/10.1016/j.jssc.2016.09.026.

[69]   F. Weinhold, R.A. Klein, What is a hydrogen bond? Resonance covalency in the supramolecular domain, Chemistry Education Research and Practice. 15 (2014) 276–285. https://doi.org/10.1039/c4rp00030g.

[70]   S. Galmarini, A. Aimable, N. Ruffray, P. Bowen, Changes in portlandite morphology with solvent composition: Atomistic simulations and experiment, Cem Concr Res. 41 (2011) 1330–1338. https://doi.org/10.1016/j.cemconres.2011.04.009.

[71]   D.A. Kulik, G.D. Miron, B. Lothenbach, A structurally-consistent CASH+ sublattice solid solution model for fully hydrated C-S-H phases: Thermodynamic basis, methods, and Ca-Si-H2O   core   sub-model,   Cem   Concr   Res.   151   (2022)   106585. https://doi.org/10.1016/j.cemconres.2021.106585.

[72]   M. De Jong, W. Chen, T. Angsten, A. Jain, R. Notestine, A. Gamst, M. Sluiter, C.K. Ande, S. Van Der Zwaag, J.J. Plata, C. Toher, S. Curtarolo, G. Ceder, K.A. Persson, M. Asta, Charting the complete elastic properties of inorganic crystalline compounds, Sci Data. 2 (2015). https://doi.org/10.1038/sdata.2015.9.

[73]   G. Clavier, N. Desbiens, E. Bourasseau, V. Lachet, N. Brusselle-Dupend, B. Rousseau, Computation of elastic constants of solids using molecular simulation: comparison of constant volume   and   constant   pressure   ensemble   methods,   Mol   Simul.   43   (2017)   1413–1422. https://doi.org/10.1080/08927022.2017.1313418.

[74]   S. Speziale, H.J. Reichmann, F.R. Schilling, H.R. Wenk, P.J.M. Monteiro, Determination of the elastic constants of portlandite by Brillouin spectroscopy, Cem Concr Res. 38 (2008) 1148–1153. https://doi.org/10.1016/j.cemconres.2008.05.006.

[75]   S. Haussühl, J. Liebertz, Elastic and thermoelastic properties of synthetic Ca2MgSi2O7 (åkermanite) and Ca2ZnSi2O7 (hardystonite), Phys Chem Miner. 31 (2004) 565–567. https://doi.org/10.1007/s00269-004-0416-9.

[76]   E.I. Parkhomenko, Practical Application of Electrification of Rocks, in: Electrification Phenomena in Rocks, Springer US, Boston, MA, 1971: pp. 255–274. https://doi.org/10.1007/978-1-4757-5067-6_8.

[77]   F. Holuj, M. Drozdowski, M. Czajkowski, Brillouin Spectrum of Ca(OH)2, Solid State Commun. 56 (1985) 1019–1021.

[78]   J.E. Oh, S.M. Clark, H.R. Wenk, P.J.M. Monteiro, S.M.Clark.H.-R.W.& P.J.M.M. J.E. Oh, Experimental determination of bulk modulus of 14 Å tobermorite using high pressure synchrotron X-ray diffraction, Cem Concr Res. 42 (2012) 397–403. https://doi.org/10.1016/j.cemconres.2011.11.004.

[79]   M. Bischoff, D. Biriukov, M. Předota, A. Marchioro, Second Harmonic Scattering Reveals Ion-Specific Effects at the SiO2 and TiO2 Nanoparticle/Aqueous Interface, Journal of Physical Chemistry C. 125 (2021) 25261–25274. https://doi.org/10.1021/acs.jpcc.1c07191.

[80]   E. Bonaccorsi, S. Merlino, A.R. Kampf, The crystal structure of tobermorite 14 Å (plombierite), a C-S-H phase, Journal of the American Ceramic Society. 88 (2005) 505–512. https://doi.org/10.1111/j.1551-2916.2005.00116.x.

[81]   R.K. Mishra, R.J. Flatt, H. Heinz, Force field for tricalcium silicate and insight into nanoscale properties: Cleavage, initial hydration, and adsorption of organic molecules, Journal of Physical Chemistry C. 117 (2013) 10417–10432. https://doi.org/10.1021/jp312815g.

[82]   H. Henschel, A.T. Andersson, W. Jespers, M. Mehdi Ghahremanpour, D. Van Der Spoel, Theoretical Infrared Spectra: Quantitative Similarity Measures and Force Fields, J Chem Theory Comput. 16 (2020) 3307–3315. https://doi.org/10.1021/acs.jctc.0c00126.

[83]   A. Vidmer, G. Sclauzero, A. Pasquarello, Infrared spectra of jennite and tobermorite from first-principles, Cem Concr Res. 60 (2014) 11–23. https://doi.org/10.1016/j.cemconres.2014.03.004.

[84]   A. Morales-Melgares, Z. Casar, P. Moutzouri, A. Venkatesh, M. Cordova, A. Kunhi Mohamed, K. L. Scrivener, P. Bowen, L. Emsley, Atomic-Level Structure of Zinc-Modified

Cementitious Calcium Silicate Hydrate, J Am Chem Soc. 144 (2022) 22915–22924. https://doi.org/10.1021/jacs.2c06749.

3 Automated Atomic-Level Structure Generation of Bulk C-S-H and Their Intrinsic Properties

Ziga Casar[1], Eduardo Duque-Redondo[2], Jon Lopez[3], Hegoi Manzano[3], Aslam Kunhi Mohamed[4,5], Karen Scrivener[1] Paul Bowen[1]

[1] Laboratory of Construction Materials, Institut des Matériaux, Ecole Polytechnique Fédérale de Lausanne (EPFL), CH-1015 Lausanne, Switzerland

[2] Physical Chemsitry Department, University of the Basque Country (UPV/EHU), Leioa, Basque Country, Leioa, Spain

[3] Physics Department, University of the Basque Country (UPV/EHU), Leioa, Basque Country, Leioa, Spain

[4] Institute for Building Materials, Department of Civil, Environmental and Geomatic Engineering, ETH Zürich, CH-8093 Zürich, Switzerland

[5] Current address: Department of Civil Engineering, IIT Madras, Chennai-60036, Tamil Nadu, India

Contribution Statement

The following chapter is part of a collaborative research project with Prof. Manzano's group. For the project a new Python code for C-S-H structure generation was developed. Results for C-S-H bulk structures with Ca/Si = 1.3, 1.5, 1.7 and 1.9 are reported here. The candidate's contribution to this work includes conceptualization of the Python code for structure generation, setup of the molecular dynamics simulations, Python and bash scripting for post-postprocessing the data and writing of the original draft.

Abstract

A new Python code for the automated generation of realistic bulk C-S-H structures is introduced. The code was used to generate 400 structures with Ca/Si of 1.3, 1.5, 1.7 and 1.9.

The generated structures are in excellent agreement with experimentally measured C-S-H properties (Ca/Si, 2H/Si, MCL, Si-OH/Si and Ca-OH/Ca). Molecular dynamics was used to simulate the structures, which were then investigated for their structural features and energetic stability. The results suggest similar short-range ordering and energetic stability between all structures. These similarities are attributed to the nanocrystalline nature of C-S-H. Finally, it is shown how computational C-S-H models can be used for resolving the experimentally measured pair distribution functions.

3.1   Introduction

The cement and concrete industry is one of the biggest emitters of CO_2 on the planet [1]. The partial substitution of the clinker by supplementary cementitious materials (SCMs) can lower the CO_2 footprint of cement [2]. The usage of SCMs results in lower early-age strength. Therefore, a fundamental understanding of the unhydrated and hydrated phases in Portland cement is needed [3,4]. The focus of this work is on the main hydration product and primary binder in hydrated cement paste, calcium silicate hydrate (C-S-H).

C-S-H forms around 50 to 60% of hardened cement paste and binds together other crystalline phases and aggregates [5]. The nucleation and growth of C-S-H dictates the early hydration behavior of Portland cement, from a few hours to around one day, [6]. The hydration results in a continuous nanoporous C-S-H network, which consists of nanofoils with lengths above 100 nm and below 5 nm in thickness [7–10].

Over the past decade significant progress has been made in understanding the atomic structure of C-S-H. C-S-H can be represented as a highly defective tobermorite 14 Å [11] with a variable chemical composition and structure [5,10,12–15]. In tobermorite a calcium oxide sheet has silicate chains on either side, which follow the dreierketten silicate structure. The dreierketten structure of the silicate chain has a repetition of a silicate dimer (Q^{2p}-Q^{2p}) followed by a bridging silicate (Q^{2b}) which is oriented into the interlayer (figure 1). The interlayer separates the calcium-silicate sheets of tobermorite and contains one Ca^{2+} ion and seven water molecules. This atomic arrangement in tobermorite 14 Å results in a Ca/Si ratio of 0.83 and a mean chain length (MCL) of infinity, since the dreierketten structure of the silicate chain is not broken. In C-S-H the Ca/Si ratio varies between 1.2 to 2.1, with an average value of 1.7 in plain Portland cement. The increase in the Ca/Si ratio is partly due to missing Q^{2b} silicates [13]. This is evident from ^{29}Si nuclear magnetic resonance (NMR) where a lower intensity of the Q^{2p} and

Q^{2b} signals is observed, while the Q^1 (end of chain silicate) signal appears and dominates at high Ca/Si ratios [10,16,17]. From the proportion of those three Q species the MCL can be calculated [12,16]. With an increase in the Ca/Si ratio a decrease of the MCL is observed [5]. The MCL for Ca/Si = 1.7 is around 3.0, which means that only 25% of the Q^{2b} silicates are present in the silicate chains. The missing Q^{2b} sites are then occupied by Ca^{2+} ions, which is a defining feature of the C-S-H structure [10]. Further increase of the Ca/Si ratio comes from additional Ca^{2+} in the water dominated interlayer. The charge neutrality is achieved by the presence of OH⁻ ions as indicated by a rising Ca-OH/Ca ratio with increasing Ca/Si [5].

The highly defective atomic level structure of C-S-H is a nontrivial landscape to navigate. An extensive knowledge of the atomic level structure of calcium silicate hydrates is needed to introduce defects into tobermorite 14 Å which will satisfy the experimentally measured C-S-H properties and simultaneously fulfil the charge neutrality of the system over a wide range of Ca/Si compositions. Typical parameters from experimental measurements which are used to construct the C-S-H models are Ca/Si ratio, MCL, relative concentration of silanol (Si-OH/Si) and hydroxide groups (Ca-OH/Ca). Due to the poorly ordered nanocrystalline nature of C-S-H the models need to be of sufficient size, nanometers, to accommodate the different types of defects and yield representative structures. The process of constructing such models can be difficult, tiresome and repetitive. Therefore, an automated tool for representative C-S-H structure generation would be more than welcome and of great service to the wider modeling and experimental community.
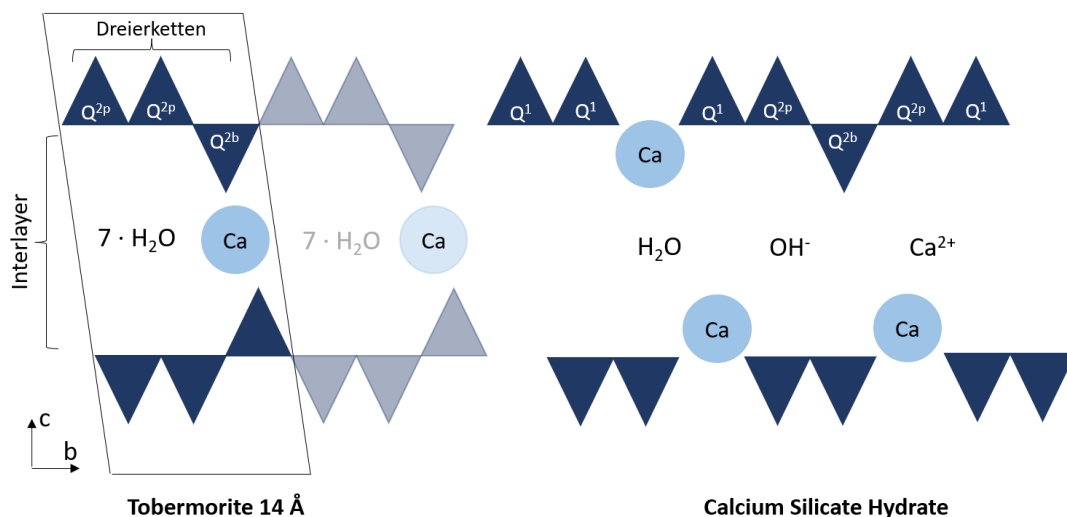
Figure 3-1. Schematic representation of the unit cell of tobermorite 14 Å and calcium silicate hydrate. The calcium oxide layers of the calcium-silicate sheets are not shown.

The first atomistic models of C-S-H appeared in 1996 [18]. In 2018 Kunhi Mohamed et al. [12] introduced the brick model, which allows for a reproducible approach for constructing models of bulk C-S-H and surfaces that are able to reproduce experimentally measured properties [5]. The approach of Kunhi Mohamed et al. [12] lies in the exact inclusion of defects into the tobermorite 14 Å structure. These defects are missing Q^{2b} silicates, calcium replacement of the Q^{2b} silicate, protonation and deprotonation of Q species silanol groups, missing Q species in the silicate dimers, variable water content and addition of Ca^{2+} and OH^- ions in the interlayer. With the precise control over the introduced defects, it is possible to conduct studies in which a given defect can be studied in detail. The authors demonstrated this approach with the comparison of the energetically stability of silanol groups in the C-S-H structure [12]. They successfully showed that the silanol groups become energetically less favorable as the Ca/Si increases, which agrees with the experimental observations [5]. This approach was even used in an earlier study (by the same group [10]), where they examined the missing Q^{2b} silicate, which site is occupied by Ca^{2+}. In this combined experimental and modeling study the authors concluded, from measured and simulated ^{1}H chemical shifts, that Ca^{2+} in the bridging sites is stabilized by an environment of strong hydrogen bonding. This finding among others leads to the conclusion that Ca^{2+} in the bridging site is a key feature of C-S-H. The brick model was later successfully used to elucidate the aluminium [17] and zinc [16] incorporation into the C-S-H structure. In both studies experimental and modeling work was combined to elucidate the exact incorporation site. This was especially difficult in the case of zinc, where the newly found $Q^{2p,Zn}$ chemical shift overlaps with the Q^1 chemical shift. By use of the brick model [12], it was possible to construct bulk C-S-H model structures which enabled this discovery.

The brick model [12] was also successfully used to construct representative models of C-S-H nanofoils with the basal (001) surface which are in excellent agreement with experimentally measured properties (see chapter 5). Different nanofoil thicknesses (measured in the number of calcium-silicate layers) were compared. It was concluded that nanofoils which are 3 layers, 2 interlayers thick are in best agreement with the experimentally reported thickness ($<$ 5 nm) and specific surface area (200-300 m2/g). This thickness underlies the importance of surfaces when discussing the atomic-level structure of C-S-H, since one third of the calcium-silicate layers are associated with the surface. Only two interlayers are considered as bulk C-S-H. It was shown that the best agreement with experimentally measured properties is achieved when the bulk and surface silicate chains have the same MCL. Further, a calcium and hydroxide ion

co-adsorption was proposed, which results in a calcium and hydroxide network on the surface, this can then achieve the experimentally observed high Ca/Si ratios.

While the local atomic structuring of the calcium-silicate sheets from ^{29}Si NMR is well resolved, there is still much unknown about the interlayer as well as surface chemistry of C-S-H nanofoils. In particular, regarding calcium. It is not known how much calcium can be packed into the interlayer, which in turn affects the amount of calcium at the C-S-H surface. The experimental X-ray diffraction spectra give a single broadened basal reflection from which the interlayer size, and therefore the water content, could be deduced. However, this measurement is highly subjected to the sample preparation methods, and therefore yields poorly reproducible results [13].

To fulfill the need of an automated tool for C-S-H structure generation, we present a new open source Python code for bulk C-S-H structure generation [REF of code]. The code uses the collected experimental data from Duque-Redondo et al. [5] and the brick model methodology from Kunhi Mohamed et al. [12] to generate automatically thousands of different representative bulk C-S-H structures with the desired chemical composition from very simple input parameters. In this work we used the automatic code, named pyCSH, to generate 100 structures for each series of Ca/Si ratios (1.3, 1.5, 1.7 and 1.9). The resulting structures were checked for fidelity and are in excellent agreement with experimentally measured properties (MCL, Si-OH/Si and Ca-OH/Ca). At a given Ca/Si ratio the layer spacing, density and pair distribution function (PDF) for each structure were calculated and analyzed. We show that with such atomistic modeling insights it is possible to resolve the short range experimental PDFs with excellent accuracy. These findings can greatly aid the experimental work, particularly when analyzing samples of different hydration times or calcium leaching. Finally, we compare the energetical stability of different defects which shows that C-S-H is made up of a plethora of defect arrangements for the same Ca/Si ratio but have very similar energies, below room temperature thermal energy which explains its poor structural order at the macroscopic scale.

3.2 Methods

3.2.1 pyCSH Python code

The pyCSH code works with the methodology of the brick model [12] which was written in C++. Defects are introduced into the unit cell of tobermorite 14 Å [11] by the arrangement of

different atom groups. The atom groups considered are shown in figure 2. The silicate chains are be formed by a Q^{2p} silicate, which can then be followed by a Q^{2b} silicate in the bridging site. The Q^{2b} silicate can either have both non-sharing oxygens deprotonated, or one can be protonated. If the dimer ends with a Q^1 silicate, the non-sharing oxygen can be either protonated or deprotonated. Following the Q^1 silicate the bridging site can be either unoccupied or occupied with a Ca^{2+} ion. The interlayer is filled with Ca^{2+} and OH^- ions and water molecules. Altogether in the interlayer 5 different positions for Ca^{2+} are possible, 10 for OH^- and 17 for water. While Kunhi Mohamed et al. [12] introduced the defect of the missing dimer silicate, it is not considered in the code[10,16]. An example of a brick which is formed from different atom groups is shown in figure 3a.
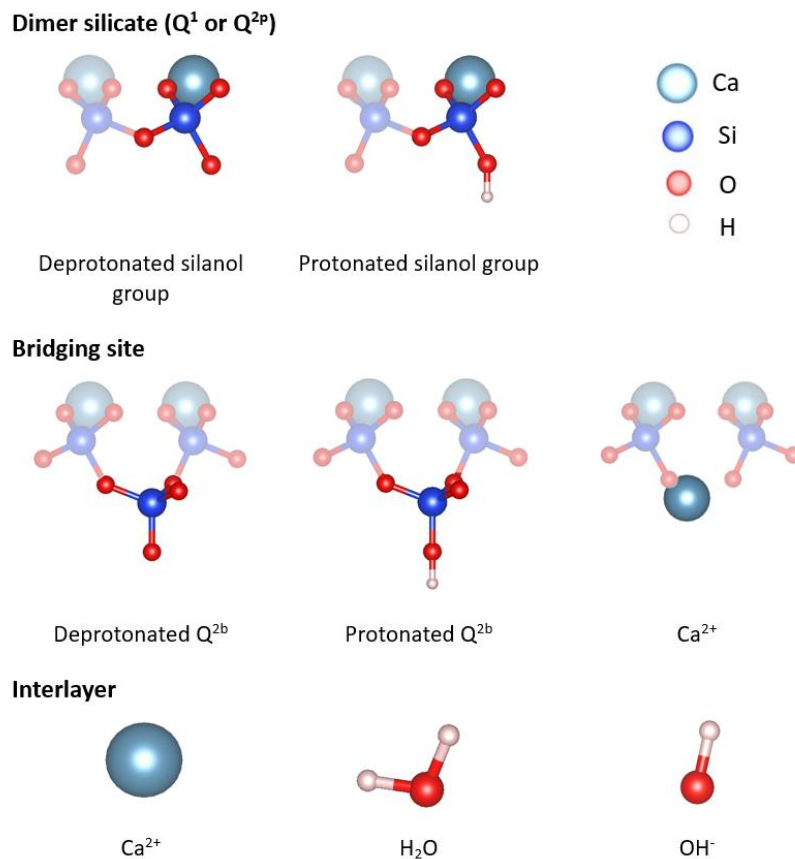
Figure 3-2. Considered atom groups to generate the representative C-S-H structures.

The automated generation of bulk C-S-H structures is outlined with the flow chart in figure 4. The code needs altogether 9 input parameters. The structural ones are the size of the system (number of defective tobermorite 14 Å unit cells (bricks) in the a, b and c crystallographic directions), the targeted Ca/Si and 2H/Si ratios, as well as the number of independent

structures which should be generated for the given Ca/Si and 2H/Si ratios. The numerical input parameters are the random seed number and the tolerances of the Ca/Si, Si-OH/Si and Ca-OH/Ca ratios, which determine if the generated structure is accepted or not. From the targeted Ca/Si ratio the corresponding Si-OH/Si, Ca-OH/Ca and MCL values are taken from the collected data in Duque-Redondo et al. [5].
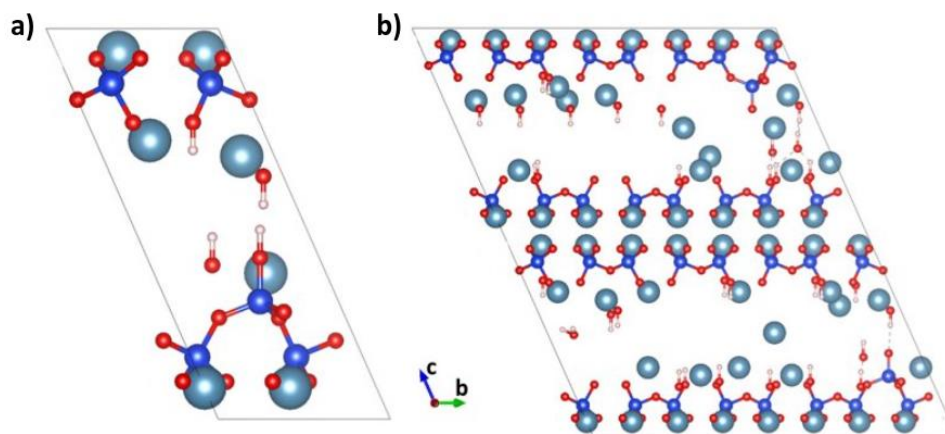
Figure 3-3. a) Example of a constructed brick from different atomic groups with a missing Q^{2b} silicate, which site is occupied by Ca^{2+}, a protonated Q^{2b}, and 2 additional Ca^{2+} and 2 OH⁻ in the interlayer, b) A 1x4x2 C-S-H super cell with Ca/Si = 1.7. Water is hidden for clarification. These are unrelaxed structures. Color legend is the same as in figure 2.

An iterative loop follows, in which a random combination of predetermined atomic groups (figure 2) forms the individual bricks of the C-S-H supercell. However, a limitation is imposed in this process. If a dimer silicate with a silanol group is placed into the silicate chain then a Q^{2b} silicate is prevented from being placed into the bridging site, which can then be only unoccupied or occupied with a Ca^{2+}. This is due to the fact that silicates interlink through oxygen and not hydroxyl groups [11,13]. The overall charge of each brick is calculated. If the charge is less than –2 e or more than +2 e the brick is discarded and a new one is constructed. Once all unit cells satisfy the charge criterium, the overall structural characteristics are calculated and compared to the experimental data (Ca/Si, Si-OH/Si, Ca-OH/Ca and MCL). If the model properties match the experimental ones inside the allowed tolerances, water insertion follows. If they do not match, new bricks are generated and evaluated. The amount of water needed is calculated from the 2H/Si ratio after the subtraction of silanol groups and hydroxide ions. ¹H NMR is used to experimentally determine the amount of water in C-S-H, whereby it is difficult to distinguish between hydrogens of water molecules and other hydrogens [19]. Therefore, the reported 2H/Si equals to (H_2O + 0.5OH⁻)/Si. The water molecules are

uniformly distributed through the entire super cell structure. The geometry of the inserted water molecule is from the TIP4P/2005 water model [20], and therefore suitable for force fields which use this water model without additional adjustments. An example of a generated C-S-H model with Ca/Si = 1.7 measuring 4 bricks in b-direction and 2 bricks in c-direction is shown in figure 3b.
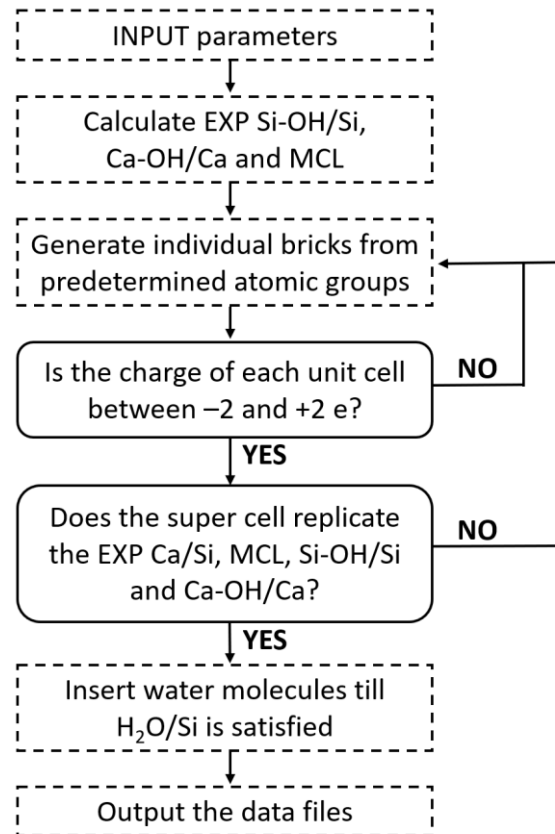
Figure 3-4. Flow chart of the pyCSH code.

In addition to the automatic generation of bulk C-S-H structures the program allows for manual creation of structures and surfaces. It is possible to take an automatically generated structure and further change it manually. The details of the alphanumerical notation that is used by the program are given in detail and explained in the supplementary section.

3.3 Molecular dynamics

Since the atoms are placed in a predetermined way with fixed coordinates a suitable equilibration protocol was devised. First, three separate 40,000 step runs in the canonical (NVT) ensemble were carried out, where first only the water molecules are allowed to move,

followed by water plus hydroxyl groups and hydroxide ions, and finally including all calcium atoms. Next, energy minimization of the simulation box was carried out. With this a more favorable atom arrangement in the interlayer is achieved. Due to the use of the adiabatic core-shell model for polarizability of silicate oxygens an additional step followed, where the motion of the cores and shells is decoupled, to prevent the drift of the total energy during the simulation. For details we refer the reader to the paper of Valavi et al. [21], the original paper of the adiabatic core-shell model [22] and the LAMMPS documentation (8.5.5. Adiabatic core/shell model) [23].

A so-called hard minimization followed, where the structure is subjected to cyclic heating. A 100 ps run in the isobaric-isothermal ensemble (NPT) ensemble at 300 K and 1 atm was carried out to relax the simulation box. This was followed by a heating and cooling step in the NVT ensemble, whereby the temperature was raised over 50 ps to 700 K, where the system was kept for 200 ps before the 50 ps cooling to 300K. This cycle was repeated one more time before the system was equilibrated in the NPT ensemble at 298.15 K and 1 atm for 400 ps.

The production run was then carried out over 20 ns in the NPT ensemble at 298.15 K and 1 atm. The trajectories were recorded every 50 ps. The temperature, pressure, energy, volume and unit cell parameters were averaged on the fly and recorded every 20 ps. The average potential energy of core-shell pairs was also averaged and recorded every 20 ps.

All simulations were carried out with LAMMPS [23]. The force field used was the Erica FF2 [21], with a time step of 0.2 fs. The only modification to the force field was the adjustment of the mass of the core-shell oxygen pair. To prevent the drift of total energy the mass of the shell was set to 0.4 g/mol, while the core mass was 15.59 g/mol. The kspace solver was the particle-particle particle-mesh solver (pppm) with an accuracy of 10^{-4}. The Nose-Hoover thermostat and barostat were used with Tdamp equal to 100 times the time step and Pdamp equal to 1000 times the time step.

The Travis trajectory analyzer and visualizer [24,25] was used to postprocess the trajectory files. The partial pair distribution functions (PDFs), $G_{\alpha\beta}(r)$, were calculated as the average of the entire 20 ns production run. From the partial PDFs the total pair distribution function, $G(r)$, for each structure was calculated as:

$$G(r) = \sum_{\alpha\beta} \frac{c_\alpha c_\beta b_\alpha b_\beta}{\langle b \rangle^2} G_{\alpha\beta}(r) \tag{1}$$

where b values are the atomic scattering lengths of the atoms, c is the weight factor representing the fraction of atomic species and the sums are over every atom in the sample (except hydrogens, which were excluded from the analysis) [26]. Fixed scattering lengths at zero degrees were used.

For the energetical comparison of structures with the same stoichiometry the reaction enthalpies are compared. For the calculation of the reaction enthalpy the enthalpies of quartz (SiO_2), lime (CaO) and water (H_2O) are compared to the enthalpy of the observed C-S-H structures via equation 2 [12]. To obtain the average enthalpies of quartz, lime and water, the systems were simulated for 20 ns, where the average enthalpy over the last 10 ns was taken into consideration. The simulation protocol for quartz, lime and water was the same as for C-S-H, as stated above.

$$n_1 \cdot CaO + n_2 \cdot SiO_2 + n_3 \cdot H_2O \rightarrow \left[(CaO)_{n_1} (SiO_2)_{n_2} (H_2O)_{n_3} \right]_{CSH} \tag{2}$$
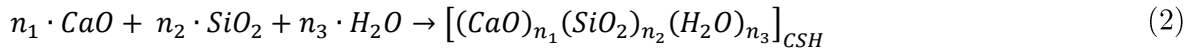
where the normalization comes by fixing $n_1 + n_2 + n_3 = 1$. A correction for water splitting needs to be considered ($H_2O + O \rightarrow 2 \cdot OH^-$) and is equal to 2.9 eV per dissociated molecule [21]. Further, the enthalpy of the C-S-H structure is adjusted for the missing Morse bond energy ($N_{OH} \cdot D$) and potential energy of the core-shell pairs (PE_{CS}) (see chapter 2):

$$H_{CSH,corr} = H_{CSH} + N_{OH} \cdot D + PE_{CS} \tag{3}$$

All LAMMPS and Travis input files are provided as part of the supplementary information section.

3.4   Results

In the results section first the generated structures are analyzed and compared to experimentally obtained C-S-H properties. Afterwards the simulated structures are analyzed on their structural properties and a comparison of the defect energetics is presented.

3.4.1 Initial structures

Figure 5 compares the four C-S-H properties (MCL, 2H/Si, Si-OH/Si and Ca-OH/Ca) for the given Ca/Si ratio between the experimentally measured systems and the pyCSH generated models. It is clear from the figure that the MCL decreases with increasing Ca/Si. However, above Ca/Si of 1.2 the experimental MCL varies significantly, with values between 2.3 and 4.0. The pyCSH values are listed in table 1. The range of predicted MCL values is in the range of experimentally determined values. For Ca/Si = 1.7 the predicted MCL (2.30 ± 0.11) is at the lower end of experimental data, while for Ca/Si = 1.9 the MCL is in the upper range (3.457 ± 0.083). Two separate ^{29}Si NMR studies on synthetic phase pure C-S-H with Ca/Si = 1.75 underline the variation in MCL as calculated from the proportion of Q species. While both studies used the same precipitation protocol [27] Kumar et al. [10] reported a MCL value of 2.55, while Morales et al. [16] reported 2.89. The targeted 2H/Si ratios are predetermined and are in the range of experimentally measured values.

Table 3-1. Mean value and standard deviation (std) of properties at a given Ca/Si of bulk C-S-H models as predicted by pyCSH.

Ca/Si	Property	Mean	Std
	MCL	3.668	0.407
	Si-OH/Si	0.294	0.034
1.3	Ca-OH/Ca	0.251	0.043
	2H/Si	1.109	0.020
	MCL	3.161	0.268
	Si-OH/Si	0.213	0.024
1.5	Ca-OH/Ca	0.384	0.036
	2H/Si	1.495	0.022
	MCL	2.299	0.117
	Si-OH/Si	0.097	0.025
1.7	Ca-OH/Ca	0.387	0.021
	2H/Si	1.780	0.022

	MCL	3.457	0.083
	Si-OH/Si	0.018	0.015
1.9	Ca-OH/Ca	0.660	0.010
	2H/Si	2.238	0.014

The generated mean Si-OH/Si for Ca/Si of 1.3 and 1.5 are slightly higher than the experimentally reported values. While the Si-OH/Si for Ca/Si 1.7 and 1.9 are closer to the linear extrapolation of the collected experimental data points. There are no experimental values reported above Ca/Si = 1.6. The experimentally determined Ca-OH/Ca shows a higher discrepancy above Ca/Si = 1.5, which may indicate that the trend is not linear for the entire range of Ca/Si ratios. The pyCSH code predicts structures which are in good agreement with the experimental linear fit of Ca-OH/Ca for Ca/Si 1.3, 1.5 and 1.9. The predicted values for Ca/Si = 1.7 (0.387 ± 0.021) are at the lower end of experimental values.
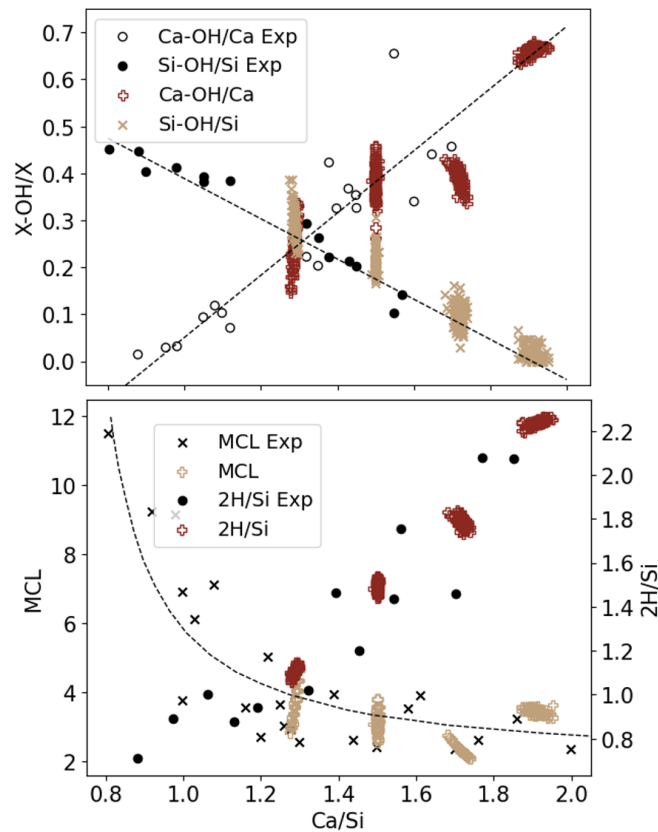
Figure 3-5. Characteristic properties (Si-OH/Si, Ca-OH/Ca, MCL, 2H/Si) of bulk C-S-H generated structures for the studied Ca/Si ratios in comparison with experimental data from Duque-Redondo et al. [5].

3.4.2 Structural analysis

The structural analysis was made after molecular dynamics relaxation of the initial bulk C-S-H structures. Roughly 5% of simulations crashed. The reported quantities are the average values of the 20 ns production run.

The layer spacing of all calculated structures, including the mean values and standard deviations for each Ca/Si is shown in figure 6. The predicted layer spacing increases from Ca/Si 1.3 (12.18 Å) to 1.5 (13.11 Å) where it stays nearly constant till Ca/Si = 1.7 (13.05 Å). The layer spacing for Ca/Si = 1.9 increases significantly thereafter (16.01 Å). For Ca/Si = 1.5 a higher spread of the layer spacings is observed (± 0.26 Å) when compared to Ca/Si = 1.7 (± 0.14 Å). The spacing for a given Ca/Si increases linearly with 2H/Si, with a difference between the maximum and minimum of 1.3 Å for Ca/Si = 1.5, which is not as strongly pronounced for Ca/Si = 1.7. The average Ca/Si = 1.5 structure holds 8% less water molecules and hydroxide ions than the Ca/Si = 1.7 structure (see (H_2O+OH^-)/Ca in table 2). The similar mean values of the layer spacing can be explained by the mean coordination number of oxygen atoms to calcium atoms (table 2). The coordination number (cutoff at 3 Å) for Ca/Si = 1.5 equals 6.22 ± 0.06, while for Ca/Si = 1.7 it equals 6.78 ± 0.06 (8% difference). A higher coordination number results in a denser packing of the bulk and therefore yields a higher density for the same layer spacing. Indeed, a slightly higher mean density (figure 7) is observed for Ca/Si = 1.7 (2.40 ± 0.013 g/cm³) in comparison to Ca/Si = 1.5 (2.37 ± 0.017 g/cm³).
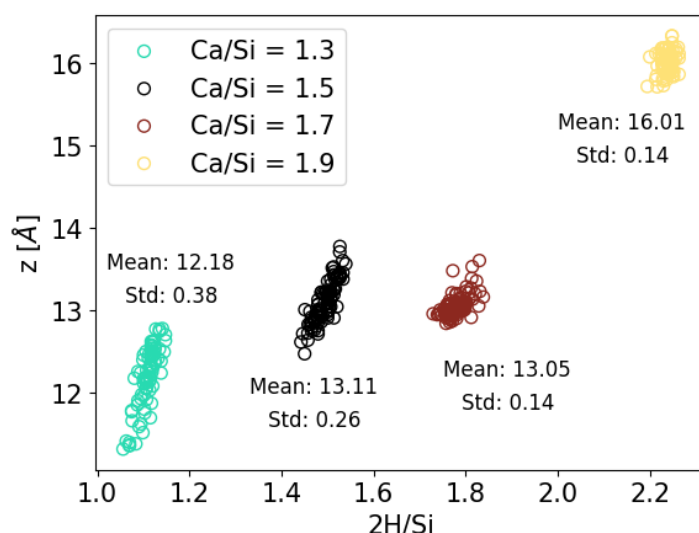
Figure 3-6. Layer spacing as a function of 2H/Si. The mean values and standard deviation of the layer spacing correspond to the given Ca/Si set .

It appears that the interlayer spacing linearly increases with increasing Ca-OH/Ca (see figure S1). Further, the calculated layer spacing is comparable at the same Ca-OH/Ca. This correlation can be explained by the following observation. The MCL is a measure of how many bridging sites of the silicate chain are occupied by Q^{2b} silicates. Assuming that each missing Q^{2b} is replaced by a Ca^{2+}, which we will consider as part of the silicate chain instead of the interlayer [10,12], one can calculate the number of remaining Ca^{2+} which are associated with the interlayer per each C-S-H brick (defective unit cell of tobermorite). Since the C-S-H brick always consists of the mainlayer Ca-Si sheet, the Ca^{2+} content can be normalized by the silicate dimer (Q^1-Q^1, Q^{2p}-Q^{2p} or Q^1-Q^{2p}) of each silicate chain (top and bottom of the interlayer). The property Ca^{2+}/dimer is listed in table 2. The mean value of those interlayer Ca^{2+} at Ca/Si = 1.5 equals 0.69 Ca^{2+}/dimer, while for Ca/Si = 1.7 equals 0.68. The roughly same amount of Ca^{2+} in the interlayers explains the comparable Ca-OH/Ca ratios and hints to identical layer spacings. Indeed, identical layer spacings are also observed for Ca/Si = 1.3 at same Ca^{2+}/dimer ratios (figure S1). The pyCSH predicted MCL for Ca/Si = 1.9 (MCL = 3.5) is higher than the one for Ca/Si = 1.7 (MCL = 2.3) which results in less calcium in the silicate chains and therefore high Ca^{2+}/dimer (1.77 versus 0.68). While the Ca/Si = 1.7 structure contains approximately the same amount of hydroxide ions as Ca/Si = 1.5, it contains more water, and its silicate chains incorporate more Ca^{2+} ions. The higher Ca^{2+} incorporation results in a higher amount of strongly bounded water next to the silicate chains (due to Ca^{2+} incorporation into the Si-chains which is known for having a tight hydration shell [29]). This would potentially result in a comparable amount of water in the mid-interlayer (water which is not coordinated to the main layer chains).

Table 3-2. Mean value and standard deviation for calcium coordination number (Ca-O CN), H_2O/Ca, (H_2O+OH^-)/Ca and Ca^{2+}/dimer for the given Ca/Si ratios. Ca^{2+}/dimer accounts only for calcium ions in the interlayer, excluding those which are predicted to be in the bridging site.

Ca/Si	Ca-O CN	H_2O/Ca	(H_2O+OH^-)/Ca	Ca^{2+}/dimer
1.3	6.11 ± 0.05	0.622 ± 0.003	0.747 ± 0.020	0.38 ± 0.14
1.5	6.22 ± 0.06	0.736 ± 0.002	0.926 ± 0.018	0.69 ± 0.12
1.7	6.78 ± 0.06	0.815 ± 0.005	1.008 ± 0.015	0.68 ± 0.06
1.9	6.35 ± 0.04	0.837 ± 0.008	1.167 ± 0.006	1.77 ± 0.03

Experimentalists estimate the layer spacing from the (001) basal reflection in the X-ray diffraction (XRD) pattern [13,30]. The general trend observed in those studies is a decrease in the layer spacing with increasing Ca/Si ratios (from 0.66 to 1.3). The layer spacing seems to be unchanged above Ca/Si = 1.3 [13]. Some authors even report constant layer spacings starting at Ca/Si = 1.1 [31]. This trend is not observed in the calculated structures with Ca/Si of 1.3 and 1.9. While the MD predicted layer spacings is around ~ 13 Å (Ca/Si = 1.5 and 1.7), the measured one for Ca/Si = 1.5 and above are typically between 11 and 12 Å [13,30]. However, these readings are from samples dried prior to the measurement, the reported values for the layer spacing of 48 h freeze dried synthetic phase pure C-S-H with Ca/Si = 1.75 equal 13.6 Å (13.9 Å for Ca/Si = 1.5) [32]. The tobermorite 14 Å has Ca^{2+}/dimer = 0.5 and is a stable crystal structure. Ca^{2+}/dimer = 0.38 at Ca/Si = 1.3 seems in comparison to tobermorite 14 Å (Ca/Si = 0.86) very low. The lack of predicted Ca^{2+}/dimer could therefore explain the predicted layer spacing, which is lower than what is experimentally observed. The large spread of the density at low Ca/Si ratios might originate from the distribution of silicates in bridging sites (Q^{2b}). Bridging sites in opposite positions implies steric repulsions which increases the basal space and consequently reduces the density.
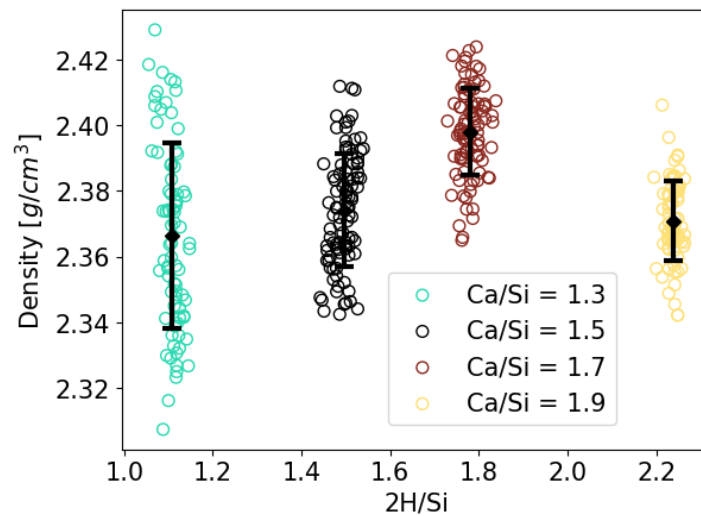
Figure 3-7. Density. The lines determine the standard deviation around the mean value.

The pair distribution functions (PDF) in figure 8 are obtained by taking the mean value over all PDFs of the same Ca/Si ratio. A comparison between individual PDFs with the mean PDF is given in SI section 5 and shows a negligible deviation, suggesting that all structures at a given Ca/Si relax into very similar atomic arrangements. By analyzing the individual radial distribution functions, it is possible to assign the individual peaks to the respective atom pairs.

The recent models of C-S-H nanofoils predict a below 4 nm thick structure, which measures 3 layers, 2 interlayers in the z-axis direction [Casar2023]. Potential-mean-force calculations of the interaction of C-S-H nanofoils predict an equilibrium distance between nanofoils at 5 nm [33]. Therefore, the experimental PDFs below 20 Å can be safely used to explore the structure of a single C-S-H nanofoil. Since the silicate chain structure of the bulk and surface seems to be the same [Casar2023] bulk C-S-H models can be used to help resolve the experimental PDFs (figure 8).

There is no significant difference between the MD predicted PDFs, as indicated by figure 8. The first three peaks (Si-O at 1.6 Å, Ca-O at 2.39 Å and O-O at 2.65 Å) correspond to the first distances inside the calcium-silicate sheets. This suggests that although the chains at different Ca/Si ratios have a different number of defects (missing Q^{2b} silicates and protonation of silanol groups) the local atomic environment is not changed. However, with the increase in Ca/Si the intensity of the MD predicted Si-O peak decreases relative to the Ca-O peak, which was previously experimentally observed [34]. This decrease in intensity can be attributed to a lower relative number of silicate groups. Riteveld analysis of XRD spectra of C-S-H synthesized from silica and calcium oxide shows a decrease in Si-O distance with increasing Ca/Si until Ca/Si 1.3, from where it stays constant for higher Ca/Si ratios [31]. Grangeon et al. [34] hydrated $Ca(OH)_2$ and SiO_2 in water for one day and one year. Again, the measured PDF did not show differences in structural features below 20 Å, suggesting that short range ordering of C-S-H does not change with additional hydration time.

Grangeon et al. [34] reported the partial PDFs of freeze dried C-S-H hydrated from $Ca(OH)_2$ and amorphous SiO2.. While they analyzed samples with Ca/Si from 0.57 to 1.47, the results suggest similar short range structural features for the different samples. Table 3 shows the comparison of structural features (peaks) between the experimentally reported PDFs of Grangeon et al. and our PDFs from simulated pyCSH generated structures (For Ca/Si 1.3 to 1.7). While the reported experimental PDF is for the in-house synthetized tobermorite [34], it shows very similar short-range ordering to the C-S-H samples. The partial experimental PDFs show more peaks than are shown in table 3, which could be attributed to the presence of surfaces and other phases than C-S-H. As seen in table 1 up to 10 Å the results are in excellent agreement, giving confidence to the pyCSH generated structures and the short range similarity between the tobermorite and C-S-H structure. Due to simulation box size, the PDF calculation was limited to ~ 10 Å.
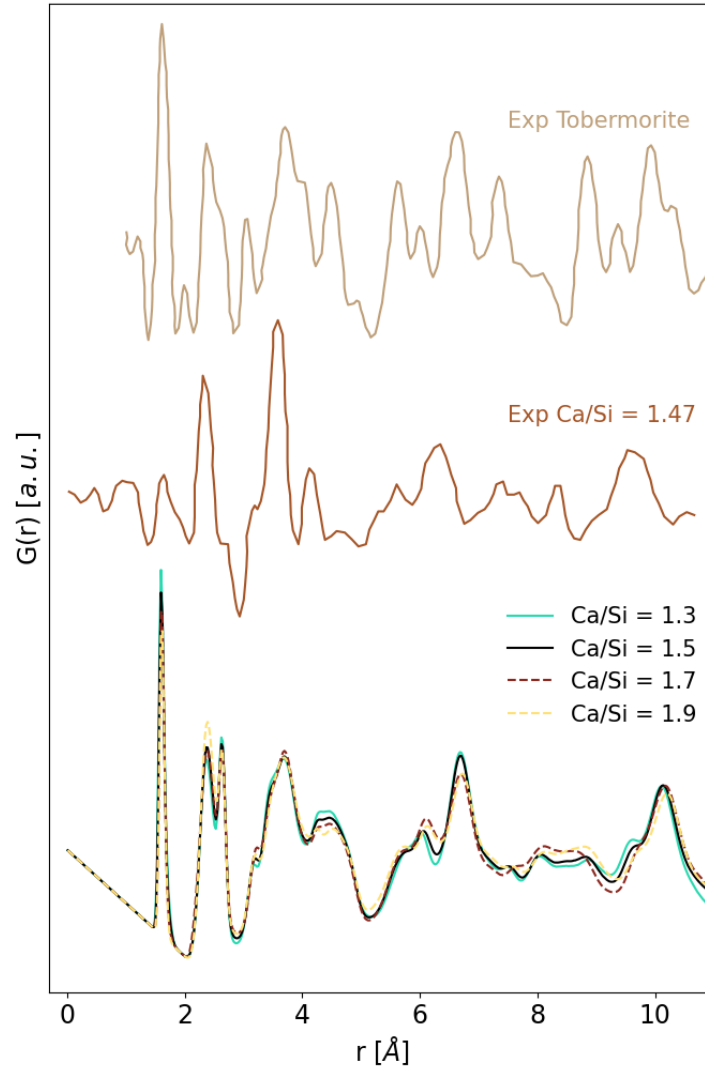
Figure 3-8. Mean pair distribution functions (PDF) of bulk C-S-H structures at the given Ca/Si ratio. The experimental (Exp) PDF are taken from Grangeon et al. [34]. For a direct comparison of experimental and calculated PDFs see SI section 2.

It is interesting to analyze the Si-Si distances, which are reported in table 3 and SI section 2. The first Si-Si distance (3.16 Å) corresponds to the separation of Si atoms of neighboring silicates (d_1 in figure 9). 4.39 Å is the distance (d_2) between silicates which are separated by a bridging site (Q^{2b} or Ca^{2+}). 5.54 Å is the approximate nearest distance between silicates of neighboring chains in the a-axis direction (d_a) as well as in the c-axis direction (silicate chain on the opposite site of the calcium-oxide layer, d_c), while 6.69 Å is the separation of a silicate with the second closest silicate of the neighboring chain in a-axis direction. A similar distance corresponds to the closest Q^{2b} silicates across the interlayer. While there are not many Q^{2b} silicates at Ca/Si = 1.5 and above, the 6.69 Å peak should gain on intensity with decreasing

Ca/Si ratios, which is indeed the case (figure 8). The 7.19 Å peak corresponds again to the separation of in-chain silicates (d_{i-c}). The peaks above 7.19 Å are harder to resolve, since distances of around 9.8 Å correspond to silicates of neighboring chains in a-axis direction, as well as to dimer silicates across the interlayer. The comparison of the Si-Si RDF (SI section 2) for all calculated Ca/Si shows indeed an excellent agreement up to 8.5 Å (in-chain silicates) after which the Ca/Si = 1.9 peaks are shifted to slightly higher distances, indicating the increased layer spacing. Distances of 10.7 Å correspond to in-chain silicates (approximate length of a pentamer) and to across the interlayer silicates.

Table 3-3. Comparison of individual peaks between MD calculated and experimental PDFs (EXP) of freeze dried tobermorite synthesized from Ca(OH)2 and amorphous SiO2 [34]. All reported values are in Å.

Si-O		Ca-O		Si-Si		Ca-Si		Ca-Ca		O-O	
MD	EXP	MD	EXP	MD	EXP	MD	EXP	MD	EXP	MD	EXP
1.60	1.60	2.39	2.42	3.16	3.07	3.47	3.59	3.79	3.85	2.65	2.64
3.83	3.63	4.56	4.5	4.39	4.3	4.77	4.62	5.33-5.72	5.64	3.11	3.12
4.28	4.27	5.91	5.71-6.11	5.54	5.58	5.26	5.13	6.66	6.65	4.74	4.89
5.96	5.9	7.13	7.36	6.69	6.72	6.08	6.00	7.57	7.37	5.59	5.77
6.87	6.58	8.16	7.75	7.19	7.36	6.71	6.52	8.76	8.86	6.66	6.72
8.09	8.12	9.01	8.96	9.86	9.71	8.51	8.21	9.28	9.20		
				10.7	10.25 ±0.25	9.70	9.52				

The calcium-silicate main layer structural features are predicted with good accuracy. Therefore, it should be possible to resolve the interlayer spacing by carefully analyzing the short range Si-Si distances. Due to different defects along the silicate chains, one should expect a slight variation in the Si-Si distance across interlayer silicate chains. Therefore, the PDF peak for the Si-Si across interlayer separation should have a lower intensity, be wider, and located below the XRD reported basal spacings. Figure 9 shows the partial Si-Si PDF from Grangeon et al. [34], where the short range Si-Si peaks (d_1, d_2 and d_{i-c}, d_a, d_c) from MD are projected onto the experimental PDF. The predicted interlayer separated dimer Si-Si experimental peak (dried samples) is marked as d_{IL} and is centered around 9 Å. This experimental value is slightly below

our MD predicted one (9.8 Å), and therefore in agreement with the layer spacings reported from XRD [13,30].
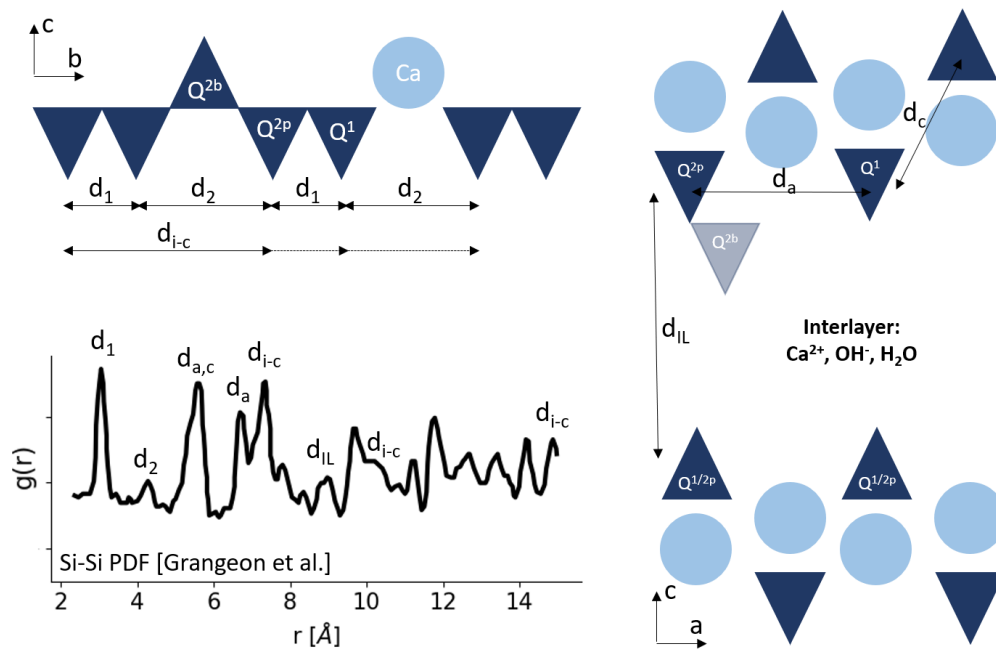
Figure 3-9. Si-Si PDF from Grangeon et al. [34] with annotated Si-Si distances as predicted from MD.

3.4.3 Energetical analysis

Kunhi Mohamed et al. [12] studied the energetical stability of silanol groups in bulk C-S-H which were composed of only one type of brick. Their findings suggest an energetical preference for the absence of silanol groups. In the current study the energetical stability of defects from a random defect configuration with representative C-S-H structures was analyzed. The formation enthalpies are calculated through equation 2, therefore the comparison can only be done for the C-S-H structures with the same stoichiometry (C_{n1}-S_{n2}-H_{n3}). Structures with the same stoichiometry have the same x-axis value in figure 9. The enthalpy of formation of structures with the same stoichiometry is normalized with respect to the lowest enthalpy of formation for a given stoichiometry. Since pyCSH randomly generates structures some of them are unique in their stoichiometry and therefore cannot be compared. Altogether 55 structures with 17 unique stoichiometries for Ca/Si = 1.3, 71 structures with 17 unique stoichiometries for Ca/Si = 1.5, 68 structures with 25 unique stoichiometries for Ca/Si = 1.7 and 34 structures with 22 unique stoichiometries for Ca/Si = 1.9 are compared.
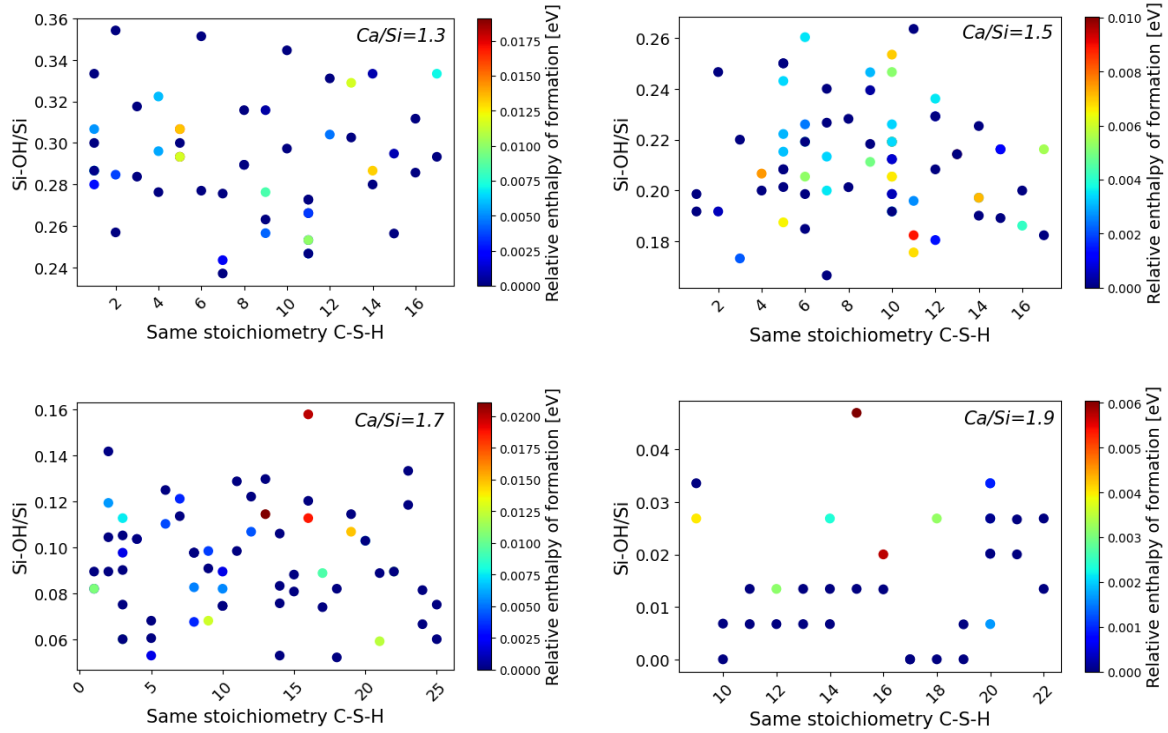
Figure 3-10. Relative enthalpy of formation as a function of Si-OH/Si for C-S-H structures with the same stoichiometry. The enthalpy of formation is normalized to the structure with the lowest defect energy for a given stoichiometry. Structures with the same stoichiometry have the same x-axis value.

While the Si-OH/Si ratio varies by up to 0.1 the variation of enthalpies of formation is minimal. The maximum difference between two structures of the same stoichiometry is 0.02 eV at Ca/Si = 1.3, 0.01 eV at Ca/Si = 1.5, 0.02 eV at Ca/Si = 1.7 and 0.006 eV at Ca/Si = 1.9. These very low differences suggests that there is no significant effect of the number of silanol groups on the energetical stability of C-S-H with randomly introduced defects. We remind the reader that k_BT at the simulated temperature (298.15 K) equals 0.0257 eV. Further, no correlation between the number of silanol groups and enthalpies of formation can be found. This implies that there are many different defect assemblies which all show very similar structural features as well as energies. Those similarities give rise to the poorly ordered nanocrystalline properties of C-S-H.

However, one should keep in mind that the comparison is a result of classical molecular dynamics, which does not allow for bond breaking and creation. In real world C-S-H we might expect spontaneous deprotonation (and protonation), particularly of silanol groups on the end of chain Q^1 silicates, where calcium is predicted to play a key role [10,35].

3.5 Discussion

All analyzed bulk C-S-H structures with Ca/Si ratios from 1.3 to 1.9 are in excellent agreement with the experimentally measured properties of C-S-H (MCL, Si-OH/Si, Ca-OH/Ca and 2H/Si) [5] and their respective PDFs show high similarities (almost identical) between each other. However, the experimental measurements show a decrease in the layer spacings till approximately Ca/Si = 1.3 after which it is practically unchanged [13]. Although predicted C-S-H structures with Ca/Si of 1.3 and 1.9 are in agreement with measured properties, both fail to comply with the experimentally reported dependence of the layer spacing with the Ca/Si ratio.

The automated construction of C-S-H bulk structures shows that none of the properties that describe the C-S-H bulk structure (Ca/Si, 2H/Si, MCL, Si-OH/Si and Ca-OH/Ca) are independent from each other. At a constant Ca/Si and 2H/Si an increase in Si-OH/Si should correspond to an increase in Ca-OH/Ca due to charge neutrality conditions. To obtain an additional silanol group a hydrogen atom from a water must be transferred to a silicate oxygen which results in a new hydroxide ion. This observation underlines the contradiction of the Si-OH/Si and Ca-OH/Ca ratios, since experimental data [5] shows that when one increases the other decreases. The contradiction is again observed when taking into account the amount of interlayer Ca^{2+} (0.69 and 0.68 Ca^{2+}/dimer). An increase in Ca^{2+}/dimer corresponds to an increase in the number of OH^- therefore to an increase in the Ca-OH/Ca, which is not observed in the C-S-H bulk models but is observed experimentally (in which measurements include the surfaces) [5]. However, for phase pure synthetic C-S-H with Ca/Si = 1.75 Kumar et al. [10] reports a MCL of 2.55, while Morales et al. [16] reports 2.89. At this Ca/Si ratio and MCL the expected Ca^{2+}/dimer are 1.16 and 1.50, respectively. While those values would result in higher Ca-OH/Ca, they are similar to the predicted values for Ca/Si = 1.9, which result in rather large layer spacing. It seems that everything points to a bulk structure which somehow differs from the measured properties. This raises the question: where does the regulation of properties happen?

As stated in the introduction (and by Casar et al. [Casar2023]), the C-S-H nanofoil is roughly around 4 nm thick (measured between surface silicate chains), whereby the bulk of C-S-H measures two layer-spacings in the z-axis direction (~ 2.6 nm). It is suggested that surface effects will play an immense role in C-S-H properties, as explained in following.

First, figure 5 shows a rather large scatter of experimental Ca-OH/Ca data points. The reported layer spacings are similar for different samples with comparable Ca/Si ratio which were treated equally prior to XRD measurements [13,30]. Therefore, a valid assumption is that the bulk C-S-H structures for a given Ca/Si are very similar, if not identical in their composition. From this it can be concluded that the C-S-H surface is indeed the one which controls the Ca-OH/Ca ratio. Depending on the calcium concentration and the pH of the solution different amounts of adsorption at the C-S-H surface would be expected. The scatter of experimental data points can then be related to the solution conditions and sample preparation (type of washing, drying).

PDFs of samples with hydration times of one day and one year show similar short-range ordering (below 20 Å) [34], which can be attributed to bulk C-S-H. This consistency of PDF peaks between the two samples points to an unchanged ordering of the calcium-silicate chains as well as the interlayer distance. Further, thermodynamic modeling predicts a decrease in the Ca/Si ratio of C-S-H in hydrated cement samples with increasing hydration times, which is supported by experimental measurements [36]. If the calcium decrease came from the removal of bulk C-S-H calcium a change in the short-range PDF peaks should be observed. The removal of calcium from the calcium-silicate layers would greatly disturb the short-range ordering (below 7 Å), while the removal of interlayer Ca^{2+} should influence the across interlayer dimer peak. Since Ca^{2+} has a strong hydration shell [29], it would be expected that if interlayer Ca^{2+} is removed it would also remove some of the water and hydroxide ions from the interlayer. This consequently would result in a shrinkage of the interlayer, which is not observed [34]. The ^{1}H NMR determined C-S-H solid density (excluding gel water) is nearly constant for all degrees of hydration and water-to-cement ratios [37]. These measurements further support the conclusion that the bulk C-S-H structure remains indeed unchanged and that changes are strongly related to surface effects.

To further outline the surface effects, one needs to turn again to thermodynamic modeling. As shown by Zunino and Scrivener [36] the model predicts a drop of Ca/Si with metakaolin addition between 90 days and 3 years from an initial Ca/Si $\approx$ 1.63 to $\approx$ 1.30. Since the layer spacing remains constant [13] one should assume that the bulk structure does not change. Indeed, the model structure of the C-S-H nanofoil with Ca/Si = 1.7 by Casar et al. [Casar2023], has a Ca/Si of ~ 1.35 after all Ca^{2+} and OH- at the surface are removed. Harris et al. [27] observed an underprediction of the Ca/Si by thermodynamic modeling at high Ca/Si (above

1.7), which is also seen in the lower initial value (Ca/Si $\approx$ 1.63) by Zunino and Scrivener [36], while the experimentally measured Ca/Si at early age OPC is around 1.85. At this Ca/Si a high Ca^{2+}/dimer is expected, which would significantly increase the interlayer spacing. Therefore, one can conclude that the bulk structure is not changed, and the increase is due to surface adsorption of Ca^{2+} and OH^-, with which also higher Ca-OH/Ca would be achieved.

To summarize. By combining atomistic modeling, experimentally measured C-S-H layer spacings and properties (Ca/Si, MCL, Si-OH/Si, Ca-OH/Ca, 2H/Si) with thermodynamic modeling one arrives at the conclusion that there are no significant differences of C-S-H bulk in terms of Ca^{2+}/dimer and that the differences in Ca/Si and Ca-OH/Ca come from surface effects. The main difference between experimental PDFs of different Ca/Si ratios [34] is the relative increase of the Ca-O peak to the Si-O peak with increasing Ca/Si. While this behavior is observed in the calculated PDFs of bulk C-S-H structures (figure 8), the Ca-O peak intensity remains lower than the Si-O intensity. This can be attributed to the exclusion of surfaces from the modeled structures and their Ca^{2+} adsorption state.

Conclusion

The present paper introduces a new Python code for automated generation of representative bulk C-S-H structures. The structures are generated with the methodology of the brick model [12], which introduces defects into the tobermorite 14 Å crystal structure. The code carries out an iterative process in which it generates bulk structures that match the measured C-S-H properties (Ca/Si, 2H/Si, MCL, Si-OH/Si and Ca-OH/Ca) which were collected by Duque-Redondo et al. [5].

Approximately 100 structures were generated and simulated for each of the investigated Ca/Si ratios (1.3, 1.5, 1.7 and 1.9). The structures differed from each other in the number and distribution of defects. It was found that all structures were in good agreement with the experimentally measured C-S-H properties. All structures have very similar structural features (PDFs) as well as are energetically very similar. However, only structures with Ca/Si = 1.5 and 1.7 are in agreement with the experimentally observed trends of the layer spacings with the changing Ca/Si. Due to this we conclude that there is a precise calcium packing criterium of the interlayer (in terms of Ca^{2+}/silicate dimer). Therefore, the Ca/Si and Ca-OH/Ca of the C-S-H nanofoil must be regulated with the MCL and over surface related effects (adsorption).

It was shown that such realistic computational models can greatly aid the experimental characterization of C-S-H. With computational insights it is possible to resolve the experimentally obtained data at the atomic level. The relatively easy to use automated pyCSH package can produce many structures with equivalent properties at any desired Ca/Si and 2H/Si ratio. This will allow experimentalists to create structures for particular compositions and get better understanding of the atomistic arrangements. In conjunction with the production of surfaces from Casar et al[Casar2023], which is currently being added to the pyCSH package, a better understanding of additive interactions (e.g. superplasticizers, accelerators) with C-S-H will boost our capacity to better design sustainable cements and concretes in the near future.

References

[1]   K.L. Scrivener, V.M. John, E.M. Gartner, Eco-efficient cements: Potential, economically viable solutions for a low-CO2, cement-based materials industry, Cem Concr Res. 114 (2018) 2–26. https://doi.org/https://doi.org/10.1016/j.cemconres.2018.03.015.

[2]   B. Lothenbach, K. Scrivener, R.D. Hooton, Supplementary Cementitious Materials, Cem Concr Res. 41 (2011) 1244–1256.

[3]   O. Heinz, H. Heinz, Cement Interfaces: Current Understanding, Challenges, and Opportunities, Langmuir. 37 (2021) 6347–6356. https://doi.org/10.1021/acs.langmuir.1c00617.

[4]   A. Kunhi Mohamed, A. Bouibes, M. Bauchy, Z. Casar, Molecular modelling of cementitious materials: current progress and benefits, RILEM Technical Letters. 7 (2022) 209–219. https://doi.org/10.21809/rilemtechlett.2022.175.

[5]   E. Duque-Redondo, P.A. Bonnaud, H. Manzano, A comprehensive review of C-S-H empirical and computational models, their applications, and practical aspects, Cem Concr Res. 156 (2022) 106784. https://doi.org/10.1016/j.cemconres.2022.106784.

[6]   A. Ouzia, K. Scrivener, The needle model: A new model for the main hydration peak of alite, Cem Concr Res. 115 (2019) 339–360. https://doi.org/10.1016/j.cemconres.2018.08.005.

[7]   M.R. Andalibi, A. Kumar, B. Srinivasan, P. Bowen, K. Scrivener, C. Ludwig, A. Testino, On the mesoscale mechanism of synthetic calcium-silicate-hydrate precipitation: A population balance modeling approach, J Mater Chem A Mater. 6 (2018) 363–373. https://doi.org/10.1039/c7ta08784e.

[8]   X. Zhu, I.G. Richardson, Morphology-structural change of C-A-S-H gel in blended cements,   Cem   Concr   Res.   168   (2023)   107156. https://doi.org/10.1016/j.cemconres.2023.107156.

[9]   H. Viallis-Terrisse, A. Nonat, J.C. Petit, Zeta-potential study of calcium silicate hydrates interacting with alkaline cations, J Colloid Interface Sci. 244 (2001) 58–65. https://doi.org/10.1006/jcis.2001.7897.

[10]   A. Kumar, B.J. Walder, A. Kunhi Mohamed, A. Hofstetter, B. Srinivasan, A.J. Rossini, K. Scrivener, L. Emsley, P. Bowen, The Atomic-Level Structure of Cementitious Calcium Silicate Hydrate, The Journal of Physical Chemistry C. 121 (2017) 17188–17196. https://doi.org/10.1021/acs.jpcc.7b02439.

[11]   E. Bonaccorsi, S. Merlino, A.R. Kampf, The crystal structure of tobermorite 14 Å (plombierite), a C-S-H phase, Journal of the American Ceramic Society. 88 (2005) 505–512. https://doi.org/10.1111/j.1551-2916.2005.00116.x.

[12]   A. Kunhi Mohamed, S.C. Parker, P. Bowen, S. Galmarini, An atomistic building block description of C-S-H - Towards a realistic C-S-H model, Cem Concr Res. 107 (2018) 221–235. https://doi.org/10.1016/j.cemconres.2018.01.007.

[13]   I.G. Richardson, Model structures for C-(A)-S-H(I), Acta Crystallogr B Struct Sci Cryst Eng Mater. 70 (2014) 903–923. https://doi.org/10.1107/S2052520614021982.

[14]   R.J.M. Pellenq, A. Kushima, R. Shahsavari, K.J. Van Vliet, M.J. Buehler, S. Yip, F.J. Ulm, A realistic molecular model of cement hydrates, Proc Natl Acad Sci U S A. 106 (2009) 16102–16107. https://doi.org/10.1073/pnas.0902180106.

[15]   G. Kovačević, B. Persson, L. Nicoleau, A. Nonat, V. Veryazov, Atomistic modeling of crystal structure of Ca1.67SiHx, Cem Concr Res. 67 (2015) 197–203. https://doi.org/10.1016/j.cemconres.2014.09.003.

[16]   A. Morales-Melgares, Z. Casar, P. Moutzouri, A. Venkatesh, M. Cordova, A. Kunhi Mohamed, K. L. Scrivener, P. Bowen, L. Emsley, Atomic-Level Structure of Zinc-Modified Cementitious Calcium Silicate Hydrate, J Am Chem Soc. 144 (2022) 22915–22924. https://doi.org/10.1021/jacs.2c06749.

[17]   A. Kunhi Mohamed, P. Moutzouri, P. Berruyer, B.J. Walder, J. Siramanont, M. Harris, M. Negroni, S.C. Galmarini, S.C. Parker, K.L. Scrivener, L. Emsley, P. Bowen, The Atomic-Level Structure of Cementitious Calcium Aluminate Silicate Hydrate, J Am Chem Soc. 142 (2020) 11060–11071. https://doi.org/10.1021/jacs.0c02988.

[18]   P. Faucon, J.M. Delaye, J. Virlet, Molecular Dynamics Simulation of the Structure of Calcium Silicate Hydrates I. Ca4xSi6O142x(OH)42x(H2O)2(0x1), 1996.

[19]   B. Lothenbach, A. Nonat, Calcium silicate hydrates: Solid and liquid phase composition, Cem Concr Res. 78 (2015) 57–70. https://doi.org/10.1016/j.cemconres.2015.03.019.

[20]   J.L.F. Abascal, C. Vega, A general purpose model for the condensed phases of water: TIP4P/2005, Journal of Chemical Physics. 123 (2005). https://doi.org/10.1063/1.2121687.

[21]   M. Valavi, Z. Casar, A. Kunhi, P. Bowen, S. Galmarini, Molecular dynamic simulations of cementitious systems using a newly developed force field suite ERICA FF, Cem Concr Res. 154 (2022) 106712. https://doi.org/10.1016/j.cemconres.2022.106712.

[22]   P.J. Mitchell, D. Fincham, Shell model simulations by adiabatic dynamics, Journal of Physics: Condensed Matter. 5 (1993) 1031–1038. https://doi.org/10.1088/0953-8984/5/8/006.

[23]   A.P. Thompson, H.M. Aktulga, R. Berger, D.S. Bolintineanu, W.M. Brown, P.S. Crozier, P.J. in 't Veld, A. Kohlmeyer, S.G. Moore, T.D. Nguyen, R. Shan, M.J. Stevens, J. Tranchida, C. Trott, S.J. Plimpton, LAMMPS - a flexible simulation tool for particle-based

materials modeling at the atomic, meso, and continuum scales, Comput Phys Commun. 271 (2022) 108171. https://doi.org/10.1016/j.cpc.2021.108171.

[24]   M. Brehm, M. Thomas, S. Gehrke, B. Kirchner, TRAVIS—A free analyzer for trajectories from molecular simulation, Journal of Chemical Physics. 152 (2020). https://doi.org/10.1063/5.0005078.

[25]   M. Brehm, B. Kirchner, TRAVIS - A free analyzer and visualizer for monte carlo and molecular dynamics trajectories, J Chem Inf Model. 51 (2011) 2007–2023. https://doi.org/10.1021/ci200217w.

[26]   T. Egami, S.J.L. Billinge, Underneath the Bragg peaks Structural Analysis of Complex Materials, Elsevier, Oxford, 2003.

[27]   M. Harris, G. Simpson, K. Scrivener, P. Bowen, A method for the reliable and reproducible precipitation of phase pure high Ca/Si ratio (>1.5) synthetic calcium silicate hydrates (C-S-H), Cem Concr Res. 151 (2022) 106623. https://doi.org/10.1016/j.cemconres.2021.106623.

[28]   C. Labbez, B. Jönsson, I. Pochard, A. Nonat, B. Cabane, Surface charge density and electrokinetic potential of highly charged minerals: Experiments and Monte Carlo simulations on calcium silicate hydrate, Journal of Physical Chemistry B. 110 (2006) 9219–9230. https://doi.org/10.1021/jp057096+.

[29]   M. F. Döpke, J. Lützenkirchen, O. A. Moultos, B. Siboulet, J.-F. Dufrêche, J. T. Padding, R. Hartkamp, Preferential Adsorption in Mixed Electrolytes Confined by Charged Amorphous Silica, The Journal of Physical Chemistry C. 123 (2019) 16711–16720. https://doi.org/10.1021/acs.jpcc.9b02975.

[30]   S. Grangeon, F. Claret, Y. Linard, C. Chiaberge, X-ray diffraction: A powerful tool to probe and understand the structure of nanocrystalline calcium silicate hydrates, Acta Crystallogr B Struct Sci Cryst Eng Mater. 69 (2013) 465–473. https://doi.org/10.1107/S2052519213021155.

[31]   G. Renaudin, J. Russias, F. Leroux, F. Frizon, C. Cau-dit-Coumes, Structural characterization of C-S-H and C-A-S-H samples-Part I: Long-range order investigated by Rietveld analyses, J Solid State Chem. 182 (2009) 3312–3319. https://doi.org/10.1016/j.jssc.2009.09.026.

[32]   M.N. Harris, Precipitation, Characterization, Kinetic, and Thermodynamic Modelling of Synthetic C-S-H Systems (C-S-H, CASH, CSH+$), EPFL, 2022. https://doi.org/https://doi.org/10.5075/epfl-thesis-9917.

[33]   S. Masoumi, D. Ebrahimi, H. Valipour, M.J. Abdolhosseini Qomi, Nanolayered attributes of calcium-silicate-hydrate gels, Journal of the American Ceramic Society. 103 (2020) 541–557. https://doi.org/10.1111/jace.16750.

[34]   S. Grangeon, A. Fernandez-Martinez, A. Baronnet, N. Marty, A. Poulain, E. Elkaïm, C. Roosz, S. Gaboreau, P. Henocq, F. Claret, Quantitative X-ray pair distribution function analysis of nanocrystalline calcium silicate hydrates: A contribution to the understanding of cement chemistry, J Appl Crystallogr. 50 (2017) 14–21. https://doi.org/10.1107/S1600576716017404.

[35]   H. Manzano, S. Moeini, F. Marinelli, A.C.T. Van Duin, F.J. Ulm, R.J.M. Pellenq, Confined water dissociation in microporous defective silicates: Mechanism, dipole distribution, and impact on substrate properties, J Am Chem Soc. 134 (2012) 2208–2215. https://doi.org/10.1021/ja209152n.

[36]   F. Zunino, K. Scrivener, Microstructural developments of limestone calcined clay cement (LC3) pastes after long-term (3 years) hydration, Cem Concr Res. 153 (2022). https://doi.org/10.1016/j.cemconres.2021.106693.

[37]   A.C.A. Muller, K.L. Scrivener, A.M. Gajewicz, P.J. McDonald, Densification of C-S-H measured by 1H NMR relaxometry, Journal of Physical Chemistry C. 117 (2013) 403–412. https://doi.org/10.1021/jp3102964.

4 The Atomic-Level Structure of Zinc-Modified Cementitious Calcium Silicate Hydrate

Anna Morales-Melgares,[1,2,+] Ziga Casar,[2,+] Pinelopi Moutzouri,[1] Amrit Venkatesh,[1] Manuel Cordova,[1] Aslam Kunhi Mohamed,[3] Karen L. Scrivener,[2,*] Paul Bowen,[2,*] Lyndon Emsley[1,*]

[1]Laboratory of Magnetic Resonance, Institut des Sciences et Ingénierie Chimiques, Ecole Polytechnique Fédérale de Lausanne (EPFL), CH-1015 Lausanne, Switzerland

[2]Laboratory of Construction Materials, Institut des Matériaux, Ecole Polytechnique Fédérale de Lausanne (EPFL), CH-1015 Lausanne, Switzerland

[3]Institute for Building Materials, Department of Civil, Environmental and Geomatic Engineering, ETH Zürich, CH-8093 Zürich, Switzerland

[+] AMM and ZC equally contributed to this manuscript.

Contribution Statement

This chapter was published as the same named journal article in Journal of American Chemical Society. The candidate's contributions to it were the generation of the atomistic C-S-H models, force field pre-relaxation of the structures, analyzing the calculated DFT shifts, the interpretation of experimental data and writing of parts of the original draft.

Abstract

It has recently been demonstrated that the addition of zinc can enhance the mechanical strength of tri-calcium silicates (C₃S) upon hydration, but the structure of the main hydration product of cement, calcium silicate hydrate (C-S-H), in zinc-modified formulations remains unresolved. Here we combine ^{29}Si DNP enhanced solid-state nuclear magnetic resonance (NMR), density functional theory (DFT) based chemical shift computations and molecular dynamics (MD) modelling to determine the atomic-level structure of zinc-modified C-S-H. The structure contains two main new silicon species ($Q^{(1,Zn)}$ and $Q^{(2p,Zn)}$) where zinc substitutes $Q^{(1)}$ silicon species in dimers and bridging $Q^{(2b)}$ silicon sites, respectively. Structures determined as

a function of zinc content show that zinc promotes an increase in the dreierketten mean chain lengths.

4.1   Introduction

Due to it being the second most used substance on earth (after water), concrete accounts for around 8% of anthropogenic CO_2 emissions [1]. The most promising approach to lower this carbon footprint is the partial substitution of the clinker by supplementary cementitious materials (SCMs) such as fly ash, blast furnace slag, limestone and calcined clays. The SCMs have much lower associated CO_2, but blending them with clinker tends to lower the early-age strength of the resulting concrete [2,3] This means that increasing the reaction rate of cement formation would allow higher substitution levels and lower CO_2 emissions.

It has been demonstrated that the addition of zinc to C_3S or alite (the main phase in clinker) can enhance the one-day mechanical strength of the hydrated paste substantially ($\times$ 3) [4-6]. This accelerated strength development is related to the faster growth of longer and thicker calcium-silicate-hydrate (C-S-H) particles, which is the main phase (around 50% by volume) in the cement paste part of the final hardened concrete [7-9]. Ouzia and Scrivener [10] demonstrated that C-S-H nucleates and grows predominantly as outgrowths on the surface of alite grains during the hardening reaction (hydration). The rate of reaction peaks at about 10 hours (at 20°C). After this, the reaction rate drops to a low rate at one day as the period of fast growth of C-S-H ends. Small amounts of zinc oxide in alite were found to enhance the heat flow and the degree of hydration, and also result in longer and thicker outgrowths of C-S-H [11]. There is a concomitant enhancement of compressive strength of concrete during the early-stages of hardening, for up to seven days [5]. Although zinc addition could potentially increase the overall cost of cement, understanding of the role of zinc in C-S-H growth and kinetics, would open pathways to synthetic tunability of the rate of reaction of lower-CO_2 materials. However, the atomic-level mechanism of action that links the presence of small amounts of zinc to the enhanced growth of C-S-H, and so to the faster development of strength, is not known. Therefore, it would be of great value to determine how zinc is incorporated into the C-S-H structure at the atomic-level.

A number of techniques have been used previously to probe the structure of C-S-H [12-14], but interpretation is hampered by the lack of long-range order. Indeed, the atomic level structure of C-S-H materials with industrially relevant Ca:Si ratios (i.e. higher than 1.5) was only

determined recently [15,16], by the use of a combination of solid-state NMR spectroscopy, molecular dynamics, and density functional theory (DFT) based chemical shift calculations.

Here we determine the atomic-level structure of zinc-modified synthetic C-S-H using dynamic nuclear polarization (DNP) enhanced solid-state NMR spectroscopy, in concert with other standard characterization methods. Notably we discover that the structure contains new silicate species that are directly related to the incorporation of zinc, and have not been observed previously to the best of our knowledge. We also find that increasing zinc content leads to increasing silicate chain lengths in the structure, which is concomitant with the observed increase in the length of the C-S-H outgrowths at the meso-scale.

4.2   Methods

4.2.1   Synthesis

Samples were synthesised through the dropwise precipitation method previously developed by Kumar et al. [15] and standardized by Harris et al. [17] A polymethacrylate batch reactor was placed in a water bath to maintain a temperature between 19-21°C. 200 mL of a 50 mM sodium silicate solution in deionized water was placed in the batch reactor and 5 mL of 10 M NaOH was added to regulate the final pH between 12.8 and 13.0 in order to ensure a target Ca:Si molar ratio of approximately 1.75. The two solutions were mixed and purged under a flow of nitrogen gas for 15 min prior to the reaction. 200 mL of 90 mM calcium nitrate tetrahydrate (and zinc nitrate hexahydrate with varying concentrations depending on the target $(Zn:Si)_i$) was added through a piston pump at a rate of 2 mL/min, followed by stirring at 1100 rpm for 3h after which the precipitate was collected, washed with 60 ml of a 50% ethanol/water solution and filtered under vacuum. The supernatant of each sample was also collected. The amounts of reactants used for each sample can be found in Table S1 in the Supporting Information (SI).

4.2.2   X-Ray Diffraction (XRD)

Powder XRD was performed on a qualitative basis to observe the presence of undesired phases (i.e. portlandite) [18]. The main C-S-H peaks appear at 29.4, 32.1 and 50.1 $\pm$ 0.1° [19]. A Bruker Discovery X-Ray diffractometer with double bounced monochromatic CuK alpha radiation (λ = 1.54 Å) was used. A fixed divergence slit of 0.25 mm was used and the

experimental time for all samples was 30 min. Spectra and further details are given in SI section IIa.

4.2.3 Inductively Coupled Plasma (ICP)

Samples were prepared by dispersing 20 mg of C-S-H gel or 1 ml of the supernatant in 10 ml or 9 ml of concentrated nitric acid, respectively. Then the samples were diluted up to 3 orders of magnitude prior to analysis. Experiments were conducted using a Spectro Arcos ICP-OES analyser from Ametek. Further details are given in SI section IIc.

4.2.4 Electron Microscopy

A Tecnai OSIRIS TEM system at 200 kV in bright field mode with a single tilt holder and FEI SmartCAM CCD camera was used to observe the sample morphology (SI section IIb). The TEM grids employed to observe these samples are copper-based grids coated with a thin film of carbon. 100-300 mg of C-S-H gel was dispersed in ca. 20 mL of isopropanol (IPA). The samples were dried prior to analysis.

4.2.5 Electron Dispersive X-Rays (EDX)

The same instrument used for TEM analysis was used to conduct STEM and STEM-EDX experiments. In STEM mode a bright field detector (BF) and a high-angle annular dark-field detector (HAADF) were used, whereas in EDX mode a twin pole piece with a Super-X EDX system and 4 SDD detectors with a 0.9 rad solid angle were used.

4.2.6 NMR Spectroscopy

Samples were prepared for DNP enhanced NMR [20-22] by adapting previously used protocols for C-S-H materials [15-16]. About 300 mg of C-S-H gel was mixed with 3 mg of AMUPol [23] and dried under a N_2 flow to approximately 200 mg before packing into sapphire rotors and sealing with PTFE inserts and zirconia drive caps. Since the poorly crystalline C-S-H structure contains a substantial amount of water which is not all removed, no additional impregnating medium is required [15]. All experiments were performed using a 400 MHz Bruker Avance III HD NMR spectrometer equipped with a 263 GHz Bruker gyrotron [24] or klystron microwave source and a HXY 3.2 mm low-temperature MAS DNP probe in ^{1}H-^{29}Si configuration at 100

K. [1]H DNP enhancements were measured as the ratio of the ^{1}H$\rightarrow^{29}$Si cross polarization (CP) signal intensity between spectra recorded with and without microwaves and found to be between 30 and 40. All spectra were acquired at a magic angle spinning (MAS) frequency of 8 kHz, except for SUPER [25] and 2D spin diffusion experiments, which were performed at 5 kHz. For multi-CPMAS experiments, presaturation pulse trains were applied on ^{1}H and ^{29}Si channels. The ^{29}Si chemical shifts were referenced to tetrakis (trimethylsilyl)silane (TMSS). Topspin was used to acquire and process NMR spectra while fitting of the chemical shift anisotropy patterns was performed with ssNake [26]. Additional experimental details are provided in the SI.

4.2.7 Atomistic structure modelling

The previously reported brick model was used to generate candidate zinc-modified C-S-H structures [27]. LAMMPS [28] was used for structure energy minimization and the Erica FF2 [29] force field extended with the required zinc interatomic potentials [30] was used. A single or double brick unit cell was constructed with a target Ca:(Si+Zn) ratio while maintaining the characteristic features of the C-S-H structure.[15] Some silicate tetrahedra were replaced with zinc polyhedra including 4-coordinate ZnO_4^{6-} and $ZnO_2(OH)_2^{4-}$, and 5-coordinate $ZnO_2(OH)_3^{5-}$ species. To achieve charge balance, the number of interlayer calcium ions (Ca^{2+}) and hydroxides (OH^-) were adjusted. A classical energy minimization with the Erica FF2 force field was carried out prior to the DFT energy minimization in order to discard energetically unfavourable structures and save computational time. Full details and codes used are provided with the raw data.

4.2.8 Chemical shift computations

The atomic positions and lattice parameters of the structures obtained from molecular dynamics modelling were first optimized using the Perdew-Burke-Ernzerhof (PBE) [31] functional and Grimme D2 dispersion correction [32,33]. Projector augmented wave scalar relativistic pseudopotentials obtained from PSlibrary version 1.0.0 were used [34, 35]. Semicore s and p electrons were included for zinc and calcium, and nonlinear core-correction was applied for heavy atoms. Wavefunction and charge density energy cut-offs were set to 160 and 1280 Ry, respectively. A Monkhorst-Pack grid of k-points corresponding to a maximum spacing of 0.05 Å^{-1} was used [36]. After geometry optimization, a single-point computation was performed

with the same parameters, and chemical shieldings were computed using the GIPAW method [37, 38].

The conversion from computed shieldings (σ) to ^{29}Si chemical shifts (δ) was carried out by linear regression ($\delta = -1.05 \, \sigma + 345.32$) using a reference set of crystal structures containing willemite [39], hemimorphite [40], foshagite [41] and α-quartz [42] with their corresponding experimental shifts [43,44]. All NMR computations were carried out using the plane-wave DFT program Quantum ESPRESSO v6.5 [45, 46]. Simulated ^{29}Si spectra for individual Si sites were generated using a kernel density estimate of Gaussian kernels as implemented in the scipy Python library [47].

4.3   Results and discussion

4.3.1   Chemical composition and morphology

As described previously, single-phase C-S-H can be synthesized using a dropwise precipitation method, which allows for a controlled synthesis of C-S-H with a specific Ca:Si ratio [17]. This approach was modified to produce zinc-modified C-S-H by adding certain amounts of zinc nitrate hexahydrate to the aqueous calcium nitrate solution depending on the target Zn to Si ratio (denoted as $(Zn:Si)_i$ where the subscript i indicates that it is the initial ratio used in the synthesis). The initial calcium and zinc nitrate solution had a concentration of calcium of 90 mM and a concentration of zinc of 0, 7.5 or 20 mM depending on their target $(Zn:Si)_i$ (e.g. 0, 0.15 and 0.40, respectively). The initial sodium metasilicate solution had a concentration of 50 mM.

As described by Anseau et al. [48] both zinc and aluminium can form complexes with silicate monomers, which are the main species in solution at the pH used here. Therefore, zinc is expected to behave similarly to aluminium and to substitute for silicate species, as seen in the case of aluminium incorporation in C-A-S-H structures synthesized through dropwise precipitation [16]. In addition, previous studies on C3S hydration in presence of zinc show that zinc is in tetrahedral coordination and substitutes for silicate species in C-S-H chains [49, 50]. DFT-relaxed structures in which zinc substituted for calcium in the main layer presented 6-fold coordination and unusually long bond lengths (see SI section VII), therefore, substitution of main layer calcium by zinc was neglected.

The possible sites where the different zinc polyhedra can be incorporated into the C-S-H structure (Figure 1A) are illustrated in Figure 1B. These structures are the result of zinc substitutions of $Q^{(2b)}$, $Q^{(2p)}$ or $Q^{(1)}$ sites in conventional C-S-H. In addition, the figure also shows how zinc can also be present on top of the silicate chains, facing into the interlayer, where it could coordinate to one or both $Q^{(1)}$ species of a silicate dimer.

If zinc substitutes for the $Q^{(2b)}$ site, it yields two identical new neighbouring silicate species which, following the Q site nomenclature, are named $Q^{(2p,Zn)}$. If zinc substitutes for a $Q^{(2p)}$ site, it yields a $Q^{(2b,Zn)}$ species and either a $Q^{(1,Zn)}$ or a $Q^{(2p,Zn)}$ depending on whether the chain unit is a pentamer or a higher degree unit, respectively. If zinc substitutes for a $Q^{(1)}$ site it can yield a $Q^{(1,Zn)}$ or a $Q^{(2p,Zn)}$, depending on whether the chain unit is a dimer or a higher degree unit. If zinc is adjacent to both silicates in a $Q^{(1)}$ - $Q^{(1)}$ dimer it coordinates to one or both $Q^{(1)}$ species and protrudes into the interlayer becoming a $Q^{(2p,Zn\_int)}$. Finally, this model also includes the possibility of two zinc units substituting for two silicate chain sites simultaneously (i.e. $Q^{(1)}$ and $Q^{(2p)}$) producing a new silicate species which is isolated from other silicate linkages as is represented in Figure 1B in the case of $Q^{(2p,2Zn)}$ species.
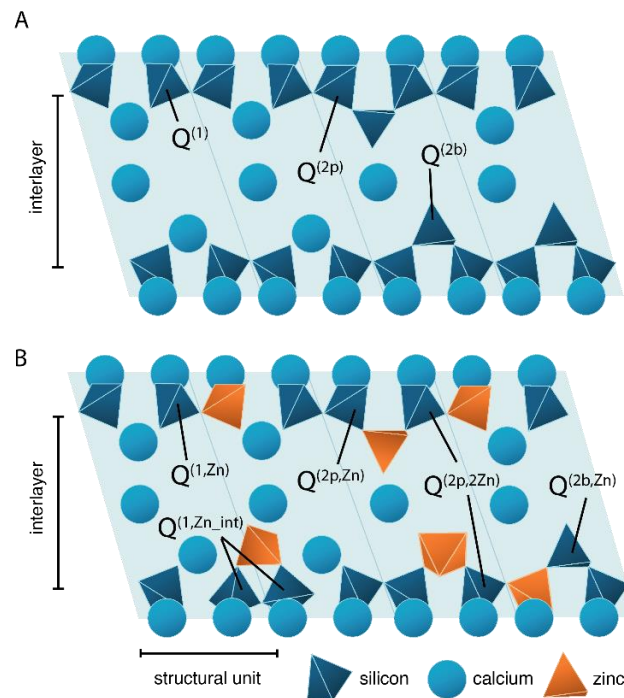
Figure 4-1. A) Schematic of the dreierketten chains in conventional C-S-H showing all the silicate species present: Q(1), Q(2b) and Q(2p). B) Schematic of zinc-modified C-S-H, showing all the new silicate sites that could potentially be present: Q(1,Zn), Q(2p,Zn),

In summary, this scheme includes the possibility of five different four-coordinated zinc species and one five-coordinated zinc species substituting for a $Q^{(2b)}$ site.

In order to determine the atomic-level structure of zinc-modified C-S-H the chemical composition, purity and incorporation of zinc in the C-S-H structure needs to be verified prior to structure determination. A series of XRD experiments were performed to confirm that our material is a single-phase, pure C-S-H sample and no secondary phases such as portlandite are observed (Figure S1). Additionally, inductively-coupled plasma (ICP) analysis of the supernatant shows that only around 1-2% of the added zinc remains in solution after synthesis (Table S2), indicating the incorporation of the vast majority of the zinc into the precipitated zinc-modified C-S-H.
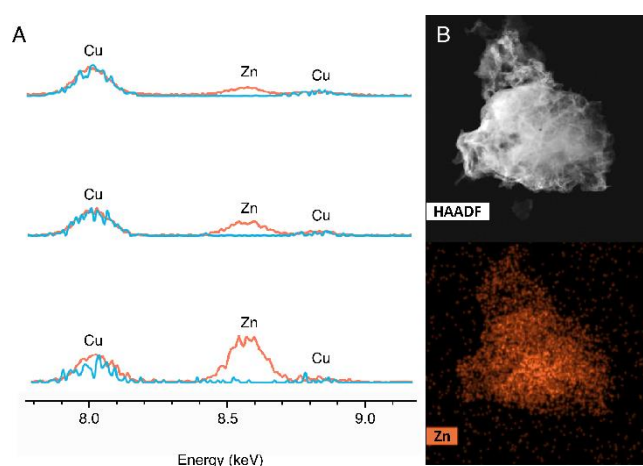
Figure 4-2. A) STEM-EDX spectra of C-S-H samples with a $(Zn:Si)_i$ ratio of 0.03 (top), 0.08 (centre) and 0.15 (bottom). For each $(Zn:Si)_i$ spectra corresponding to regions including (orange) and excluding (blue) C-S-H particles are shown. The intensities of the Zn signals are normalized with respect to the Cu absorption line at 8 keV from the TEM grid. B) A HAADF-STEM X-ray composition map of a C-S-H particle with a $(Zn:Si)_i$ ratio of 0.15, showing an apparent Zn uptake.

Figure 2A shows normalized EDX spectra of samples with different initial Zn to Si ratios of 0.03, 0.08 and 0.15 in the reagent solutions. Comparison of the EDX spectra recorded from a region excluding (blue) and including a C-S-H particle (orange) show a clear trend: samples which have been synthesized with an increased concentration of zinc nitrate show higher zinc counts in the EDX experiment, pointing to an incorporation of zinc in C-S-H (Figure 2A). Furthermore, HAADF and TEM data show no appreciable differences between the observed

morphology of conventional C-S-H and zinc-modified C-S-H, with all samples showing a nanofoil morphology which is consistent with literature (Figure 2B and Figure S2).

4.3.2 Characterization by DNP NMR

In order to determine the zinc-modified C-S-H structure DNP-enhanced ^{29}Si 1D multi-CPMAS NMR spectra [51] and 2D INADEQUATE spectra [15, 22, 52, 53] were obtained.

To be able to acquire the relatively insensitive 1D and 2D ^{29}Si solid-state spectra necessary to determine the populations and the connectivities of the different silicon sites in the materials, we prepared a series of zinc-modified C-S-H formulations. These were chosen to yield enhancement of NMR signals by MAS DNP [20, 21], by adapting the procedures developed previously [15, 16, 20] by incorporating a small amount of the organic biradical AMUPol [23] into the C-S-H sample. When the sample is frozen at 100 K, AMUPol allows efficient transfer of large electron polarization to protons in the frozen sample when microwaves are applied. The enhanced ^{1}H magnetization is then transferred to ^{29}Si nuclei through CP.

Figure 3A compares the ^{29}Si DNP-enhanced multi-CP spectra from three samples with (Zn:Si)$_i$ of 0, 0.15 and 0.40. The multi-CPMAS pulse sequence, which is based on the repetition of CP periods [51], yields ^{29}Si NMR spectra which allow for quantitative analysis of the different silicate species in C-S-H samples [51, 54]. The spectrum of the sample with (Zn:Si)$_i$ of 0 shows the well-characterized ^{29}Si peaks expected in conventional high Ca:Si ratio C-S-H whose signals are attributed to Q$^{(1)}$ (–78.9 ppm), Q$^{(2b)}$ (–81.4 ppm), and Q$^{(2p)}$ (–84.4 ppm) silicate species [15, 55-57]. The spectra of the samples with (Zn:Si)$_i$ of 0.15 and 0.40 show the presence of new Q sites at around –72 and –79 ppm; details regarding the spectral deconvolution are provided below. All the different species present in the zinc-modified C-S-H spectra are more clearly shown in Figure 3B where the deconvolution of the different Q sites is carried out. The presence of the new ^{29}Si signals around –72 and –79 ppm suggests the incorporation of zinc in the C-S-H structure as it indicates that the chemical environment of at least one silicate species is changed with respect to conventional C-S-H samples. The new species that gives rise to the signal at –72 ppm has a chemical shift similar to those of silicate monomers (Q$^{(0)}$) which typically range from –60 ppm to –75 ppm [58]. Silicate monomers (Q$^{(0)}$) are however discarded since, although observed in minor amounts in works from other groups with different synthetic routes [59-61], they are not usually observed in C-S-H samples [15, 16], and they are not a

characteristic feature of the high Ca:Si ratio C-S-H structures synthesized through our dropwise precipitation method [15, 16].
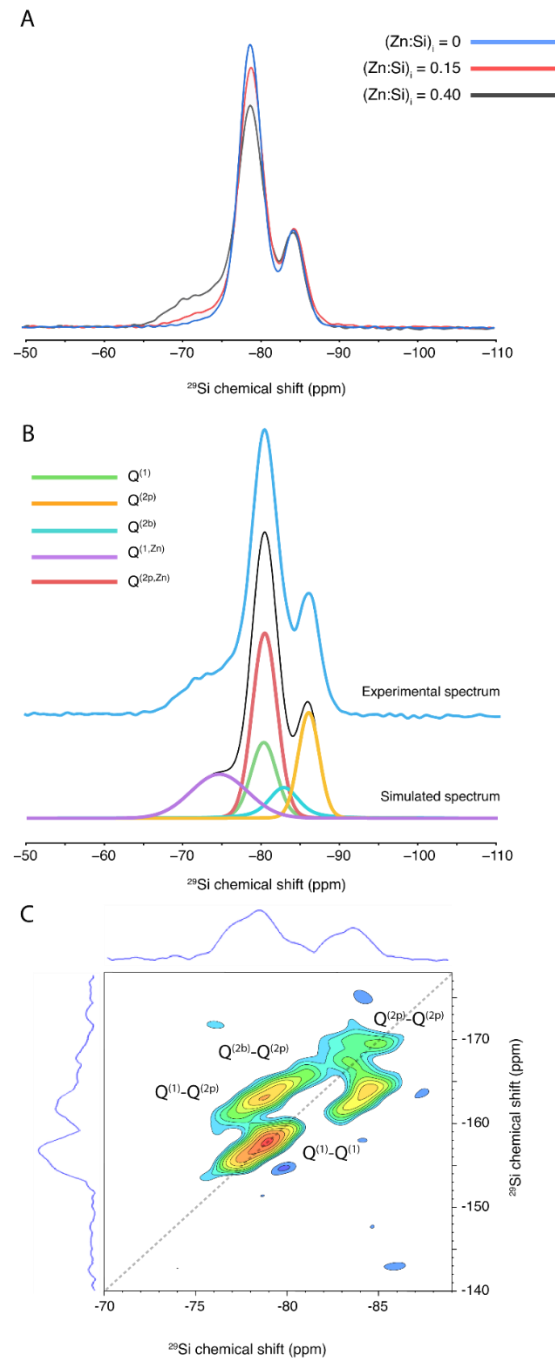
Figure 4-3. DNP-enhanced A) ^{29}Si{^{1}H} 1D multi-CPMAS spectra of samples with (Zn:Si)$_i$ of 0, 0.15 and 0.40, B) 1D multi-CPMAS spectrum of the sample with (Zn:Si)$_i$ of 0.40 (top) showing deconvolution into the different Q sites (bottom), and C) 2D ^{29}Si-^{29}Si INADEQUATE spectrum of a zinc-modified C-S-H sample with a (Zn:Si)$_i$ ratio of 0.40.

The spectra in Figure 3A were normalized to total intensity and show evidence of two trends. As the $(Zn:Si)_i$ is increased, the signal at -78.9 ppm decreases while the new signal at around -72 ppm increases in intensity. To further investigate the species present DNP enhanced natural abundance homonuclear ^{29}Si - ^{29}Si refocused INADEQUATE spectra were acquired [15, 22, 52, 53]. A 2D INADEQUATE spectrum of a zinc-modified C-S-H gel with $(Zn:Si)_i$ of 0.40 is shown in Figure 3C (and spectra corresponding to $(Zn:Si)_i$ of 0 and 0.15 are shown in SI section Vb).

This spectrum shows the expected connectivities in conventional C-S-H samples [15]: $Q^{(1)}$-$Q^{(1)}$, $Q^{(2p)}$-$Q^{(1)}$, $Q^{(2p)}$-$Q^{(2b)}$ and $Q^{(2p)}$-$Q^{(2p)}$. Signals corresponding to $Q^{(2b)}$-$Q^{(1)}$ or $Q^{(2b)}$-$Q^{(2b)}$ connectivities are not present, as is consistent with the connectivity of the C-S-H silicate chains. Additionally, no correlations with the new ^{29}Si species at -72 ppm are observed. Through-space exchange spectroscopy experiments (EXSY) were also carried out and confirmed that this new species, although not having through-bond correlations with other Q sites, has close through-space correlations mediated by spin diffusion, which further confirms its incorporation in the C-S-H internal structure. Results from the ^{29}Si - ^{29}Si EXSY experiments are shown in Figures S9 and S10.

4.3.3 Candidate structure generation: stability of zincate species in zinc-modified C-S-H

To determine the possible sites for incorporation of zinc species into the silicate chains of C-S-H at the atomic-level, ninety-eight different zinc-modified C-S-H structural units with Ca:Si ratios ranging from 1.2 to 2.25 were generated via brick models.[27] For each structure, DFT [32, 34] based chemical shifts were calculated and compared to the experimental chemical shifts obtained from 1D and 2D NMR experiments. In order to calibrate the calculated shifts, the mean shifts of the well-established characteristic sites present in conventional C-S-H gels ($Q^{(1)}$, $Q^{(2p)}$, $Q^{(2b)}$) were computed (Figure 4B) and were found to be in good agreement with experiments and literature. All possible DFT-based calculated chemical shifts for all the silicon sites in the ninety-eight candidate structures are provided with the raw data.

DFT was also used to compute the absolute energies of each structure to investigate differences in stability. Figure 4A shows a selection of relevant structures, where 4-coordinated zinc substitutes for $Q^{(1)}$, $Q^{(2p)}$ or $Q^{(2b)}$ silicates or is adjacent to two silicates and in the interlayer. The calculated energies of all candidate structures corresponding to a Ca:Si ratio of 1.67 and

2.0 are shown in Figure S4. Table S3 shows the relative calculated energies of all the candidate structures, ordered in sets according to their Ca:Si ratio. The calculated energies are normalized to the structure where zinc substitutes for a $Q^{(2b)}$ site and is coordinated as $ZnO_2(OH)_2$, which is consistently the most stable Q site substitution at Ca:Si ratios of 1.67.

4.3.4 NMR Crystallography with DFT-based calculated chemical shifts

The DFT-calculated ^{29}Si isotropic shifts resulting from each structure are shown in Figure 4B and Figure S5, and also provided with the raw data. Results from energy minimization and chemical shift calculations through DFT were then compared to experimental data from both 1D multi-CPMAS and 2D INADEQUATE experiments in order to verify or discard the relaxed structures, as discussed below.

At the Ca:Si ratios used in this work, zinc substituting for a $Q^{(2b)}$ site is predicted to be the most favourable structure owing to its lowest mean energies, while zinc substituting for a $Q^{(1)}$ site is predicted to be energetically more favourable than zinc substituting for a $Q^{(2p)}$ site (Figure S4). This is consistent with the experimental 2D ^{29}Si-^{29}Si INADEQUATE NMR results, since zinc substitution in a $Q^{(2p)}$ site should yield $Q^{(2b,Zn)}$-$Q^{(2p)}$ and $Q^{(2b,Zn)}$-$Q^{(2p,Zn)}$ correlations in the region between –74.8 ppm and –84.4 ppm, which are not observed. Based on both the calculated energies and the NMR results we conclude that zinc does not substitute for the $Q^{(2p)}$ species in C-S-H.

When zinc substitutes for a $Q^{(1)}$ site in a dimer the mean calculated isotropic chemical shift of the generated $Q^{(1,Zn)}$ species, as shown in Figure 4B, is –71.5 ppm which is also the measured value for a Zn-Si dimer complex [48]. This value agrees with the signal observed experimentally at approximately –72 ppm and is also consistent with the fact that there are no ^{29}Si - ^{29}Si correlations with this chemical shift in the 2D INADEQUATE NMR experiments. Additionally, our DFT calculations predict a lower span (Ω) of the chemical shift anisotropy (CSA) tensor for $Q^{(1,Zn)}$ when compared to the other species, which is in agreement with our experimental results (see SI section Vd).

Having identified unambiguously the $Q^{(1,Zn)}$ species, we note however that it can only account for ca. 60-70 % of the total zinc content (see SI section Ve). Therefore, the remaining zinc atoms must be incorporated in other sites of the structure.

In all the 1D multi-CPMAS spectra with the (Zn:Si)$_i$ ratio between 0 and 0.4, the ratio of the integrated signal intensities of the Q$^{(2p)}$ and Q$^{(2b)}$ sites are found to be consistently equal to two, as expected. Upon inclusion of a fifth site in the deconvolution of the ^{29}Si NMR spectra with a signal intensity constrained to account for the remaining 30-40 % of zinc, the only possible chemical shift for the second new ^{29}Si species is found to be –79 ppm (Figure 3B).

With DFT, substitution for Q$^{(2b)}$ is always predicted to be the most favourable energetically at Ca:Si ratio 1.67 (Table S3), and the resulting two symmetrical ^{29}Si sites, denoted Q$^{(2p,Zn)}$, have a calculated mean chemical shift of –79 ppm.

Due to the overlap of the Q$^{(2p,Zn)}$ species with the Q$^{(1)}$ species (–78.9 ppm), these two species are indistinguishable in 1D ^{29}Si NMR spectra. The Q$^{(2p,Zn)}$ species can be connected either to Q$^{(2p)}$ or Q$^{(1)}$ species, which would yield similar correlations as those observed between Q$^{(1)}$-Q$^{(1)}$ and Q$^{(2p)}$-Q$^{(1)}$ species, making them again indistinguishable in the INADEQUATE spectra. However, we note that the only substitution site that is compatible with both the 1D multi-CPMAS and 2D INADEQUATE experiments is Q$^{(2b)}$ leading to two symmetrical Q$^{(2p,Zn)}$ species. These considerations, taken together with the fact that the integrated area corresponding to the conventional Q$^{(2p)}$ sites cannot account for all the expected new species arising from zinc incorporation, led us to determine that the only region where the signal corresponding to Q$^{(2p,Zn)}$ species could be is indeed overlapping with the signal that corresponds to Q$^{(1)}$ species. Therefore, we assign a second new ^{29}Si species at –79 ppm to be Q$^{(2p,Zn)}$. The substitution at the bridging site is also analogous to the previously determined C-A-S-H structure [16].

Based on the evidence shown, Q$^{(1,Zn)}$ and Q$^{(2p,Zn)}$ species are identified as the main silicate species arising from zinc incorporation in C-S-H systems.

Finally, we consider two other energetically possible sites Q$^{(2p,2Zn)}$ and Q$^{(1,Zn\_int)}$ (see Figure 4B). Q$^{(2p,2Zn)}$ species (Figure 1), with a calculated chemical shift of –73.0 ppm, can only be present in a pentamer or a higher degree unit if zinc substitutes for the Q$^{(1)}$ and Q$^{(2b)}$ species simultaneously, creating a Zn-Si-Zn linkage at the start of the chain. The calculated chemical shift is similar to that of Q$^{(1,Zn)}$ species, and would yield a signal in the 1D ^{29}Si experiments while yielding no ^{29}Si-^{29}Si correlations in the 2D ^{29}Si INADEQUATE NMR experiments, which is compatible with our results. This species requires a high (Zn:Si)$_i$ as well as a high degree of polymerization to occur, as it is the combination of a zinc substitution for a Q$^{(1)}$ and a Q$^{(2b)}$

simultaneously. Due to the fact that this species ($Q^{(2p,2Zn)}$) requires two Zn substitutions to occur, though possible they are rendered less probable and are discarded in the further analysis.
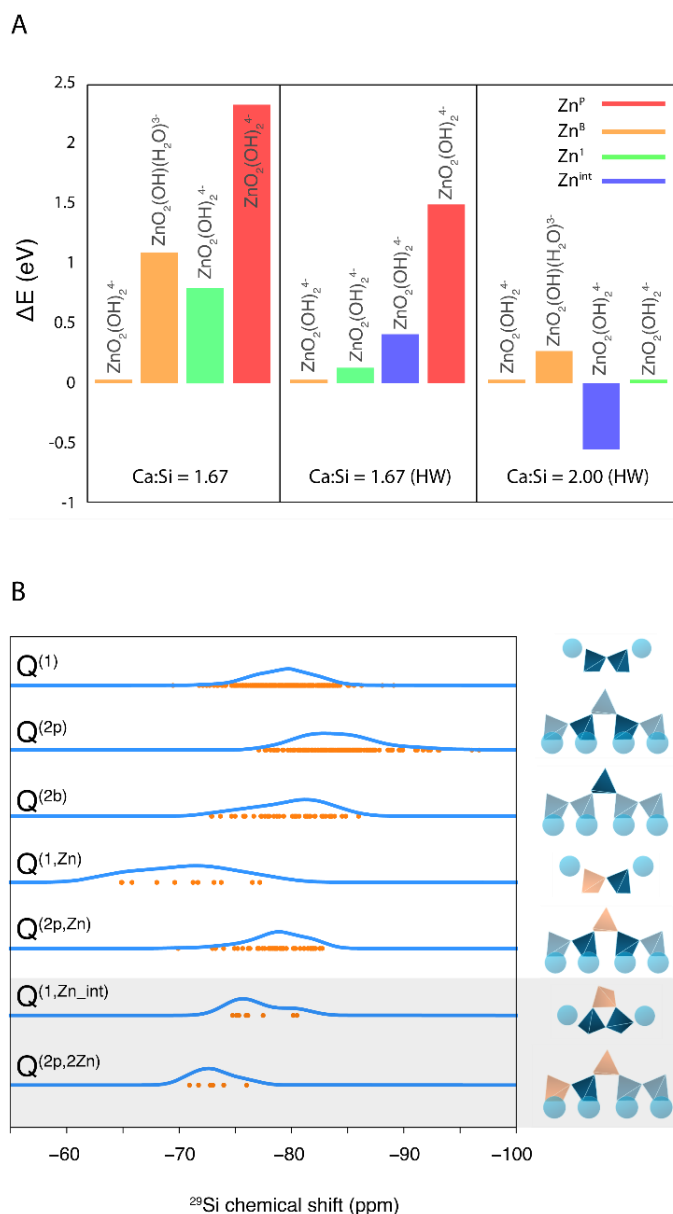
Figure 4-4. A) Relative calculated energies of representative zinc-modified C-S-H structures according to each substitution site with different Ca:Si ratios and interlayer amounts. Each column is normalized to the substitution of zinc in the bridging site with a $\Delta E = 0$ eV. Nomenclature: Zn^B = zinc in the $Q^{(2b)}$ site, Zn^P = zinc in the $Q^{(2p)}$ site, Zn^1 = zinc in the $Q^{(1)}$ site, Zn^{Int} = zinc on top of a $Q^{(1)}$-$Q^{(1)}$ dimer site, HW = High Water content. All structures are labeled with their corresponding zinc species which may coordinate to hydroxides or water. B) DFT calculated shifts from the silicate species obtained from brick models for zinc-modified C-S-H and their respective schematic structures.

$Q^{(1,Zn\_int)}$ (Figure 1) has a calculated chemical shift at around –75 ppm which would overlap with the signal from $Q^{(1)}$ species. Similarly to $Q^{(2p,Zn)}$ species, $Q^{(1,Zn\_int)}$ species would also be unresolvable in ^{29}Si-^{29}Si INADEQUATE NMR experiments since their predicted correlation would overlap with the $Q^{(1)}$-$Q^{(1)}$ correlation. However, to our knowledge, there are no known structures which exhibit such a Zn-Si feature. Therefore, again, though possible, this species is not considered further.

A summary of the predicted silicate species which arise from zinc incorporation into C-S-H, and their DFT calculated chemical shift distributions is shown in Figure 4B. Our experimental results identify that zinc-modified C-S-H includes $Q^{(1)}$, $Q^{(2p)}$, $Q^{(2b)}$, $Q^{(1,Zn)}$ and $Q^{(2p,Zn)}$, and while $Q^{(2p,2Zn)}$ and $Q^{(1,Zn\_int)}$ species are predicted to be feasible with regard to the energetics, they cannot be verified through ^{29}Si NMR experiments and no such species have been found in the literature, they are therefore shown in Figure 4B as possible structures but they are discarded for the following C-S-H chain length and Q population analyses.

4.3.5 Chain length and population analysis

Quantitative analyses of Q species populations and C-S-H chain length distributions were carried out assuming the silicate species present in zinc-modified C-S-H samples are $Q^{(1)}$, $Q^{(2b)}$, $Q^{(2p)}$, $Q^{(1,Zn)}$ and $Q^{(2p,Zn)}$.
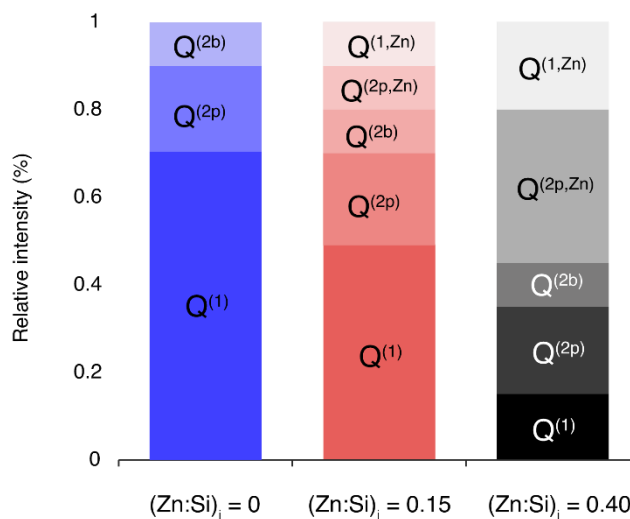
Figure 4-5. Results of the quantitative population analysis in the three samples with (Zn:Si)i of 0, 0.15 and 0.40.

The spectra acquired from samples with $(Zn:Si)_i$ of 0, 0.15 and 0.40 were analysed by fitting each of the constituent Q sites with a Gaussian lineshape, whose integrals are used to determine the relative populations of Q species in each sample (Figure 5). As mentioned above, at a $(Zn:Si)_i$ ratio of 0 (conventional C-S-H), the typical ^{29}Si signals for C-S-H with high Ca:Si ratios are present: $Q^{(1)}$ at -78.9 ppm, $Q^{(2b)}$ at -81.4 ppm and $Q^{(2p)}$ at -84.4 ppm. The population analysis from multi-CPMAS matches the results of Kumar et al. [15] for pure single-phase C-S-H samples with Ca:Si ratios of 1.75.

Figure 5 shows a quantitative Q species population analysis of the three samples with different $(Zn:Si)_i$ ratios. These results show that conventional C-S-H has a population distribution in which the majority (70%) of the silicate species are $Q^{(1)}$ sites, which is consistent with the literature for high Ca:Si ratios, while 20% are $Q^{(2p)}$ sites and 10% are $Q^{(2b)}$ sites. As zinc is incorporated into the C-S-H structure, the population of $Q^{(1)}$ species decreases, while the populations of $Q^{(2p)}$ and $Q^{(2b)}$ species remain constant. The populations of $Q^{(1,Zn)}$ and $Q^{(2p,Zn)}$ increase upon zinc incorporation. $Q^{(1,Zn)}$ species constitute 10% of all silicate species in samples with $(Zn:Si)_i$ of 0.15, while constituting 23% of all silicate species in the sample with $(Zn:Si)_i$ of 0.40. The $Q^{(2p,Zn)}$ species increases from 10% in the sample with $(Zn:Si)_i$ of 0.15 to 34% in the sample with $(Zn:Si)_i$ of 0.40. This analysis suggests a conversion of $Q^{(1)}$ species into $Q^{(1,Zn)}$ and $Q^{(2p,Zn)}$ species as more zinc is incorporated into the C-S-H structure.

The effect of zinc on the Q-site populations can be related to changes in the distribution of mean chain lengths. Understanding the effect of zinc on the mean chain length distributions could allow for a fine tunability of this material for its implementation at a macroscopic scale. To assess the chain length distribution of zinc-modified C-S-H, it is again assumed that the only species present in the material are $Q^{(1)}$, $Q^{(2p)}$, $Q^{(2b)}$, $Q^{(1,Zn)}$ and $Q^{(2p,Zn)}$. Integrals from the multi-CPMAS population analysis can be combined with the 2D connectivities seen in the INADEQUATE spectra to estimate the molar fractions of dimers in the system following the approach of Kumar et al.[15] as described in the SI section Vf. Removing SiO_2 units from bridging sites creates defects which shorten and break the chains, generating dimers (x_0), pentamers (x_1), octamers (x_2), and higher degree units with increasing numbers of SiO_2 bridging sites (x_n). The extent of defects determines the mean chain length, as well as its distribution into dimers, pentamers, octamers or longer silicate-zincate units. The chain lengths for each sample are estimated by calculating the molar fraction of $Q^{(1)}$-$Q^{(1)}$ and $Q^{(1)}$-$Q^{(1,Zn)}$ dimers (x_0) and

deriving the molar fraction of the silicate-zincate species which have higher degrees of polymerization (x_n).

Table 4-1. Molar fractions of dimers (x0), higher degree units (xn) and mean chain length (MCL) for samples with (Zn:Si)i of 0, 0.15 and 0.40.

(Zn:Si)$_i$ ratio	x$_0$	x$_n$	MCL
0.00	0.86	0.14	2.9
0.15	0.48	0.52	3.3
0.40	0.38	0.62	4.5

Table 1 shows the molar fractions of the three samples with different (Zn:Si)$_i$ ratios. The molar fraction of the higher degree units (x_n), which is a direct sign of a higher degree of polymerization, is lowest in the pure C-S-H sample (Zn:Si)$_i$ = 0. The molar fraction of higher degree units increases to 0.52 in the sample with (Zn:Si)$_i$ = 0.15, and to 0.62 in the sample with a (Zn:Si)$_i$ = 0.40.

In addition to the molar fractions of dimers and higher degree units present in zinc-modified C-S-H, the mean chain length (MCL) of each system was calculated. MCL is calculated according to equation 1 below [27].

$$MCL = \frac{Total\ Si + \ Zn\ species}{0.5(non\ bridging\ species) - (bridging\ species)} \tag{1}$$

The MCL of the conventional C-S-H sample (with a (Zn:Si)$_i$ = 0) is 2.9, and is consistent with the literature for high Ca:Si ratios.[27] The sample with (Zn:Si)$_i$ = 0.15 has a calculated MCL of 3.3, and the sample with (Zn:Si)$_i$ = 0.40 has a MCL of 4.5. This shows that the presence of $Q^{(2p,Zn)}$ species in zinc-modified C-S-H systems leads to increased MCL with respect to unmodified C-S-H. We conclude that zinc-modified C-S-H has a higher degree of polymerization when compared to conventional C-S-H.

Figure 6 shows a representative atomic-level structure of the zinc-modified C-S-H determined here. It has the characteristic C-S-H $Q^{(1)}$ (–78.9 ppm), $Q^{(2p)}$ (–81.4 ppm) and $Q^{(2b)}$ (–84.36 ppm) species, as well as the newly discovered $Q^{(1,Zn)}$ and $Q^{(2p,Zn)}$ species, and in this example the (Zn:Si)$_i$ is 0.15. Additional representative structures that incorporate the DFT-predicted $Q^{(1,Zn\_int)}$ and $Q^{(2p,2Zn)}$ species are shown in SI section VI.

4.3.6 Formation of zinc-modified C-S-H

We have identified two sites for the incorporation of octahedrally coordinated zinc oxyhydroxide species $(ZnO_2(OH)_2{}^{4-})$ into C-S-H. This was done experimentally at a Ca:Si ratio of 1.75 and explored between 1.25 and 2.25 with atomistic modelling. As mentioned above, the incorporation of small amounts of zinc in the hydration of the key cement phases leads to significant acceleration in hydration kinetics and accompanying increase in hardened strength [5, 11]. Synthetic C-S-H systems generally show a thin sheet morphology (Fig. 2B and S2) indicating growth is mainly in the a-b directions and very limited along the c axis. Three of the zinc sites are found in the silicate chains, which lie parallel to the b direction. During the growth of C-S-H the main silicate species in solution is the neutral complex $CaSiO_2(OH)_2$ (present at 2 mM concentrations) [62]. To link these species to form the calcium-silicate sheets that make up C-S-H, bridging species such as monomeric silicates (0.05 mM) or Ca^{2+} (10 mM) are needed. The main zinc species in solution is $ZnO_2(OH)_2{}^{4-}$ (2 mM) at the pHs used here and in cementitious systems [48]. Here we have found that this species is readily incorporated into both the bridging position and the $Q^{(1)}$ end chain position, and can hence accelerate the growth of C-S-H by simply increasing the number of growth units in solution. From ICP measurements of the supernatant (Figure S3) we see that even at a molar ratio of 0.4 Zn:Si the vast majority (98-99%) of the zinc is incorporated into the C-S-H. Taking the ensemble of our observations together, we suggest the acceleration seen in hydration [4-6] could be due to the enhanced concentration of effective monomeric growth species (Zn $>>$ Si) at the early stages of growth.

Additionally, $[(HO)_3ZnOSiO_2OH]^{4-}$ and $[(HO)_3ZnO(SiO_2)O(SiO_2)OH]^{6-}$ species have been postulated at pH above 14, and they may also play a role in the chain formation process [48].

To validate the hypotheses generated from the atomic-level structures of zinc-modified C-S-H determined here, detailed thermodynamic modelling and kinetic experiments on synthetic C-S-H in the presence of zinc will be carried out in future studies, for example using the population balance approach developed by Andalibi et al. [62] to model both growth rates and monitor solution speciation as a function of reaction time.

Conclusions

We precipitated pure single-phase C-S-H in the presence of zinc with a target Ca:Si ratio of 1.75, analogous to industrially relevant compositions, from a solution of aqueous sodium

metasilicate, calcium nitrate and zinc nitrate under controlled pH, temperature and atmospheric conditions. TEM was used to observe the microstructure of the precipitated product, and EDX confirmed the local composition. DNP enhanced 1D $^1H \rightarrow ^{29}Si$ multi-CPMAS NMR was used to measure quantitative populations of Q species, and natural abundance 2D ^{29}Si-^{29}Si INADEQUATE spectra were used to determine the connectivities between the silicate species.
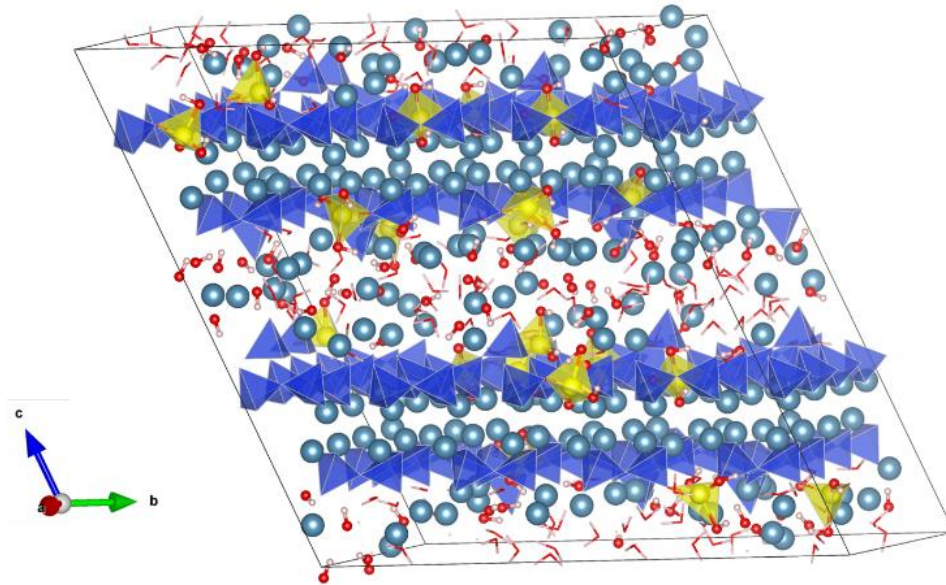
Figure 4-6. Representative atomic-level structure of zinc-modified C-S-H as determined with $(Zn:Si)_i$ = 0.15. Silicate tetrahedra are depicted in blue; zincate tetrahedra are depicted in yellow; and calcium ions are depicted in light blue.

These data, in combination with atomistic modelling and DFT chemical shift calculations were used to determine the atomic-level structure of zinc-modified synthetic C-S-H.

Specifically, as shown in Figure 6, two new silicate sites are present in the structure: $Q^{(1,Zn)}$ and $Q^{(2p,Zn)}$. By determining the structure in three samples with different $(Zn:Si)_i$ ratios we find that zinc promotes an increase of the mean chain lengths.

The structure suggests that the enhanced hydration kinetics in zinc-containing cementitious systems could be due to the enhanced concentration of effective monomeric species at the early stages of growth. Considering that real cementitious systems also contain aluminium and that

aluminium is known to incorporate into the C-S-H structure, work is in progress to the study the impact of dual incorporation of zinc and aluminium in C-S-H.

References

[1]   Scrivener, K. L.; Kirkpatrick, R. J. Innovation in Use and Research on Cementitious Material. *Cem. Concr. Res.* **2008**, *38* (2), 128-136.

[2]   Megat Johari, M. A.; Brooks, J. J.; Kabir, S.; Rivard, P. Influence of Supplementary Cementitious Materials on Engineering Properties of High Strength Concrete. *Constr. Build. Mater.* **2011**, *25* (5), 2639-2648.

[3]   Juenger, M. C. G.; Siddique, R. Recent Advances in Understanding the Role of Supplementary Cementitious Materials in Concrete. *Cem. Concr. Res.* **2015**, *78* (A), 71-80.

[4]   Stephan, D.; Maleki, H.; Knöfel, D.; Eber, B.; Härdtl, R. Influence of Cr, Ni, and Zn on the Properties of Pure Clinker Phases: Part I. C_3S. *Cem. Concr. Res.* **1999**, *29* (4), 545-552.

[5]   Li, X.; Scrivener, K. L. Impact of ZnO on C_3S hydration and C-S-H Morphology at Early Ages. *Cem. Concr. Res.* **2022**, *154*, 106734.

[6]   Odler, I.; Abdul-Maula, S. Polymorphism and Hydration of Tricalcium Silicate Doped with ZnO. *J. Am. Ceram. Soc.* **1983**, *66* (1), 1-4.

[7]   Bullard, J. W.; Jennings, H. M.; Livingston, R. A.; Nonat, A.; Scherer, G. W.; Schweitzer, J. S.; Scrivener, K. L.; Thomas, J. J. Mechanisms of Cement Hydration. *Cem. Concr. Res.* **2011**, *41* (12), 1208-1223.

[8]   Scrivener, K. L.; Juilland, P.; Monteiro, P. J. M. Advances in understanding hydration of Portland cement. *Cem. Concr. Res.* **2015**, *124* (A), 38-56.

[9]   Scrivener, K.; Ouzia, A.; Juilland, P.; Kunhi Mohamed, A. Advances in Understanding Cement Hydration Mechanisms. *Cem. Concr. Res.* **2019**, *124*, 105823.

[10]   Ouzia, A.; Scrivener, K. The Needle Model: A New Model for the Main Hydration Peak of Alite. *Cem. Concr. Res.* **2019**, *115*, 339-360.

[11]   Bazzoni, A.; Ma, S.; Wang, Q.; Shen, X.; Cantoni, M.; Scrivener, K. L. The Effect of Magnesium and Zinc Ions on the Hydration Kinetics of C_3S. *J. Am. Ceram. Soc.* **2014**, *97* (11), 3684-3693.

[12]   Nonat, A.; Lecoq, X. The Structure, Stoichiometry and Properties of C-S-H Prepared by C_3S hydration under Controlled Condition. In *Nuclear magnetic resonance spectroscopy of cement-based materials*, Springer, 1998; pp 197-207.

[13]   Nonat, A. The Structure and Stoichiometry of C-S-H. *Cem. Concr. Res.* **2004**, *34* (9), 1521-1528.

[14]   Klur, I.; Pollet, B.; Virlet, J.; Nonat, A. C-S-H Structure Evolution with Calcium Content by Multinuclear NMR. In *Nuclear magnetic resonance spectroscopy of cement-based materials*, Springer, 1998; pp 119-141.

[15]   Kumar, A.; Walder, B. J.; Kunhi Mohamed, A.; Hofstetter, A.; Srinivasan, B.; Rossini, A. J.; Scrivener, K.; Emsley, L.; Bowen, P. The atomic-level structure of cementitious calcium silicate hydrate. *J. Phys. Chem. C* **2017**, *121* (32), 17188-17196.

[16]   Kunhi Mohamed, A.; Moutzouri, P.; Berruyer, P.; Walder, B. J.; Siramanont, J.; Harris, M.; Negroni, M.; Galmarini, S. C.; Parker, S. C.; Scrivener, K. L.; Emsley, L.; Bowen, P. The Atomic-Level Structure of Cementitious Calcium Aluminate Silicate Hydrate. *J. Am. Chem. Soc.* **2020**, *142* (25), 11060-11071.

[17]   Harris, M.; Simpson, G.; Scrivener, K.; Bowen, P. A Method for the Reliable and Reproducible Precipitation of Phase Pure high Ca/Si ratio (> 1.5) Synthetic Calcium Silicate Hydrates (C-S-H). *Cem. Concr. Res.* **2022**, *151*, 106623.

[18]   Maddalena, R.; Hamilton, A. Low-pressure Silica Injection for Porosity Reduction in Cementitious Materials. *Constr. Build. Mater.* **2017**, *134* (1), 610-616.

[19]   Renaudin, G.; Russias, J.; Leroux, F.; Frizon, F.; Cau-dit-Coumes, C. Structural Characterization of C–S–H and C–A–S–H Samples—Part I: Long-Range Order Investigated by Rietveld Analyses. *J. Solid State Chem.* **2009**, *182* (12), 3312-3319.

[20]   Rossini, A. J.; Zagdoun, A.; Lelli, M.; Lesage, A.; Coperet, C.; Emsley, L. Dynamic Nuclear Polarization Surface Enhanced NMR Spectroscopy. *Accounts. Chem. Res.* **2013**, *46* (9), 1942-1951.

[21]   Lesage, A.; Lelli, M.; Gajan, D.; Caporini, M. A.; Vitzthum, V.; Miéville, P.; Alauzun, J.; Roussey, A.; Thieuleux, C.; Mehdi, A.; Bodenhausen, G.; Cóperet, C.; Emsley, L. Surface Enhanced NMR Spectroscopy by Dynamic Nuclear Polarization. *J. Am. Chem. Soc.* **2010**, *132* (44), 15459-15461.

[22]   Rossini, A. J.; Zagdoun, A.; Hegner, F.; Schwarzwälder, M.; Gajan, D.; Copéret, C.; Lesage, A.; Emsley, L. Dynamic Nuclear Polarization NMR Spectroscopy of Microcrystalline Solids. *J. Am. Chem. Soc.* **2012**, *134* (40), 16899-16908.

[23]   Sauvée, C.; Rosay, M.; Casano, G.; Aussenac, F.; Weber, R. T.; Ouari, O.; Tordo, P. Highly Efficient, Water-Soluble Polarizing Agents for Dynamic Nuclear polarization at high frequency. *Angew. Chem.* **2013**, *125* (41), 11058-11061.

[24]   Ni, Q. Z.; Daviso, E.; Can, T. V.; Markhasin, E.; Jawla, S. K.; Swager, T. M.; Temkin, R. J.; Herzfeld, J.; Griffin, R. G. High Frequency Dynamic Nuclear Polarization. *Accounts. Chem. Res.* **2013**, *46* (9), 1933-1941.

[25]   Liu, S.-F.; Mao, J.-D.; Schmidt-Rohr, K. A Robust Technique for Two-Dimensional Separation of Undistorted Chemical-Shift Anisotropy Powder Patterns in Magic-Angle-Spinning NMR. *J. Magn. Reson.* **2002**, *155* (1), 15-28.

[26]   van Meerten, S. G. J.; Franssen, W. M. J.; Kentgens, A. P. M. ssNake: A Cross-Platform Open-Source NMR Data Processing and Fitting Application. *J. Magn. Reson.* **2019**, *301*, 56-66.

[27]   Kunhi Mohamed, A.; Parker, S. C.; Bowen, P.; Galmarini, S. An Atomistic Building Block Description of C-S-H-Towards a Realistic C-S-H Model. *Cem. Concr. Res.* **2018**, *107*, 221-235.

[28]   Thompson, A. P.; Aktulga, H. M.; Berger, R.; Bolintineanu, D. S.; Brown, W. M.; Crozier, P. S.; in't Veld, P. J.; Kohlmeyer, A.; Moore, S. G.; Nguyen, T. D. LAMMPS-a Flexible Simulation Tool for Particle-Based Materials Modeling at the Atomic, Meso, and Continuum Scales. *Comput. Phys. Commun.* **2022**, *271*, 108171.

[29]   Valavi, M.; Casar, Z.; Kunhi Mohamed, A.; Bowen, P.; Galmarini, S. Molecular Dynamic Simulations of Cementitious Systems Using a Newly Developed Force Field Suite ERICA FF. *Cem. Concr. Res.* **2022**, *154*, 106712.

[30]   Lewis, G. V.; Catlow, C. R. A. Potential Models for Ionic Oxides. *J. Phys. C* **1985**, *18* (6), 1149-1161.

[31]   Perdew, J. P.; Burke, K.; Ernzerhof, M. Generalized Gradient Approximation Made Simple. *Phys. Rev. Lett.* **1996**, *77* (18), 3865-3868.

[32]   Grimme, S. Semiempirical GGA-Type Density Functional Constructed with a Long-Range Dispersion Correction. *J. Comput. Chem.* **2006**, *27* (15), 1787-1799.

[33]   Barone, V.; Casarin, M.; Forrer, D.; Pavone, M.; Sambi, M.; Vittadini, A. Role and Effective Treatment of Dispersive Forces in Materials: Polyethylene and Graphite Crystals as Test Cases. *J. Comput. Chem.* **2009**, *30* (6), 934-939.

[34]   Kresse, G.; Joubert, D. From Ultrasoft Pseudopotentials to the Projector Augmented-Wave Method. In *Phys. Rev. B*, 1999; Vol. 59, pp 1758-1775.

[35]   Corso, A. D. Pseudopotentials Periodic Table : From H to Pu. *Comput. Mater. Sci.* **2014**, *95*, 337-350.

[36]   Monkhorst, H. J.; Pack, J. D. Special Points for Brillouin-Zone Integrations. *Phys. Rev. B* **1976**, *13* (12), 5188-5192.

[37]   Pickard, C. J.; Mauri, F. All-Electron Magnetic Response with Pseudopotentials: NMR Chemical Shifts. *Phys. Rev. B* **2001**, *63* (24), 245101.

[38]   Yates, J. R.; Pickard, C. J.; Mauri, F. Calculation of NMR Chemical Shifts for Extended Systems using Ultrasoft Pseudopotentials. **2007**, *76* (2), 024401.

[39]   Klaska, K.-H.; Eck, J.; Pohl, D. New Investigation of Willemite. *Acta Crystallogr. B: Struct. Sci. Cryst. Eng. Mater.* **1978**, *1978* (B34), 3324-3325.

[40]   Hill, R. J.; Gibbs, G. V.; Craig, J. R. A Neutron-Diffraction Study of Hemimorphite. *Z. Kristallogr. Cryst. Mater.* **1977**, *146* (1-6), 241-259.

[41]   Gard, J. A.; Taylor, H. F. W. The Crystal Structure of Foshagite. *Acta Crystallogr.* **1960**, *13* (10), 785-793.

[42]   Smith, G. S.; Alexander, L. E. Refinement of the Atomic Parameters of [Alpha]-Quartz. *Acta Crystallogr.* **1963**, *16* (6), 462-471.

[43]   Chandrappa, G. T.; Ghosh, S.; Patil, K. C. Synthesis and Properties of Willemite, Zn_2SiO_4, and M^{2+}:Zn_2SiO_4 (M=Co and Ni). *J. Mater. Synth. Process.* **1999**, *7*, 283-279.

[44]   Lippmaa, E.; Maegi, M.; Samoson, A.; Engelhardt, G.; Grimmer, A.-R. Structural Studies of Silicates by Solid-State High-Resolution Silicon-29 NMR. *J. Am. Chem. Soc.* **1980**, *102* (15), 4889-4893.

[45]   Giannozzi, P.; Baroni, S.; Bonini, N.; Calandra, M.; Car, R.; Cavazzoni, C.; Ceresoli, D.; Chiarotti, G. L.; Cococcioni, M.; Dabo, I.; Dal Corso, A.; de Gironcoli, S.; Fabris, S.; Fratesi, G.; et al. QUANTUM ESPRESSO: a Modular and Open-Source Software Project for Quantum Simulations of Materials. *J. Phys. Condens. Matter* **2009**, *21*, 395502.

[46]   Giannozzi, P.; Andreussi, O.; Brumme, T.; Bunau, O.; Buongiorno Nardelli, M.; Calandra, M.; Car, R.; Cavazzoni, C.; Ceresoli, D.; Cococcioni, M.; Colonna, N.; Carnimeo, I.; Dal Corso, A.; de Gironcoli, S.; et al. Advanced Capabilities for Materials Modelling with Quantum ESPRESSO. *J. Phys. Condens. Matter* **2017**, *217* (29), 465901.

[47]   Virtanen, P.; Gommers, R.; Oliphant, T. E.; Haberland, M.; Reddy, T.; Cournapeau, D.; Burovski, E.; Peterson, P.; Weckesser, W.; Bright, J. SciPy 1.0: Fundamental Algorithms for Scientific Computing in Python. *Nat. Methods* **2020**, *17* (3), 261-272.

[48]   Anseau, M. R.; Leung, J. P.; Sahai, N.; Swaddle, T. W. Interactions of Silicate Ions with Zinc (II) and Aluminum (III) in Alkaline Aqueous Solution. *Inorg. Chem.* **2005**, *44* (22), 8023-8032.

[49]   Tommaseo, C. E.; Kersten, M. Aqueous Solubility Diagrams for Cementitious Waste Stabilization Systems. 3. Mechanism of Zinc Immobilizaton by Calcium Silicate Hydrate. *Environ. Sci. Technol.* **2002**, *36* (13), 2919-2925.

[50]   Rose, J.; Moulin, I.; Masion, A.; Bertsch, P. M.; Wiesner, M. R.; Bottero, J.-Y.; Mosnier, F.; Haehnel, C. X-Ray Absorption Spectroscopy Study of Immobilization Processes for Heavy Metals in Calcium Silicate Hydrates. 2. Zinc. *Langmuir* **2001**, *17* (12), 3658-3665.

[51]   Johnson, R. L.; Schmidt-Rohr, K. Quantitative Solid-State ^{13}C NMR with Signal Enhancement by Multiple Cross Polarization. *J. Magn. Reson.* **2014**, *239*, 44-49.

[52]   Fyfe, C. A.; Grondey, H.; Feng, Y.; Kokotailo, G. T. Natural-Abundance Two-Dimensional Silicon-29 MAS NMR Investigation of the Three-Dimensional Bonding Connectivities in the Zeolite Catalyst ZSM-5. *J. Am. Chem. Soc.* **1990**, *112* (24), 8812-8820.

[53]   Lesage, A.; Bardet, M.; Emsley, L. Through-Bond Carbon-Carbon Connectivities in Disordered Solids by NMR. *J. Am. Chem. Soc.* **1999**, *121* (47), 10987-10993.

[54]   Bertarello, A.; Berruyer, P.; Skantze, U.; Sardana, S.; Sardana, M.; Elmore, C. S.; Schade, M.; Chiarparin, E.; Schantz, S.; Emsley, L. Quantification of Magic Angle Spinning Dynamic Nuclear Polarization NMR Spectra. *J. Magn. Reson.* **2021**, *329*, 107030.

[55]   Alonso, C.; Fernandez, L. Dehydration and Rehydration Processes of Cement Paste Exposed to High Temperature Environments. *J. Mater. Sci.* **2004**, *39* (9), 3015-3024.

[56]   Sato, H.; Grutzeck, M. Effect of Starting Materials on the Synthesis of Tobermorite. *MRS Online Proceedings Library (OPL)* **1991**, *245*, 235-240.

[57]   Hong, S. H.; Young, J. F. Hydration Kinetics and Phase Stability of Dicalcium Silicate Synthesized by the Pechini Process. *J. Am. Ceram. Soc.* **1999**, *82* (7), 1681-1686.

[58]   Wang, L.; Geddes, D. A.; Walkley, B.; Provis, J. L.; Mechtcherine, V.; Tsang, D. C. W. The Role of Zinc in Metakaolin-Based Geopolymers. *Cem. Concr. Res.* **2020**, *136*, 106194.

[59]   Brunet, F.; Bertani, P.; Charpentier, T.; Nonat, A.; Virlet, J. Application of [29]Si Homonuclear and [1]H— ^{29}Si Heteronuclear NMR Correlation to Structural Studies of Calcium Silicate Hydrates. *J. Phys. Chem. B* **2004**, *108* (40), 15494-15502.

[60]   Cong, X.; Kirkpatrick, R. J. ^{29}Si MAS NMR Study of the Structure of Calcium Silicate Hydrate. *Adv. Cem. Based Mater.* **1996**, *3* (3-4), 144-156.

[61]   Pustovgar, E.; Sangodkar, R. P.; Andreev, A. S.; Palacios, M.; Chmelka, B. F.; Flatt, R. J.; d'Espinose de Lacaillerie, J.-B. Understanding Silicate Hydration from Quantitative Analyses of Hydrating Tricalcium Silicates. *Nat. Commun.* **2016**, *7* (1), 10952.

[62]   Andalibi, M. R.; Kumar, A.; Srinivasan, B.; Bowen, P.; Scrivener, K.; Ludwig, C.; Testino, A. On the Mesoscale Mechanism of Synthetic Calcium–Silicate–Hydrate Precipitation: a Population Balance Modeling Approach. *J. Mater. Chem. A* **2018**, *6* (2), 363-373.

5 Atomic-Level and Surface Structure of Calcium Silicate Hydrate Nanofoils

Ziga Casar[1+], Aslam Kunhi Mohamed[2*], Paul Bowen[1], Karen Scrivener[1]

[1] Laboratory of Construction Materials, Institut des Matériaux, Ecole Polytechnique Fédérale de Lausanne (EPFL), CH-1015 Lausanne, Switzerland

[2] Institute for building Materials, Department of Civil, Environmental and Geomatic Engineering, ETH Zürich, CH-8093 Zürich, Switzerland

[*] Current address: Department of Civil Engineering, IIT Madras, Chennai-60036, Tamil Nadu, India

Contribution Statement

The following chapter was submitted as a same named journal article to the Journal of Physical Chemistry C and is being revised. All structures, simulations, data postprocessing and findings, such as the correlation of surface silanol densities with the mean chain length, as well as the proposed co-adsorption, are the candidate's original work. The candidate wrote the original draft of the article.

Abstract

Deciphering the calcium silicate hydrate (C-S-H) surface is crucial for unraveling the mechanisms of cement hydration and property development. Experimental observations of C-S-H in cement systems suggest a surface termination which is fundamentally different from the silicate terminated surface assumed in many atomistic level studies. Here, a new multiparameter approach to describing the (001) basal C-S-H surface is developed which considers how the surface termination affects the overall properties (Ca/Si ratio, mean chain length, relative concentration of silanol and hydroxide groups). Contrary to current beliefs it is concluded that the (001) C-S-H surface is dominantly calcium terminated. Finally, an adsorption mechanism for calcium and hydroxide ions is proposed, which is in agreement with the surface charge densities observed in previous studies.

5.1 Introduction

The production of cementitious materials is responsible for 5-8% of anthropogenic CO_2 emissions [1]. With the rising world population and the related needs for infrastructure, the demand for cement will increase. To lower the carbon footprint of cement, fundamental understanding of the chemistry at the phase interfaces is needed [2].

The main hydration product of Portland and blended cements is calcium silicate hydrate (C-S-H). C-S-H forms around 50 to 60% by volume of hardened cement paste and is the primary binder that binds together other crystalline hydration products and aggregates and gives cohesion to the material [3]. Nucleation and growth of C-S-H is the underlying mechanism behind the main hydration stage occurring between a few hours and one day [4]. C-S-H forms a continuous nano porous network that reduces the transport of ions, such as chloride [5], which causes durability issues in steel reinforced concrete structures.

Transmission electron microscopy (TEM) images of C-S-H from samples of hydrated tricalcium silicate (C_3S) [6, 7] and TEM images of high Ca/Si pure phase synthetic C-S-H [8, 9] show a nanofoil morphology, as seen in figure 1. The nanofoils have a length around 100-200 nm [8, 10-12] and thickness below 5 nm [10, 11, 13, 14]. The measured specific surface area is in the range between 200 and 300 m^2/g [15-19]. These observations underline the importance of C-S-H surfaces [20].

The bulk structure of C-S-H is reasonably well understood [3, 8, 21, 22]. C-S-H can be considered as a highly defective 14Å tobermorite with variable chemical composition and structure. While there is no long-range order, X-ray diffraction patterns give broad C-S-H peaks which can be attributed to atomic distances within the calcium-silicate sheets [9, 14, 23]. The calcium-silicate sheets are made of calcium oxide layers to which silicate chains are attached on either side. These sheets are separated by interlayers containing water molecules and ions (figure 1). Contrary to 14Å tobermorite, which has a Ca/Si ratio of 0.83, C-S-H has a variable Ca/Si ratio of 1.2 to 2.1, with an average of 1.7 in plain Portland cements, at early ages. In 14Å tobermorite the silicate chains are composed of a dreierketten structure with silicate dimers, which are linked with bridging silicate tetrahedra Q^{2b} (see Si-Surface 2 in figure 3) [24]. ^{29}Si nuclear magnetic resonance (NMR) experiments on phase pure high Ca/Si C-S-H show the prevalence of the Q^1 end-of-chain dimeric silicate species [8, 25, 26], which is a consequence of missing Q^{2b} silicates. Kumar et al. [8] showed that most of the bridging sites

are occupied with calcium ions instead, which contributes to high Ca/Si ratios in C-S-H. At Ca/Si = 1.75 only 30% of bridging sites are occupied with a Q^{2b} silicate and the remaining 70% with calcium ions [26]. The calcium in these bridging sites is stabilized by an environment of strong hydrogen bonding.

The ratio of Q species is used to derive the mean chain length (MCL) [27]. Assuming a dreierketten structure and absence of silicate monomers [8, 28], an MCL = ∞ represents the 14Å tobermorite with no missing Q^{2b} silicates, MCL = 2 would be a structure with no Q^{2b} silicates, and at Ca/Si = 1.75 the calculated MCL ranges from 2.55 to 2.89 [8, 26]. ^{29}Si NMR shows the complete absence of any Q^3 silicate [8, 26], making it clear that there is no connectivity between silicates of opposite silicate chains via the interlayer, as observed in 11Å tobermorite [29]. Other studies have found an increase of hydroxide groups and decrease of silanol groups with increasing Ca/Si ratios [3, 22, 30]. All these findings indicate that the high Ca/Si ratios observed can be attributed to the calcium substitution of the bridging Q^{2b} silicate, and the addition of Ca^{2+} and OH^- ions in the interlayer.

In contrast to the bulk, the atomic structure of the surface of C-S-H is poorly characterized. Previous studies of interactions with C-S-H surfaces are summarized by Duque-Redondo et al. [3] and Kunhi Mohamed et al. [31] In most previous studies, authors have considered the energetically most favorable tobermorite basal (001) surface [32] to have a Q^{2b} silicate termination (Si-Surface 2 in figure 3). Due to the low Ca/Si of 14Å tobermorite some authors introduced defects to raise the Ca/Si ratio up to 1.4 [33-35].

The present paper shows how the brick model [21] combined with results from experimental measurements (Ca/Si ratio, MCL, relative concentration of silanol and hydroxyl groups) can be used to construct pragmatic models of realistic C-S-H surfaces. By considering the C-S-H structure characteristics, a correlation between system properties and the surface silanol density is found. A mechanism for calcium and hydroxide adsorption is proposed, which gives excellent agreement with previous studies on surface charge densities. Finally, a full atomistic model of the C-S-H nanofoil structure is proposed.
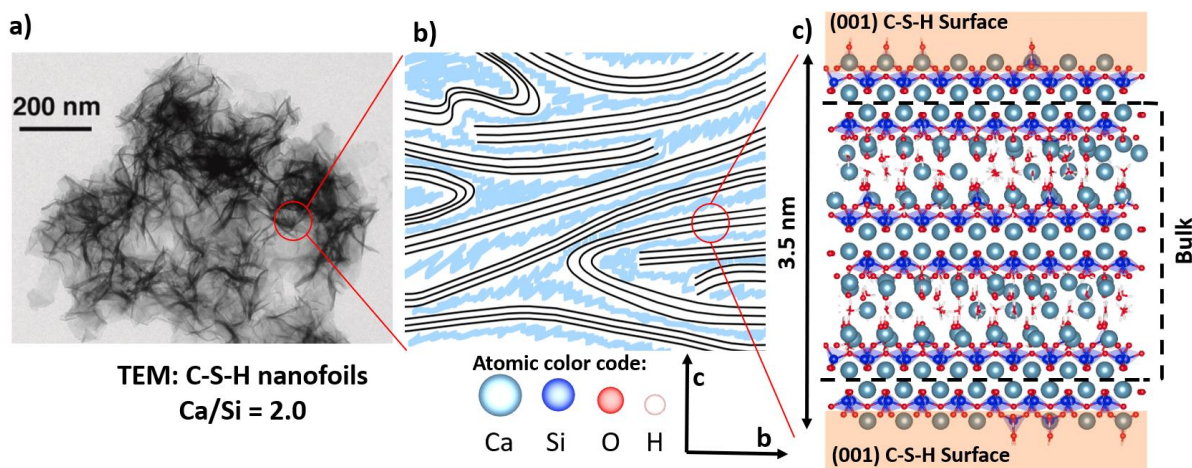
Figure 5-1. C-S-H nanofoils: a) TEM image of synthetic C-S-H with Ca/Si = 2.0, adapted with permission from ref [8] b) schematic representation of the C-S-H nanorporous network (black lines represent the individual calcium-silicate sheets and blue dots represent water), and c): computational model of 3 layers, 2 interlayers thick Ca/Si = 1.7 C-S-H nanofoil with the dominant (001) basal surfaces.

5.2   Methods

Sections of C-S-H nanofoils were modeled as periodic structures in the a and b axis direction and with water molecules on both sides of the basal (001) surface in c axis direction (see SI section S1). The (001) surface is parallel to the calcium-silicate sheet [32]. The C-S-H sections were generated with the brick model from Kunhi Mohamed et al. [31] The model allows a systematic introduction of defects into the 14Å tobermorite structure from Bonaccorsi et al. [24], to give C-S-H bulk structures with representative Ca/Si ratios, consistent with experimental data [3]. The model is gaining acceptance [3, 36-39] and can be used to construct C-S-H surfaces, which can then be used for molecular simulations of adsorption processes [40]. One main advantage of the brick model is the alphanumeric code (notation), which means the structure is exactly described [3]. The details on model construction can be found in the supporting information (S1).

The in-house code for generating structures according to the brick model positions the atoms in a predetermined way. This can result in initial atomic positions which can be far from the minimum of the potential energy surface. Therefore, a suitable equilibration protocol was used. First a quasi-minimization step was carried out, followed by an isothermal-isobaric (NPT) run to relax the simulation box and achieve a bulk water density of approximately 1 g/cm³. Afterwards the system was heated to 700 K in the canonical (NVT) ensemble to ensure enough

energy to reach a more stable minimum before the production run. The final production run was carried out in the NPT ensemble at 300K and 1 bar with a timestep of 0.28 fs for at least 20 ns. All simulations were carried out with LAMMPS[41] and a modified version of the CemFF2 force field [24, 42]. CemFF2 (and Erica FF2) use the adiabatic core-shell model [43] for the polarizability of silicate oxygens which is needed for the right prediction of structural properties of calcium silicate hydrates [42,44]. The force field uses harmonic angles and formal charges of the silicates, therefore it does not overpredict the electrostatic forces. An overprediction of the electrostatic forces would result in higher adsorption of cations on the negatively charged silicates,[45] as can be the case for the popular ClayFF [46] and CSH-FF [47] force fields. For further reading on interatomic potentials and the advantages of polarizable force fields for silica and related systems the reader is referred to the excellent review paper of Müser et al. [48] The calcium-water interaction was adopted from Mamatkulov et al. [49], which has proved reliable in adsorption studies on charged amorphous silicate surfaces [45]. A detailed description of the simulation protocols and force field parameters, as well as structure files are provided in the SI (S2 and S3 sections).

The experimental results which were used in conjunction with the brick model are: i) X-ray fluorescence (XRF) and inductive coupled plasma spectrometry (ICP-OES) for the measurement of the Ca/Si ratio [9], ii) ^{29}Si NMR for the quantitative analysis of different silicate species (Q-sites) [88, 25, 26], which are usually expressed as the MCL and iii) IR and Raman spectroscopy for the relative concentration of silanol (Si-OH/Si) and hydroxide groups (Ca-OH/Ca) [3]. All of these experimental methods measure overall properties, not just the bulk, but, including the surface. The origin of experimental data is elaborated on in SI section 1.1.

Since C-S-H exists only at high pH, a 90% deprotonation of surface silanol groups was assumed for the calculation of characteristics of the structures (Ca/Si ratio, mean chain length, relative concentration of silanol and hydroxide groups). This deprotonation level agrees with the value for C-S-H in calcium solution at pH 13 as predicted by grand canonical Monte Carlo simulations [50]. The experimentally observed characteristics for the C-S-H nanofoil models were taken from Duque-Redondo et al. (table 2) [3].

5.3   Results

Using the brick model from Kunhi Mohamed et al. [21] a basal C-S-H (001) surface can be constructed as follows (figure 2). First, the size of the system needs to be decided, for example a 4x4x2 system

would mean that a structure which measures 4 C-S-H bricks (defective building blocks of tobermorite 14Å unit cells) in the a-axis direction, 4 in the b-axis direction and 2 in the c-axis direction is generated, creating a structure which is 2 interlayers thick. Second, defects need to be selected which will be introduced into the C-S-H bricks. These defects need to be chosen with care so that the overall bulk properties mimic the experimentally measured properties (Ca/Si ratio, mean chain length, relative concentration of silanol and hydroxyl groups). The defects which can be used are described in ref [21]. Third, Ca-Si chains are added to the top and bottom of the bulk structure in order to generate the C-S-H nanofoil with the (001) surface. For a detailed description we refer the reader to the S1 section of the supplementary information.
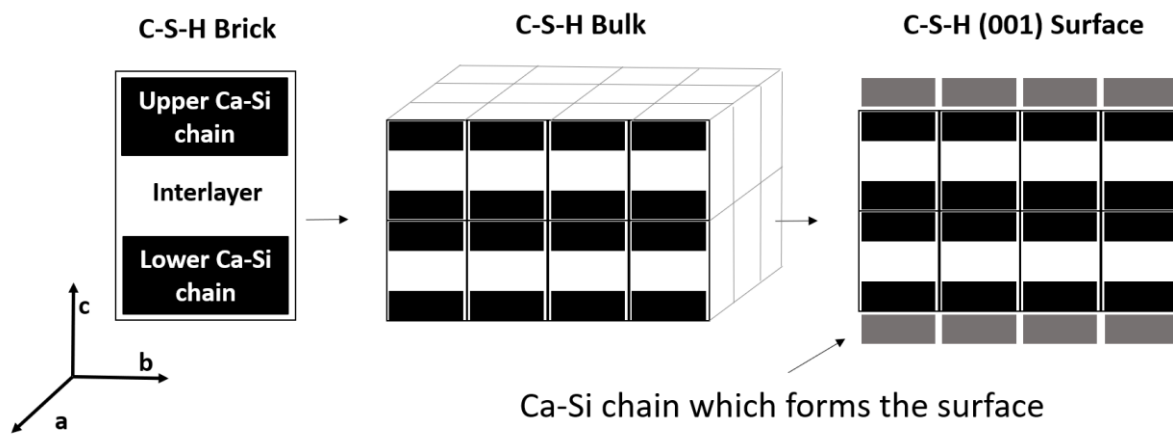
Figure 5-2. Schematic representation on how to construct the C-S-H (001) surface with the building brick description [21].

5.3.1 Thickness and surface area

In the c-direction, the C-S-H bulk structure is flanked by two (001) surfaces (figure 2). The bulk structure has a Ca/Si of 1.7. The examined structures differ from each other by the number of calcium-silicate layers (table 1).

The C-S-H structure with 3 layers, 2 interlayers (figure 1), measures 3.5 nm from the Q^{2b} bridging silicate on one surface to the Q^{2b} silicate on the other surface. For comparison, the structure with 4 layers, 3 interlayers measures 4.9 nm in thickness. The experimentally measured thickness for C-S-H with Ca/Si = 1.0 is 3.5 nm [14] and calculated 4 nm [10] for Ca/Si = 2.0. Adsorbed ions were not considered in the present model.

To verify the choice of thickness of the computational model, the surface area as a function of number of layers was calculated. Since the exact atomic composition of a computational atomistic system is known it is possible to calculate the mass of the system and therefore its specific surface area as $SSA = area / mass$. In table 1, the approximate specific (001) surface area for the (001) surface model systems as a function of the number of layers is reported, whereby one (1) layer corresponds to a C-S-H nanofoil with a single layer and no interlayers. The calculated specific surface area is only for the (001) surfaces and neglects other surfaces, such as the lateral (100) surfaces, and is therefore slightly underestimated.

Table 5-1. Calculated specific surface area and thickness as a function of the number of interlayers. The thickness is measured between surface Q^{2b} silicates, and it does not include adsorbed ions.

Number of layers (Number of interlayers)	Approximated specific (001) surface area [m²/g]	Approximated thickness of the C-S-H nanofoil [nm]
1 (0)	870	0.8 nm
2 (1)	360	2.2 nm
3 (2)	220	3.5 nm
4 (3)	160	4.9 nm
5 (4)	130	6.3 nm
Exp	200-300 [16, 17, 19]	3.5-4.0 nm [10, 14]

As seen from table 1, the 3 layers, 2 interlayers C-S-H model results in SSA of approximately 220 m²/g, which is consistent with experimental observations. It can be concluded that the C-S-H nanofoils are indeed about 100-200 nm long [8, 10-12], and only 3 layers, 2 interlayers thick, which results in a thickness of 3.5 nm.

5.3.2 Surface termination

Due to the narrow thickness of C-S-H nanofoils (3 layers, 2 interlayers), the surface associated calcium-silicate chains represent one third (1/3) of all calcium-silicate chains. Therefore, it is expected that the surface termination will play a vital role in overall characteristics of the structures (Ca/Si ratio, mean chain length, relative concentration of silanol and hydroxide groups). Four different (001) surface terminations were considered (figure 3):

- Si-Surface 1: Only Q^1-Q^1 dimers exist. All bridging sites are unoccupied. Each Q^1 has one silanol group, resulting in a surface silanol density (SSD) of 4.8 OH/nm^2

- Si-Surface 2: Dimers are linked with bridging silicates Q^{2b}. Silanol groups are only found on Q^{2b} silicates (two silanol groups per Q^{2b}). SSD = 4.8 OH/nm^2

- Ca-Surface: Dimers are linked with bridging calcium ions – Ca_B. No silanol groups on the surface. SSD = 0 OH/nm^2

- Mixed-Surface: Dimers are linked with either Q^{2b} or Ca_B. Silanol groups can be found only on Q^{2b} silicates (SSD < 4.8 OH/nm^2), as for the interlayers.
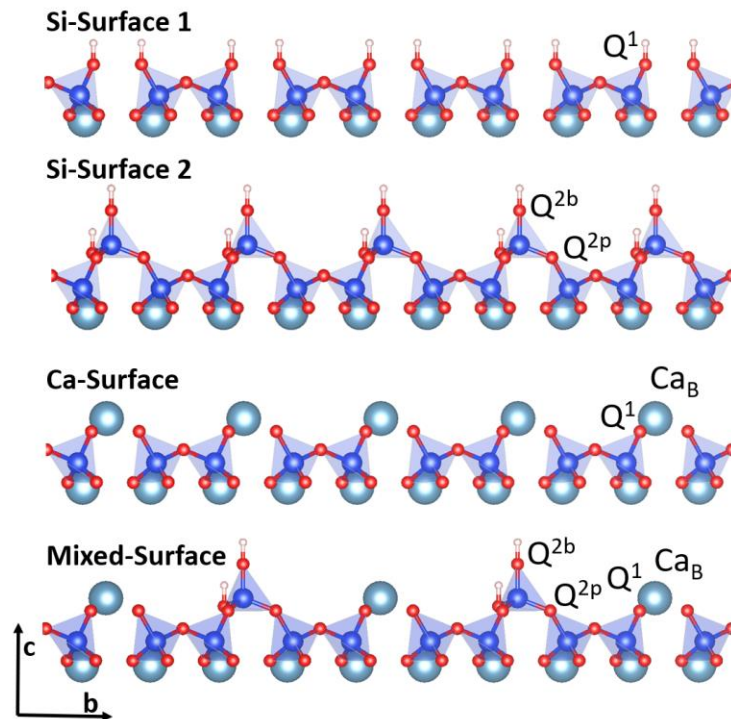
Figure 5-3. Investigated surface terminations. Color legend same as in figure 1.

As can be observed in figure 3 the considered surface terminations result in very different local Ca/Si ratios and MCL. The Si-Surface 2 has the lowest Ca/Si ratio (0.66) and longest MCL (∞), while the Ca-Surface has the highest Ca/Si (1.5) and lowest MCL (2). It is expected that a large difference in observed structural characteristics of the surface and the bulk would greatly influence the overall characteristics of the C-S-H nanofoil.

First considering the most widely assumed Si-Surface 2 [32, 35, 36, 51]. As seen in figure 4 and figure 5, to reach an overall (entire nanofoil) Ca/Si of 1.7 the Ca/Si of the bulk C-S-H structure would need to be 2.5. This is due to the low Ca/Si ratio of the surface (Ca/Si$_{surf}$ = 0.66). The

surface silicate dimers are always linked with Q^{2b} silicates ($MCL_{surf} = \infty$), therefore the theoretical MCL of the bulk would need to be 1.76. MCL of 2 represents silicate chains with all Q^{2b} silicates absent. For MCL lower than 2, the structure would need to have missing Q^1 silicates in the Q^1-Q^1 dimer pairs. If one Q^1 of the dimer is absent, the remaining silicate species is not connected to any other silicate, and it would appear as Q^0 species in the ^{29}Si NMR spectra. Experimental ^{29}Si NMR of phase pure synthetic C-S-H do not show any Q^0 peaks [8, 25, 26]. Thus, it is reasonable to assume that such a surface termination of the C-S-H nanofoil with Ca/Si of 1.7 is not possible.
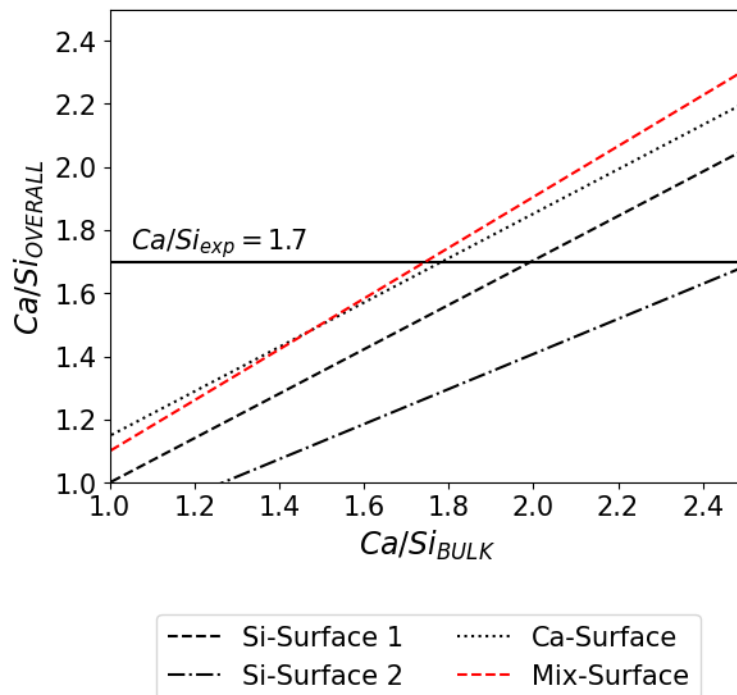
Figure 5-4. Correlation between the overall Ca/Si ratio on the Ca/Si of the bulk structure for the 3 layers, 2 interlayers C-S-H structures with given (001) surfaces terminations.

The Si-Surface 1 and Ca-Surface have the same structure of the silicate chains. Due to the absence of Q^{2b} silicates, the corresponding surface MCL in then 2.0. Therefore, a bulk structure with a high MCL is needed ($MCL_{bulk} = 3.74$). Due to the calcium in the bridging site (Ca_B), the surface Ca/Si of the Ca-Surface equals 1.5, while for the Si-Surface 1 equals 1.0. The MCL decreases with an increase in the Ca/Si ratio [3, 27]. It is contradictory to have different Ca/Si of the bulk (2.0 for Si-Surface 1 and 1.79 for Ca-Surface), while maintaining the same MCL. The lower Ca/Si difference between the surface and bulk would make the Ca-Surface termination more likely than the Si-Surface 1. However, Ca_B fulfills the charge neutrality of the

bridging site, as well as the surface in general, which is contrary to the experimental observations which suggest high surface charge densities [16, 17, 50, 52]. Finally, due to the lack of surface silanol groups the Si-OH/Si ratio of the bulk would be required to be 13%. Assuming again that silanol groups are preferentially found on Q^{2b} silicates, this would result in 41% of non-sharing bulk Q^{2b} oxygens to be protonated. Kunhi Mohamed et al. [21] showed that silanol groups become energetically less favorable as the Ca/Si ratio increases, which is also supported by the falling Si-OH/Si ratio [3].

Assuming the C-S-H nanofoil grows in b-axis direction, in the direction of silicate chains. Therefore, all silicate chains grow from the same solution. There is no obvious reason why the silicate chains on the surface should be different from the ones in the bulk, in terms of MCL. In order to minimize the discrepancy of the surface and bulk the Mixed-Surface was constructed with a MCL_{surf} of 3.0. Simultaneously a bulk MCL with 3.0 is achieved. To obtain an overall Ca/Si of 1.7, a bulk Ca/Si of 1.91 is needed. However, due to the required bulk Si-OH/Si of 11% (overall Si-OH/Si of 9%) such a high Ca/Si ratio of the bulk is unlikely [21]. Therefore, a bulk with Ca/Si of 1.72 was chosen, which results in an overall Ca/Si of 1.48. The Ca/Si ratio can be increased with calcium adsorption onto the surface. In dropwise precipitation of pure phase high Ca/Si ratio C-S-H a discrepancy between thermodynamically calculated and measured calcium concentrations in solution is observed [9]. The difference increases with the increase in Ca/Si ratio. This finding suggests that the amount of adsorption increases with increasing Ca/Si. To achieve the desired Ca/Si of 1.7 four Ca^{2+} ions need to be adsorbed per surface Q^{2b} site.

While there is a wide variety of possible surface terminations, it is evident that the MCL is the first characteristic to be considered when defining a C-S-H nanofoil model. The differences between the overall and bulk characteristics decrease with increasing thickness (number of layers). However, the MCL remains dominant for the construction of the C-S-H nanofoil model (SI section 1.3). Since C-S-H can be considered as a defective tobermorite structure, the surface termination of a mixed type (Ca_B and Q^{2b}) is a logical choice. Finally, the experimental evidence suggests a high calcium affinity at the surface, with which the right Ca/Si can be achieved and is discussed in the next sections [9].
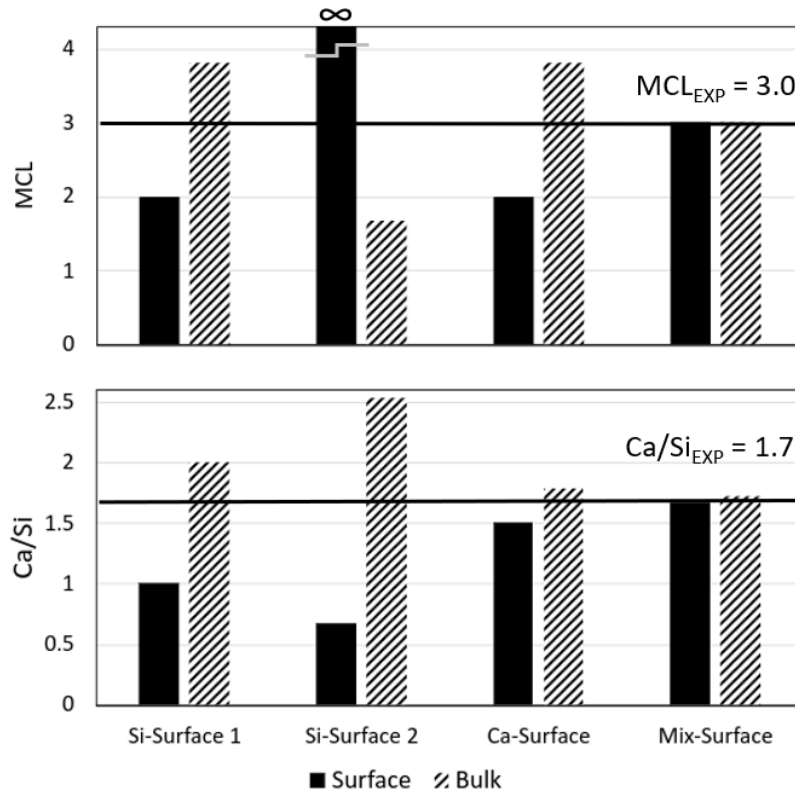
Figure 5-5. MCL and Ca/Si of the surface and bulk for C-S-H nanofoils with Ca/Si = 1.7 and selected surface terminations. The horizontal line represents the targeted experimental values.

5.3.3 Surface silanol density

Minerals immersed in an aqueous solution undergo a pH-dependent protonation of surface oxygens and deprotonation of chemisorbed water molecules, therefore developing a surface charge [53]. In calcium silicate hydrate silanol groups can only be found on non-sharing oxygens of Q^{2b} silicates. This is supported by the declining amount of silanol groups with the decrease in MCL [3]. Since the MCL represents the ratio between Q^{2b} and Q^1 silicates (SI 1) it can be used to express the surface silanol density (SSD):

$$SSD = 4.8 \frac{MCL - 2}{1 + MCL} \left[\frac{OH}{nm^2} \right]$$

(1)

It is evident that lower MCL values (higher Ca/Si) correspond to lower surface charge density. From equation (1), one can calculate the SSD for the Si-Surface 2 (MCL = ∞) to be 4.8 OH/nm², since $\lim_{MCL \to \infty} 4.8 (MCL - 2)/(1 + MCL) = 4.8$. This is the reported value for the Si-

Surface 2 termination in literature [50]. At the opposite limit of MCL = 2 (Ca-Surface), the calculated SSD equals 0 OH/nm^2, since no Q^{2b} silicates are present on the surface. The studied surface termination (Mixed-Surface) with MCL = 3 corresponds to SSD of 1.2 OH/nm^2.

5.3.4 Calcium adsorption

High SSDs result in high (negative) surface charges, which should be balanced by cation adsorption. Calcium ions have a tight hydration shell, which does not allow for water molecules to shift within the hydration shell, therefore favoring outer sphere adsorption [45, 54, 55]. The MD simulations carried-out (see SI 5) on the 90% deprotonated Si-Surface 2 reveal that on an average around 14% of the Ca^{2+} become inner sphere adsorbed. The large hydration radius and the repulsive electrostatic forces likely hinder the adsorption of Ca^{2+}. However, at pH above 13.3 the dominant species in solution is the Ca(OH)$^+$ complex and not Ca^{2+}[56, 57]. It is expected that hydroxide ions will act as an adsorption bridge for Ca^{2+}, as observed on gibbsite [58] and suggested by montmorillonite and kaolinite [59], as well as illite [60] clays in aqueous calcium hydroxide solutions. The amount of adsorbed Ca^{2+} and OH$^-$ suggests an extensive coverage on the basal surfaces of those clays [59, 60]. The faster uptake of ions by kaolinite in comparison to montmorillonite could be explained by the aluminate terminated basal surface of kaolinite which has a high hydroxyl surface density, while the montmorillonite basal surface is a flat silicate surfaces without out-of-plane oxygens.

The zeta potential is related to the charge state of the surface and gives clues regarding the physical and chemical properties of interfacial systems [53]. Zeta potential values of C-S-H in high pH and calcium rich solutions are consistently highly positive [16, 17, 50, 61], suggesting an overcompensation of the negative surface charge by strongly adsorbed counterions, which are expected to be relatively immobile [53]. Experimental zeta potentials on C-S-H with Ca/Si = 1.4 are negative when titrated with CaCl$_2$ and positive when titrated with Ca(OH)$_2$ [61], indicating the role of hydroxide ions in the adsorption process. Further, in the synthesis of phase pure C-S-H a correlation between pH and Ca/Si is observed. To achieve higher Ca/Si higher pHs are needed [9, 57]. This again suggests an essential role of hydroxide ions in the precipitation of C-S-H.

The Mixed-Surface with additional calcium on the surface requires hydroxide ions to mediate the absorption of all the calcium in proximity of the surface. While it could be thought that Ca^{2+} and Ca(OH)$^+$ would adsorb onto the deprotonated silanol groups of the Q^{2b} silicates, this

adsorption behavior is rarely observed (SI section 6). Roughly 30% of the solution Ca^{2+} is inner sphere adsorbed, exclusively on top of a dimer (Q^1-Q^1 or Q^{2p}-Q^{2p}). This adsorption site was previously reported by Kalinichev et al. [62] While Ca^{2+} coordinates to at least two oxygens of the silicate dimer and sometimes simultaneously to the deprotonated silanol groups of the opposite silicate chain Q^{2b}, a hydroxide is acting as an adsorption bridge to the main layer calcium. The MD results suggest the formation of a calcium-hydroxide network on top of the (001) surface, which starts from Ca_B and inner sphere adsorbed calcium on top of the dimers (Figure 6, and SI 6)
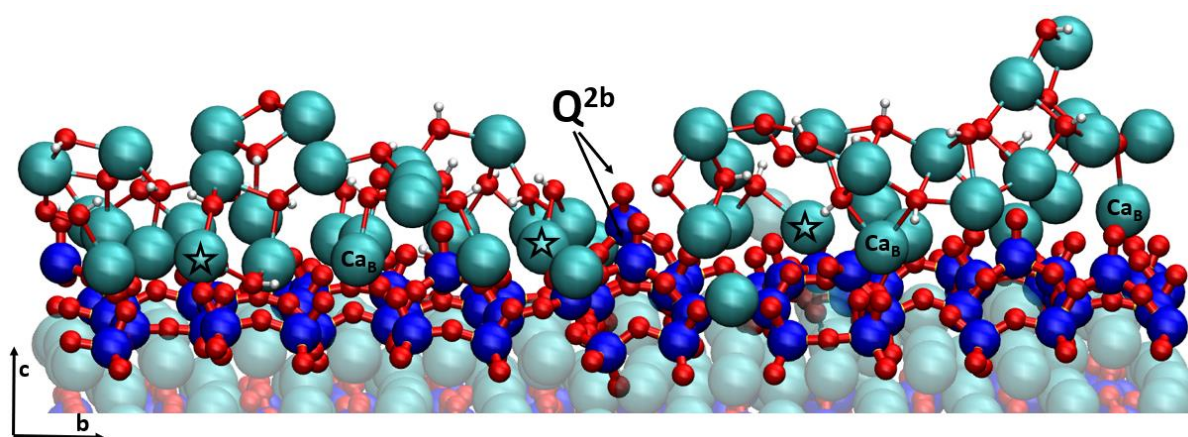
Figure 5-6. Calcium-hydroxyl network on the Mixed-Surface. Arrows point to deprotonated Q^{2b} silicates, Ca_B marks calcium in the bridging site, while stars mark inner sphere adsorbed calcium, which are the starting points for the Ca-OH network. For clarity only selected calcium atoms are marked. Ca-OH connectivity is shown with 'bonds'. Water molecules are not shown for clarity. Color code: Ca-cyan, Si-blue, O-Red, H-White.

5.3.5 Surface charge

Labbez et al. [50] carried out a combined experimental and theoretical approach in order to investigate the charging and electrokinetic behavior of C-S-H. While the model was very simplistic it successfully predicted the experimentally obtained zeta potential. In a later study Churakov et al. [63] investigated the intrinsic acidity of surface sites in C-S-H with the use of density functional theory ab initio molecular dynamics, further confirming the results of Labbez et al.

The experiments were carried out on C-S-H with Ca/Si = 0.66, for which an Si-Surface 2 can be assumed (SSD = 4.8 OH/nm^2). Labbez et al. used the model to predict the ionization fraction, α, and surface charge density, σ, for surface silanol densities 2.8 and 0.8 in solution with 2 mM CaX_2 (where X is a

monovalent anion) at varying pH. The ionization fraction gives the percentage of deprotonated silanol groups and was used for our prediction of the surface charge density. Considering our newly proposed definition of SSD, one can back calculate the MCL of the assumed structures and predict the corresponding Ca/Si ratio of the studied C-S-H. The 2.8 and 0.8 SSDs correspond to C-S-H with Ca/Si ratios of 1.1 and 2.1 which are the lower and upper limits of a realistic C-S-H structure, therefore offering a valuable case to test our new atomistic model.
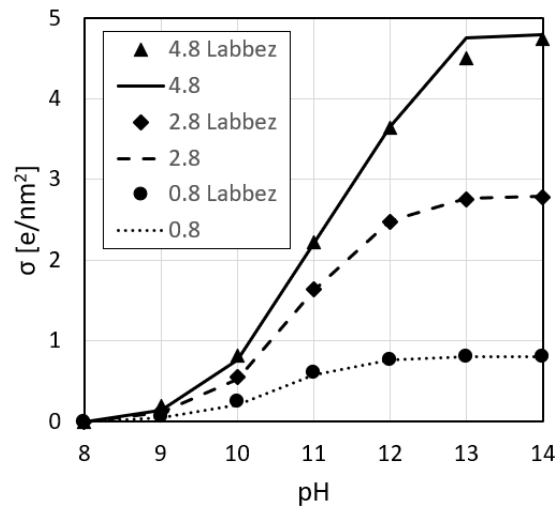
Figure 5-7. Surface charge density (σ) vs pH for different surface silanol densities (4.8, 2.8 and 0.8 OH/nm^2) for our model (lines) and Grand Canonical Monte Carlo simulations from Labbez et al. [50].

The surface charge density (σ) calculation (figure 7) follows the assumption that for each deprotonated silanol group one calcium is adsorbed, effectively increasing the local charge by +1e per adsorbed calcium. At a 100% deprotonation (pH 14) [50] this results in a +2 e charge per bridging silicate, resulting in a surface charge density equal to the surface silanol density. As can be seen from figure 7, this is in very good agreement with the predicted surface charge density of Labbez et al. [50] As explained previously, it is unlikely to adsorb so much Ca^{2+} onto the surface, without co-adsorption of hydroxide groups. However, the same surface charge can be achieved with the adsorption of $n \cdot Ca^{2+}$ and co-adsorption of $2(n-2) \cdot OH^-$ per deprotonated silanol group, where n is an integer. With this the surface charge densities from Labbez et al. can be achieved, while allowing for an additional amount of calcium at the surface, as suggested by experimental observations [9]. Simultaneously, the calcium-hydroxide network on the surface increases the Ca-OH/Ca ratio of the C-S-H nanofoil. With this an

excellent agreement of the proposed C-S-H nanofoil model and experimentally determined C-S-H characteristics is achieved (table 2).

Table 5-2. Comparison of C-S-H characteristics of the C-S-H nanofoil model (bulk, surface and overall) with the experimental ones. **90% deprotonation of surface silanol groups assumed.

Property	C-S-H bulk	C-S-H Surface	C-S-H nanofoil	Experimental [3]
Ca/Si	1.72	1.66	1.7	1.7
MCL	3.0	3.0	3.0	3.0
Si-OH/Si	11%	2.1%**	9%	9%
Ca-OH/Ca	37%	44%	39%	45%

5.4   Discussion

The key assumptions of the C-S-H nanofoil model are as follows: 1) the nanofoils are 3 layers, 2 interlayers thick, 2) the MCL of all the silicate chains in C-S-H is the same, and 3) the bulk Ca/Si ratio is similar to the overall nanofoil Ca/Si ratio, without considering the subsequent Ca^{2+} and OH^- adsorption on the surface as discussed below. With these 3 assumptions a C-S-H nanofoil model with the (001) basal surface for Ca/Si of 1.7 was constructed and which is in excellent agreement with experimentally measured C-S-H properties (table 2). With the same assumptions it is possible to construct C-S-H nanofoils with different Ca/Si ratios (see SI section 1).

With this model the adsorbed Ca^{2+} at the (001) surface (Ca^{2+}/nm^2) can then be modelled. As seen in figure 8 with the increase in the Ca/Si ratio an increase in Ca^{2+}/nm^2 is expected. This increased adsorption of Ca^{2+} agrees with the experimental observation of calcium concentrations in supernatant of phase pure synthetic C-S-H as predicted by thermodynamic modeling and inductive coupled plasma (ICP) measurements [9]. Thermodynamic modeling consistently predicts a higher amount of calcium in supernatant than measured by ICP (3.8 mmol/l versus 0.39 mmol/l at Ca/Si = 1.7) [9], the Ca^{2+} adsorbed on the surface can explain this deficit.

The newly proposed surface model can explain some previously unclear observations about zeta potentials. Viallis-Terrisse et al. [17], Labbez et al. [50] and Yoshida et al. [16] reported negative experimental values of zeta potential for C-S-H with Ca/Si of 0.66 and 1.34 in solutions with [Ca^{2+}] < 2 mM. As suggested by our model, the surface charge for Ca/Si < 1.4 is expected to be negative (charge in figure 8). A negative surface charge corresponds to negative zeta potentials, as explained below.

When initial suspensions were titrated with Ca(OH)$_2$ an increase in the zeta potential was observed with sign reversal at [Ca^{2+}] ≈ 2 mM, suggesting further adsorption of Ca^{2+} and OH$^-$ at the surface.
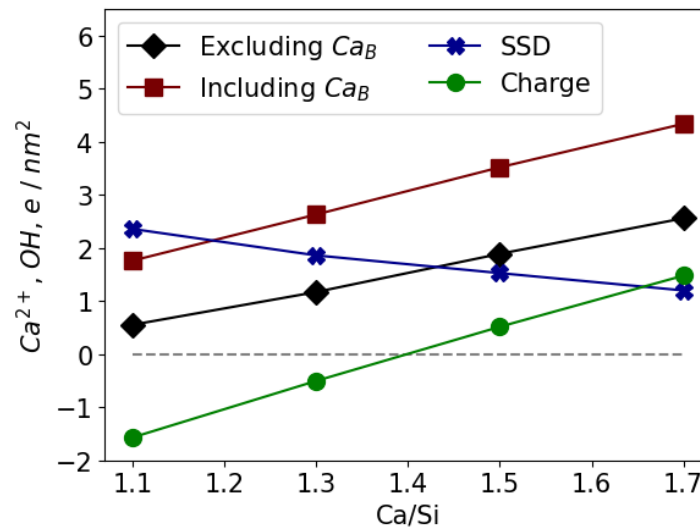
Figure 5-8. Surface silanol density (SSD in OH/nm^2), Ca^{2+} adsorption (Ca^{2+}/nm^2) and surface charge density (e/nm^2) at the (001) surface of the 3 layer, 2 interlayer thick C-S-H nanofoil as predicted by our model for different Ca/Si ratios. Including Ca$_B$ (calcium in the bridging site of the silicate chains) accounts for all calcium at the surface. Excluding Ca$_B$ accounts only for Ca^{2+} which is predicted to form the Ca^{2+}-OH$^-$ network, and contributing to the surface charge. Ca$_B$ fulfills the charge neutrality in its adsorption site and therefore does not contribute to the surface charge. Details on the model structures are listed in SI section 1.

Labbez et al. [50] increased the pH of the solution by addition of NaOH whereby a decrease in the zeta potential was observed. This observation could be explained by OH$^-$ adsorption or replacement of Ca^{2+} by Na$^+$ at the surface [45, 60]. Both mechanisms would result in lower surfaces charges and therefore in lower zeta potentials.

Haas and Nonat reported positive zeta potentials for samples with Ca/Si > 0.9 in solutions with [Ca^{2+}] > 2 mM This could be explained by an excess of positive charge at the surface due to Ca^{2+} and OH$^-$ adsorption as found for this model [65].

The relationship between surface charge densities, Ca^{2+} and OH$^-$ adsorption and zeta potentials can be explained as follows. The proposed co-adsorption of Ca^{2+} and OH$^-$ (see section Surface charge) increases the surface charge by +1 e per deprotonated surface silanol group. The SSD (OH/nm^2) along with the predicted Ca^{2+}/nm^2, is shown in figure 8. In figure 8 the measure

including Ca$_B$ represents the total amount of calcium at the C-S-H (001) basal surface which includes the calcium in the bridging site (Ca$_B$) as well as Ca^{2+} which is part of the Ca^{2+}-OH$^-$ network. Excluding Ca$_B$ accounts only for Ca^{2+} which forms the adsorbed network and effectively contributes to the charged state of the nanofoil. Experimental observations show that a pH above 12.5 is needed for C-S-H to have a nanofoil morphology [57]. At such pHs it is expected that more than 90% of the surface silanol groups will be deprotonated (see Labbez et al. [50] and table S11). From the predicted amount of adsorbed Ca^{2+} (and OH$^-$) and the assumption of a 90% deprotonated (001) surface one can calculate the expected surface charge at a given Ca/Si ratio. As seen in figure 8 our C-S-H nanofoil model predicts negative surface charges below Ca/Si = 1.4 and positive surface charges for higher Ca/Si ratios.
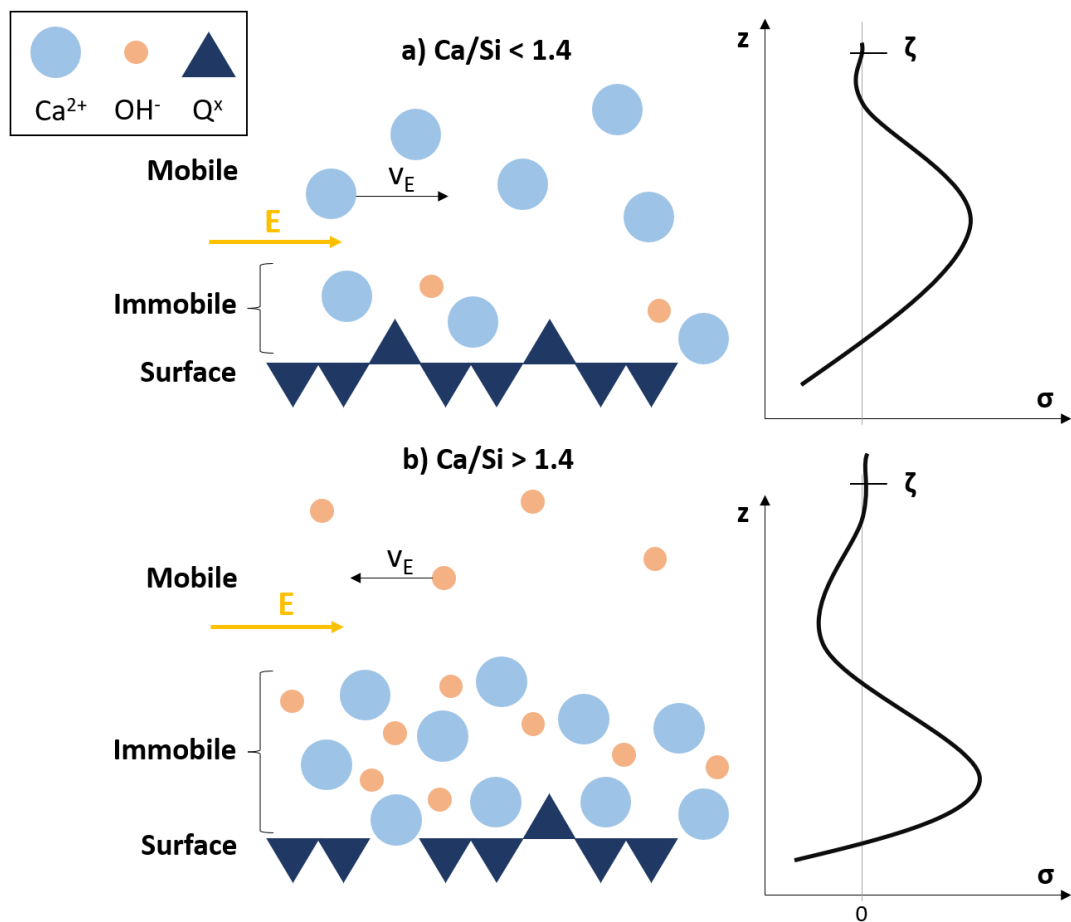
Figure 5-9. Schematic representation of the (001) C-S-H surface a) For nanofoils with Ca/Si < 1.4, where a negative charge density (σ) is expected and b) for nanofoils with Ca/Si > 1.4 where a positive surface charge is expected. The zeta potential (ζ) is measured in the charge neutral region above the surface (z-axis direction) where charge neutrality and constant bulk mobilities are achieved. Q^x stands for silicate tetrahedra.

As explained by Předota et al. [53, 64] the potential-driven velocities next to charged surfaces can be directly measured. Afterwards they can be divided by the applied field strength to provide electrophoretic or electro-osmotic mobilities which can be converted to zeta potentials by various theoretical relations. Figure 9 shows the schematic of a C-S-H (001) surface of a nanofoil with a Ca/Si ratio below and above 1.4 and will be used to explain the expected zeta potential values.
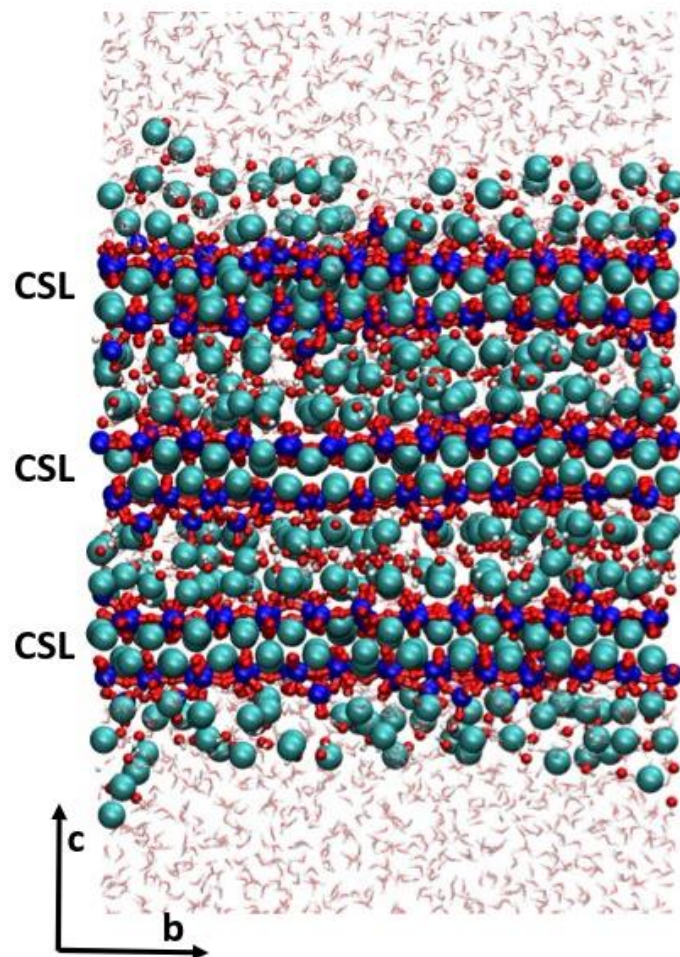
Figure 5-10. Snapshot of the full Ca/Si = 1.7 C-S-H nanofoil model with the Mixed-Surface termination and calcium-hydroxide adsorption, as described in table 2. CSL – calcium-silicate layers. Color code: Ca-cyan, Si-blue, O-Red, H-White.

As explained above, the charge density (σ) of the surface is negative due to deprotonation of silanol groups on Q^{2b} silicates. A certain number of ions will be adsorbed on the surface (inner and outer sphere adsorption). These ions are expected to be rather immobile [53]. As seen in figure 8, the quantity of adsorbed Ca^{2+} (and OH^-) for Ca/Si < 1.4 is expected to be less than needed to compensate for the negative surface charge. Therefore, the charge will be compensated by a region dominated by

mobile cations above the surface (also referred to as the diffuse layer). The mobile ions of the diffuse layer determine the sign and amplitude of electrophoretic and electro-osmotic mobilities. In the case of mobile cations, the zeta potential is expected to be negative [53, 64]. For nanofoils with Ca/Si > 1.4 the surface is expected to have a high degree of Ca^{2+} (and OH^-) adsorbed, resulting in positive charges in the immobile region. Therefore, the mobile region is expected to be anion dominated, which would result in positive zeta potentials.

Finally, after addressing the surface charge density of the nanofoil, some structural features of C-S-H can be addressed. Some experimental observations show a slow a decrease in the Ca/Si ratio of C-S-H over time [67]. By comparing our C-S-H nanofoil model with experimental data on zeta potential measurements we conclude that the amount of Ca^{2+}-OH^- adsorption depends on the solution condition (pH and $[Ca^{2+}]$). Changes in pore solution (calcium concentration) over time most likely affect the adsorption and desorption of Ca^{2+} and OH^- and consequently cause a decrease in the Ca/Si ratio. However, the surface charge of C-S-H should remain unchanged, as theorized for clays in contact with lime solution [60]. The comparison of pair distribution functions of C-S-H samples after 1 day and 1 year of hydration show similar short-range ordering, suggesting that the bulk C-S-H structure remains unchanged [66]. These findings further support the existence of the proposed Ca^{2+}-OH^- adsorption network.

Conclusions

The present article shows an approach which considers multiple measurable characteristics of C-S-H for describing C-S-H nanofoils with the basal (001) surface. The characteristics which are used are: Ca/Si ratio, mean chain length (proportion of silicate species), and the relative concentration of silanol and hydroxide groups. The brick model [21] was used to construct a model structure of the (001) C-S-H nanofoil with Ca/Si of 1.7 which best agrees with the collected experimental characteristics by Duque-Redondo et al. [3] (table 2 and SI section 1.1) and is shown in figure 10. There are four key findings:

- The comparison of the C-S-H nanofoil model with thickness and specific surface area measurements shows that the nanofoils consist of only 3 layers, 2 interlayers in thickness.
- The widely assumed Q^{2b} terminated silicate surface conflicts with the characteristics of C-S-H. A mixed silicate-calcium terminated surface, with roughly 75% calcium termination at Ca/Si = 1.7, is in better agreement with the experimental data.

- The surface silanol density is a function of the mean chain length (and therefore the Ca/Si ratio).

- Calcium and hydroxide co-adsorption are needed to reach high Ca/Si ratios.

The C-S-H nanofoil model predicts the surface silanol density as a function of the MCL (and therefore the Ca/Si ratio) and the amount of adsorbed Ca^{2+} and OH^- at the surface as a function of the Ca/Si ratio (figure 8). From these two parameters the surface charge is calculated. The model predicts negative surface charges for Ca/Si < 1.4 which agrees with experimental zeta potential studies of C-S-H in solutions with $[Ca^{2+}]$ < 2 mM (figure 9). The proposed calcium-hydroxide adsorption network provides an explanation for positively measured zeta potentials of C-S-H in contact with $[Ca^{2+}]$ > 2 mM solution.

With the use of the brick model [21] C-S-H surfaces which match the overall C-S-H characteristics can now be constructed and be used to help interpret experimental data and further investigate the interaction of other ions (e.g. chloride, sulphate, sodium) and molecules (accelerators, superplasticizers). This will lead to a far better understanding of surface phenomena that is of great importance for creating and using ecofriendly cements and concrete.

References

[1]   Scrivener, K. L.; John, V. M.; Gartner, E. M. Eco-Efficient Cements: Potential, Economically Viable Solutions for a Low-CO2, Cement-Based Materials Industry. *Cem Concr Res* **2018**, *114*, 2–26. https://doi.org/https://doi.org/10.1016/j.cemconres.2018.03.015.

[2]   Heinz, O.; Heinz, H. Cement Interfaces: Current Understanding, Challenges, and Opportunities. *Langmuir* **2021**, *37* (21), 6347–6356. https://doi.org/10.1021/acs.langmuir.1c00617.

[3]   Duque-Redondo, E.; Bonnaud, P. A.; Manzano, H. A Comprehensive Review of C-S-H Empirical and Computational Models, Their Applications, and Practical Aspects. *Cem Concr Res* **2022**, *156*, 106784. https://doi.org/10.1016/j.cemconres.2022.106784.

[4]   Ouzia, A.; Scrivener, K. The Needle Model: A New Model for the Main Hydration Peak of Alite. *Cem Concr Res* **2019**, *115*, 339–360. https://doi.org/10.1016/j.cemconres.2018.08.005.

[5]   Wilson, W.; Gonthier, J. N.; Georget, F.; Scrivener, K. L. Insights on Chemical and Physical Chloride Binding in Blended Cement Pastes. *Cem Concr Res* **2022**, *156*, 106747. https://doi.org/10.1016/j.cemconres.2022.106747.

[6]   Bazzoni, A.; Suhua, M.; Wang, Q.; Shen, X.; Cantoni, M.; Scrivener, K. L. The Effect of Magnesium and Zinc Ions on the Hydration Kinetics of C3S. *Journal of the American Ceramic Society* **2014**, *97* (11), 3684–3693. https://doi.org/10.1111/jace.13156.

[7]   Zhu, X.; Richardson, I. G. Morphology-Structural Change of C-A-S-H Gel in Blended Cements. *Cem Concr Res* **2023**, *168*, 107156. https://doi.org/10.1016/j.cemconres.2023.107156.

[8]   Kumar, A.; Walder, B. J.; Kunhi Mohamed, A.; Hofstetter, A.; Srinivasan, B.; Rossini, A. J.; Scrivener, K.; Emsley, L.; Bowen, P. The Atomic-Level Structure of Cementitious Calcium Silicate Hydrate. *The Journal of Physical Chemistry C* **2017**, *121* (32), 17188–17196. https://doi.org/10.1021/acs.jpcc.7b02439.

[9]   Harris, M.; Simpson, G.; Scrivener, K.; Bowen, P. A Method for the Reliable and Reproducible Precipitation of Phase Pure High Ca/Si Ratio (>1.5) Synthetic Calcium Silicate Hydrates (C-S-H). *Cem Concr Res* **2022**, *151* (October 2021), 106623. https://doi.org/10.1016/j.cemconres.2021.106623.

[10]   Andalibi, M. R.; Kumar, A.; Srinivasan, B.; Bowen, P.; Scrivener, K.; Ludwig, C.; Testino, A. On the Mesoscale Mechanism of Synthetic Calcium-Silicate-Hydrate Precipitation: A Population Balance Modeling Approach. *J Mater Chem A Mater* **2018**, *6* (2), 363–373. https://doi.org/10.1039/c7ta08784e.

[11]   Schönlein, M.; Plank, J. A TEM Study on the Very Early Crystallization of C-S-H in the Presence of Polycarboxylate Superplasticizers: Transformation from Initial C-S-H Globules to Nanofoils. *Cem Concr Res* **2018**, *106*, 33–39. https://doi.org/10.1016/j.cemconres.2018.01.017.

[12]   Rodriguez, E. T.; Richardson, I. G.; Black, L.; Boehm-Courjault, E.; Nonat, A.; Skibsted, J. Composition, Silicate Anion Structure and Morphology of Calcium Silicate

Hydrates (C-S-H) Synthesised by Silica-Lime Reaction and by Controlled Hydration of Tricalcium Silicate (C3S). *Advances in Applied Ceramics* **2015**, *114* (7), 362–371. https://doi.org/10.1179/1743676115Y.0000000038.

[13]   Allen, A. J.; Thomas, J. J.; Jennings, H. M. Composition and Density of Nanoscale Calcium-Silicate-Hydrate in Cement. *Nat Mater* **2007**, *6* (4), 311–316. https://doi.org/10.1038/nmat1871.

[14]   Skinner, L. B.; Chae, S. R.; Benmore, C. J.; Wenk, H. R.; Monteiro, P. J. M. Nanostructure of Calcium Silicate Hydrates in Cements. *Phys Rev Lett* **2010**, *104* (19), 1–4. https://doi.org/10.1103/PhysRevLett.104.195502.

[15]   Tennis, P. D.; Jennings, H. M. Model for Two Types of Calcium Silicate Hydrate in the Microstructure of Portland Cement Pastes. *Cem Concr Res* **2000**, *30* (6), 855–863. https://doi.org/10.1016/S0008-8846(00)00257-X.

[16]   Yoshida, S.; Elakneswaran, Y.; Nawa, T. Electrostatic Properties of C–S–H and C-A-S-H for Predicting Calcium and Chloride Adsorption. *Cem Concr Compos* **2021**, *121*, 104109. https://doi.org/10.1016/j.cemconcomp.2021.104109.

[17]   Viallis-Terrisse, H.; Nonat, A.; Petit, J. C. Zeta-Potential Study of Calcium Silicate Hydrates Interacting with Alkaline Cations. *J Colloid Interface Sci* **2001**, *244* (1), 58–65. https://doi.org/10.1006/jcis.2001.7897.

[18]   Jennings, H. M. Model for the Microstructure of Calcium Silicate Hydrate in Cement Paste. *Cem Concr Res* **2000**, *30* (1), 101–116. https://doi.org/10.1016/S0008-8846(99)00209-4.

[19]   Brunauer, S.; Kantro, D. L.; Weise, C. H. The Surface Energy of Tobermorite. *Can J Chem* **1958**, *37* (4). https://doi.org/https://doi.org/10.1139/v59-097.

[20]   Scrivener, K.; Ouzia, A.; Juilland, P.; Kunhi Mohamed, A. Advances in Understanding Cement Hydration Mechanisms. *Cem Concr Res* **2019**, *124*, 105823. https://doi.org/10.1016/j.cemconres.2019.105823.

[21]   Kunhi Mohamed, A.; Parker, S. C.; Bowen, P.; Galmarini, S. An Atomistic Building Block Description of C-S-H - Towards a Realistic C-S-H Model. *Cem Concr Res* **2018**, *107* (March), 221–235. https://doi.org/10.1016/j.cemconres.2018.01.007.

[22]   Cong, X.; James Kirkpatrick, R. 29Si MAS NMR Study of the Structure of Calcium Silicate Hydrate. *Advanced Cement Based Materials* **1996**, *3* (3–4), 144–156. https://doi.org/10.1016/s1065-7355(96)90046-2.

[23]   Maddalena, R.; Li, K.; Chater, P. A.; Michalik, S.; Hamilton, A. Direct Synthesis of a Solid Calcium-Silicate-Hydrate (C-S-H). *Constr Build Mater* **2019**, *223*, 554–565. https://doi.org/10.1016/j.conbuildmat.2019.06.024.

[24]   Bonaccorsi, E.; Merlino, S.; Kampf, A. R. The Crystal Structure of Tobermorite 14 Å (Plombierite), a C-S-H Phase. *Journal of the American Ceramic Society* **2005**, *88* (3), 505–512. https://doi.org/10.1111/j.1551-2916.2005.00116.x.

[25]   Kunhi Mohamed, A.; Moutzouri, P.; Berruyer, P.; Walder, B. J.; Siramanont, J.; Harris, M.; Negroni, M.; Galmarini, S. C.; Parker, S. C.; Scrivener, K. L.; et al. The Atomic-Level Structure of Cementitious Calcium Aluminate Silicate Hydrate. *J Am Chem Soc* **2020**, *142* (25), 11060–11071. https://doi.org/10.1021/jacs.0c02988.

[26]   Morales-Melgares, A.; Casar, Z.; Moutzouri, P.; Venkatesh, A.; Cordova, M.; Kunhi Mohamed, A.; L. Scrivener, K.; Bowen, P.; Emsley, L. Atomic-Level Structure of Zinc-Modified Cementitious Calcium Silicate Hydrate. *J Am Chem Soc* **2022**, *144* (50), 22915–22924. https://doi.org/10.1021/jacs.2c06749.

[27]   Richardson, I. G. Model Structures for C-(A)-S-H(I). *Acta Crystallogr B Struct Sci Cryst Eng Mater* **2014**, *70* (6), 903–923. https://doi.org/10.1107/S2052520614021982.

[28]   Richardson, I. G. Model Structures for C-(A)-S-H(I). *Acta Crystallogr B Struct Sci Cryst Eng Mater* **2014**, *70* (6), 903–923. https://doi.org/10.1107/S2052520614021982.

[29]   Hamid, S. A. The Crystal Structure of the 11Å Natural Tobermorite Ca2.25[Si3O7.5(OH)1.5].1H2O. *Zeitschrift fur Kristallographie* **1981**, *154*, 189–198. https://doi.org/https://doi.org/10.1524/zkri.1981.154.3-4.189.

[30]   Brunet, F.; Bertani, P.; Charpentier, T.; Nonat, A.; Virlet, J. Application of 29Si Homonuclear and 1H-29Si Heteronuclear NMR Correlation to Structural Studies of Calcium Silicate Hydrates. *Journal of Physical Chemistry B* **2004**, *108* (40), 15494–15502. https://doi.org/10.1021/jp031174g.

[31]   Kunhi Mohamed, A.; Weckwerth, S. A.; Mishra, R. K.; Heinz, H.; Flatt, R. J. Molecular Modeling of Chemical Admixtures; Opportunities and Challenges. *Cem Concr Res* **2022**, *156*, 106783. https://doi.org/10.1016/j.cemconres.2022.106783.

[32]   Jamil, T.; Javadi, A.; Heinz, H. Mechanism of Molecular Interaction of Acrylate-Polyethylene Glycol Acrylate Copolymers with Calcium Silicate Hydrate Surfaces. *Green Chemistry* **2020**, *22* (5), 1577–1593. https://doi.org/10.1039/c9gc03287h.

[33]   Hou, D.; Li, T.; Wang, P. Molecular Dynamics Study on the Structure and Dynamics of NaCl Solution Transport in the Nanometer Channel of CASH Gel. *ACS Sustain Chem Eng* **2018**, *6* (7), 9498–9509. https://doi.org/10.1021/acssuschemeng.8b02126.

[34]   Duque-Redondo, E.; Kazuo, Y.; López-Arbeloa, I.; Manzano, H. Cs-137 Immobilization in C-S-H Gel Nanopores. *Physical Chemistry Chemical Physics* **2018**, *20* (14), 9289–9297. https://doi.org/10.1039/c8cp00654g.

[35]   Androniuk, I.; Landesman, C.; Henocq, P.; Kalinichev, A. G. Adsorption of Gluconate and Uranyl on C-S-H Phases: Combination of Wet Chemistry Experiments and Molecular Dynamics Simulations for the Binary Systems. *Physics and Chemistry of the Earth* **2017**, *99*, 194–203. https://doi.org/10.1016/j.pce.2017.05.005.

[36]   Bu, J.; Gonzalez Teresa, R.; Brown, K. G.; Sanchez, F. Adsorption Mechanisms of Cesium at Calcium-Silicate-Hydrate Surfaces Using Molecular Dynamics Simulations. *Journal of Nuclear Materials* **2019**, *515*, 35–51. https://doi.org/10.1016/j.jnucmat.2018.12.007.

[37]   Honorio, T.; Masara, F.; Benboudjema, F. Heat Capacity, Isothermal Compressibility, Isosteric Heat of Adsorption and Thermal Expansion of Water Confined in C-S-H. *Cement* **2021**, *6*, 100015. https://doi.org/10.1016/j.cement.2021.100015.

[38]   Svenum, I. H.; Ringdalen, I. G.; Bleken, F. L.; Friis, J.; Höche, D.; Swang, O. Structure, Hydration, and Chloride Ingress in C-S-H: Insight from DFT Calculations. *Cem Concr Res* **2020**, *129*, 105965. https://doi.org/10.1016/j.cemconres.2019.105965.

[39]   Basquiroto de Souza, F.; Sagoe-Crentsil, K.; Duan, W. Determining the Disordered Nanostructure of Calcium Silicate Hydrate (C-S-H) from Broad X-Ray Diffractograms. *Journal of the American Ceramic Society* **2022**, *105* (2), 1491–1502. https://doi.org/10.1111/jace.18132.

[40]   Abdolhosseini Qomi, M. J.; Brochard, L.; Honorio, T.; Maruyama, I.; Vandamme, M. Advances in Atomistic Modeling and Understanding of Drying Shrinkage in Cementitious Materials. *Cem Concr Res* **2021**, *148*, 106536. https://doi.org/10.1016/j.cemconres.2021.106536.

[41]   Thompson, A. P.; Aktulga, H. M.; Berger, R.; Bolintineanu, D. S.; Brown, W. M.; Crozier, P. S.; in 't Veld, P. J.; Kohlmeyer, A.; Moore, S. G.; Nguyen, T. D.; et al. J. LAMMPS - a Flexible Simulation Tool for Particle-Based Materials Modeling at the Atomic, Meso, and Continuum Scales. *Comput Phys Commun* **2022**, *271*, 108171. https://doi.org/10.1016/j.cpc.2021.108171.

[42]   Valavi, M.; Casar, Z.; Kunhi, A.; Bowen, P.; Galmarini, S. Molecular Dynamic Simulations of Cementitious Systems Using a Newly Developed Force Field Suite ERICA FF. *Cem Concr Res* **2022**, *154*, 106712. https://doi.org/10.1016/j.cemconres.2022.106712.

[43]   Mitchell, P. J.; Fincham, D. Shell Model Simulations by Adiabatic Dynamics. *Journal of Physics: Condensed Matter* **1993**, *5*, 1031–1038. https://doi.org/10.1088/0953-8984/5/8/006.

[44]   Tilocca, A.; Leeuw, N. H. De; Cormack, A. N. Shell-Model Molecular Dynamics Calculations of Modified Silicate Glasses. *Phys Rev B* **2006**, *73*, 104209. https://doi.org/10.1103/PhysRevB.73.104209.

[45]   F. Döpke, M.; Lützenkirchen, J.; A. Moultos, O.; Siboulet, B.; Dufrêche, J.-F.; T. Padding, J.; Hartkamp, R. Preferential Adsorption in Mixed Electrolytes Confined by Charged Amorphous Silica. *The Journal of Physical Chemistry C* **2019**, *123* (27), 16711–16720. https://doi.org/10.1021/acs.jpcc.9b02975.

[46]   Cygan, R. T.; Liang, J. J.; Kalinichev, A. G. Molecular Models of Hydroxide, Oxyhydroxide, and Clay Phases and the Development of a General Force Field. *J Phys Chem B* **2004**, *108*, 1255–1266. https://doi.org/10.1021/jp0363287.

[47]   Shahsavari, R.; Pellenq, R. J. M.; Ulm, F. J. Empirical Force Fields for Complex Hydrated Calcio-Silicate Layered Materials. *Physical Chemistry Chemical Physics* **2011**, *13* (3), 1002–1011. https://doi.org/10.1039/c0cp00516a.

[48]   Müser, M. H.; Sukhomlinov, S. V.; Pastewka, L. Interatomic Potentials: Achievements and Challenges. *Advances in Physics: X.* 2023, 2093129. https://doi.org/10.1080/23746149.2022.2093129.

[49]   Mamatkulov, S.; Fyta, M.; Netz, R. R. Force Fields for Divalent Cations Based on Single-Ion and Ion-Pair Properties. *J Chem Phys* **2013**, *138* (2), 024505. https://doi.org/10.1063/1.4772808.

[50]   Labbez, C.; Jönsson, B.; Pochard, I.; Nonat, A.; Cabane, B. Surface Charge Density and Electrokinetic Potential of Highly Charged Minerals: Experiments and Monte Carlo Simulations on Calcium Silicate Hydrate. *Journal of Physical Chemistry B* **2006**, *110* (18), 9219–9230. https://doi.org/10.1021/jp057096+.

[51]   Sanchez, F.; Zhang, L. Molecular Dynamics Modeling of the Interface between Surface Functionalized Graphitic Structures and Calcium-Silicate-Hydrate: Interaction Energies, Structure, and Dynamics. *J Colloid Interface Sci* **2008**, *323* (2), 349–358. https://doi.org/10.1016/j.jcis.2008.04.023.

[52]   Labbez, C.; Nonat, A.; Pochard, I.; Jönsson, B. Experimental and Theoretical Evidence of Overcharging of Calcium Silicate Hydrate. *J Colloid Interface Sci* **2007**, *309* (2), 303–307. https://doi.org/10.1016/j.jcis.2007.02.048.

[53]   Předota, M.; Machesky, M. L.; Wesolowski, D. J. Molecular Origins of the Zeta Potential. *Langmuir* **2016**, *32* (40), 10189–10198. https://doi.org/10.1021/acs.langmuir.6b02493.

[54]   Janusz, W.; Patkowski, J.; Chibowski, S. Competitive Adsorption of Ca2+ and Zn(II) Ions at Monodispersed SiO2/Electrolyte Solution Interface. *J Colloid Interface Sci* **2003**, *266* (2), 259–268. https://doi.org/10.1016/S0021-9797(03)00469-7.

[55]   Bischoff, M.; Biriukov, D.; Předota, M.; Marchioro, A. Second Harmonic Scattering Reveals Ion-Specific Effects at the SiO2 and TiO2 Nanoparticle/Aqueous Interface. *Journal of Physical Chemistry C* **2021**, *125* (45), 25261–25274. https://doi.org/10.1021/acs.jpcc.1c07191.

[56]   Kulik, D.; Berner, U.; Curti, E. Modelling Chemical Equilibrium Partitioning with the GEMS-PSI Code. *Paul Scherrer Institut, Switzerland* **2004**, *Technical report* (CH-0401), 109–123.

[57]   Shen, X.; Feng, P.; Zhang, Q.; Lu, J.; Liu, X.; Ma, Y.; Jin, P.; Wang, W.; Ran, Q.; Hong, J. Toward the Formation Mechanism of Synthetic Calcium Silicate Hydrate (C-S-H) - PH and Kinetic Considerations. *Cem Concr Res* **2023**, *172*, 107248. https://doi.org/10.1016/j.cemconres.2023.107248.

[58]   Siretanu, I.; Ebeling, D.; Andersson, M. P.; Stipp, S. L. S.; Philipse, A.; Stuart, M. C.; Van Den Ende, D.; Mugele, F. Direct Observation of Ionic Structure at Solid-Liquid Interfaces: A Deep Look into the Stern Layer. *Sci Rep* **2014**, *4*. https://doi.org/10.1038/srep04956.

[59]   Diamond, S.; Kinter, E. B. Adsorption of Calcium Hydroxide by Montmorillonite and Kaolinite. *J Colloid Interface Sci* **1966**, *22*, 240–249.

[60]   Konan, K. L.; Peyratout, C.; Bonnet, J. P.; Smith, A.; Jacquet, A.; Magnoux, P.; Ayrault, P. Surface Properties of Kaolin and Illite Suspensions in Concentrated Calcium

Hydroxide Medium. *J Colloid Interface Sci* **2007**, *307* (1), 101–108. https://doi.org/10.1016/j.jcis.2006.10.085.

[61]   Nägele, E. The Zeta-Potential of Cement. *Cem Concr Res* **1985**, *15* (3), 453–462. https://doi.org/10.1016/0008-8846(85)90118-8.

[62]   Kalinichev, A. G.; Wang, J.; Kirkpatrick, R. J. Molecular Dynamics Modeling of the Structure, Dynamics and Energetics of Mineral–Water Interfaces: Application to Cement Materials. **2007**, *37*, 337–347. https://doi.org/10.1016/j.cemconres.2006.07.004.

[63]   Churakov, S. v.; Labbez, C.; Pegado, L.; Sulpizi, M. Intrinsic Acidity of Surface Sites in Calcium Silicate Hydrates and Its Implication to Their Electrokinetic Properties. *Journal of Physical Chemistry C* **2014**, *118* (22), 11752–11762. https://doi.org/10.1021/jp502514a.

[64]   Biriukov, D.; Fibich, P.; Předota, M. Zeta Potential Determination from Molecular Simulations. *Journal of Physical Chemistry C* **2020**, *124* (5), 3159–3170. https://doi.org/10.1021/acs.jpcc.9b11371.

[65]   Haas, J.; Nonat, A. From C–S–H to C–A–S–H: Experimental Study and Thermodynamic Modelling. *Cem Concr Res* **2015**, *68*, 124–138. https://doi.org/10.1016/j.cemconres.2014.10.020.

[66]   Grangeon, S.; Fernandez-Martinez, A.; Baronnet, A.; Marty, N.; Poulain, A.; Elkaïm, E.; Roosz, C.; Gaboreau, S.; Henocq, P.; Claret, F. Quantitative X-Ray Pair Distribution Function Analysis of Nanocrystalline Calcium Silicate Hydrates: A Contribution to the Understanding of Cement Chemistry. *J Appl Crystallogr* **2017**, *50* (1), 14–21. https://doi.org/10.1107/S1600576716017404.

[67]   Zunino, F.; Scrivener, K. Microstructural Developments of Limestone Calcined Clay Cement (LC3) Pastes after Long-Term (3 Years) Hydration. *Cem Concr Res* **2022**, *153*. https://doi.org/10.1016/j.cemconres.2021.106693.

6 Summary and Outlook

This chapter gives a short summary of the progress made over the past four years in elucidating the atomic-level structure of C-S-H. This is followed by a short summary of each of the main chapters of the thesis. The summaries are short, since each chapter represents a published, submitted, or not yet published paper, and therefore each chapter ended with a proper conclusion. Finally, the future work section addresses the next challenges in further elucidating the atomic-level structure of C-S-H and how this knowledge will be used to help design more sustainable concrete for the built environment.

6.1   How it started and where it ended

For the past 50 years C-S-H has been intensively investigated. However, the major breakthroughs in elucidating the atomic-level structure occurred after 2017. The first breakthrough paper came from Kumar et al. [1], followed by two separate papers by Kunhi Mohamed et al. [2,3]. The significance of these studies over the past ones is in the fact that they successfully combined precise experimental work with atomistic modeling techniques, which enabled these breakthroughs.

The main contributions by Kumar et al. [1] are the precipitation protocol for synthesizing phase pure high Ca/Si ratio (1.5 < Ca/Si < 2.0) C-S-H and the combination of NMR experiments with DFT modeling. The synthesis, which was later standardized and published by Harris et al. [4], enabled the production and study of C-S-H without secondary phases. As explained in chapter 3, the presence of secondary phases (most notably portlandite), often interferes with the interpretation of experimental data. Combining experimental NMR data and DFT calculations showed, based on the comparison of measured and calculated ^{1}H NMR shifts, that dimers of the silicate chains can be linked with Ca^{2+}. This finding is now regarded as a key structural feature which distinguishes C-S-H from other calcium silicate hydrate minerals (the tobermorite family). The key nature of this discovery was highlighted in thermodynamic modelling by Kulik et al. [5] whereby once the Ca in bridging sites was incorporated the thermodynamic fitting of experimental data was significantly improved. Kunhi Mohamed et al. [2] used this methodology of C-S-H production and NMR investigation combined with DFT calculations to inspect the incorporation sites of aluminium in C-A-S-H. They showed that the preferential coordination of aluminium depends on the local Ca/Si and

2H/Si ratios. The second main finding in their study was that the so-called TAH phase (third aluminium hydrate), which was hypothesized to exist as an independent phase inside C-A-S-H is actually a 6-fold coordinated aluminium ($[AlO_2(OH)_4]^{5-}$) which is incorporated into the silicate chain. Finally, none of those findings would have been possible without the prior development of the brick model, which again came from Kunhi Mohamed et al. [3]. The brick model is the first methodology for constructing representative C-S-H atomistic models which can result in structures that mimic the experimentally measured properties (Ca/Si, mean chain length, Ca-OH/Ca, Si-OH/Si, 2H/Si) [6]. The model also allows for reproducibility due to its exact nomenclature.

The main objective of this thesis was to follow in the steps of Kumar et al. and Kunhi Mohamed et al., with the aim of gaining further insights into the atomic-level structure of C-S-H. Which was carried out with success. Firstly, in order to investigate the C-S-H structure and specifically later the interactions at the C-S-H surfaces, a more reliable, accurate force field was needed. As chapter 2 shows, the previous force fields had some limitations, which were addressed and improved. The top-down and bottom-up approaches in force field development were simultaneously combined. While the top-down approach validates the force field against structural (unit cell parameters, bond distances, etc.), energetical (reaction enthalpies) and mechanical properties (elastic constants), the bottom-up approach ensures the force fields' accuracy at the Ab initio level (vibrational density of states). It was shown that the newly developed generalized fully charge force field performs very well indeed.

While Kunhi Mohamed et al. [3] introduced the brick model it is not trivial to use. The brick model has now been rewritten as a Python program (previously C++ with a Python interface) and the generation of bulk C-S-H structures is automated This allows the unskilled programmer but knowledgeable cement researcher to use it and investigate C-S-H atomistic scale structures. The program was then used, in chapter X, for the first ever study of randomized representative C-S-H structures. It was shown that the automatically generated structures (with ca/Si of 1.5 and 1.7) match the experimental measured properties (Ca/Si, 2H/Si, Ca-OH/Ca, Si-OH/Si, mean chain length) with excellent accuracy. Further, the structures were investigated on their structural features and defect energies. It was shown that while the structures differed a lot in their assembly of defects the resulting structural features and defect energies exhibited minimal differences. These similarities clarify the nanocrystalline nature of C-S-H. The close examination of the calculated pair distribution functions and their

comparison with experimentally reported ones, showed that the computational models can be safely used as an aid in the interpretation of complex experimental data. The work is being extended in collaboration with Prof. Hegoi Manzano's group at the University of Basque Country. Whereby another 200 structures with the Ca/Si ratio of 1.3 and 1.9 are being investigated and will further strengthen the interpretation of the structures presented in this chapter.

Minor elements, particularly zinc, are viewed as a promising way to control the reactivity of C$_3$S (pure alite), with the potential to extend it to the control of cement reactivity. Again, the limitation lies in understanding at the atomic-level how zinc is incorporated and why does this pertain to an acceleration. With the precipitation methods from Kumar et al. [1,7] phase pure C-S-H samples (with and without zinc) were produced experimentally in the partner PhD of the SNF project and then investigated and studied [8]. As in the investigation of C-A-S-H [2], the combination of NMR, MD and DFT enabled us (i.e. myself and the SNF project partners) to resolve the zinc incorporation sites. However, while Kunhi Mohamed et al. [2] could make use of ^{27}Al NMR, the ^{67}Zn NMR was too difficult to resolve, therefore only ^{29}Si NMR was used. While the newly emerged –72 ppm peak (Q$^{(1,Zn)}$), which was associated with zinc incorporation was relatively easy to resolve, the –79 ppm peak would have stayed unresolved if it had not been for all the previous work on C-S-H. Due to the current excellent understanding of the structure of calcium-silicate chains in C-S-H it was possible to discover the Q$^{(2p,Zn)}$ site, which albeit has the same chemical shift as the Q^1 silicate could be distinguished by atomistic modelling (Ziga Casar) and quantitative NMR (Anna Melgares Molares).

C-S-H is the primary hydration phase which forms 50-60% by volume of hardened cement paste and binds together other crystalline hydration products and aggregates and controls the transport of ions through the hardened cement paste. All these C-S-H features are closely connected not only to the atomic-level structure of bulk C-S-H, but foremost to the C-S-H nanofoil including its basal (001) surface. With the methodology of the brick model nanofoils were constructed. It was shown that only foils which measure 3 layers, 2 interlayers in thickness reproduce the experimentally measured thickness of < 5 nm [9,10] and specific surface area of $200-300$ m^2/g [11,12]. The previous literature assumes that the C-S-H (001) surface is silicate deprotonated (Q^{2b} silicates). This assumption was challenged, in chapter 5, by investigating different surface terminations, whereby it was shown that a mixed surface termination results in C-S-H nanofoils which best match the experimentally measured properties (Ca/Si, mean

chain length, Si-OH/Si and Ca-OH/Ca). The mixed surface termination assumes that the mean chain length of the surface silicate chains is the same as the bulk silicate chains. Therefore, the mean chain length dictates the number of Q^{2b} silicates on the surface, which also gives rise to the surface silanol density and therefore the specific surface charge. Since at the representative Ca/Si = 1.7 approximately 30% of bridging sites are occupied by a Q^{2b} silicate the remaining sites are occupied by a Ca^{2+}. This suggests a surface termination fundamentally different from the previous assumptions in the literature which were mainly based in silicate terminations.

In conclusion, significant progress has been made in elucidating the bulk C-S-H as well as the C-S-H surface. The investigation of bulk C-S-H revealed that no significant differences were found in the structural features (pair distribution function) between Ca/Si = 1.5 and 1.7. This observation suggests that surface effects play an important role in the overall properties of C-S-H nanofoils and control the many phenomena associated with C-S-H. The same was found when investigating the structuring of the C-S-H (001) basal surface.

6.2   Where do we go now

The atomic description of the structure of the C-S-H nanofoil, which agrees with experimentally measured properties, enables a wide range of studies, which are of great importance for elucidating different phenomena in practical cementitious systems. Of particular interest is it to address the surface chemistry of C-S-H as well as the resulting porosity and its effect on ion transport and mechanical properties, including (i) elucidating ion adsorption at the C-S-H-solution interface, (ii) resolving the structure of the electric double layer on C-S-H particles, and (iii) determining the microstructural (origin of pore sizes) and transport properties (water and chloride diffusion) of C-S-H pore networks.

As shown in chapter 5, it is expected that a complicated network of Ca^{2+} and OH^- will be formed on the C-S-H surface. In order to explore surface chemistry, a systematic study of free energy of adsorption should be carried out. Species of interest are Ca^{2+} and OH^-, as well as the $Ca(OH)^+$ complex, which is predicted to exist at high pH in higher concentrations than the Ca^{2+} ion [13], as well as Na^+. It is hypothesized that Na^+ ions may displace adsorbed Ca^{2+} ions and form inner sphere complexes. While Ca^{2+} is known to prefer outer sphere complexes [14], the role of OH^- is of high interest, as it may act as a bridge for Ca^{2+} adsorption [15]. With such a study the actual adsorption state at the C-S-H surface could be determined.

While simulations can provide valuable information they are not to be trusted without a proper comparison to experimental work. Due to the complex nanofoil morphology it is difficult to use advanced characterization techniques. Zeta potential is likely the most suitable experimental technique, which can be directly related to atomistic simulations in order to understand the atomistic structure at the solid-liquid interface of C-S-H. Predota et al. [16,17] developed a methodology to extract the zeta potential using non-equilibrium MD (NEMD) simulations. With this methodology it could be possible to validate the models and gain confidence into them.

The utilization of more advanced surface characterizations techniques, such as atomic force microscopy and sum frequency generation spectroscopy, is limited by the sample preparation, since they require to grow the material on a subtract. While difficult, not impossible. de Souza [18] succeeded growing C-S-H on graphene oxide, with which they achieved a layer-by-layer ordering. While they investigated C-S-H with low Ca/Si ratio (below 1.3) they precipitated C-S-H with the dropwise method, similar to the method of Harris et al. [4] that was used to synthetize C-S-H samples in chapter 4 of this thesis by the SNF partner PhD, Anna Molares Melgares (LMC-EPFL).

Colloidal interactions between nanoparticles often define the pore size distribution and control the formation of the pore network. The pore structure, in turn, influences the physical and mechanical properties and controls the durability of the material [19,20]. In hardened concrete paste the pore sizes range from approximately 1 nm to a few tens of nanometers. It is not yet understood what guides the pore dimension in hardened cement paste. There is also no clean distinction between the C-S-H interlayers (within the particles) and the smallest interparticle nanopores. Use of SCMs has been shown to alter the pore size distribution [19] and, therefore, detailed understanding of the pore formation at the atomic level is of high importance.

Large-scale classical MD simulations have been successfully used to analyze the structure and energetics of pores in assemblages of clay nanoparticles [20,21]. The analysis of such simulations can help elucidate the microstructural (pore size), thermodynamic (enthalpy and free energy of hydration), mechanical, and transport properties (diffusion) [21–23]. At short interparticle distances (below 3 nm) stabilization is achieved by inter-atomic interactions in overlapping electric double layers between charged surfaces. In such conditions, the DLVO theory fails as short-range phenomena (adsorption, hydrogen bonding) become predominant. Simulations can

provide detailed atomistic-level insights on the impacts of salinity and counterion type on the free energy of interaction between charged particles. For example, studies of the free energy of interaction between charged clay particles indicate that the hydration repulsion component increases with counterion hydration energy, while the Coulomb attraction component (associated with specific Coulomb interactions in the electric double layer) increases with decreasing counterion tendency for complexation, and the oscillatory component (associated with water layering on the mineral surface) increases with the abundance of counterion outer-sphere surface complexes .

Applying this methodology in combination with C-S-H nanofoil models from chapter 5 could generate insight into the origin of pore sizes and, also, new knowledge of the pore solution composition, which remains elusive. The resulting knowledge and microstructural models would enable detailed studies of C-S-H transport properties, including chloride diffusivity which is a key factor in steel reinforcement bars in practice.

The main goal in the future is to obtain an understanding of the surface chemistry of C-S-H nanofoils. This knowledge will contribute to the yet still unknown mechanisms of nucleation, growth, and aggregation of C-S-H. These insights will enable better engineering of cement reactivity, enabling higher substitution degrees of SCMs and consequently lowering the CO_2 footprint of modern cement mixtures. Furthermore, the research will generate new understanding of the C-S-H pore network, which remains unresolved in the cement community but is critical to predict the transport of chloride and other ions which can affect lifetime of structures. This knowledge would help establish the theoretical framework to design concrete with targeted pore sizes, with the aim of lowering the diffusivity of chloride while maintaining the mechanical properties and increasing the service life of concrete structures, which would indirectly lower the CO_2 footprint of cement.

References

[1]   A. Kumar, B.J. Walder, A. Kunhi Mohamed, A. Hofstetter, B. Srinivasan, A.J. Rossini, K. Scrivener, L. Emsley, P. Bowen, The Atomic-Level Structure of Cementitious Calcium Silicate Hydrate, The Journal of Physical Chemistry C. 121 (2017) 17188–17196. https://doi.org/10.1021/acs.jpcc.7b02439.

[2]   A. Kunhi Mohamed, P. Moutzouri, P. Berruyer, B.J. Walder, J. Siramanont, M. Harris, M. Negroni, S.C. Galmarini, S.C. Parker, K.L. Scrivener, L. Emsley, P. Bowen, The Atomic-Level Structure of Cementitious Calcium Aluminate Silicate Hydrate, J Am Chem Soc. 142 (2020) 11060–11071. https://doi.org/10.1021/jacs.0c02988.

[3]   A. Kunhi Mohamed, S.C. Parker, P. Bowen, S. Galmarini, An atomistic building block description of C-S-H - Towards a realistic C-S-H model, Cem Concr Res. 107 (2018) 221–235. https://doi.org/10.1016/j.cemconres.2018.01.007.

[4]   M. Harris, G. Simpson, K. Scrivener, P. Bowen, A method for the reliable and reproducible precipitation of phase pure high Ca/Si ratio (>1.5) synthetic calcium silicate hydrates (C-S-H), Cem Concr Res. 151 (2022) 106623. https://doi.org/10.1016/j.cemconres.2021.106623.

[5]   D.A. Kulik, G.D. Miron, B. Lothenbach, A structurally-consistent CASH+ sublattice solid solution model for fully hydrated C-S-H phases: Thermodynamic basis, methods, and Ca-Si-H2O core sub-model, Cem Concr Res. 151 (2022) 106585. https://doi.org/10.1016/j.cemconres.2021.106585.

[6]   E. Duque-Redondo, P.A. Bonnaud, H. Manzano, A comprehensive review of C-S-H empirical and computational models, their applications, and practical aspects, Cem Concr Res. 156 (2022) 106784. https://doi.org/10.1016/j.cemconres.2022.106784.

[7]   M.N. Harris, Precipitation, Characterization, Kinetic, and Thermodynamic Modelling of Synthetic C-S-H Systems (C-S-H, CASH, CSH+$), EPFL, 2022. https://doi.org/https://doi.org/10.5075/epfl-thesis-9917.

[8]   A. Morales-Melgares, Z. Casar, P. Moutzouri, A. Venkatesh, M. Cordova, A. Kunhi Mohamed, K. L. Scrivener, P. Bowen, L. Emsley, Atomic-Level Structure of Zinc-Modified Cementitious Calcium Silicate Hydrate, J Am Chem Soc. 144 (2022) 22915–22924. https://doi.org/10.1021/jacs.2c06749.

[9]   E.T. Rodriguez, I.G. Richardson, L. Black, E. Boehm-Courjault, A. Nonat, J. Skibsted, Composition, silicate anion structure and morphology of calcium silicate hydrates (C-S-H) synthesised by silica-lime reaction and by controlled hydration of tricalcium silicate (C3S),

Advances in Applied Ceramics. 114 (2015) 362–371. https://doi.org/10.1179/1743676115Y.0000000038.

[10]   L.B. Skinner, S.R. Chae, C.J. Benmore, H.R. Wenk, P.J.M. Monteiro, Nanostructure of calcium silicate hydrates in cements, Phys Rev Lett. 104 (2010) 1–4. https://doi.org/10.1103/PhysRevLett.104.195502.

[11]   P.D. Tennis, H.M. Jennings, Model for two types of calcium silicate hydrate in the microstructure of Portland cement pastes, Cem Concr Res. 30 (2000) 855–863. https://doi.org/10.1016/S0008-8846(00)00257-X.

[12]   S. Yoshida, Y. Elakneswaran, T. Nawa, Electrostatic properties of C–S–H and C-A-S-H for predicting calcium and chloride adsorption, Cem Concr Compos. 121 (2021) 104109. https://doi.org/10.1016/j.cemconcomp.2021.104109.

[13]   Sandra Caroline Galmarini, Atomistic Simulation of Cementitious Systems, EPFL Thesis No. 5754 (2013). https://doi.org/10.5075/epfl-thesis-5754.

[14]   M. Bischoff, D. Biriukov, M. Předota, A. Marchioro, Second Harmonic Scattering Reveals Ion-Specific Effects at the SiO2 and TiO2 Nanoparticle/Aqueous Interface, Journal of Physical Chemistry C. 125 (2021) 25261–25274. https://doi.org/10.1021/acs.jpcc.1c07191.

[15]   S. Galmarini, P. Bowen, Atomistic simulation of the adsorption of calcium and hydroxyl ions onto portlandite surfaces - Towards crystal growth mechanisms, Cem Concr Res. 81 (2016) 16–23. https://doi.org/10.1016/j.cemconres.2015.11.008.

[16]   M. Předota, M.L. Machesky, D.J. Wesolowski, Molecular Origins of the Zeta Potential, Langmuir. 32 (2016) 10189–10198. https://doi.org/10.1021/acs.langmuir.6b02493.

[17]   D. Biriukov, P. Fibich, M. Předota, Zeta Potential Determination from Molecular Simulations, Journal of Physical Chemistry C. 124 (2020) 3159–3170. https://doi.org/10.1021/acs.jpcc.9b11371.

[18]   F. Basquiroto de Souza, E. Shamsaei, S. Chen, K. Sagoe-Crentsil, W. Duan, Controlled growth and ordering of poorly-crystalline calcium-silicate-hydrate nanosheets, Commun Mater. 2 (2021). https://doi.org/10.1038/s43246-021-00191-6.

[19]   P. Pipilikaki, M. Beazi-Katsioti, The assessment of porosity and pore size distribution of limestone Portland cement pastes, Constr Build Mater. 23 (2009) 1966–1970. https://doi.org/10.1016/j.conbuildmat.2008.08.028.

[20]   X. Shen, I.C. Bourg, Molecular dynamics simulations of the colloidal interaction between smectite clay nanoparticles in liquid water, J Colloid Interface Sci. 584 (2021) 610–621. https://doi.org/10.1016/j.jcis.2020.10.029.

[21]   T. R. Underwood, I. C. Bourg, Large-Scale Molecular Dynamics Simulation of the Dehydration of a Suspension of Smectite Clay Nanoparticles, The Journal of Physical Chemistry C. 124 (2020) 3702–3714. https://doi.org/10.1021/acs.jpcc.9b11197.

[22]   M. Holmboe, I.C. Bourg, Molecular dynamics simulations of water and sodium diffusion in smectite interlayer nanopores as a function of pore size and temperature, Journal of Physical Chemistry C. 118 (2014) 1001–1013. https://doi.org/10.1021/jp408884g.

[23]   J.L. Suter, P. V Coveney, H. Chris Greenwell, M.-A. Thyveetil, Large-Scale Molecular Dynamics Study of Montmorillonite Clay: Emergence of Undulatory Fluctuations and Determination of Material Properties, Journal of Physical Chemistry C. 111 (2007) 8248–8259. https://doi.org/10.1021/jp070294b.

A Appendix

A2   Supplementary Information – Chapter 2

A2-1   Force field parametrization

For details we refer the reader to the main text of the manuscript.

Table S1. List of atomic species in the force field

Atomic species	Charge	Description	Reference
Ca	+2	Calcium	Tilocca et al. [1]
Si	+4	Silicon	Tilocca et al. [1]
O	+0.84819	Core oxygen	Tilocca et al. [1]
O(S)	-2.84819	Shell oxygen	Tilocca et al. [1]
Ow	-1.1128	Water oxygen	Abascal & Vega [2]
Hw	+0.5564	Water hydrogen	Abascal & Vega [2]
Oh	-1.4	Hydroxide oxygen	Freeman et al. [3]
H	+0.4	Hydroxide hydrogen	Freeman et al. [3]
Al	+3	Aluminium	Mohamed et al. [4]
Zn	+2	Zinc	Lewis & Catlow [5]
Cl	-1	Chloride	Joung & Cheatham [6]

Table S2. Buckingham potentials.

	A [eV]	ρ [Å]	C [eV Å^6]	Source
Ca-O(S)	2152.3566	0.309227	0.09944	Tilocca et al. [1]
Si-O(S)	1283.90	0.3205	10.66	Tilocca et al. [1]
Si-Ow	1283.556	0.3202	10.66	Mohamed et al. [4]
Si-Oh	983.50	0.3255	10.66	De Leeuw et al. [7]
O(S)-O(S)	22764.3	0.149	27.88	Tilocca et al. [1]
O(S)-Ow	22764.3	0.149	28.92	Mohamed et al. [4]
O(S)-Oh	22764.3	0.149	13.94	De Leeuw et al. [7]
O(S)-Hw	512.00	0.250	0.00	Mohamed et al. [4]
Al-O(S)	1474.40	0.3006	0.00	Mohamed et al. [4]
Zn-O(S)	499.60	0.3595	0.00	Lewis & Catlow [5]
Zn-Oh	370.00	0.3595	0.00	This work

Table S3. Lennard-Jones 12-6 potentials.

Atom 1	Atom 2	ε [eV]	σ [Å]	Source
Ca	Ca	1.2119E-02	2.83310	Mamatkulov et al. [8]
Ca	Ow	9.8463E-03	2.99600	LB rule
Ca	Oh	1.9915E-03	3.38500	LB rule
Al	Ow	1.1796E-03	2.86445	Li et al. [9]
Al	Oh	1.8136E-03	2.99500	LB rule
Zn	Ow	7.3425E-03	3.15845	LB rule
Ow	Ow	8.0310E-03	3.15890	Abascal & Vega [2]
Ow	Oh	1.2300E-02	3.28945	LB rule
Oh	Oh	1.8911E-02	3.42000	This work
Cl	Cl	5.0569E-04	4.91780	Joung & Cheatham [6]
Cl	Ow	2.0113E-03	4.03835	LB rule
Cl	Ca	2.4756E-03	3.87545	LB rule

LB rule stands for Lorentz-Berthelot mixing rule (see main text).

Table S4. Lennard-Jones 9-6 potentials (N-M potential).

Atom 1	Atom 2	E_0 [eV]	r_0 [Å]	n	m	Source
Ow	H	0.055556	2.00	9	6	Mohamed et al. [4]
O(S)	H	0.007300	2.71	9	6	Mohamed et al. [4]
Oh	H	0.007300	2.71	9	6	Freeman et al. [3]

Table S5. Morse bond.

	D [eV]	α [1/ Å]	r_0 [Å]	Source
Oh-H	7.0525	3.1749	0.942	Freeman et al. [3]

Table S6. Harmonic bonds.

	K [eV/Å²]	r₀ [Å]	Source
O-O(S)	37.5	0.0	Tilocca et al. [1]
Ow-Hw	9.7563	0.9572	Abascal & Vega [2]

Table S7. Harmonic angles.

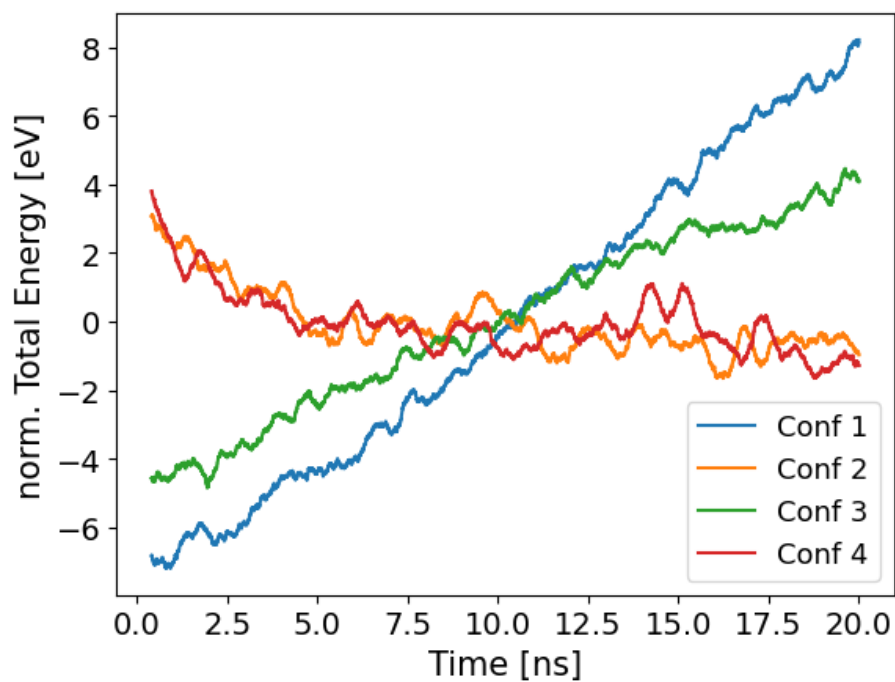|	K [eV]	Θ [°]	Source
O-Si-O Oh-Si-O Oh-Si-Oh	7.74815	109.47	Tilocca et al. [1] De Leeuw et al. [7]
Si-Oh-H	7.74815	141.5	Mohamed et al. [4]
O-Zn-O Oh-Zn-O Oh-Zn-Oh	0.1	105.0	This work
Zn-Oh-H	0.1	109.0	This work

Figure S1. Total energy of tobermorite 14Å normalized by the mean total energy of the 20ns production run. Conf 1: Pdamp = 0.2, shell mass = 0.3; Conf 2: Pdamp = 0.2, shell mass = 0.4; Conf 3: Pdamp = 0.6, shell mass = 0.2; Conf 4: Pdamp = 0.6, shell mass = 0.4
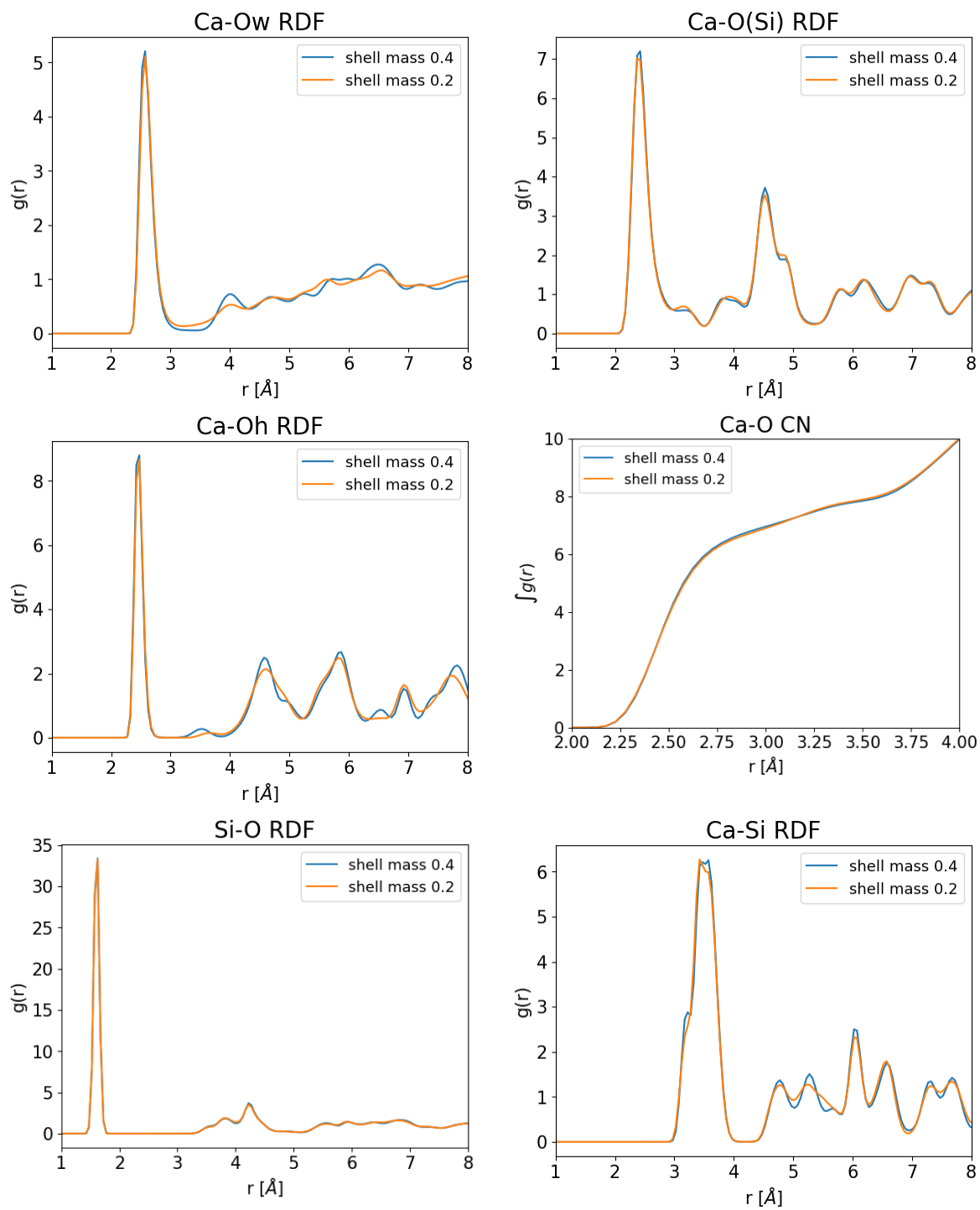
Figure S2. Comparison of RDFs for tobermorite simulated with two different shell masses.

A2-3   Structural validation

All simulated systems were a replication of the unit cell in all crystallographic directions. The minimum size of the super cell was at least 2 nm in each axis.

Table S8. Unit cell parameters of known crystals as predicted by MD and determined by experiments or DFT.

Crystal	a	b	c	α	β	γ
Cao	4.82	4.82	4.82	90.00	90.00	90.00
Exp [10]	4.81	4.81	4.81	90.00	90.00	90.00
$Ca(OH)_2$	3.67	3.67	4.68	90.00	90.00	120.00
Exp [11]	3.59	3.59	4.87	90.00	90.00	120.00
$Al(OH)_3$	4.82	4.82	12.66	90.00	90.00	120.00
DFT [12]	4.76	4.76	12.99	90.00	90.00	120.00
$Ca_3Al_2O_{12}H_{12}$	13.63	13.63	13.63	90.00	90.00	90.00
Exp [13]	12.56	12.56	12.56	90.00	90.00	90.00
SiO_2	4.91	4.91	5.34	90.00	90.00	120.00
Exp [14]	4.91	4.91	5.20	90.00	90.00	120.00
$Ca_3Al_2O_6$	16.09	16.27	16.14	89.93	89.91	90.04
Exp [15]	15.26	16.26	15.26	90.00	90.00	90.00
$CaSiZnO_5H_2$	5.20	15.95	5.39	90.00	105.35	90.01
Exp [16]	5.09	15.83	5.39	90.00	103.26	90.00
$CaZn_2Si_2O_7.H_2O$	12.83	6.22	8.58	87.67	89.98	90.45
Exp [17]	12.53	6.31	8.56	90.00	90.00	90.00
$Ca_2Si_2ZnO_7$	8.03	8.03	4.99	90.01	90.00	90.00
Exp [18]	7.83	7.83	5.01	90.00	90.00	90.00
Zn_2SiO_4	13.79	13.79	9.44	90.00	90.00	120.00
Exp [19]	13.95	13.95	9.32	90.00	90.00	120.00
ZnO	3.22	3.22	5.16	90.00	90.00	120.01
Exp [20]	3.25	3.25	5.20	90.00	90.00	120.00
ε-$Zn(OH)_2$	5.37	5.37	7.99	89.10	87.30	117.31
Exp [21]	4.91	5.14	8.47	90.00	90.00	90.00
β-$Zn(OH)_2$	3.70	3.70	4.92	90.00	90.00	90.00
Exp [22]	3.19	3.19	4.71	90.00	90.00	120.00
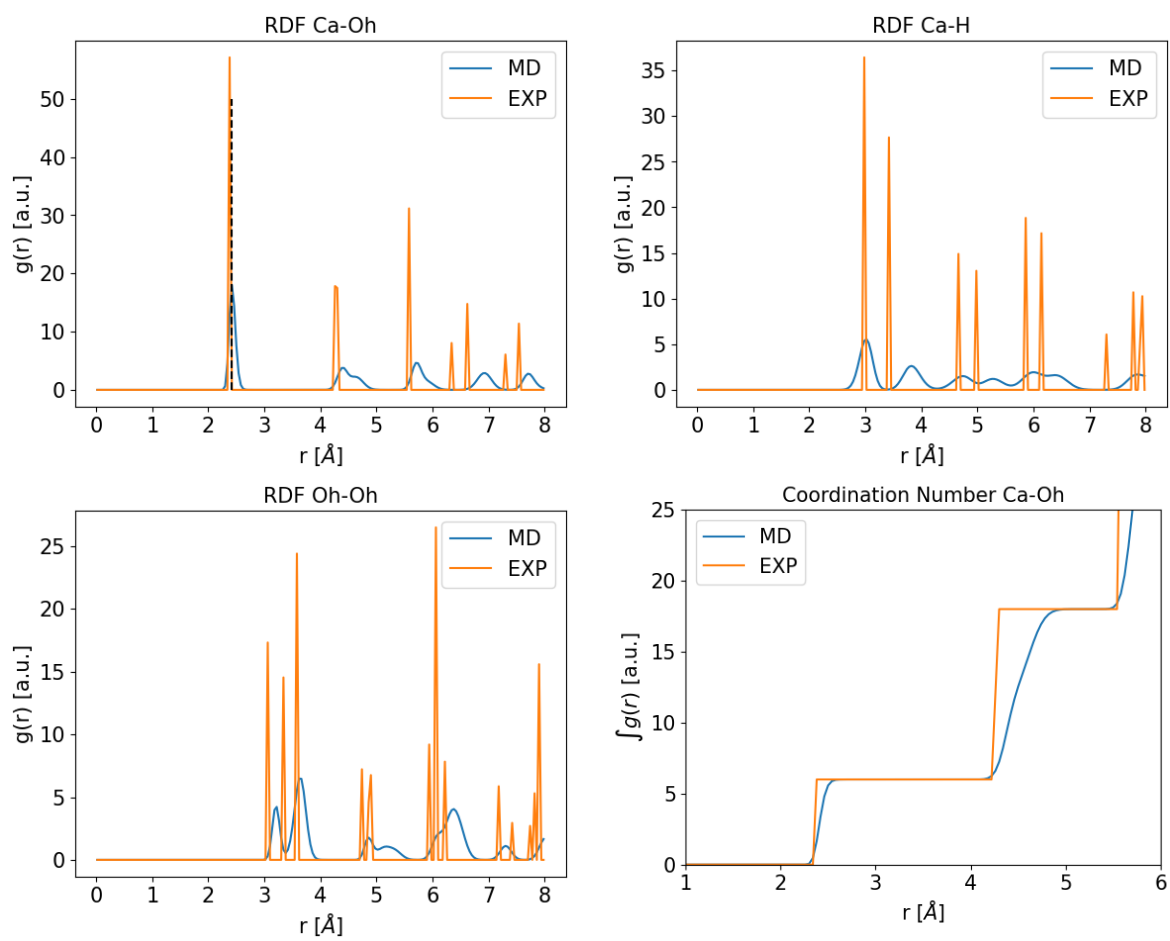
Figure S3. Comparison of MD and EXP [11] structural features of Portlandite.
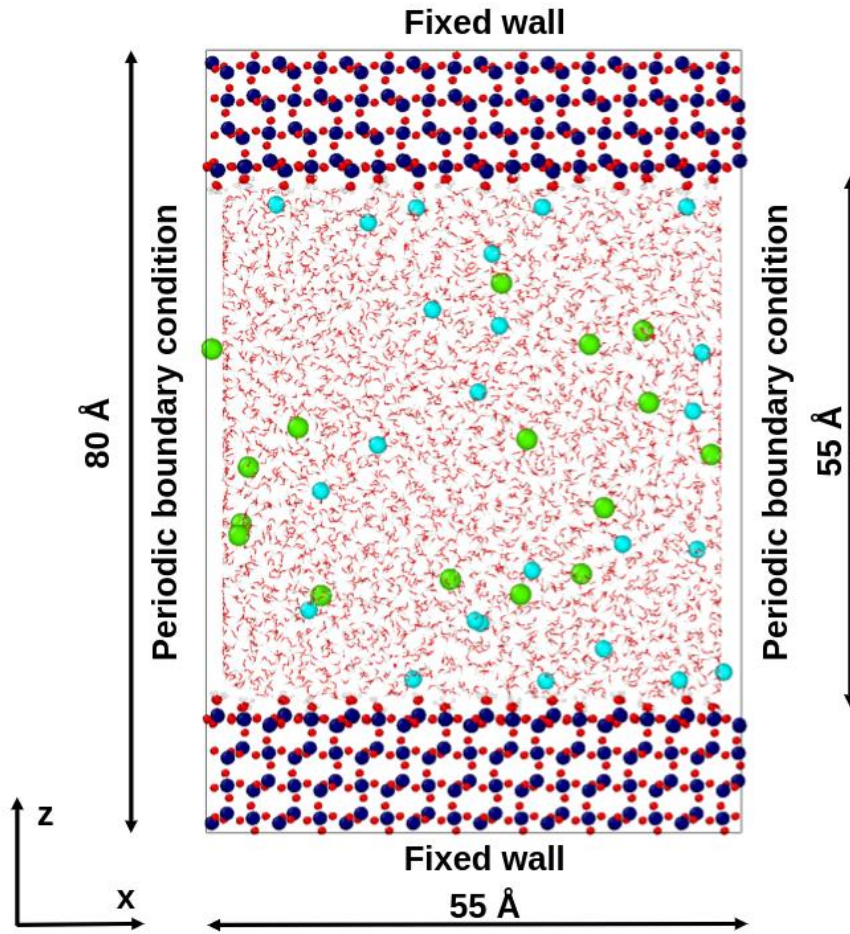
Figure S4. SiO₂ surface in contact with Ca²⁺ and Cl⁻ solution. Color code: Si- dark blue, O – red, H – white, Ca – light blue, Cl – green.
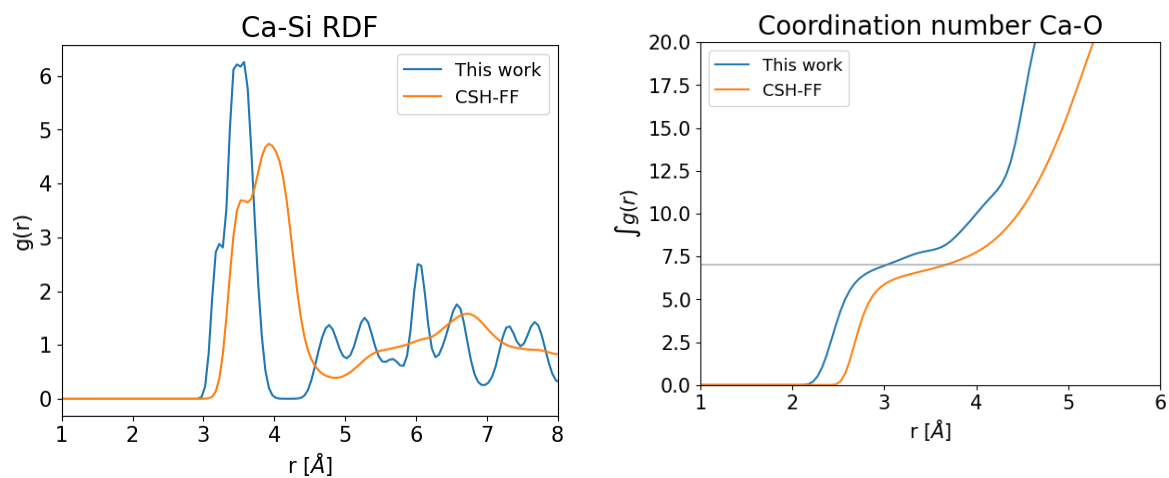
Figure S5. Comparison of structural features between our newly developed force field and CSH-FF [23]. The gray line in the 'Coordination number Ca-O' graph lies at coordination number 7.
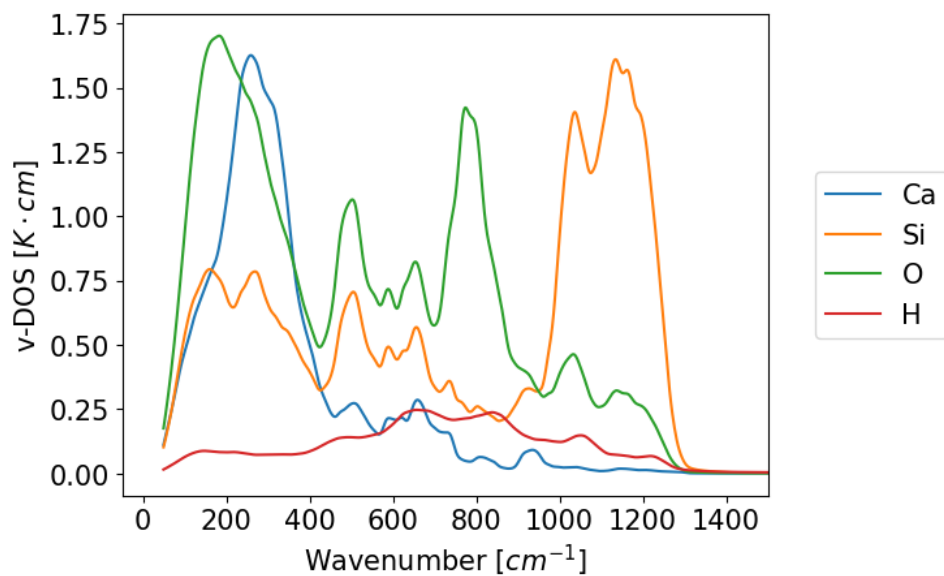
Figure S6. Projected v-DOS as predicted by the force field.

Table S9. Measured and Ab initio calculated v-DOS as reported in Vidmer et al. [24]

Ab initio	Experimental	Description
100-200	250	Deformation of Si and Ca polyhedra
200-350	300	Deformation of Ca polyhedra
370-520	445	Deformation of Si tetrahedra
510	530	H_2O liberations
650	670	O-Si-O bending, H_2O liberations
705	Not observed	H_2O liberations
815	830	Si-O stretching
930	969	Si-O stretching
985	1050	Si-O stretching
1060	1120	Si-O stretching
1155	1200	H_2O interaction with O-Si neighbor
1610	1640	H_2O bending
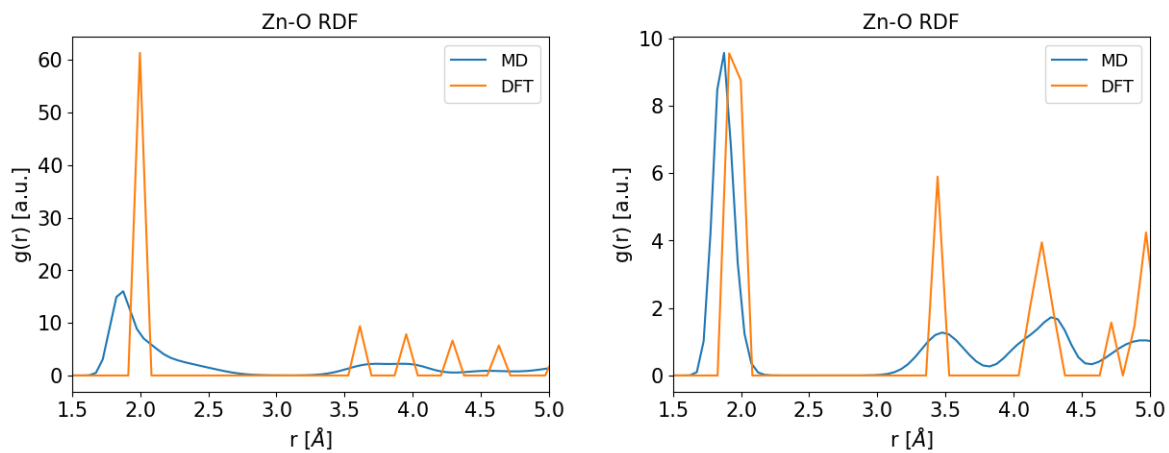
Figure S7. Zinc – oxygen RDF comparison between MD and DFT [25].
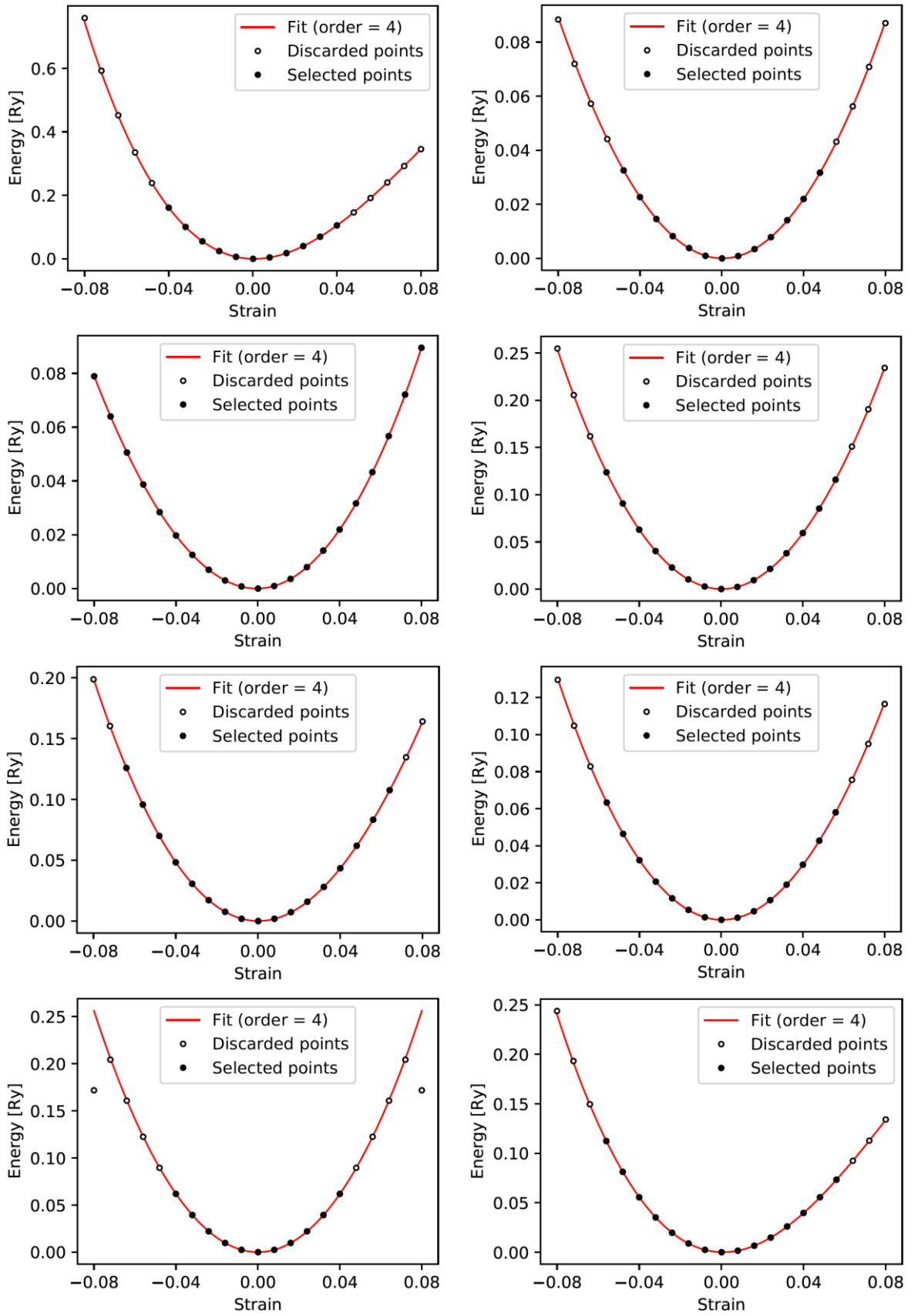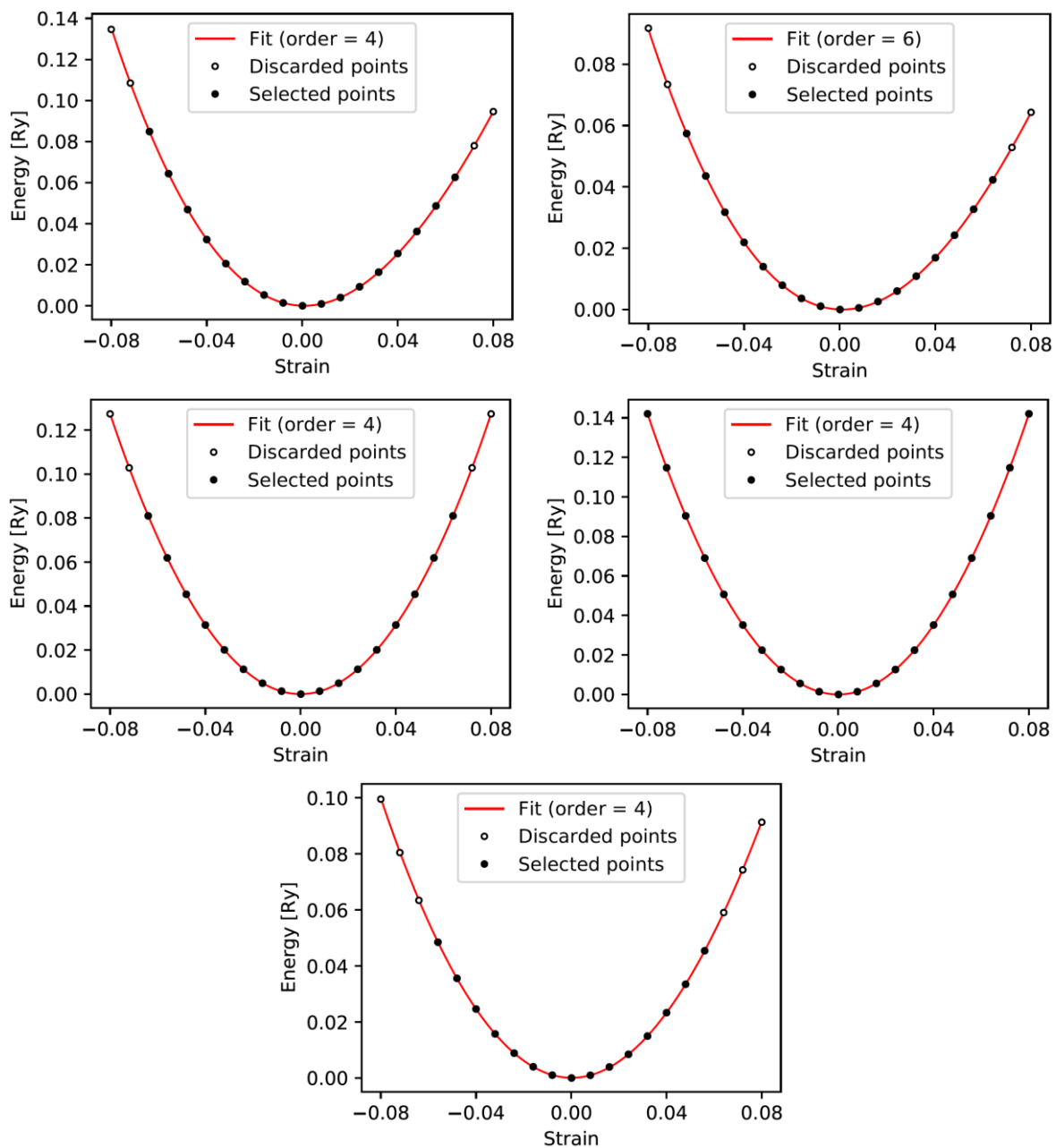
Figure S8. Energy-Strain curves for Clinohedrite.
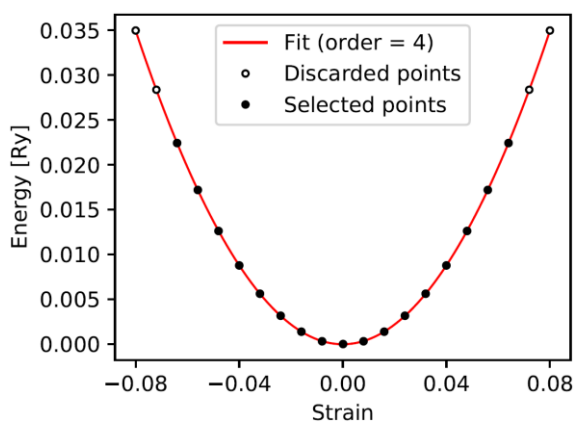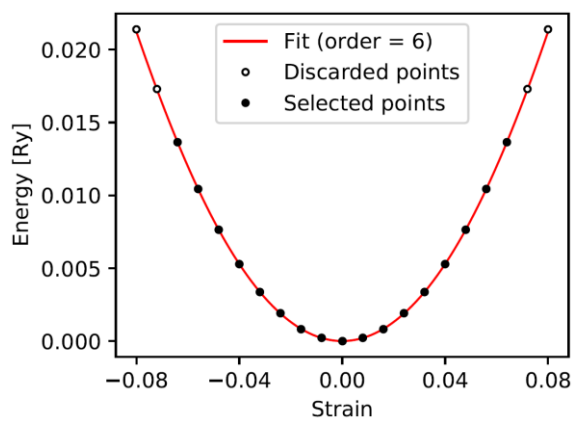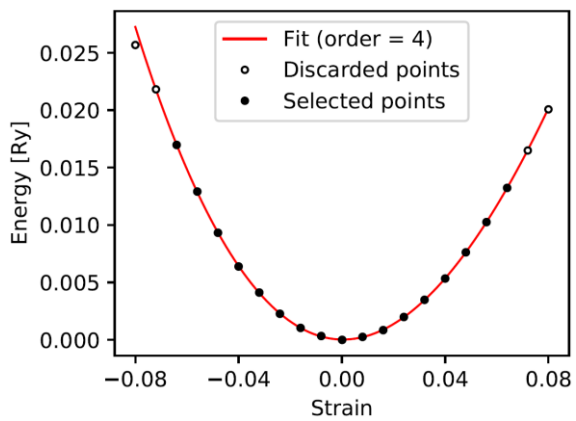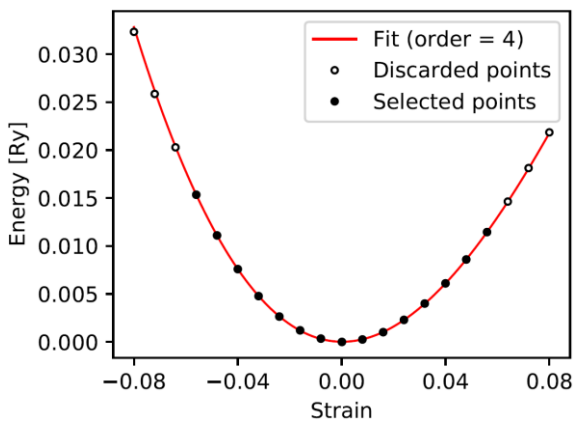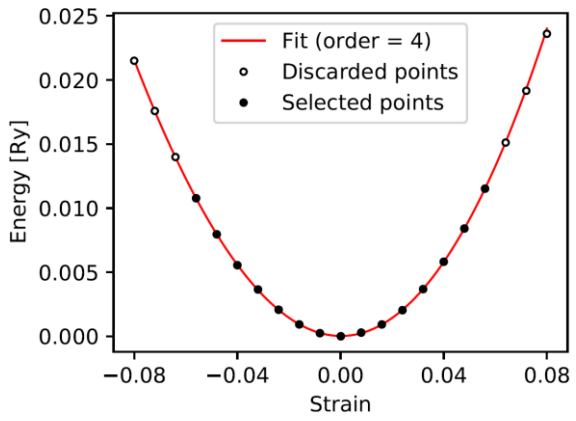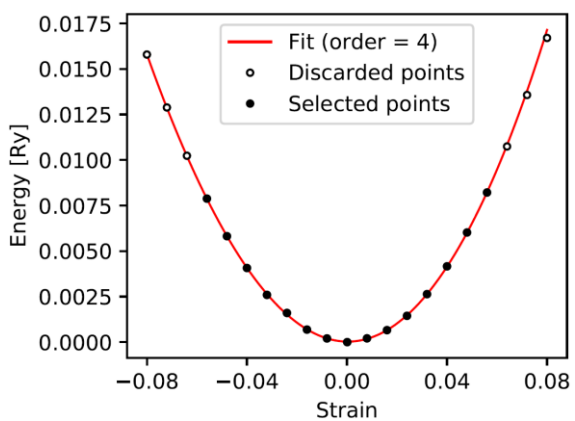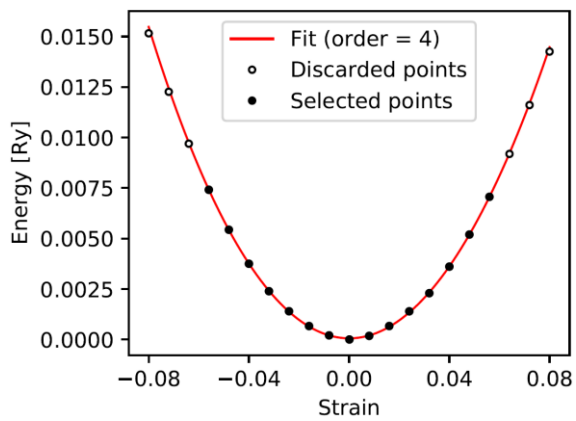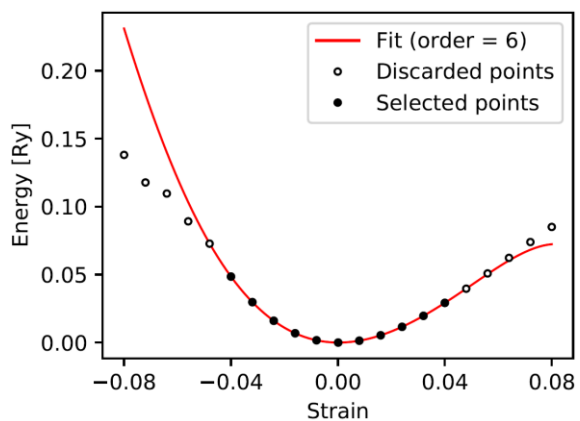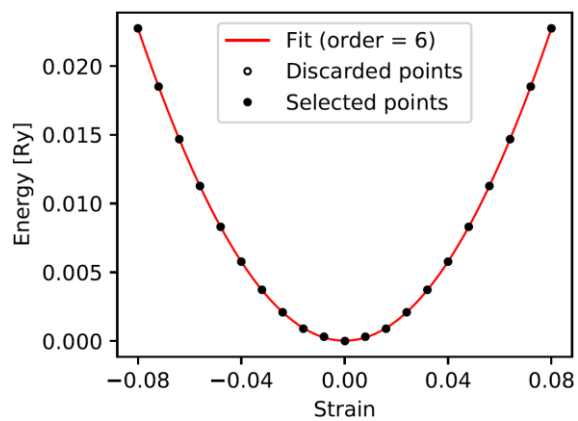
Figure S8. Energy-Strain curves for Clinohedrite.

Table S10. The elastic constants for ε-Zn(OH)$_2$ and clinohedrite, as predicted by DFT.

Elastic Constant in Voigt notation	ε-Zn(OH)$_2$ [GPa]	Clinohedrite [GPa]
c_{11}	68.2	142.6
c_{12}	41.8	64.7
c_{13}	39.5	58.5
c_{22}	90.0	183.4
c_{23}	50.5	71.9
c_{33}	76.9	122.6
c_{44}	17.2	49.7
c_{45}	0.0	-4.1
c_{55}	29.0	55.5
c_{66}	18.9	38.0

References

[1]   A. Tilocca, N.H. De Leeuw, A.N. Cormack, Shell-model molecular dynamics calculations of modified silicate glasses, Phys Rev B. 73 (2006) 104209. https://doi.org/10.1103/PhysRevB.73.104209.

[2]   J.L.F. Abascal, C. Vega, A general purpose model for the condensed phases of water: TIP4P/2005, Journal of Chemical Physics. 123 (2005). https://doi.org/10.1063/1.2121687.

[3]   C.L. Freeman, J.H. Harding, D.J. Cooke, J.A. Elliott, J.S. Lardge, D.M. Duffy, New forcefields for modeling biomineralization processes, Journal of Physical Chemistry C. 111 (2007) 11943–11951. https://doi.org/10.1021/jp071887p.

[4]   A. Kunhi Mohamed, P. Moutzouri, P. Berruyer, B.J. Walder, J. Siramanont, M. Harris, M. Negroni, S.C. Galmarini, S.C. Parker, K.L. Scrivener, L. Emsley, P. Bowen, The Atomic-Level Structure of Cementitious Calcium Aluminate Silicate Hydrate, J Am Chem Soc. 142 (2020) 11060–11071. https://doi.org/10.1021/jacs.0c02988.

[5]   G. V. Lewis, C.R. A Catlow, W.C. Mackrodt, R.F. Stewart, W.C. Mackrodt, R.F. Stewart, C.R.A. Catlow, A.M. Stoneham, Potential models for ionic oxides, Journal of Physics C: Solid State Physics. 18 (1985) 1149–1161. https://doi.org/10.1088/0022-3719/18/6/010.

[6]   I.S. Joung, T.E. Cheatham, Determination of alkali and halide monovalent ion parameters for use in explicitly solvated biomolecular simulations, Journal of Physical Chemistry B. 112 (2008) 9020–9041. https://doi.org/10.1021/jp8001614.

[7]   N.H. De Leeuw, S.C. Parker, C.R.A. Catlow, G.D. Price, Modelling the effect of water on the surface structure and stability of forsterite, Phys Chem Miner. 27 (2000) 332–341. https://doi.org/10.1007/s002690050262.

[8]   S. Mamatkulov, M. Fyta, R.R. Netz, Force fields for divalent cations based on single-ion and ion-pair properties, J Chem Phys. 138 (2013). https://doi.org/10.1063/1.4772808.

[9]   P. Li, L.F. Song, K.M. Merz, Parameterization of highly charged metal ions using the 12-6-4 LJ-type nonbonded model in explicit water, Journal of Physical Chemistry B. 119 (2015) 883–895. https://doi.org/10.1021/jp505875v.

[10]   D.W. Goodwin, A.J. Lindop, The Crystal Structure of CaO .2Al2O3, Acta Crystallographica, Section B. 26 (1970).

[11]   D.M. Henderson, H.S. Gutowsky, A nuclear magnetic resonance determination of hydrogen positions in Ca(OH)2, Am Mineral. 47 (1962) 1231–1251.

[12]   E. Balan, M. Lazzeri, G. Morin, F. Mauri, First-principles study of the OH-stretching modes of gibbsite, American Mineralogist. 91 (2006) 115–119. https://doi.org/10.2138/am.2006.1922.

[13]   G.A. Lager, T. Armbruster, J. Faber, Neutron and X-ray diffraction study of hydrogarnet Ca3Al2(O4H4)3, American Mineralogist. 72 (1987) 756–765.

[14]   L. Levien, C.T. Prewitt, D.J. Weidner, C.T. Prewir, D.J. Weidner, Structure and Elastic Properties of Quartz at Pressure, American Mineralogist. 65 (1980) 920–930. http://rruff.info/doclib/am/vol65/AM65_920.pdf.

[15]   P. Mondal, J.W. Jeffery, The crystal structure of tricalcium aluminate, Ca3Al2O6, Acta Crystallogr B. 31 (1975) 689–697. https://doi.org/10.1107/S0567740875003639.

[16]   C.C. Venetopoulos, P.J. Rentzeperis, Redetermination of the crystal structure of clinohedrite, CaZnSiO4*H2O, Zeitschrift Fur Kristallographie. 144 (1976) 377–392.

[17]   H. Yang, N.G. Jenkins, R.T. Downs, Redetermination of junitoite, CaZn2Si2O7*H2O, Acta Crystallographica, Section E. 68 (2012).

[18]   S.J. Louisnathan, Refinement of the crystal structure of hardystonite, Ca2ZnSi2O7, Zeitschrift Fur Kristallographie. 130 (1969) 427–437.

[19]   K.-H. Klaska, J.C. Eck, D. Pohl, New investigation of willemite, Acta Crystallographica, Section B. 34 (1978) 3324–3325.

[20]   K. Kihara, G. Donnay, Anharmonic thermal vibrations in ZnO Model: 2-c, at T = 293 K, The Canadian Mineralogist. 23 (1985) 647–654.

[21]   H. Jacobs, A. Niemann, W. Kockelmann, Low temperature investigations of hydrogen bridge bonds in the hydroxides beta-Be(OH)2 and epsilon-Zn(OH)2 by Raman-spectroscopy as well as X-ray and neutron diffraction Sample: T = 298 K, Z Anorg Allg Chem. 631 (2005) 1247–1254.

[22]   M.I. Baneeva, S.V. Popova, Investigation of zinc hydroxide at high pressures and temperatures, GEOKHIMIJA. 8 (1969) 1014–1016.

[23]   R. Shahsavari, R.J.M. Pellenq, F.J. Ulm, Empirical force fields for complex hydrated calcio-silicate layered materials, Physical Chemistry Chemical Physics. 13 (2011) 1002–1011. https://doi.org/10.1039/c0cp00516a.

[24]   A. Vidmer, G. Sclauzero, A. Pasquarello, Infrared spectra of jennite and tobermorite from   first-principles,   Cem   Concr   Res.   60   (2014)   11–23. https://doi.org/10.1016/j.cemconres.2014.03.004.

[25]   A. Morales-Melgares, Z. Casar, P. Moutzouri, A. Venkatesh, M. Cordova, A. Kunhi Mohamed, K. L. Scrivener, P. Bowen, L. Emsley, Atomic-Level Structure of Zinc-Modified Cementitious Calcium Silicate Hydrate, J Am Chem Soc. 144 (2022) 22915–22924. https://doi.org/10.1021/jacs.2c06749.

A3   Supplementary Information – Chapter 3

A3-1   pyCSH Nomenclature

The following section explains the nomenclature (String) of pyCSH. For each individual string the notation in the brick model [20] is given, followed by the stoichiometry (Stoichio) and the charge of the group of atoms. In the iterative loop for automatic structure generation, which is explained in the main text, pyCSH combines different strings (atomic groups). With those different combinations defective tobermorite unit cells are created (see figures 2 and 3 in main text).

For example, tobermorite 14 Å is in the brick model written as: $< S' < C\ 7 >\ 'S >$. This notation determines that the unit cell is constructed, in the order of symbols, with a dimer silicate ($<$), which is followed by a Q^{2b} bridging site (S) that has one silanol group (') and the upper silicate chain ends with a dimer silicate ($<$). Then the interlayer follows, which holds one Ca^{2+} (C) and seven water molecules (7). The lower chain for tobermorite is identical to the upper chain, therefore a dimer silicate ($>$), a Q^{2b} (S) with a protonated silanol group (') and again a dimer silicate ($>$). In the pyCSH code the nomenclature is exact, and each individual group of atoms needs to be written out. The same tobermorite structure is therefore written as: <L SUo <R CII wMUL wMDL w14 w15 w16 wDL wUL >L SDo >R. Each position (atomic coordinates) for each string is predetermined. Therefore, it is necessary to write out the string for each water molecules, while in the brick model notation one simply specifies that there are seven of them. It is the same for Ca^{2+} in the interlayer. While the notation used above will insert CII, which is Ca^{2+} positioned in the middle of the interlayer, one could as well choose CIU (Ca^{2+} positioned closer to the upper silicate chain) or CID (Ca^{2+} positioned closer to the lower silicate chain.

Table S1. Dimmers

String	Brick model	Stoichio	Charge	Comment
<L	<	$CaSiO_4$	-2	
>L	>	$CaSiO_3$	0	
<R	<	$CaSiO_3$	0	
>R	>	$CaSiO_4$	-2	
<Lo	< '	$CaSiO_3OH$	-1	
>Lo	> '	$CaSiO_2OH$	1	Protonated Oxygen
<Ro	' <	$CaSiO_2OH$	1	
>Ro	' >	$CaSiO_3OH$	-1	

Table S2. Bridging sites.

String	Brick model	Stoichio	Charge
SU	S	SiO_2	0
SD	S	SiO_2	0
SUo	S'	$SiOOH$	1
SDo	S'	$SiOOH$	1
CU	C	Ca	2
CD	C	Ca	2

Table S3. Interlayer calcium.

String	Brick model	Stoichio	Charge	Comment
CII				Middle Interlayer
CIU				Behind Bridging
CID	C	Ca	2	
XU				Pairing site
XD				

Table S4. Hydroxide ions.

String	Brick model	Stoichio	Charge	Comment
oDL oDR oUL oUR				Interlayer
oXU oXD	o	OH	-1	Bonded to XU/XD
oMDL oMDR oMUL oMUR				Bonded to dimmer Ca

Table S5. Water.

String	Brick model	Stoichio	Charge	Comment
wDR wDL wIL wIR wIR2 wUL wXD wXU w14 w15 w16	1,2,3, ...	H_2O	0	
wMDL wMUL wMDR wMDL				Bonded to dimmer Ca

A3-2   Overlap

When using the automatic mode of pyCSH no special care needs to be taken. When using the manual mode, one needs to avoid overlaps.

A3-3   Upper Chain

You can choose between option 1 and 2, and for each option you can only take one string for left, center and right.

Table S6. Possible configurations of the upper chain.

	Left	Center	Right
1	<L	SU SUo	<R
2	<Lo	CU	<Ro
	<L	Ø	<R

A3-4   Lower Chain

You can choose between option 1 and 2, and for each option you can only take one string for left, center and right.

Table S7. Possible configurations of the lower chain.

	Left	Center	Right
1	>L	SD SDo	>R
2	>Lo	CD	>Ro
	>L	Ø	>R

A3-5   Interlayer

Interlayers can have any combination of Interlayer Calcium, Hydroxyls, and Water, as long as overlaps are avoided. Below is the table which summarizes the overlap of different strings. Every row (1 to 9) lists strings from which only one can be presented in the unit cell.

Table S8. Overlaps in the interlayer.

	String 1	String 2	String 3	String 4
1	oMUL	wMUL		
2	oMDL	wMDL		
3	oMDR	wMDR	SD	SDo
4	oMUR	wMUR	SU	SUo
5	oDL	wDL		
6	oDR	wDR	SD	SDo
7	oUL	wUL	SU	SUo
8	oXD	wXD		
9	oXU	wXU		
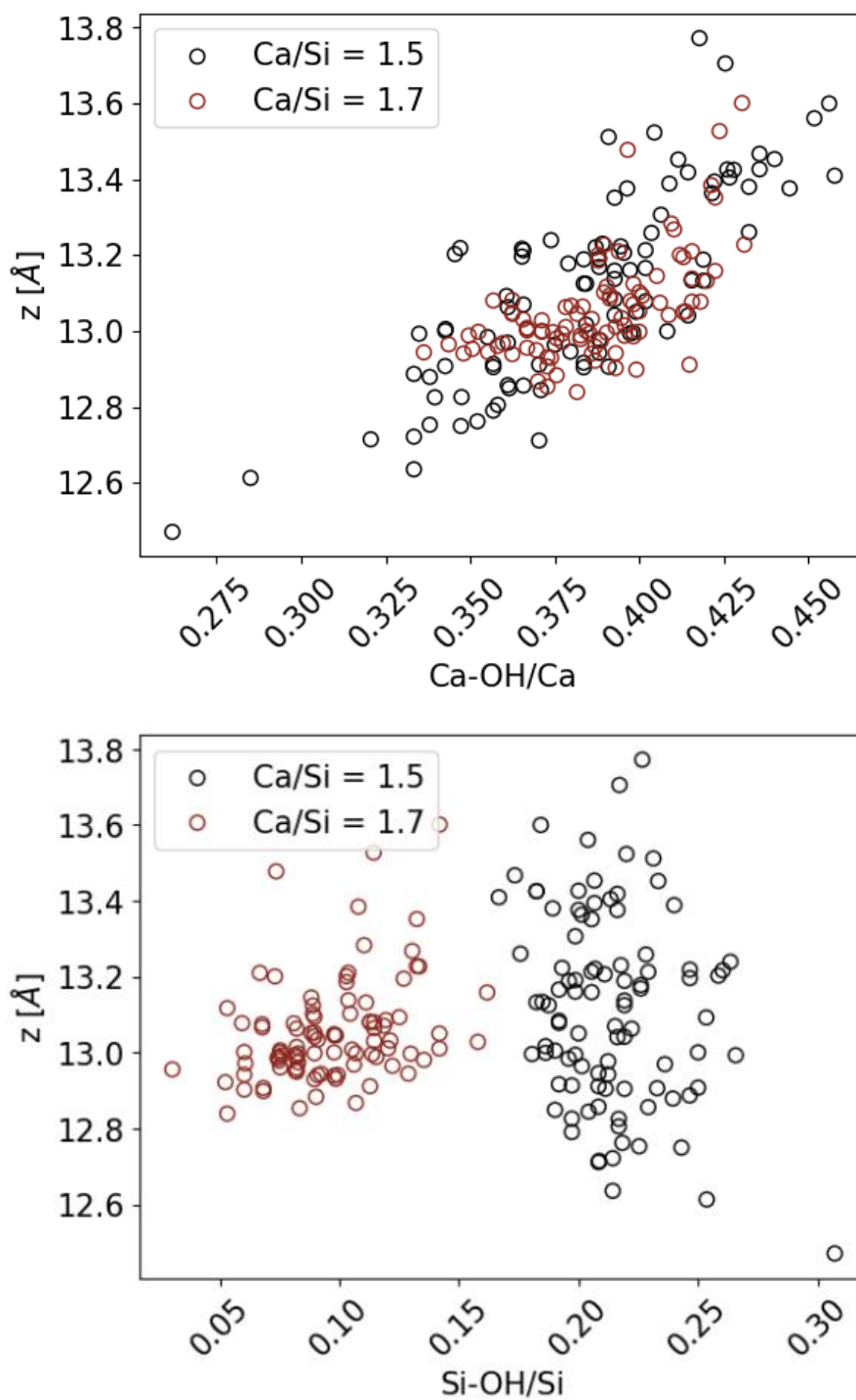
Figure S1. Layer spacing (z [Å]) as a function of Ca-OH/Ca and Si-OH/Si
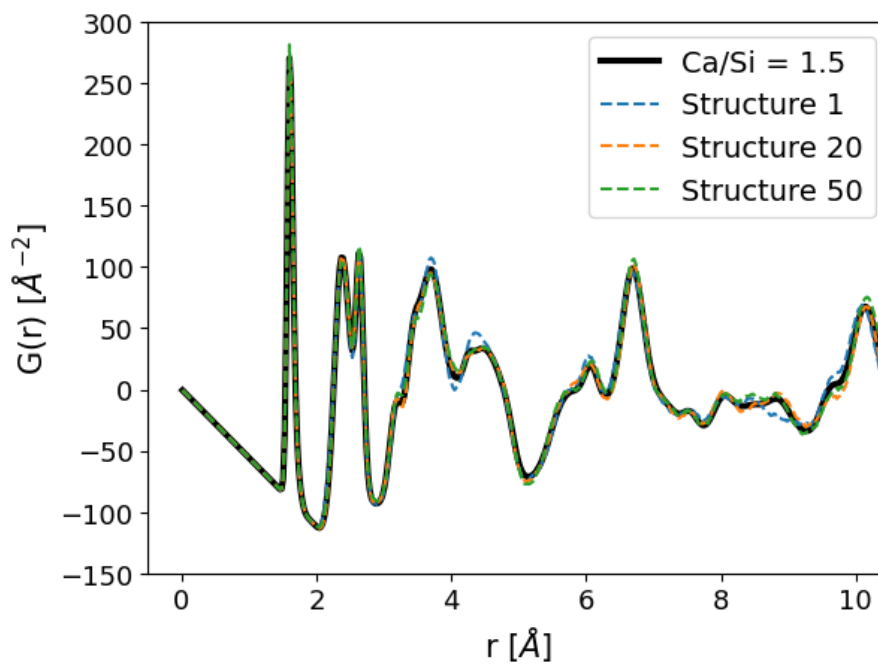
Figure S2. Comparison of three individual PDFs and the mean PDF for Ca/Si = 1.5
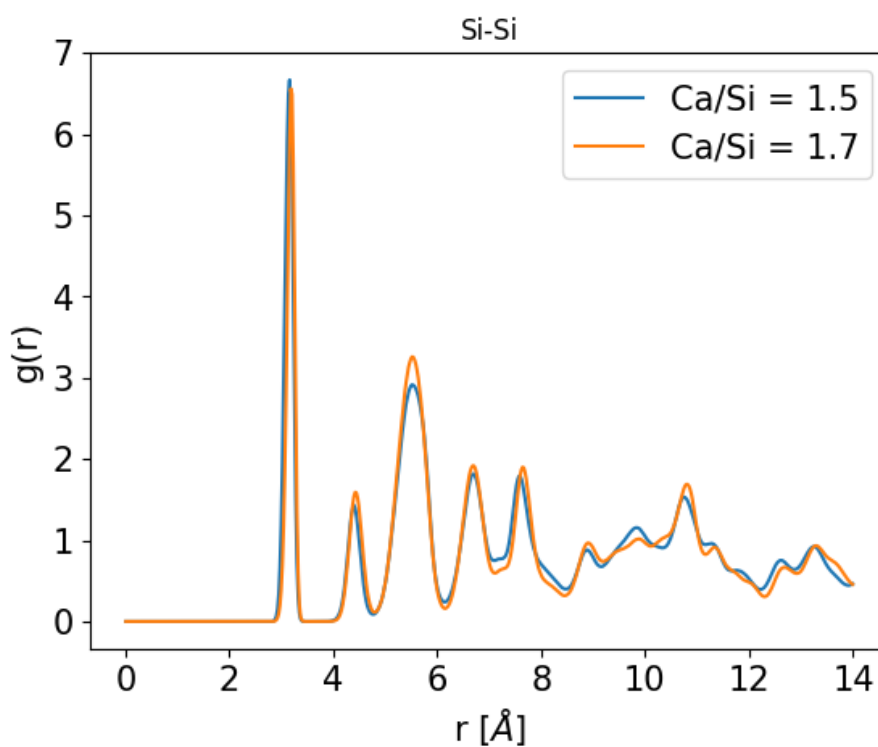
Figure S3. Mean Si-Si RDF for Ca/Si = 1.5 and 1.7.
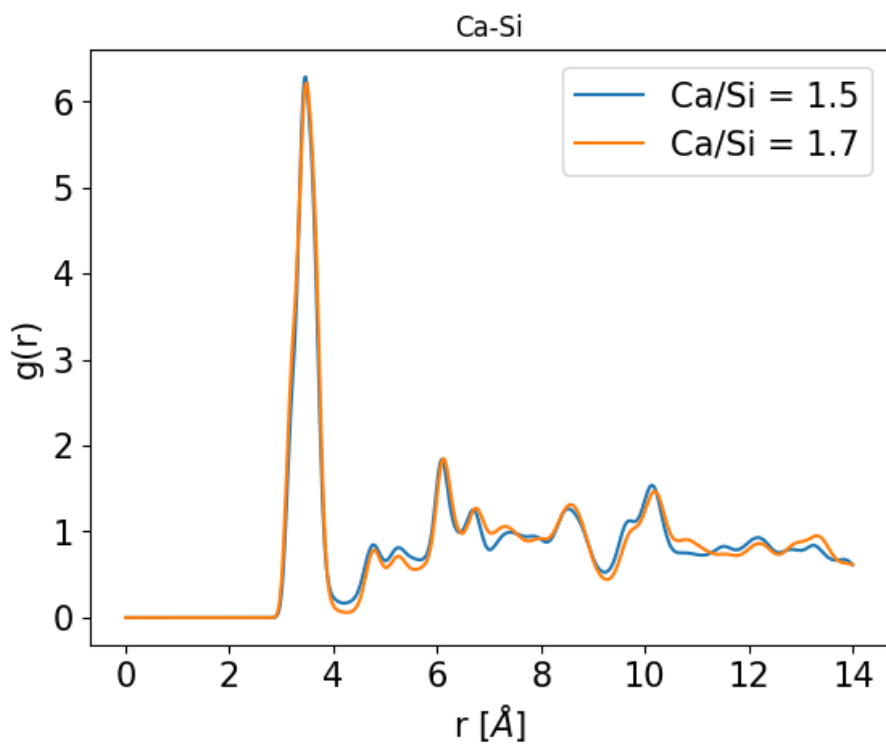
Figure S4. Mean Ca-Si RDF for Ca/Si = 1.5 and 1.7
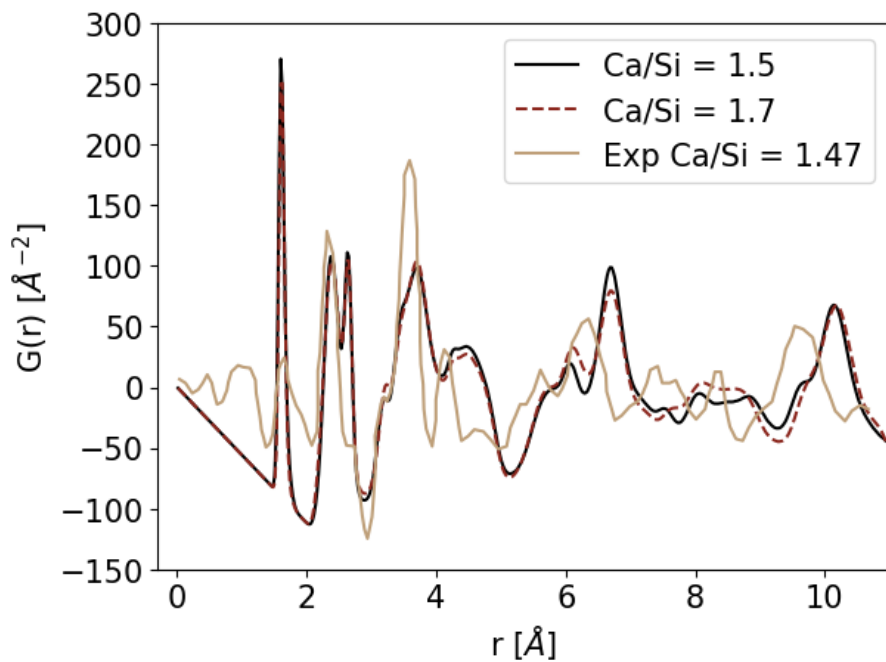
Figure S5. Comparison of experimental PDF (Ca/Si = 1.47) [130] with the calculated ones.
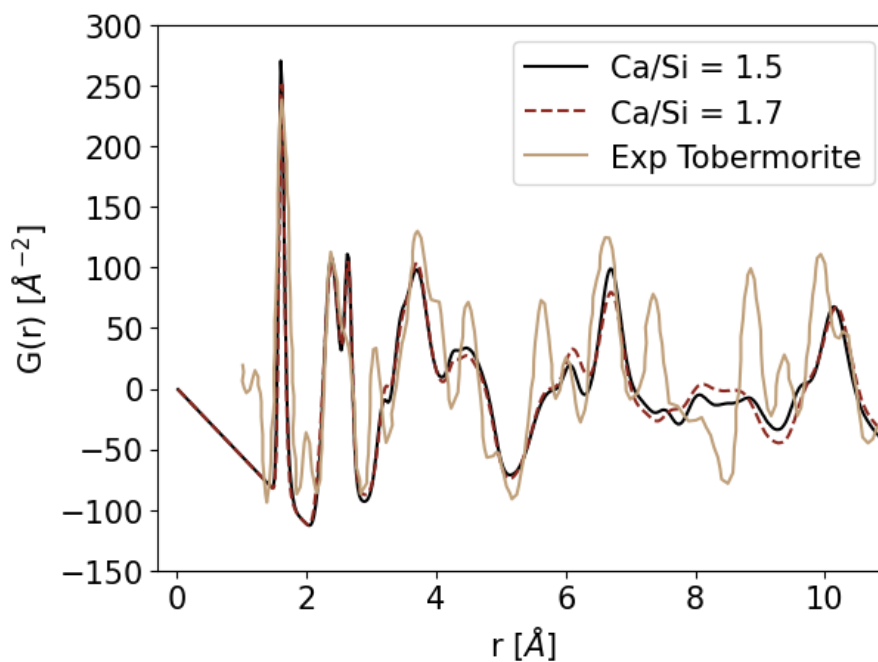
Figure S6. Comparison of experimental PDF (tobermorite) [130] with the calculated ones.

References

[1]   A. Kunhi Mohamed, S.C. Parker, P. Bowen, S. Galmarini, An atomistic building block description of C-S-H - Towards a realistic C-S-H model, Cem Concr Res. 107 (2018) 221–235. https://doi.org/10.1016/j.cemconres.2018.01.007.

[2]   S. Grangeon, A. Fernandez-Martinez, A. Baronnet, N. Marty, A. Poulain, E. Elkaïm, C. Roosz, S. Gaboreau, P. Henocq, F. Claret, Quantitative X-ray pair distribution function analysis of nanocrystalline calcium silicate hydrates: A contribution to the understanding of cement chemistry, J Appl Crystallogr. 50 (2017) 14–21. https://doi.org/10.1107/S1600576716017404.

A4   Supplementary Information – Chapter 4

Contribution Statement

The candidate gathered and arranged all the DFT and MD data, as well as produced all the figures of the atomic-level structure of Zn-C-S-H. The candidate wrote parts of the original draft.

A4-1   I. Composition of reactants during the synthesis of zinc-modified C-S-H

The initial composition of the reactants used to precipitate our C-S-H and zinc-modified C-S-H samples is described below in absolute amounts (mmol).

Table S1: Amounts (mmol) of reactants used to synthesize the zinc-modified C-S-H samples in this work.

(Zn:Si)i	Zinc nitrate hexahydrate (mmol)	Sodium metasilicate (mmol)	Calcium nitrate tetrahydrate (mmol)	Sample characterization
0	0	10	18	XRD, EDX, NMR
0.03	0.3	10	18	EDX
0.05	0.5	10	18	XRD
0.08	0.8	10	18	EDX
0.15	1.5	10	18	XRD, NMR
0.27	2.7	10	18	XRD
0.40	4	10	18	XRD, NMR
0.54	5.4	10	18	XRD

A4-2   II. Materials characterization

IIa. XRD

X-ray diffraction data were recorded with a Bruker Discovery X-Ray diffractometer equipped with a double bounced monochromatic CuK alpha radiation source ($\lambda = 1.54$ Å). Experiments were performed for 30 min to determine the presence of possible secondary phases (i.e. portlandite).
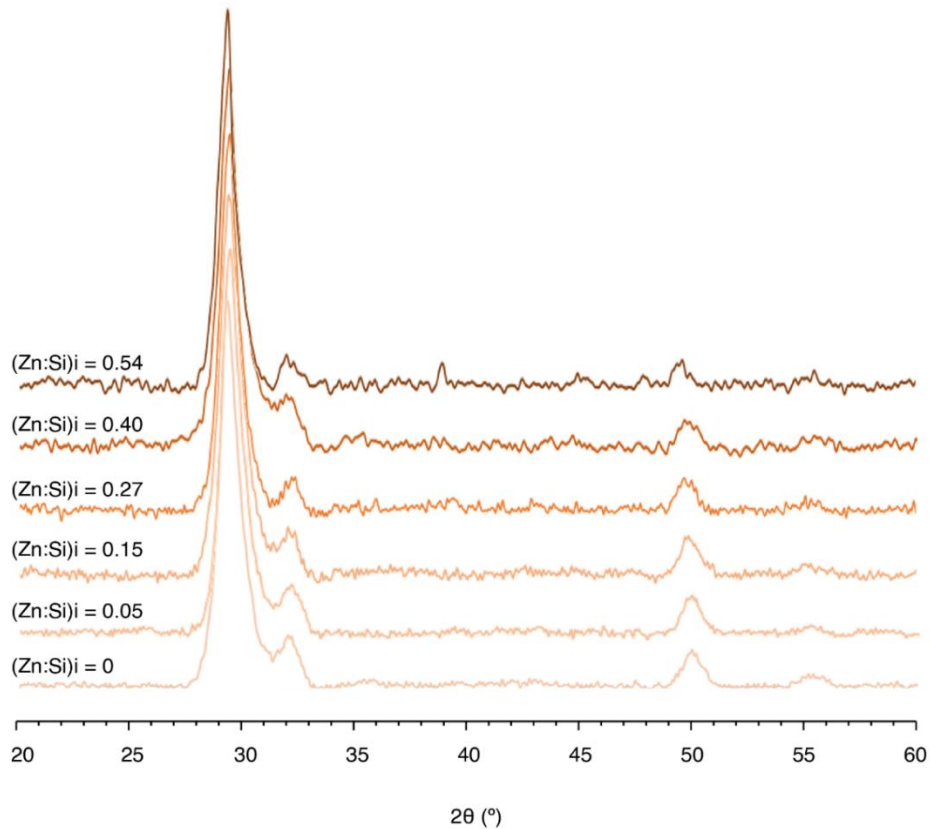
Figure S1: XRD data of zinc-modified C-S-H samples with $(Zn:Si)_i$ of 0, 0.05, 0.15, 0.27, 0.40 and 0.54.

Only the intrinsic peaks of C-S-H present at 29.4, 32.1 and 50.1° [1] and signs of $CaCO_3$ at 38.9° [2], due to carbonation effects, are observed. There are no signs of portlandite or ettringite. Thus, results from XRD show that the rapid precipitation method used for the synthesis of zinc modified C-S-H yields single-phase C-S-H [3].

IIb. TEM

A FEI Tecnai Osiris analytical TEM instrument, operating with a 200-kV high brightness FEG electron gun and at a point resolution of 0.24 nm, was used to analyse the morphology of zinc-modified C-S-H. Figure S2 shows TEM micrographs of conventional C-S-H (Figures S2A and S2B) and zinc modified C-S-H (Figure S2C) samples that show, consistently with literature, a nanofoil morphology, typical for synthetic high Ca:Si ratio C-S-H. In figures S2B and S2C agglomerates from conventional and zinc modified C-S-H with $(Zn:Si)_i$ of 0.15 can be seen, respectively. There were no appreciable differences in morphology between samples with increasing zinc content (here only samples with $(Zn:Si)_i$ of 0 and 0.15 are shown).
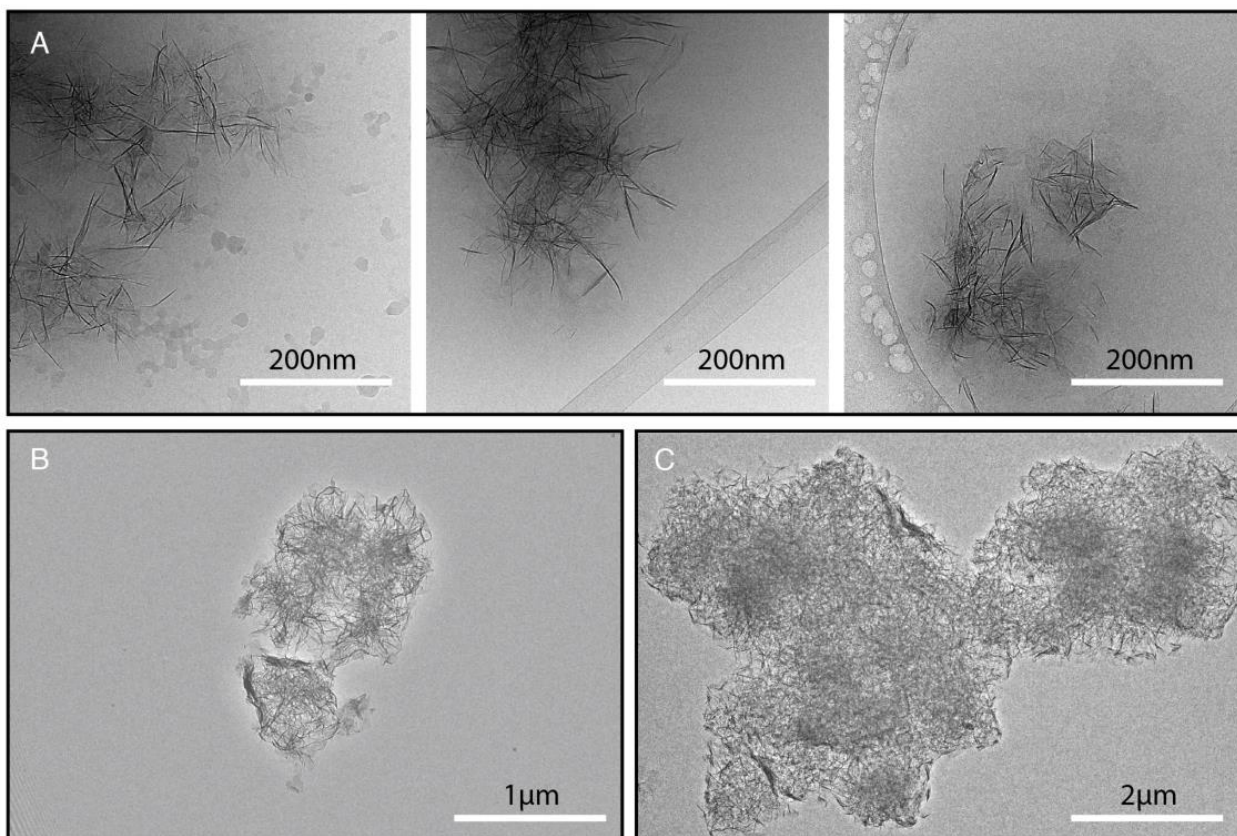
Figure S2: TEM micrographs of synthetic A) conventional C-S-H small particles, B) a conventional C-S-H agglomerate and C) a zinc-modified C-S-H ($(Zn:Si)_i$ of 0.15) agglomerate.

IIc. Supernatant ICP

ICP was carried on the supernatant of samples with $(Zn:Si)_i$ ratios of 0, 0.15 and 0.40 in order to verify the amount of zinc that remained in the pore solution after precipitation. The concentration of zinc in the remaining pore solution allows for the calculation of the amount of zinc incorporated into the C-S-H structure. The mass of zinc nitrate hexahydrate before synthesis is known in each case and can be used to calculate the initial concentration of zinc prior to synthesis. The initial concentration of zinc is then compared to the final concentration of zinc in the pore solution to obtain the molar percentage of zinc which is incorporated in the C-S-H structure. ICP experiments on the supernatant were conducted on several samples with different $(Zn:Si)_i$, always giving a molar percentage of final zinc in the pore solution of 1-2% and, consequently, an incorporation percentage of 98-99%. An example of this calculation is given in equation (1) for the sample with $(Zn:Si)_i$ of 0.40 and results comparing the percentage of zinc incorporation and the $(Zn:Si)_i$ is shown in Figure S3.

Table S2: Supernatant ICP results from samples with (Zn:Si)$_i$ of 0, 0.15 and 0.40.

	Ca		Si		Zn	
	Conc [mmol/L]	RSD$^{\#}$ [%]	Conc [mmol/L]	RSD$^{\#}$ [%]	Conc [mmol/L]	RSD$^{\#}$ [%]
0	11.05	0.40	0.04	0.07	0.00	4.528
0.15	11.87	1.22	0.03	0.38	0.03	0.799
0.40	9.16	1.41	0.04	0.38	0.12	0.209

$^{\#}$Relative Standard Deviation

$$1169 \, mg \, Zn(NO_3)_2 \cdot \frac{1 \, mol}{297.5 \, g} \cdot \frac{1}{0.405 \, L} = 9.70 \frac{mmol}{L} \; \rightarrow \frac{0.12}{9.70} = 1.24\% \qquad (1)$$
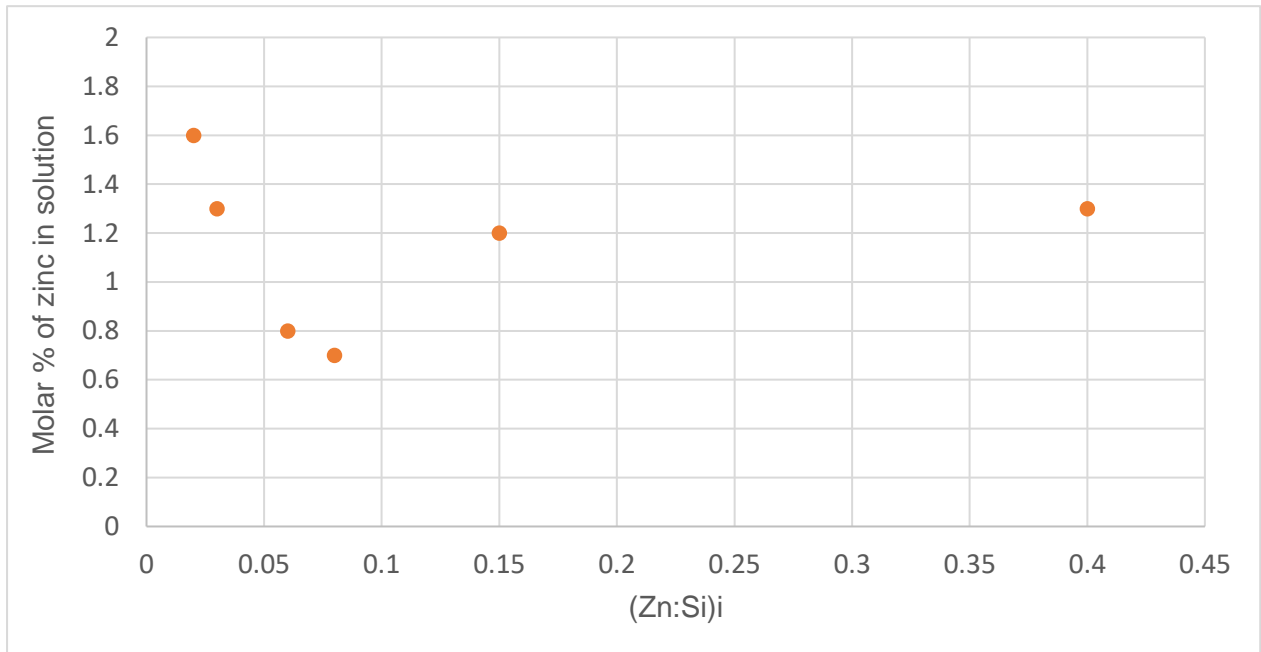
Figure S3: Supernatant ICP analysis showing the molar percentage of zinc that remains in solution after precipitation and collection of the solid. Conventional C-S-H with (Zn:Si)$_i$ of 0 is not shown since the remaining zinc in solution is just null.

A4-3 III. DFT-relaxed energies

Table S3 shows the energies of all the geometry optimized zinc modified C-S-H brick structures. The atomic coordinate files and the corresponding DFT files can be found in the additional SI material (along with the raw NMR data and LAMMPS input files) which are indicated with their Ca:Si ratio (folder names) and structure indices (file suffix).

Table S3: DFT relaxed energies of all the brick structures studied.

Ca:Si	Structure index	Zn-species	Zn position	Total Energy [eV]	Relative Energy [eV]*
1.2	1	$ZnO_2(OH)_2$	Q2b	-59254.31	0
1.2	3	ZnO_4	Q1	-59251.05	3.26
1.4	1	$Zn(OH)_4$	Q2b	-69429.74	0
1.4	2	$ZnO_2(OH)_2$	Q2p	-69430.01	-0.27
1.4	3	$Zn(OH)_4$	Q2p	-69429.06	0.68
1.67	1	$ZnO_2(OH)_2$	Q2b	-66444.38	0.81
1.67	2	$ZnO_2(OH).H_2O$	Q2b	-66444.11	1.08
1.67	3	$ZnO_2(OH)_3$	Q2b	-66443.97	1.22
1.67	4	$ZnO_2(OH)_2$	Q2b	-66445.19	0
1.67	5	$ZnO_2(OH)_2$	Q2b	-66445.06	0.13
1.67	7	$ZnO_2(OH)_2$	Q2p	-66442.88	2.31
1.67	8	$ZnO_3(OH)$	Q2p	-66445.06	0.13
1.67	9	$ZnO_3(OH)$	Q1	-66442.88	2.31
1.67	10	$ZnO_2(OH)_2$	Q1	-66443.15	2.04
1.67	11	$ZnO(OH)_3$	Q1	-66443.83	1.36
1.67	12	$ZnO_2(OH)_2$	Q2p	-66442.61	2.58
1.67	13	$ZnO_2(OH)_2$	Q2p	-66442.34	2.85
1.67	14	$ZnO_2(OH)_2$	Q1	-66444.52	0.67
1.67	15	$ZnO(OH)_3$	Q1	-66443.83	1.36
1.67	16	$ZnO(OH)_3$	Q1	-66443.83	1.36
1.67	17	$ZnO_2(OH)_2$	Q2p	-66442.34	2.85
1.67-HW	1	$ZnO_2(OH)_2$	Q2b	-70041.73	1.49
1.67-HW	2	$ZnO_2(OH)_2$	Q2b	-70043.22	0
1.67-HW	4	$ZnO_2(OH)_2$	Q2b	-70043.09	0.13
1.67-HW	5	$ZnO_2(OH)_2$	Q2p	-70040.77	2.45
1.67-HW	7	$ZnO_2(OH)_2$	Q2p	-70041.73	1.49

1.67-HW	8	$ZnO_2(OH)_2$	Q2p	-70041.32	1.9
1.67-HW	9	$ZnO(OH)_3$	Q1	-70042.41	0.81
1.67-HW	10	$ZnO(OH)_3$	Q1	-70043.09	0.13
1.67-HW	11	$ZnO(OH)_3$	Q1	-70041.73	1.49
1.67-HW	13	$ZnO(OH)_3$	Q1	-70042.13	1.09
1.67-HW	14	$ZnO_2(OH)_2$	Int	-70042.81	0.41
1.67-HW	15	$ZnO(OH)_2$	Int	-70042.81	0.41
1.67-HW	16	$ZnO(OH)_3$	Int	-70042.27	0.95
1.67-HW	17	$ZnO(OH)_3$	Q1	-70041.99	1.23
1.67-HW	18	$ZnO_2(OH)_2$	Q1	-70042.41	0.81
1.67-HW	19	$ZnO(OH)_3$	Q1	-70042.32	0.9
1.67-HW	20	$ZnO(OH)_3$	Q1	-70040.91	2.31
1.67-HW	21	$ZnO_2(OH)_2$	Q1	-70042.36	0.86
1.67-HW	22	$ZnO_2(OH).H_2O$	Int	-70043.22	0
1.75	1	$ZnO_2(OH)_2+ZnO_2(OH)_2$	Q2p+Q2p	-75130.22	0
1.75	2	$ZnO_2(OH)_2+ZnO_2(OH)_2$	Q2p+Q2p	-75128.81	1.41
1.75	3	$ZnO_2(OH)_2+ZnO_2(OH)_2$	Q2p+q2p	-75128.94	1.28
1.75	4	$ZnO_2(OH)_2+ZnO_2(OH)_2$	Q2b+Q1	-75129.97	0.25
1.75	5	$ZnO_2(OH)_2+ZnO_2(OH)_2$	Q2b+Q1	-75130.07	0.15
1.75	6	$ZnO_2(OH)_2+ZnO_2(OH)_2$	Q1+Q1	-75129.17	1.05
1.75	7	$ZnO_2(OH)_2+ZnO_2(OH)_2$	Q1+Q1	-75127.45	2.77
1.75	8	$ZnO_2(OH)_2+ZnO_2(OH)_2$	Q1+Q1	-75128.35	1.87
1.88	1	$ZnO_2(OH)_2+ZnO_2(OH)_2$	Q2p+Q2p	-76917.26	1.04
1.88	2	$ZnO_2(OH)_2+ZnO_2(OH)_2$	Q2p+Q2p	-76917.27	1.03
1.88	3	$ZnO_2(OH)_2+ZnO_2(OH)_2$	Q2b+Q2p	-76918.33	0
1.88	4	$ZnO_2(OH)_2+ZnO_2(OH)_2$	Q2b+Q2p	-76916.83	1.47
1.88	5	$ZnO_2(OH)_2+ZnO_2(OH)_2$	Q2b+Q2p	-76918.13	0.17
1.88	6	$ZnO_2(OH)_2+ZnO_2(OH)_2$	Q2b+Q1	-76916.56	1.74
1.88	7	$ZnO_2(OH)_2+ZnO_2(OH)_2$	Q2b+Q1	-76917.37	0.93
1.88	8	$ZnO_2(OH)_2+ZnO_2(OH)_2$	Q2b+Q1	-76917.91	0.39
1.88	9	$ZnO_2(OH)_2+ZnO_2(OH)_2$	Q2b+Q1	-76918.18	0.12

1.88	10	$ZnO_2(OH)_2$+$ZnO_2(OH)_2$	Q1+Q2p	-76917.5	0.8
1.88	11	$ZnO_2(OH)_2$+$ZnO_2(OH)_3$	Q2p+Q2p	-76917.37	0.93
1.88	12	$ZnO_2(OH)_2$+$ZnO_2(OH)_2$	Q2b+Q1	-76915.92	2.38
1.88	13	$ZnO_2(OH)_2$+$ZnO_2(OH)_2$	Q2b+Q1	-76917.91	0.39
1.88	14	$ZnO(OH)_3$+$ZnO(OH)_3$	Q2p+Q2p	-76916.55	1.75
1.88	15	$ZnO(OH)_3$+$ZnO(OH)_3$	Q2p+q2p	-76917.5	0.8
2	1	$ZnO_2(OH)_2$	Q2b	-70056.56	0.13
2	2	$ZnO_2(OH)_2$	Q2b	-70056.69	0.00
2	3	$ZnO_2(OH)_2$	Q2b	-70056.56	0.13
2	4	$ZnO_2(OH).H_2O$	Q2b	-70056.42	0.27
2	5	$ZnO_2(OH).H_2O$	Q2b	-70055.47	1.22
2	6	$ZnO_2(OH)_2$	Q2b	-70055.74	0.95
2	7	$ZnO_2(OH)_2$	Q2b	-70055.74	0.95
2	8	$ZnO_2(OH)_2$	Q2p	-70055.33	1.36
2	9	$ZnO_3(OH)$	Q2p	-70055.2	1.49
2	10	$ZnO_3(OH)$	Q2p	-70055.74	0.95
2	11	$ZnO_2(OH)_2$	Q2p	-70056.01	0.68
2	12	ZnO_4	Q2p	-70054.11	2.58
2	13	$ZnO_3(OH)$	Q1	-70054.92	1.77
2	15	$ZnO_3(OH)$	Q1	-70055.06	1.63
2	16	$ZnO(OH)_3$	Q1	-70056.28	0.41
2	17	$ZnO_2(OH)_2$	Int	-70056.15	0.54
2	18	$ZnO_2(OH)_2$	Int	-70057.24	-0.55
2	19	$ZnO_2(OH)_2$	Int	-70055.47	1.22
2	20	$ZnO_2(OH)_2$	Q1	-70056.15	0.54
2	21	$ZnO(OH)_3$	Q1	-70056.69	0.00
2	22	$ZnO(OH)_3$	Q1	-70055.57	1.12
2	23	$ZnO(OH)_3$	Q1	-70054.24	2.45
2.25	1	$ZnO_2(OH)_2$	Q2b	-40841.31	0.59
2.25	2	$ZnO_2(OH)_2$	Q2b	-40841.45	0.45
2.25	3	$ZnO_2(OH)_2$	Q2b	-40841.86	0.04
2.25	4	$ZnO(OH)_3$	Int	-40842.54	-0.64
2.25	5	$ZnO(OH)_3$	Int	-40841.99	-0.09
2.25	6	$ZnO_3(OH)$	Q2p	-40840.77	1.13
2.25	7	$ZnO_2(OH)_2$	Q2p	-40840.77	1.13
2.25	8	ZnO_3	Q2p	-40840.9	1
2.25	10	$ZnO_2(OH)_2$	Q2p	-40841.04	0.86
2.25	11	$ZnO_2(OH)_2$	Q2p	-40840.9	1
2.25	12	$ZnO_2(OH)_2$	Q1	-40840.86	1.04
2.25	15	$ZnO_2(OH)_2$	Int	-40841.51	0.39
2.25	16	$ZnO_2(OH)_2$	Int	-40840.65	1.25

*The relative energies are calculated with respect to the lowest energy structure where zinc substitutes for a $Q^{(2b)}$ site, in each set corresponding to a specific Ca:Si ratio.
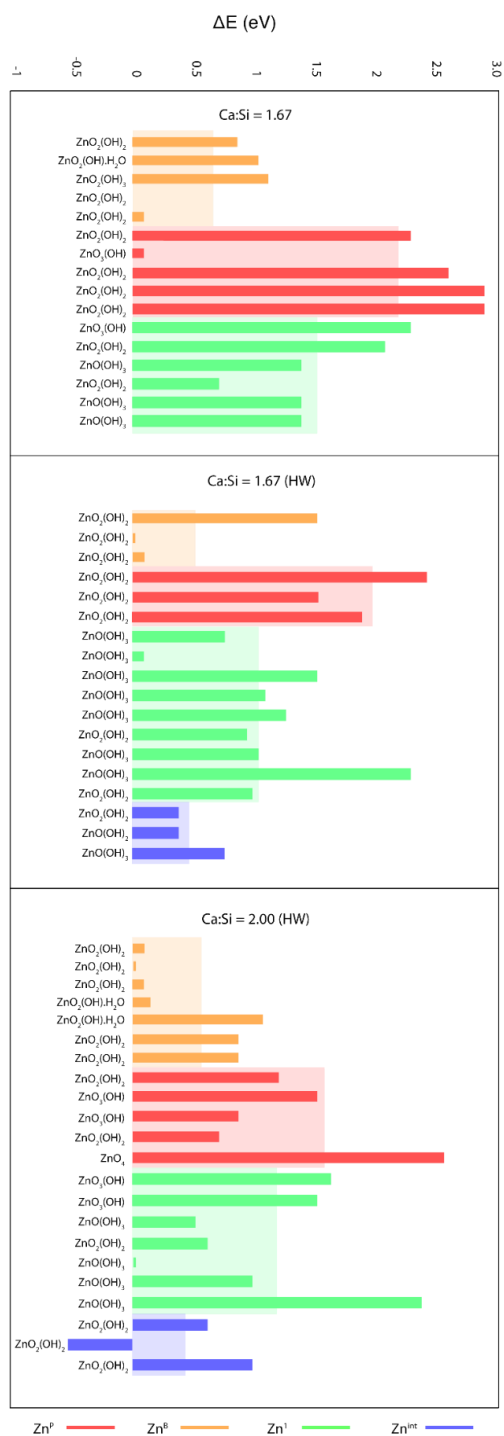
Figure S4: Relative DFT calculated energies of zinc-modified C-S-H structures according to each substitution site with different Ca:Si ratios (1.67 and 2.0) and interlayer water amounts. The energies in each set, corresponding to a specific Ca:Si ratio, are normalized ($\Delta E = 0$ eV) with respect to the lowest energy Zn^B structure where zinc is substituted at the bridging site. Nomenclature: Zn^B = zinc in the $Q^{(2b)}$ site, Zn^P = zinc in the $Q^{(2p)}$ site, Zn^1 = zinc in the $Q^{(1)}$ site, Zn^{Int} = zinc on top of a $Q^{(1)}$-$Q^{(1)}$ dimer site, HW = High Water content. All structures are labeled with their corresponding zinc species which may coordinate to hydroxides or water.

A4-4 IV. DFT-based chemical shift calculations

Figure S5 shows the DFT-calculated ^{29}Si chemical shifts from selected zinc modified C-S-H brick structures. The computed chemical shifts for the different Q species are compared with the DFT-calculated energies of the structures and NMR experimental data to verify or discard the different species depicted here. As stated in the main text, all structural units where zinc substitutes for a $Q^{(2p)}$ site were discarded either due to unrealistically higher energies or due to the fact that correlations regarding the Q species that would arise if zinc was substituting for a paring site are absent in INADEQUATE spectra.
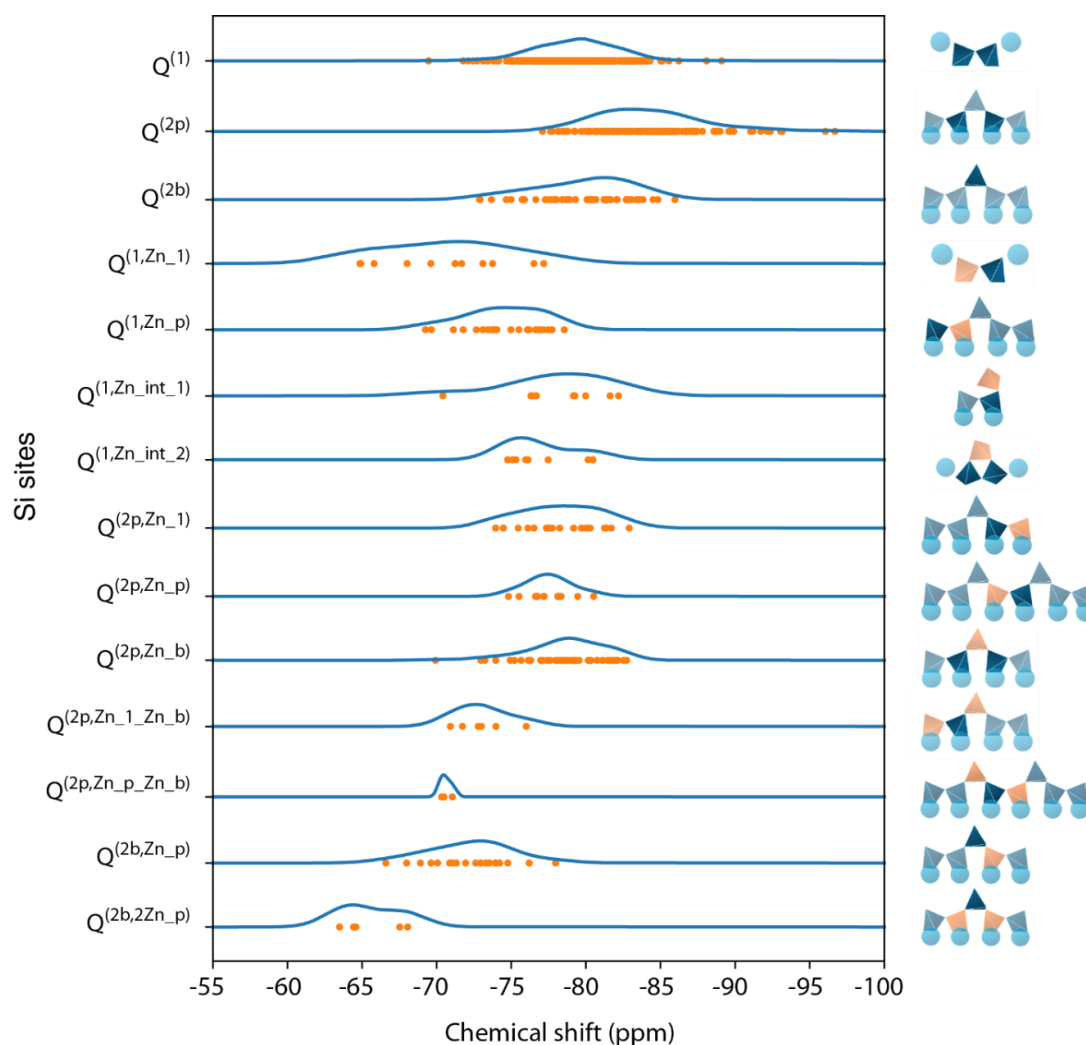
Figure S5: DFT-based calculated chemical shifts for a set of selected zinc-modified C-S-H brick structures which include zinc substitutions for $Q^{(1)}$, $Q^{(2b)}$ and $Q^{(2p)}$ sites. Individual computed chemical shift values are represented as orange dots. In each line, the chemical shift values in orange are obtained for the silicon sites depicted in dark blue.

A4-5 V. DNP enhanced NMR experiments

Va.   Experimental NMR parameters

All spectral processing was performed with TopSpin version 4.0.8 and CSA fits were carried out with ssNake [4]. All experiments were carried out at 9.4 T, 100 K and at a MAS rate of 8 kHz, unless stated otherwise. The NMR parameters of each set of experiments are shown in Tables S4, S5 and S6.

Table S4: NMR parameters for ^{29}Si multiCP experiments

(Zn:Si)$_i$	0	0.15	0.4
Magnetic field (T)	9.4	9.4	9.4
MAS rate (kHz)	8	8	8
^{1}H pulse/dec RF (kHz)	71	71	71
^{29}Si pulse RF (kHz)	71	71	71
^{29}Si CP contact RF (kHz)	50	42	31
CP contact time (ms)	6	4	8
Recycle delay (s)	3	2.5	3
Number of CP periods (n)	11	5	8
Delay between CP periods (s)		5	
Size of FID	3978		
Size of real spectrum	65536		
Spectral width (ppm)	2506.3		
εDNP	41	27	20
Scans	16	16	16
Figure	3A	3A	3A
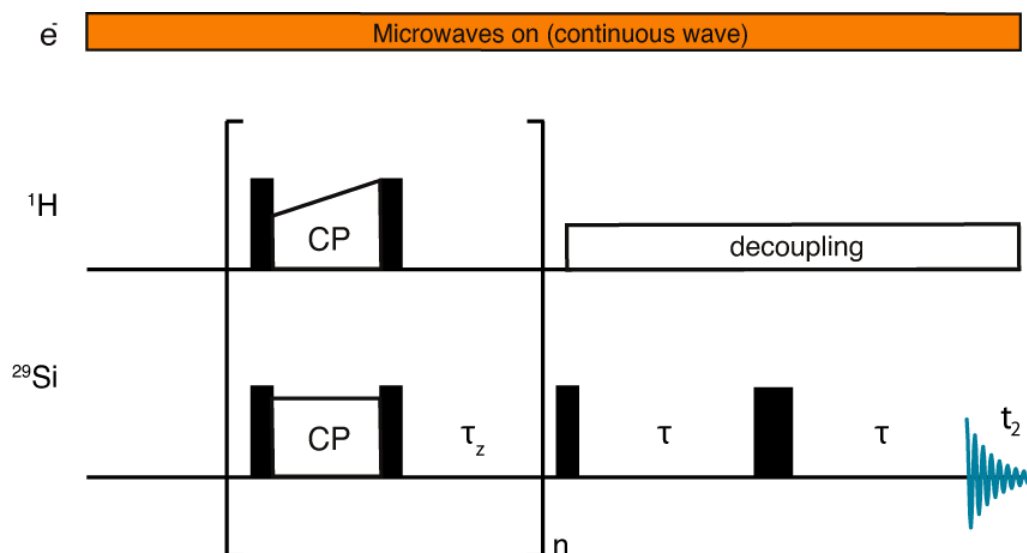
Figure S6: Pulse sequence used for the multi-CPMAS experiments.

Table S5: NMR parameters for ^{29}Si-^{29}Si INADEQUATE experiments

(Zn:Si)$_i$	0	0.15	0.4
Magnetic field (T)	9.4	9.4	9.4
MAS rate (kHz)	8	8	8
^{1}H pulse/dec RF (kHz)	64	64	64
^{29}Si pulse RF (kHz)	80	80	80
^{29}Si CP contact RF (kHz)	42	31	42
CP contact time (ms)	6	5	9
Recycle delay (s)	3.75	2.86	1.5
INADEQUATE tau periods (ms)	25	25	25
Size of FID (F1)	96		
Size of FID (F2)	2048		
Size of real spectrum (F1)	1024		
Size of real spectrum (F2)	16384		
Acquisition mode	States-TPPI		
Spectral width F1 (ppm)	100.5	100.5	100.6
Spectral width F2 (ppm)	628.5	628.4	1256.9
Scans	128	256	1408
Figure	S8A	S8B	3C, S8C
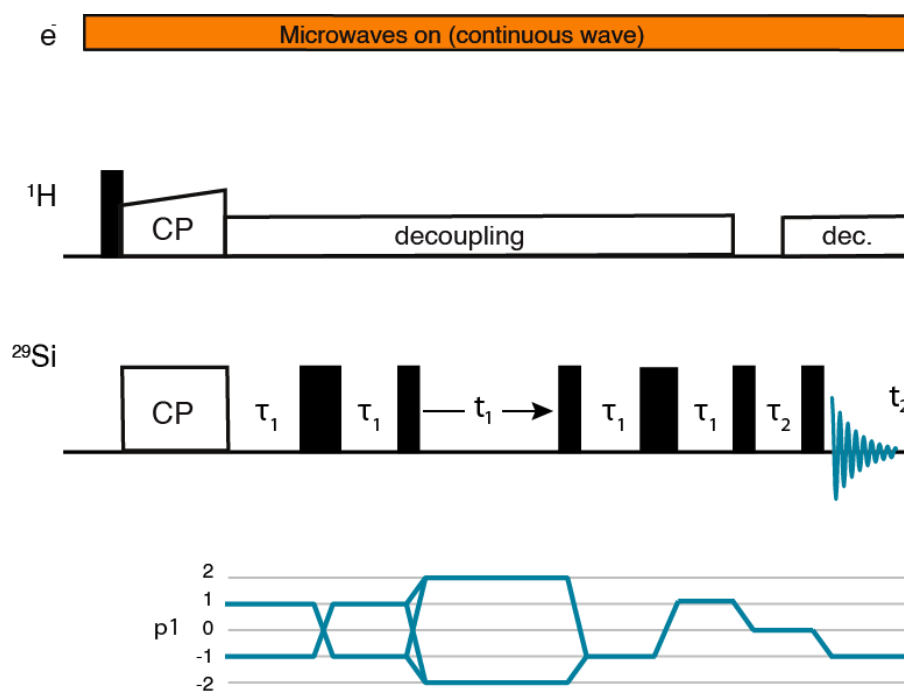
Figure S7: Pulse sequence and coherence pathway of the INADEQUATE experiments.

Table S6: NMR parameters for ^{29}Si-^{29}Si EXSY and SUPER experiments

Experiment	EXSY	SUPER
$(Zn{:}Si)_i$	0.4	0.4
Magnetic field (T)	9.4	9.4
MAS rate (kHz)	5	5
^{1}H pulse/dec RF (kHz)	100	100
^{29}Si pulse RF (kHz)	69	69
^{29}Si CP contact RF (kHz)	72	72
CP contact time (ms)	3.5	3.5
^{29}Si CSA recoupling RF (kHz)	N/A	61
^{1}H cw decoupling during delays in CSA recoupling (kHz)	N/A	30
Recycle delay (s)	1.5	1.5
Size of FID (F1)	256	48
Size of FID (F2)	4096	4096

Size of real spectrum F1	256	1024
Size of real spectrum F2	4096	4096
Spectral width F1 (ppm)	62.7	62.7
Spectral width F2 (ppm)	1253.2	1253.2
Scans	12	256
Figure	S9, S10	S11

Vb. Through-bond analysis

2D INADEQUATE spectra were recorded for conventional and zinc-modified C-S-H samples with different $(Zn:Si)_i$ to establish ^{29}Si-^{29}Si though-bond connectivities. The 2D experimental spectra were initially sheared to produce a COSY-like representation and fit to six different 2D Gaussian distributions centred at the expected $Q^{(1)}$-$Q^{(1)}$, $Q^{(1)}$-$Q^{(2p)}$, $Q^{(2p)}$-$Q^{(1)}$, $Q^{(2p)}$-$Q^{(2b)}$, $Q^{(2b)}$-$Q^{(2p)}$ and $Q^{(2p)}$-$Q^{(2p)}$ frequency pairs, using Topspin v4.0.8.

Figure S8 shows three INADEQUATE experiments which correspond to C-S-H samples with $(Zn:Si)_i$ ratios of 0, 0.15 and 0.40, respectively. Figure S8A shows the expected connectivities between $Q^{(1)}$-$Q^{(1)}$, $Q^{(2p)}$-$Q^{(1)}$, $Q^{(2p)}$-$Q^{(2b)}$ and $Q^{(2p)}$-$Q^{(2p)}$ species. On the other hand, consistentl with the geometry of the C-S-H silicate chains, correlations between $Q^{(2b)}$-$Q^{(1)}$ or $Q^{(2b)}$-$Q^{(2b)}$ species are not observed. Figure S8B and S8C show the same correlations whereas no signals corresponding to $Q^{(1,Zn)}$ connectivities are detected. This is consistent with our hypothesis that this species is not bonded to other silicate species, but only to a zincate species as a Si-O-Zn dimer.
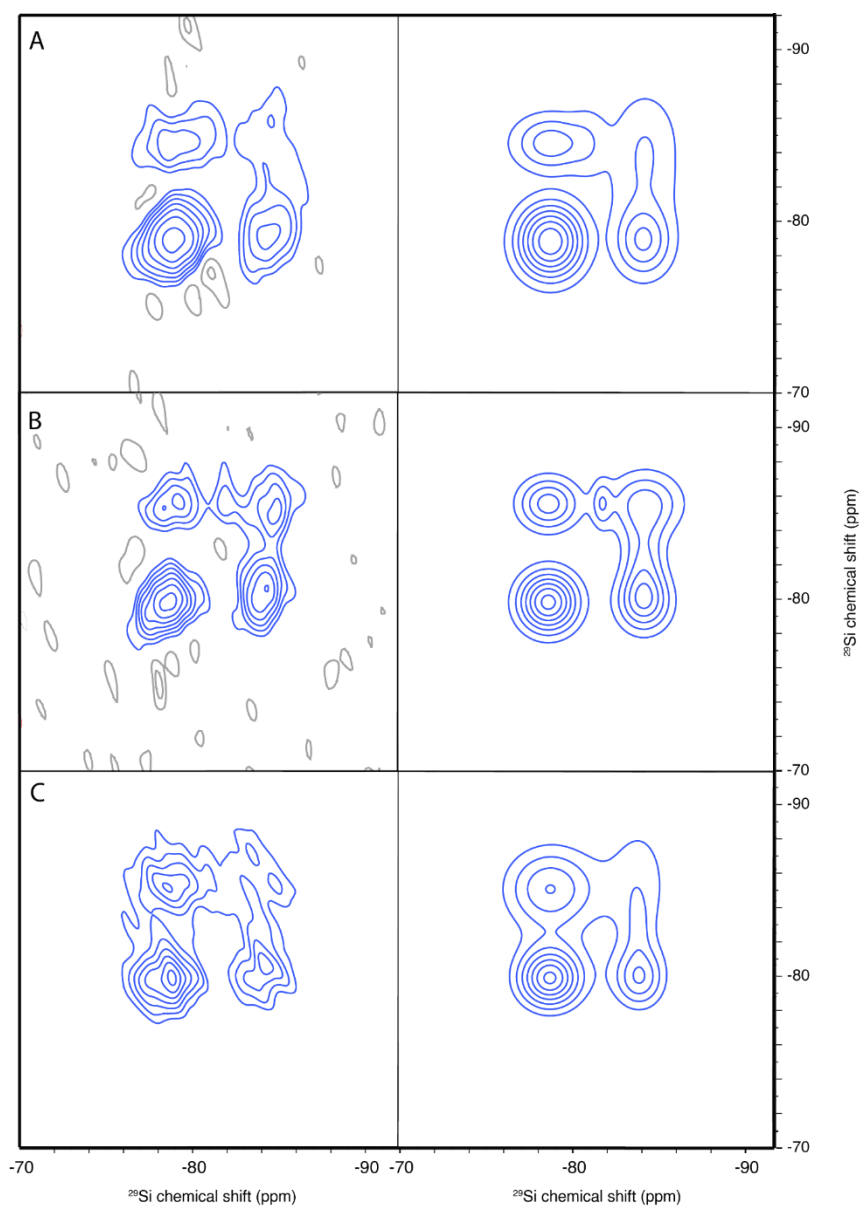
Figure S8: INADEQUATE spectra for C-S-H samples with (Zn:Si)$_i$ of A) 0, B) 0.15 and C) 0.40 with a COSY-type representation and their respective 2D deconvolutions.

Vc. Through-space analysis

Exchange spectroscopy (EXSY) experiments were carried out at a MAS rate of 5 kHz for a zinc-modified C-S-H sample with (Zn:Si)$_i$ of 0.40. Figure S9 shows a series of EXSY experiments with increasing mixing times: 500 μs, 0.1 s, 100 s and 150 s.
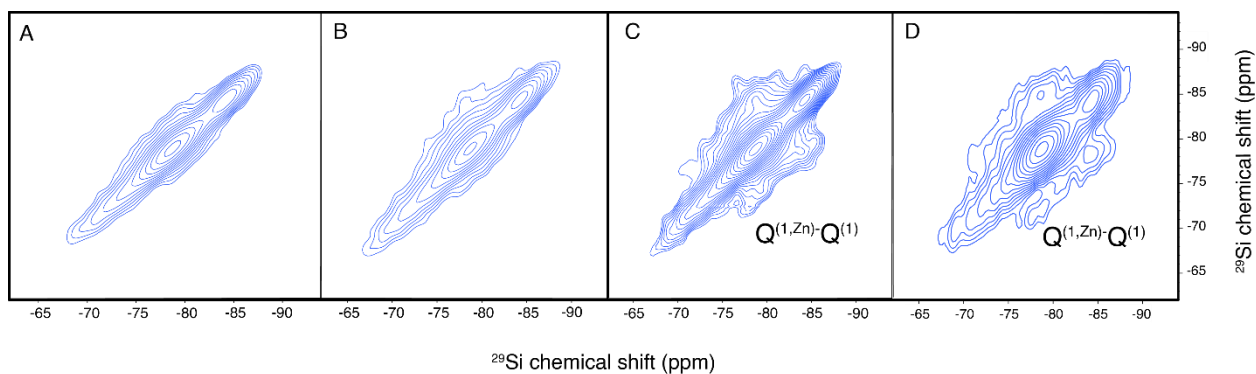
Figure S9: 2D ^{29}Si EXSY spectra from a zinc-modified C-S-H sample with $(Zn:Si)_i$ of 0.40 acquired with a mixing time of A) 500 µs, B) 0.1 s, C) 100 s, and D) 150 s.

At mixing times of 100 s and 150 s (Figure S9C, S9D) a correlation between ^{29}Si species at –78.9ppm and –72ppm can be observed which suggests that the new ^{29}Si species at –72ppm is in close proximity and therefore part of the zinc-modified C-S-H structure, even if not directly bonded to another silicate species. This further confirms the assignment of this species as a $Q^{(1,Zn)}$ Zn-Si pair. Additionally, Figure S10 shows the changes in the cross-peak intensity with increasing mixing time.
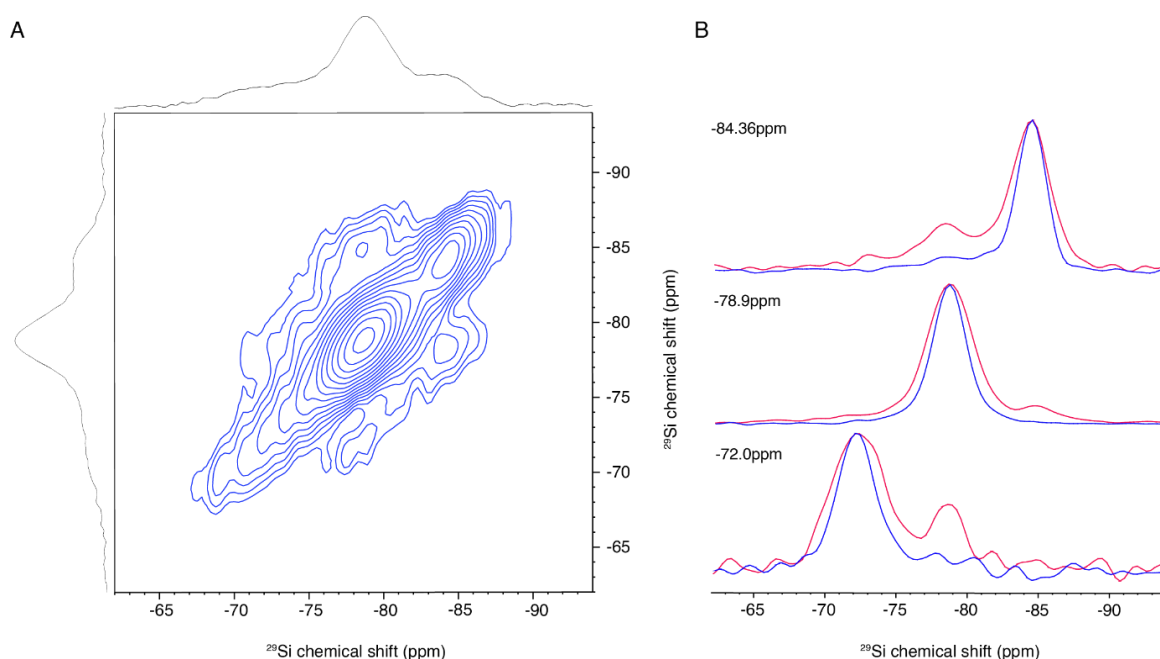
Figure S10: A) DNP-enhanced 2D ^{29}Si EXSY spectrum of a zinc-modified C-S-H sample with $(Zn:Si)_i$ of 0.40 at a mixing time of 150 s and B) 1D horizontal cross-sections extracted at –72 ppm, –78.9 ppm and –84.4 ppm and at mixing times of 150 (red) and 0.1 s (blue).

Vd. Chemical shift anisotropy analysis

A DNP-enhanced ^{29}Si CP-SUPER experiment [5] was performed on a zinc-modified C-S-H sample with (Zn:Si)$_i$ of 0.40 (Figure S11). The F1 spectral width was scaled using an anisotropic chemical shift scaling factor of 0.155 and the spectrum was then sheared parallel to F1 with a shearing factor of 3.3 (0.512/0.155, where 0.512 is the shearing factor to equalize the isotropic shift scaling factor with the anisotropic shift scaling factor) [5]. Columns were extracted at the isotropic chemical shifts of interest: -72 ppm (corresponding to Q$^{(1,Zn)}$ species), -78.9 ppm (corresponding to Q$^{(1)}$ and Q$^{(2p,Zn)}$ species), and -84.36 ppm (corresponding to Q$^{(2p)}$ species) and the CSA pattern of the resulting 1D anisotropic spectra was fitted with the ssNake program [4]. The results presented in table S6 are expressed in the Herzfeld-Berger convention [6].

Table S7: Skew and span numerical results from the CSA fits.

Isotropic shift	Skew ($\varkappa$)	Span (Ω)
-72 ppm	-0.151	59.67
-78.9 ppm	-0.166	65.50
-84.36 ppm	0.204	80.73
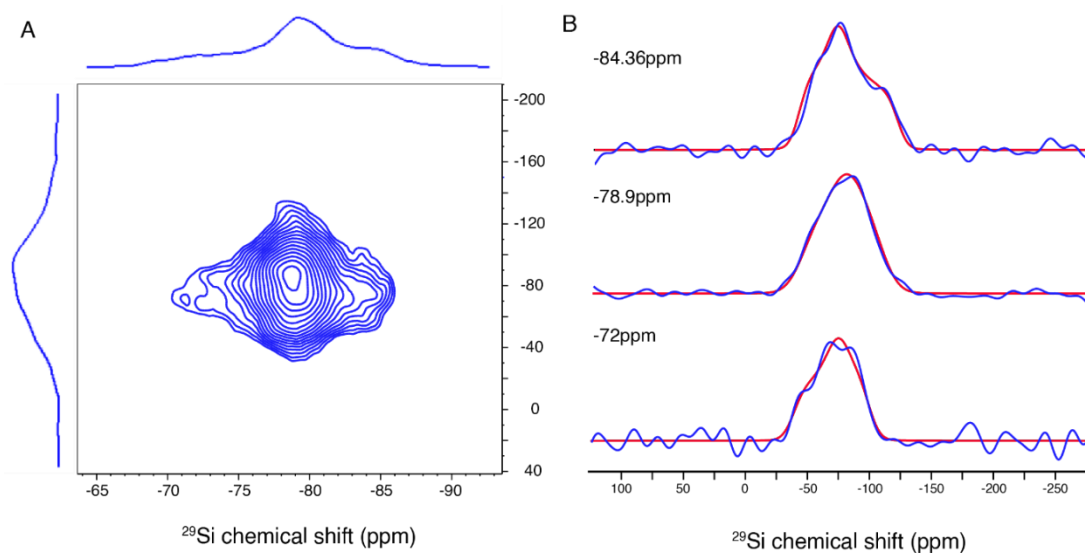
Figure S11: A) DNP-enhanced 2D ^{29}Si CP-SUPER spectrum of a zinc-modified C-S-H sample with (Zn:Si)$_i$ of 0.40 and B) 1D anisotropic spectra (blue) extracted at the pertinent isotropic shifts: -72 ppm, -78.9 ppm and -84.36 ppm together with their respective CSA fits (red).

Figure S12 shows the DFT calculated spans (Ω) of the species expected at -72 ppm, -78.9 ppm and -84.26 ppm. In general, we see a good agreement between the DFT calculated and fitted spans, especially for $Q^{(1,Zn1)}$ species which in both cases shows the lower span. Some inconsistencies can be observed for the signal at -78.9 ppm whose span is overestimated in the DFT calculations. However, this can be due to the fact that in this region there is a spectral overlap between $Q^{(1)}$ species and $Q^{(2p,Zn)}$ species which might affect the accuracy of the CSA fits.
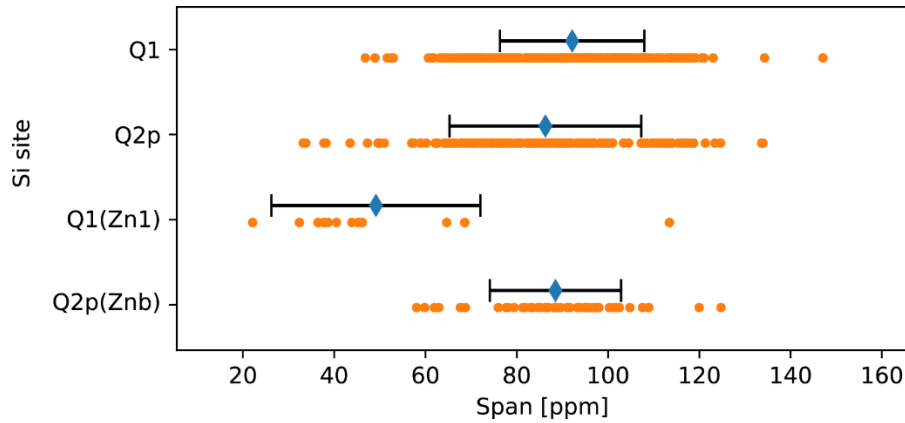
Figure S12: DFT calculated mean span (Ω) values (blue) for the silicate species $Q^{(1)}$, $Q^{(2p)}$, $Q^{(1,Zn)}$ and $Q^{(2p,Zn)}$, and their standard error (black bars).

Ve. Quantification of Q species

Results from ICP of the supernatants show that 99-98% of the zinc atoms are incorporated in the C-S-H structure (Table S2, Section IIc). The integrated intensity of the signal at –72 ppm accounts for $Q^{(1,Zn)}$ species, and the integrated intensity of the signal at –79 ppm accounts for both $Q^{(1)}$ species and $Q^{(2p,Zn)}$ species; these two signals (–72 and –79 ppm) are assumed to include the totality of silicate species which are connected to zincate species in zinc-modified C-S-H, but the $Q^{(2p,Zn)}$ and $Q^{(1)}$ signals are unresolvable. However, the percentage of zinc participating in $Q^{(1,Zn)}$ sites can be calculated by dividing the $(Zn{:}Si)_i$ ratio by the molar fraction of $Q^{(1,Zn)}$ sites. This operation yields the molar fraction of zinc atoms that participate in $Q^{(1,Zn)}$ dimers:

$$\frac{\left(Q^{(1,Zn)}{:}Si\right)}{(Zn{:}Si)} = \left(Q^{(1,Zn)}{:}Zn\right) \qquad (2)$$

The percentage of zinc corresponding to this site is found to be around 2/3rd of the total zinc (70% in the case of (Zn:Si)$_i$ of 0.15 and 60% in the case of (Zn:Si)$_i$ of 0.40). By definition, the molar fraction of Q$^{(1,Zn)}$ species is equal to the molar fraction of Zn^1 species. Because these zinc species represent a known fraction of the total zinc species, the rest of the zinc is assumed to be occupying the bridging site: Zn^b, which is consistently the most energetically favourable zinc substitution. Hence, the number of Q$^{(2p,Zn)}$ species needs to be double the number of Zn^b species since every zinc in a bridging site yields two Q$^{(2p,Zn)}$ species. Because the signals from Q$^{(2p,Zn)}$ and Q$^{(1)}$ species overlap, the intensity from Q$^{(2p,Zn)}$ species is subtracted from the intensity from Q$^{(1)}$ species.

With the fractions of Q$^{(2p,Zn)}$ and Q$^{(1)}$ species properly recalculated, and the fractions of Q$^{(1,Zn)}$, Q$^{(2p)}$ and Q$^{(2b)}$ species that were obtained through the deconvolutions of the 1D multiCP spectra, we can plot the molar fractions of every Q species in each sample and provide a quantification analysis, as shown in the main text (Figure 5). Table S7 shows the integrals of all five sites considered in the deconvolutions.

Table S8: integrals resulting from the deconvolution of the three multi-CPMAS spectra corresponding to samples with (Zn:Si)i of 0, 0.15 and 0.40, respectively.

(Zn:Si)$_i$	Q$^{(1)}$	Q$^{(2p)}$	Q$^{(2b)}$	Q$^{(1,Zn)}$	Q$^{(2p,Zn)}$
0	1.32E+11	3.63E+10	1.82E+10	0.00E+00	0.00E+00
0.15	7.67E+10	3.26E+10	1.63E+10	1.65E+10	1.57E+10
0.4	3.68E+10	4.81E+10	2.40E+10	5.86E+10	8.59E+10

Vf. Quantification of chain distributions

The positions of the isotropic ^{29}Si shifts extracted from the deconvolution of the conventional C-S-H 1D multiCP spectrum and their widths are used to construct six 2D Gaussian distributions that are centred at the frequency pairs of the expected ^{29}Si connectivities at high Ca:Si ratio C-S-H samples. These 2D Gaussians have fixed widths and chemical shifts and are used to deconvolve the INADEQUATE NMR spectra from Figure S8. These yield the following six intensities: I(Q1|Q1), I(Q1|Q2p), I(Q2p|Q2b), I(Q2b|Q2p), I(Q2p|Q2b) and I(Q2p|Q2p). The intensity of a peak can be expressed as:

$$I(B|A) = f(B|A)P(B|A)P_w(A) \qquad (3)$$

where f(B|A) is an amplitude transfer factor that accounts for differences such as CP efficiency, J-coupling distributions and T_2' relaxation between the different silicate species. $P_w(A)$ is the population of a Q species as calculated from the 1D multiCP population analysis but renormalized over pair participation. For example, the $Q^{(2)}$ sites are neighbouring with two other silicates and therefore the populations of $Q^{(2)}$ are multiplied by two. P(B|A) is the conditional probability that a [29]Si nucleus B which has evolved with a partner nucleus A has been detected and it is directly related to the mole fraction of dimers, since:

$$P\left(Q^{(1)}|Q^{(1)}\right) = X_{Q1-Q1} \qquad (4)$$

In the case of conventional C-S-H the intensity of the signal centred at −78.9 ppm in F1 and at −78.9 ppm in F2 corresponds solely to $Q^{(1)} - Q^{(1)}$ connectivities. Therefore, the molar fraction of dimers in a zinc-free sample can be directly derived from equation (4) since x_{Q1-Q1} is the dimer molar fraction in the sample (given that the intensities have been normalized for pair participation). Therefore, $1-x_{Q1-Q1}$ is the molar fraction of building blocks which have a higher degree of polymerization (i.e. pentamers, octamers, undecamers, etc). In conventional C-S-H, the molar fraction of dimers ($x_{Q1-Q1} = x_0$) is 0.86, which is consistent for high Ca:Si ratio C-S-H samples[2].

However, the calculation of the molar fraction of dimers (x_0) for samples with incorporated zinc needs to take into consideration both the $Q^{(1)} - Q^{(1)}$ connectivity intensity from the 2D INADEQUATE deconvoluted spectra and the percentage of zinc that has been incorporated into the C-S-H structure. The latter is carried out in order to account for $Q^{(1)} - Zn$ connectivities, which are heterogeneous dimers and are therefore included in the dimer molar fraction (x_0) in samples with zinc. In addition, the signal corresponding to $Q^{(1)} - Q^{(1)}$ dimers needs to be re-scaled since this signal also accounts for the $Q^{(1)} - Q^{(2p,Zn)}$ connectivities given by zinc substitutions of $Q^{(2b)}$ sites. I(Q1|Q1) is re-normalized considering that there is a percentage of this signal which is due to $Q^{(1)} - Q^{(2p,Zn)}$ connectivities, which is given by the 1D multiCP analysis described in section Ve.

After re-normalization of all the intensities involved, we obtain the population P(Q1|Q1) which corresponds to the molar fraction of $Q^{(1)} - Q^{(1)}$ dimers (x_{Q1-Q1}) that yield a signal in INADEQUATE experiments. However, the $Q^{(1)} - Zn$ connectivity signals are not present in 2D INADEQUATE experiments since the silicate species is isolated from other silicates. We

add the molar fraction of Si – Zn dimers ($x_{Q1Zn-Q1}$), which is equal to the population of $Q^{(1,Zn)}$ species in each case, to the analysis. Adding the populations of $Q^{(1)} - Q^{(1)}$ dimers and $Q^{(1)} -$ Zn dimers yields the total dimer molar fraction (x_0) in each case. Results from this analysis yield the molar fractions of dimer structures (x_0) and of higher degree units (x_n) and is summarized in Table 1 in the main text and is in agreement with an increased mean chain length as more zinc is incorporated in the C-S-H structure.

A4-6 VI. Structures of Zinc-modified C-S-H

Figure S13 shows a representative [7] (with a Ca:Si ratio of 1.7 and the Q populations described in the main text) 2D structure of a sample of zinc-modified C-S-H with a $(Zn:Si)_i$ of 0.15 with the $Q^{(1,Zn)}$ and $Q^{(2p,Zn)}$ sites. Figures S14 shows a representative structure of a sample with $(Zn:Si)_i$ of 0.15, but with also the two additional DFT-predicted sites ($Q^{(2p,2Zn)}$ and $Q^{(1, Zn\_int)}$). Figures S15 shows a representative atomic-level structures with four layers of silicate chains of zinc-modified C-S-H with $(Zn:Si)_i$ of 0.4 with the two new sites found in this work. Finally, Figure S16 shows a representative structure of the sample with $(Zn:Si)_i$ but including all four possible sites.

Figure S13: 2D representative atomic-level structure of zinc-modified C-S-H as determined with $(Zn:Si)_i$ = 0.15 and Ca:Si = 1.7 (the 3D model is shown in Figure 6). The structure measures approximately 39 Å x 31 Å. Silicate tetrahedra are depicted in blue; zincate tetrahedra are depicted in yellow; and calcium ions are depicted in light blue. In this structure, the two sites discovered in this work ($Q^{(1,Zn)}$ and $Q^{(2p,2Zn)}$) are shown.
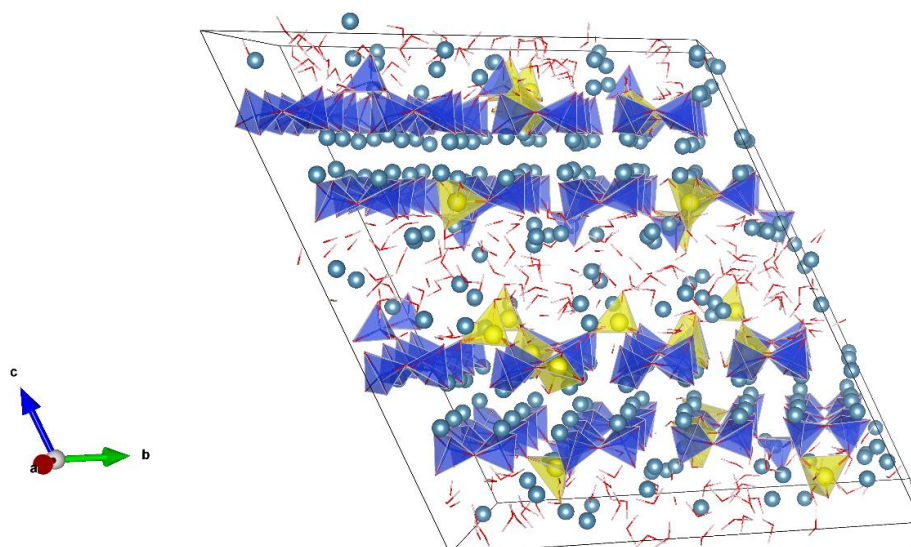
Figure S14: Representative atomic-level structure of zinc-modified C-S-H as determined with $(Zn:Si)_i$ = 0.15 and Ca:Si = 1.7. The structure measures approximately 27 Å × 31 Å × 31 Å. Silicate tetrahedra are depicted in blue; zincate tetrahedra are depicted in yellow; and calcium ions are depicted in light blue. In this structure, the two additional DFT-predicted sites ($Q^{(2p,2Zn)}$ and $Q^{(1,Zn\_int)}$) are also included apart from the $Q^{(1,Zn)}$ and $Q^{(2p,2Zn)}$ sites.

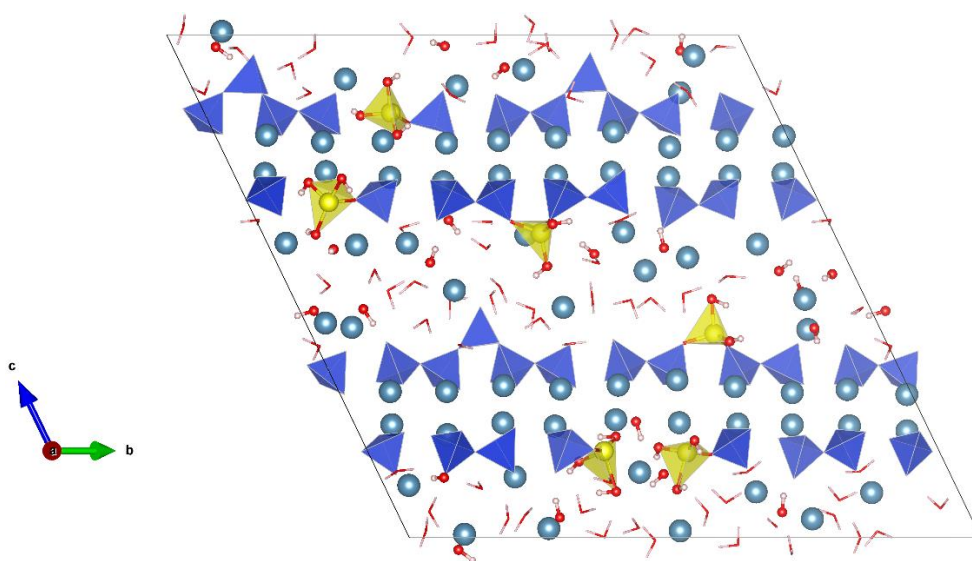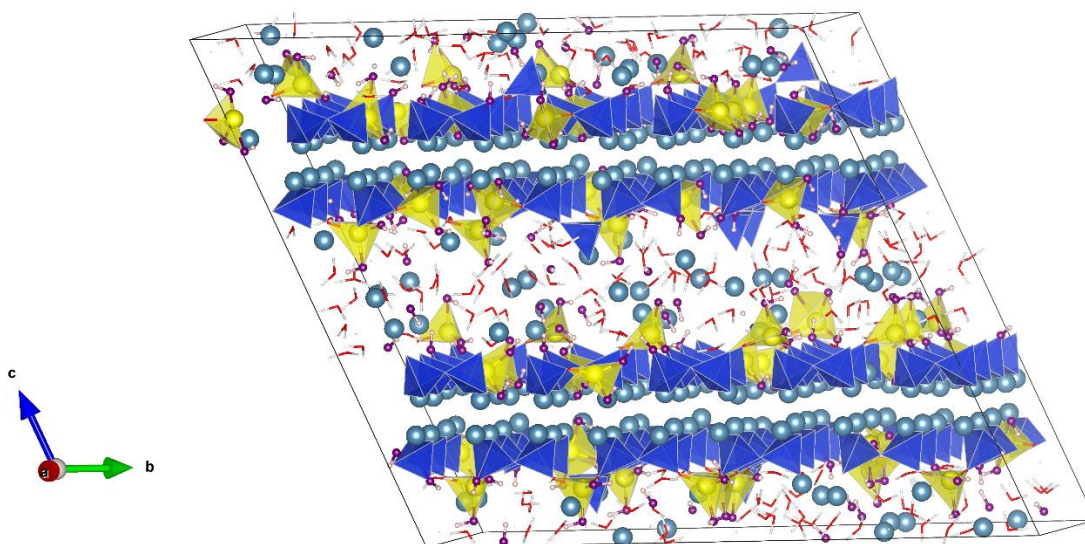**Figure S15:** Large representative atomic-level structure of zinc-modified C-S-H as determined with $(Zn:Si)_i$ = 0.4 and Ca:Si = 1.7. The structure measures approximately 27 Å × 39 Å × 31 Å and includes $Q^{(2p,Zn)}$ and $Q^{(1,Zn)}$ as the new silicon sites. Silicate tetrahedra are depicted in blue; zincate tetrahedra are depicted in yellow; and calcium ions are depicted in light blue.
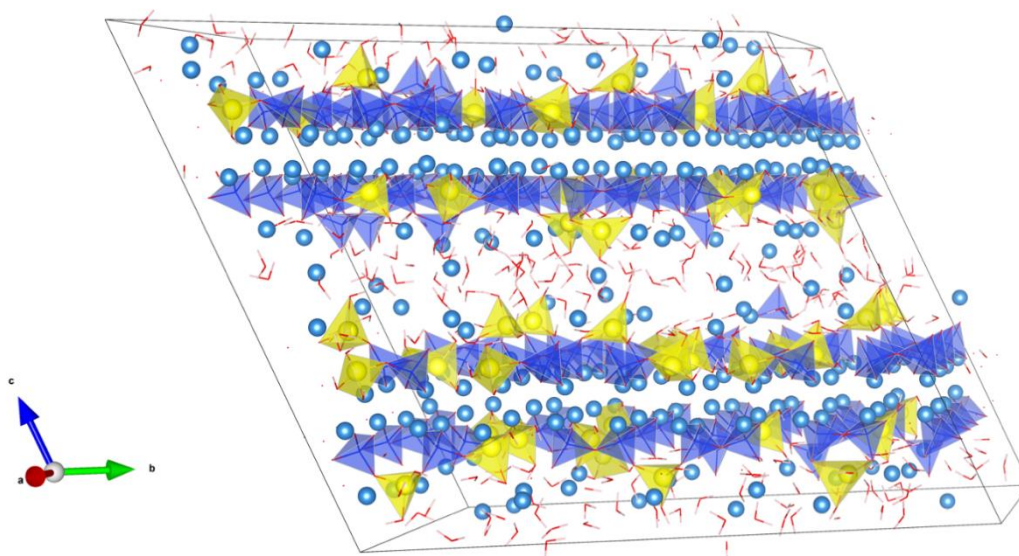
Figure S16: Large representative atomic-level structure of zinc-modified C-S-H as determined with $(Zn:Si)_i = 0.4$. Silicate tetrahedra are depicted in blue; zincate tetrahedra are depicted in yellow; and calcium ions are depicted in light blue. In this structure, the two additional DFT-predicted sites $(Q^{(2p,2Zn)}$ and $Q^{(1,Zn\_int)})$ are also included apart from the $Q^{(1,Zn)}$ and $Q^{(2p,2Zn)}$ sites.

A4-7 VII. Zinc substituting for calcium in C-S-H

The incorporation of heavy metals into C-S-H was mostly investigated with XRD and XPS in former works. It was observed that C-S-H can incorporate up to 6 wt.% zinc [8], and that this incorporation does not appear to influence the calcium and silicon content [9]. While it was first theorized that zinc replaces calcium in C-S-H [10], it was later concluded that zinc is incorporated into C-S-H in tetrahedral coordination, and according to measured Ca-Zn distances indicates that the zinc tetrahedra substitutes the silicon tetrahedra [11], which was also observed with ^{29}Si NMR [12]. The ^{29}Si NMR suggests a Zn-O-Si linkage, where a silicon tetrahedron is linked to silicon and zinc tetrahedra.

Additionally, our DFT-relaxed structures where zinc substituted for calcium in the main layer presented zinc in a quasi-6-fold coordination and with interatomic distances between zinc and oxygen which were unusually long (20% more than expected for C-S-H systems). Tetrahedral coordination was never achieved.
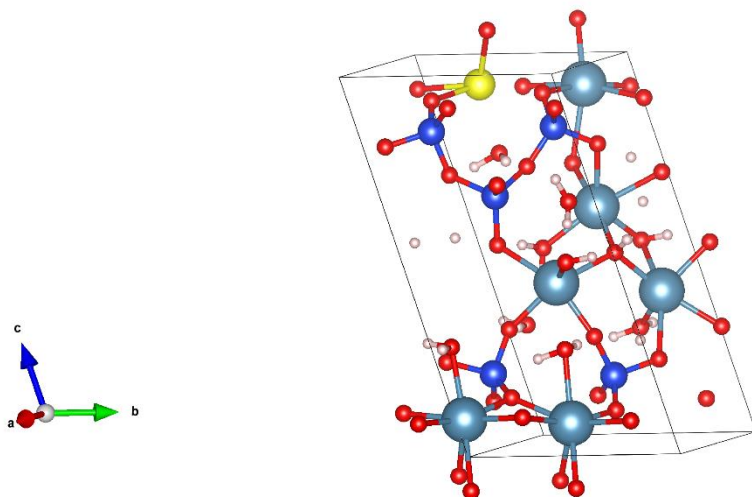
Figure S17: Structure where zinc substitutes calcium in the main layer.

References

[1]   Renaudin, G.; Russias, J.; Leroux, F.; Frizon, F.; Cau-dit-Coumes, C. Structural Characterization of C–S–H and C–A–S–H Samples—Part I: Long-Range Order Investigated by Rietveld Analyses. *J. Solid State Chem.* **2009**, *182* (12), 3312-3319.

[2]   Kumar, A.; Walder, B. J.; Kunhi Mohamed, A.; Hofstetter, A.; Srinivasan, B.; Rossini, A. J.; Scrivener, K.; Emsley, L.; Bowen, P. The Atomic-Level Structure of Cementitious Calcium Silicate Hydrate. *J. Phys. Chem. C* **2017**, *121* (32), 17188-17196.

[3]   Harris, M.; Simpson, G.; Scrivener, K.; Bowen, P. A Method for the Reliable and Reproducible Precipitation of Phase Pure high Ca/Si ratio (> 1.5) Synthetic Calcium Silicate Hydrates (C-S-H). *Cem. Concr. Res.* **2022**, *151*, 106623.

[4]   van Meerten, S. G. J.; Franssen, W. M. J.; Kentgens, A. P. M. ssNake: A Cross-Platform Open-Source NMR Data Processing and Fitting Application. *J. Magn. Reson.* **2019**, *301*, 56-66.

[5]   Liu, S.-F.; Mao, J.-D.; Schmidt-Rohr, K. A Robust Technique for Two-Dimensional Separation of Undistorted Chemical-Shift Anisotropy Powder Patterns in Magic-Angle-Spinning NMR. *J. Magn. Reson.* **2002**, *155* (1), 15-28.

[6]   Herzfeld, J.; Berger, A. E. Sideband Intensities in NMR Spectra of Samples Spinning at the Magic Angle. *J. Phys. Chem.* **1980**, *73* (12), 6021-6030.

[7]   Kunhi Mohamed, A.; Parker, S. C.; Bowen, P.; Galmarini, S. An Atomistic Building Block Description of C-S-H-Towards a Realistic C-S-H Model. *Cem. Concr. Res.* **2018**, *107*, 221-235.

[8]   Stumm, A.; Garbev, K.; Beuchle, G.; Black, L.; Stemmermann, P.; Nüesch, R. Incorporation of Zinc into Calcium Silicate Hydrates, Part I: Formation of C-S-H(I) with C/S=2/3 and its Isochemical Counterpart Gyrolite. *Cem. Concr. Res.* **2005**, *35* (9), 1665-1675.

[9]   Ziegler, F.; Scheidegger, A. M.; Johnson, C. A.; Dähn, R.; Wieland, E. Sorption Mechanisms of Zinc to Calcium Silicate Hydrate: X-Ray Absorption Fine Structure (XAFS) Investigation. *Environ. Sci. Technol.* **2001**, *35* (7), 1550-1555.

[10]   Stephan, D.; Maleki, H.; Knöfel, D.; Eber, B.; Härdtl, R. Influence of Cr, Ni, and Zn on the Properties of Pure Clinker Phases: Part I. C_3S. *Cem. Concr. Res.* **1999**, *29* (4), 545-552.

[11]   Tommaseo, C. E.; Kersten, M. Aqueous Solubility Diagrams for Cementitious Waste Stabilization Systems. 3. Mechanism of Zinc Immobilizaton by Calcium Silicate Hydrate. *Environ. Sci. Technol.* **2002**, *36* (13), 2919-2925.

[12]   Rose, J.; Moulin, I.; Masion, A.; Bertsch, P. M.; Wiesner, M. R.; Bottero, J.-Y.; Mosnier, F.; Haehnel, C. X-Ray Absorption Spectroscopy Study of Immobilization Processes for Heavy Metals in Calcium Silicate Hydrates. 2. Zinc. *Langmuir* **2002**, *17* (12), 3658-3665.

A5   Supplementary Information – Chapter 5

A5-1   Surface construction

The Ca-Si chains for the surface are composed of the same groups of atoms (figure S1) as the upper and lower Ca-Si chains of the main layer [1]. Some of the different combinations of atom groups that can be used to form a single surface block are shown in figure S1a. Surface blocks 1 to 4 give a silicon termination of the C-S-H surface, where 1 and 2 show a block with the missing Q^{2b} site, and 5 to 8 give calcium termination, where we have a calcium in the bridging site (5 and 6), or calcium in the bridging site with an additional calcium next to it (7 and 8). The surface charge arises from the pH-dependent protonation of surface oxygens and deprotonation of chemisorbed water molecules [2], which can be accounted for in the model as seen in pairs 1-2, 3-4 and 5-6, leading to a net charge. Although not shown in figure S1a, partial protonation and deprotonation, or additional hydroxides in the case of calcium termination are possible. Since classical molecular dynamics does not account for bond breakage and creation, the degree of silanol deprotonation as well as hydroxide presence on the surface needs to be chosen beforehand. Figure S1b shows an assembly of different surface blocks to form a mixed Ca-Si surface chain in the b-axis direction.
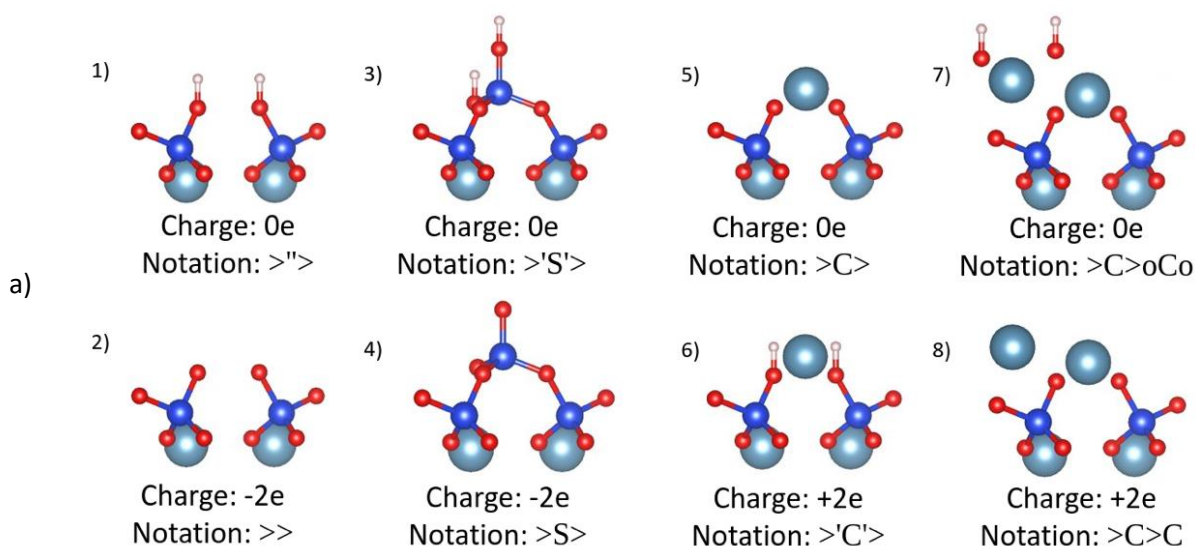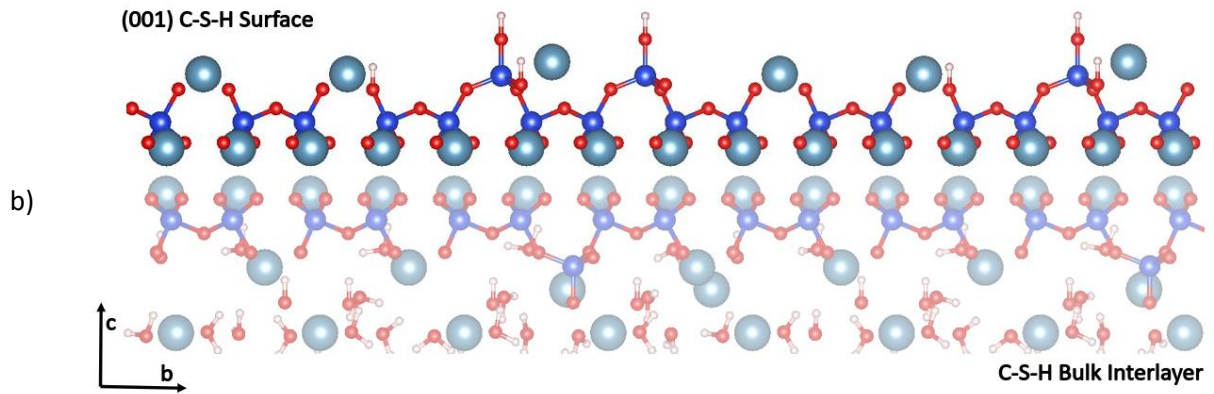
Figure S1. a) Possible C-S-H surface blocks, with net charge and building block notation [1] for the upper surface (in c direction); b) Mixed Ca-Si surface chain constructed from different surface blocks, (for the upper surface). Color code: Turquoise – calcium, dark blue – silicon, red – oxygen, white – hydrogen.

As is the case for the C-S-H bulk structure [1], there can be many possible local arrangements of different surface blocks to build a representative C-S-H surface. Local arrangements here refer to the length of individual silicate chains (dimer, pentamer, ...), the protonation of silanol groups and location of calcium and hydroxide ions at the surface. It is crucial that the constructed C-S-H structure (bulk with surface) mimics the experimental results as accurately as possible [3]. The Ca/Si ratio significantly affects a wide range of phenomena [3-10]. In particular the water structure at the surface will be directly related to the surface termination, and this will determine the hydrodynamic properties of flows through cement porosity [3, 11], since it can be substantially different to bulk water [12].

Experimental data

Figure S2 shows the collected experimental data by Duque-Redondo et al. [13] which was used throughout the manuscript. The MCL values are from references [14-18], while the Si-OH/Si and Ca-OH/Ca values are from [19-22].

The round colored markers show the data points which were used to construct the atomic-scale model of the C-S-H nanofoils. The exact values of the markers are given in table S1.
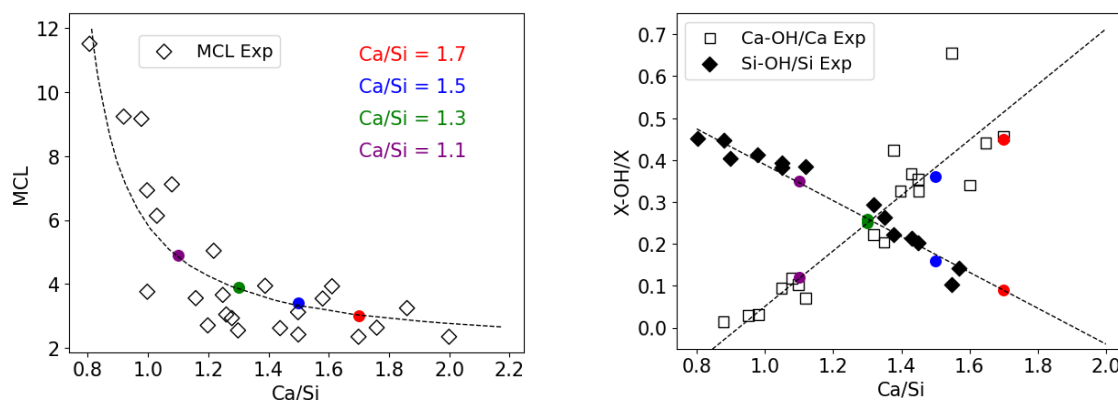
Figure S2. Collected experimental data by Duque-Redondo et al. [13] Colors correspond to the values which were used through the manuscript to construct the atomic-scale models of C-S-H nanofoils at a given Ca/Si and thickness.

Table S1. Values which were taken for the construction of the C-S-H nanofoils through the manuscript. The values were chosen from the collected data by Duque-Redondo et al. [13] and are highlighted in figure S2.

Ca/Si	MCL	Si-OH/Si	Ca-OH/Ca
1.1	4.9	0.35	0.12
1.3	3.9	0.25	0.25
1.5	3.4	0.16	0.36
1.7	3.0	0.09	0.45

C-S-H nanofoil with Mixed-Surface

This section provides a detailed explanation on how to construct a C-S-H nanofoil model with the (001) Mixed-Surface termination for any given Ca/Si ratio.

First the size of the system model needs to be specified:

- A = number of defective tobermorite 14Å unit cells in a-axis direction
- B = number of defective tobermorite 14Å unit cells in b-axis direction
- L = number of calcium-silicate sheets (layers) in z-axis direction ($L = 3$ for 3 layers, 2 interlayers C-S-H)

The mean chain length (MCL) is defined[1,23] as

$$MCL = \frac{Q^i}{0.5 \cdot Q^{i \neq 2b} - Q^{2b}}$$

(1)

where Q^i denotes either the exact number of given Q species in the atomistic model, or the proportion of Q species as given by ^{29}Si NMR.[23] i is either $2b$, $2p$ or 1. Each Q^{2b} is always accompanied by two Q^{2p} silicates, therefore the MCL can be also written as

$$MCL = \frac{Q^1 + 3Q^{2b}}{0.5 \cdot Q^1}$$

(2)

The maximum amount of Q species (Q^{MAX}) for a given model of the nanofoil equals to

$$Q^{MAX} = Q^1 + Q^{2b} + Q^{2p} + Ca_B$$

(3)

where Ca_B stands for all the bridging sites, which are missing a Q^{2b} silicate, and are presumably occupied with a calcium atom. Due to the structure of the silicate chains, one third of the Q^{MAX} are linking the dimers. This gives the next relation:

$$\frac{Q^{MAX}}{3} = Q^{2b} + Ca_B$$

(4)

Combining equations (2), (3) and (4) gives the number of Q^{2b} silicates, which is needed for ensuring the right MCL of the computational model (equation 5). The number of Q^{2b} silicates should be equally distributed between the calcium-silicate chains of the nanofoil.

$$Q^{2b} = \frac{2}{3} Q^{MAX} \frac{MCL - 2}{2 \cdot MCL + 2}$$

(5)

where Q^{MAX} is calculated from the parameters which decide the size of the atomistic system:

$$Q^{MAX} = 6 \cdot A \cdot B \cdot L \tag{6}$$

From the total amount of silicates (Si) in the system:

$$Si = \frac{2}{3}Q^{MAX} + Q^{2b} \tag{7}$$

the needed amount of calcium (Ca) for a targeted Ca/Si ratio can be calculated as

$$Ca = \left(\frac{Ca}{Si}\right)_{target} \cdot Si \tag{8}$$

Assuming there is no calcium missing from the main layer calcium-silicate sheets, one can calculate the amount of calcium atoms which is in the interlayers and on the surfaces, while excluding the amount of calcium in the bridging sites (Ca_B):

$$Ca_{int+surf} = Ca - \frac{2}{3}Q^{MAX} - Ca_B \tag{9}$$

where:

$$Ca_B = \frac{Q^{MAX}}{3} - Q^{2b} \tag{10}$$

As seen in the review paper of Duque-Redondo et al. [13] and figure S2 the Si-OH/Si ratio decreases linearly with the increase in Ca/Si ratio. The linear fit of the experimental results (see figure S2) yields:

$$\frac{Si - OH}{Si} = -0.4306\left(\frac{Ca}{Si}\right)_{target} + 0.8217 \tag{11}$$

Assuming a deprotonation rate of surface silanol groups ($D_{surf} = 0.9$ for 90% deprotonation), the number of silanol groups in the interlayers can be calculated as:

$$N^{Int}_{Si-OH} = \left(\frac{Si - OH}{Si}\right)_{eq11} \cdot Si \ - \frac{4}{2 \cdot L - 2}\left(1 - D_{surf}\right) \cdot Q^{2b} \tag{12}$$

Finally, the amount of calcium which is associated with the interlayer and surface (equation 9), needs to be divided between them. The packing of the interlayers with calcium will depend on the desired Ca/Si ratio of the bulk (Ca/Si_{bulk}):

$$Ca_{int} = \left(\frac{Ca}{Si}\right)_{bulk} \cdot Si_{bulk} - (2 \cdot L - 2) \cdot \left(2 \cdot A \cdot B + \frac{Ca_B}{2 \cdot L}\right) \tag{13}$$

$$Si_{bulk} = \frac{2 \cdot L - 2}{2 \cdot L} \cdot Si \tag{14}$$

$$Ca_{surf} = Ca_{int+surf} - Ca_{int} \tag{15}$$

Summary on constructing a C-S-H nanofoil with the (001) surfaces and targeted Ca/Si ratio

The C-S-H nanofoil was constructed with the in-house brick model code from Kunhi Mohamed et al. [1] (the code can be requested by contacting the authors). The example of the code is shown below.

Step-by-step guide to construct the nanofoil:

1. Define the targeted Ca/Si ratio and the size of the bulk C-S-H (number of layers – L, number of bricks in x-axis and y-axis direction – A and B). Use the Ca/Si ratio to define the MCL (figure S2). The MCL can also be calculated from the proportion of Q species (equation 2).

2. Calculate the nanofoil properties (Si, Q^{2b}, Ca, Ca_B, Ca_{Int}, Ca_{Surf}, …) with equations 4 to 15.

3. If starting from a CIF file of tobermorite 14 Å:

   1. Multiply the tobermorite unit cell in the x, y and z-axis direction to create a super cell of L+2 thickness, A number of unit cells in x-axis direction and B number of unit cells in y-axis direction.

   2. Delete the calcium silicate chains and interlayer Ca^{2+} and H_2O placed at z_{min} and z_{max}. With this a tobermorite nanofoil was constructed which has L layers and is terminated by (001) surfaces.

   3. On each side of each layer remove $Ca_B/(2L)$ number of Q^{2b} silicates and replace them with Ca^{2+} ions. The Q^{2b} silicates are removed by removing the Si atom and two O atoms, which are not shared with the neighboring silicates. Remaining Q^{2b} silicates should be equally distributed on the individual layers.

   4. On the surface deprotonate D_{surf} silanol groups. Start by deprotonating the upper silanol groups, followed by the lower (closer to the calcium oxide sheet) silanol groups. Silanol groups should be equally distributed on the surface.

   5. On each interlayer surface distribute $N_{SiOH}^{Int}/(L-1/L)$ silanol groups. The silanol groups should be attached to the non-sharing oxygens of the Q^{2b} silicates. Silanol groups should be equally distributed throughout the interlayer, firstly placed on the silicate oxygens which are closer to the calcium oxide sheet.

   6. The tobermorite interlayer holds one Ca^{2+} per brick. Add or remove so many Ca^{2+} in the interlayers that the total amount of Ca^{2+} (excluding Ca_B in the bridging sites) equals the calculated Ca_{Int}. Make sure each interlayer holds the same amount of Ca^{2+} and that they are equally distributed through it.

   7. Calculate the charge of each interlayer. By removing one hydrogen from the water molecule, you create an OH^- ion which lowers the charge in the interlayer by -1 e. Create so many OH^- ions to achieve charge neutrality of the bulk. Distribute the OH^- equally through the interlayers.

   8. If needed add additional H_2O molecules to the interlayers to raise the 2H/Si ratio. Make sure to equally distribute the H_2O molecules.

9. Close to each surface equally distribute $Ca_{surf}/2$ number of Ca^{2+}. Between the placed Ca^{2+} add OH^- ions. For charge neutral surface Ca_{surf} number of OH^- should be placed. If a positive surface is desired, place less OH^- ions, so many to obtain the desired surface charge.

10. Place a water slab above each surface.

4. If using the in-house brick model code:

1. Follow the same steps (1 to 8) as in step 3 to generate a description of the C-S-H nanofoil according to the brick model nomenclature (example below). Use this code to generate the model structure.

2. The brick code generates structures in DL Poly format which can be converted to XYZ format. This can be done for example with the visualization program VESTA [24].

3. Packmol [25] (uses XYZ data format) can then be used to insert $Ca_{surf}/2$ number of Ca^{2+} and the desired number of OH^- ions in the proximity of each surface. Packmol can be also used to insert a water slab between the surfaces.

Example of the Brick Model [1] code of a C-S-H nanofoil measuring 3 layers, 2 interlayers in the c-axis direction, 5 bricks in the x-axis direction and 6 bricks in the y-axis direction, without Ca_{Surf} on the surface. For a detailed description of the brick model we refer the reader to the publication of Kunhi Mohamed et al. [1]

```
              >C> >S'> >C> >C> >C> >C>
               >C> >C> >S> >C> >S> >S>            (001)
               >C> >C> >C> >C> >C> >C>
              >C> >C> >S'> >C> >S'> >S>          surface
               >C> >C> >C> >C> >C> >C>
                          Z
    <S'<oX6>Co> <Co<oX6>oC> <S'<oX6>Co> <C<oCoX5>S>
                 <Co<X6>oC> <S<X6>Co>              Bulk
     <oC<Xo6>Co> <C<oCoX5>oC> <Co<X6>oC> <C<X6>oC>
                 <C<X6>S> <Co<Xo6>S'>               (1
      <S'<X6>S> <Co<X6>S'> <Co<oXC5>oC> <S<X6>oC>  interlayer)
                 <S<XCo5>oC> <Co<X6>oC>
      <oC<X6>oC> <S'<XC5>oC> <Co<X6>oC> <oC<X6>oC>
                 <oC<oX6>C> <oC<X6>oC>
   <oC<XC5>S> <Co<X6>S> <Co<X6>C> <Co<X6>oC> <S<Xo6>C>
                     <Co<XCo5>oC>
                          Z
    <S'<oX6>Co> <Co<oX6>oC> <S'<oX6>Co> <C<oCoX5>S>
                 <Co<X6>oC> <S<X6>Co>              Bulk
     <oC<Xo6>Co> <C<oCoX5>oC> <Co<X6>oC> <C<X6>oC>
                 <C<X6>S> <Co<Xo6>S'>               (1
      <S'<X6>S> <Co<X6>S'> <Co<oXC5>oC> <S<X6>oC>  interlayer)
                 <S<XCo5>oC> <Co<X6>oC>
      <oC<X6>oC> <S'<XC5>oC> <Co<X6>oC> <oC<X6>oC>
                 <oC<oX6>C> <oC<X6>oC>
   <oC<XC5>S> <Co<X6>S> <Co<X6>C> <Co<X6>oC> <S<Xo6>C>
                     <Co<XCo5>oC>
                          Z
               <C< <S'< <C< <C< <C< <C<
               <S< <C< <S< <C< <S'< <C<            (001)
               <C< <C< <C< <C< <C< <C<
               <C< <S'< <C< <C< <C< <C<          surface
               <S< <C< <C< <C< <C< <S<
```

Comparison of different thicknesses
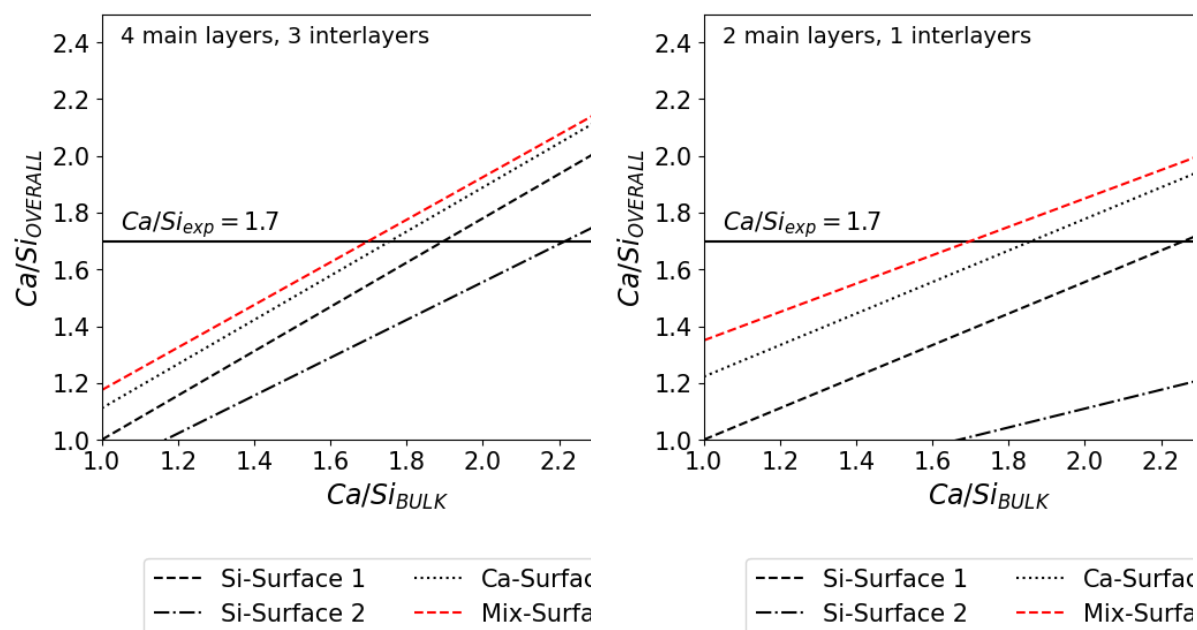
Figure S3. Correlation of the overall Ca/Si ratio on the Ca/Si of the bulk structure for the 4 layers, 3 interlayers and 2 layers, 1 interlayer C-S-H structures with given (001) surfaces terminations.

Table S2. Mean chain Length (MCL) and Ca/Si of investigated C-S-H nanofoils with overall Ca/Si = 1.7 and different surface terminations.

	MCL$_{BULK}$	MCL$_{SURFACE}$	Ca/Si$_{BULK}$
4 layers, 3 interlayers			
Si-Surface 1	3.5	2.0	1.9
Si-Surface 2	2.0	∞	2.2
Ca-Surface	3.5	2.0	1.76
Mix-Surface	3	3	1.7
2 layers, 1 interlayer			
Si-Surface 1	5.0	2.0	2.26
Si-Surface 2	1.2	∞	3.77
Ca-Surface	5.0	2.0	1.86
Mix-Surface	3	3	1.7

A5-2

A5-3 Force Field

In the following the force field parameters are listed. The force field is an improved version of the previous full charge force field of Valavi et al. [26] and Kunhi Mohamed et al. [27, 28] The TIP4P/2005 water model [29] is used in conjunction with the SHAKE algorithm. All simulations were carried out with LAMMPS. [30] For the description of the used interatomic potentials we refer the reader to the LAMMPS documentation [30] or the SI section of Valavi et al.]26]. The kspace solver used was the pppm/tip4p with an accuracy of 1e-4.

Table S3. Atomic charges.

Atomic species	Charge	Description
Ca	+2.0	Calcium
Si	+4.0	Silicon
O	+0.848	Silicate oxygen - core
O(S)	-2.848	Silicate oxygen - shell
Ow	-1.1128	Water oxygen
Hw	+0.5564	Water hydrogen
Oh	-1.4	Hydroxide oxygen
H	+0.4	Hydroxide hydrogen
Cl	-1.0	Chlorine

Table S4. Buckingham interatomic potentials.

	A [eV]	ϱ [Å]	C [eV Å^6]
Ca-O(S)	2152.3566	0.309227	0.09944
Si-O(S)	1283.9	0.3205	10.66
Si-Ow	1283.556	0.3202	10.66
Si-Oh	983.5	0.3255	10.66
O(S)-O(S)	22764.3	0.149	27.88
O(S)-Ow	22764.3	0.149	28.92
O(S)-Oh	22764.3	0.149	13.94
O(S)-Hw	512.0	0.25	0.0

Table S5. Lennard-Jones interatomic potentials.

	ε [eV]	σ [Å]
Ca-Ca	0.0121188	2.8331
Ca-Ow	0.00984634	2.996
Ca-Oh	0.0151386	3.0613
Ca-Cl	0.00247555	3.87545
O(S)-Cl	0.00309242	4.103625
Ow-Ow	0.008	3.1589
Ow-Oh	0.012299878	3.28945
Ow-Cl	0.002113497	4.03835
Oh-Oh	0.018910874	3.42
Oh-Cl	0.00309242	4.1689
Cl-Cl	0.000505691	4.9178

Table S6. N-M interatomic potentials.

	E_0 [eV]	r_0 [Å]	n	m
O(S)-H	0.0073	2.71	9	6
Ow-H	0.055	2	9	6
Oh-H	0.0073	2.71	9	6

Table S7. Harmonic bonds.

	K [eV/Å²]	r_0 [Å]
O-O(S)	37.5	0
Ow-Hw	9.7563	0.9572

Table S8. Morse bond.

	D [eV]	α [1/ Å]	r_0 [Å]
Oh-H	7.0525	3.1749	0.942

Table S9. Harmonic angles.

	K [eV]	Θ [°]
O-Si-O		
Oh-Si-O	7.74815	109.47
Oh-Si-Oh		
Si-Oh-H	7.74815	141.5

A5-4 Simulation protocol

Since the brick model inserts atoms in a predetermined way, which can result in atoms being in close proximity to each other, therefore experiencing large initial forces, a suitable equilibration protocol was used. CS ensemble refers to the core-shell equilibration. For the details on the core-shell equilibration we refer the reader to the work of Valavi et al. [26] The used thermostat is the Nose-Hoover with Tdamp values 100 times the timestep, while Pdamp was 1000 times the timestep.

Table S10. Simulation protocol.

Run	Timestep [ps]	Number of Timesteps	Ensemble	Atomic species	Temperature [K]	Pressure [bar]
1	0.0001	10e3	NVT	Ca,Ow,Hw	10 -> 300	
2	0.0001	100e3	NVT	all	10 -> 300	
3	0.00028	50e3	NVT	all	300	
4	0.00028	10e3	CS	all	300	
5	0.00028	960e3	NPT	all	300	1 bar (z direction)
6	0.00028	500e3	NPT	all	300	1 bar (x,y directions)
7	0.00028	60e3	NPT	all	300	1 bar (z direction)
8	0.00015	200e3	NVT	all	300 -> 700	
9	0.00015	200e3	NVT	all	700	
10	0.00015	100e3	NVT	all	700 -> 300	
11	0.00015	60e3	NPT	all	300	1 bar (z direction)
12	0.00028	70e6	NVT	all	300	

In the first run only calcium and water are thermostated. This is done with a smaller timestep so that the calcium and water can move away from the hydroxides (the code packs them relatively close). A slow equilibration follows, where the entire system is heated to the desired temperature. Next (4) is the core-shell equilibration, where the core-shell movement is

decoupled and rescaled, which is necessary to prevent the overheating of core-shell pairs and keeping the total energy of the system constant [31]. From (5) to (7) a series of NPT runs is carried out in order to relax the simulation box in the z-direction (obtaining bulk water properties), and x-y-directions for C-S-H structure relaxation. The entire NPT run is carried out as a series of shorter runs, since due to the shrinkage of the simulation box the kspace mesh needs to be recalculated between the runs. Next (8-10) is the heating cycle which is necessary to overcome possible energetical barriers and reach a lower energy minimum. The timestep was lowered, since at the default 0.00028 ps the Oh-H bonds of surface silanol groups were broken. The last (12) run is the production run in which the density number of atomic species in z-direction are recorded, as well as trajectories and the radial distribution function. For more information we refer the reader to the LAMMPS input file (in.ZigaFF2)

A5-5   Surface charge density

The surface charge density of the proposed model, shown in figure 5 of the main text, is calculated as follows. From table S11 the ionization fraction (α) at a given pH and surface silanol density (SSD) is chosen. From this the number of deprotonated silanol groups per surface area (DSG) is calculated as:

$$DSG = SSD \cdot \alpha \ [O^-/nm^2]$$

The assumption follows the adsorption of $n \cdot Ca^{2+}$ and $2(n-2) \cdot OH^-$ per deprotonated silanol group. Therefore, the surface charge density, σ, equals to:

$$\sigma = DSG \ [e/nm^2],$$

since the surface charge density without adsorbed calcium at the deprotonated silanols equals $-DSG$ [e/nm²], and after adsorption to $+DSG$ [e/nm²].

Table S11. Ionization fraction (α) for different surface silanol densities (4.8, 2.8 and 0.8 OH/nm^2) and pHs as predicted by Grand Canonical Monte Carlo simulations for surfaces in contact with 2 mM CaX$_2$ solutions [9]. X stands for any monovalent ion.

pH	α at 4.8 OH/nm^2	α at 2.8 OH/nm^2	α at 0.8 OH/nm^2
8	0	0	0
9	0.2	0.131	0.07
10	0.82	0.55	0.25
11	2.23	1.64	0.61
12	3.64	2.48	0.77
13	4.5	2.76	0.8
14	4.74	2.78	0.8

A5-6 Calcium adsorption: Si-Surface 2

To examine Ca^{2+} adsorption at the Si-Surface 2, the tobermorite 14 Å structure with the (001) surface was investigated. We remind the reader, the basal (001) surface of tobermorite (cut through the interlayer) is the Si-Surface 2 in the present paper. The tobermorite structure was 3 layers, 2 interlayers thick, and placed in contact with a calcium-chloride solution (figure S4). The (001) surface was modeled with 90% deprotonation of silanol groups. The negative surface charge was compensated with Ca^{2+} ions (45 ions). Additional Ca^{2+} ions (8 in total) and Cl$^-$ ions (16 ions) were placed between the surfaces. The surfaces were separated by approximately 80Å. All ions and water molecules were randomly placed between the surfaces [25].

The inspection of the system reveals that approximately 14% of Ca^{2+} were inner sphere adsorbed. Inner sphere adsorption here is defined as silicate oxygen (protonated or deprotonated) entering the first coordination shell of Ca^{2+}, which happens when the distance between the calcium and oxygen is less than 3.15 Å [32]. The preferential outer sphere adsorption is further confirmed with the radial distribution function for calcium-oxygen (figure S5), where the first peak at approximately 2.4 Å points to inner sphere adsorption, while the intensity of the second peak at 4.7 Å points to preferred outer sphere adsorption (62% of Ca^{2+}). This can also be seen from the number density distribution along the z-axis (figure S5). 24% of Ca^{2+} remain in solution.
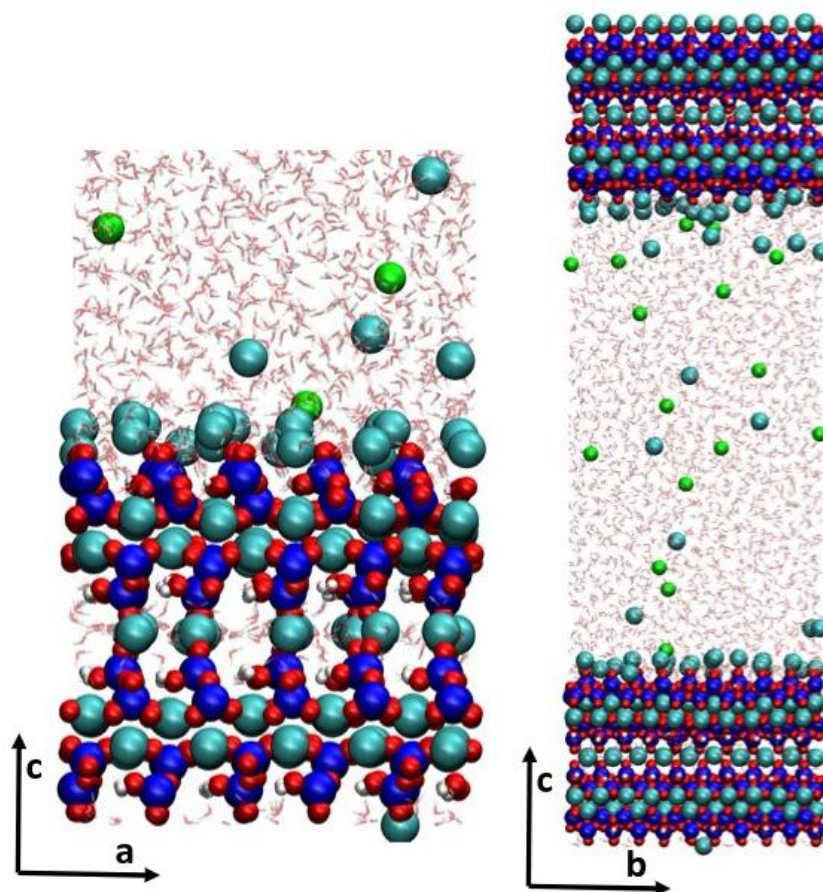
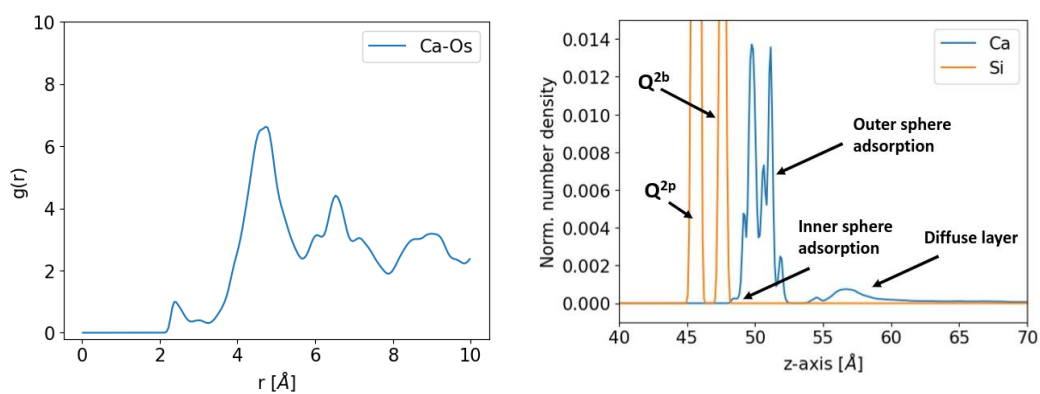Figure S4. Final snapshot of the simulated system. Color code: Ca-cyan, Si-blue, O-red, H-white, Cl-green.

Figure S5. Left: radial distribution function for calcium-silicate oxygen. Right: Number density in z-axis for calcium and silicates. The first silicate peak belongs to Q^{2p} while the second belongs to Q^{2b} silicates.

Closer inspection of the adsorption sites reveals two mechanisms for inner sphere adsorption (figure S6). First is the adsorption on top of the Q^{2p}-Q^{2p} dimer, where Ca^{2+} inner sphere adsorbs to the sharing oxygens of the silicates and an additional deprotonated silanol group. The deprotonated silanol group can be the upper non-sharing oxygen of the next in-chain Q^{2b} (shown in figure S6b), or the lower non-sharing oxygen of the neighboring silicate chain Q^{2b}. This adsorption site was first reported by Kalinichev et al. [12], where they studied calcium adsorption on the tobermorite 9 Å (001) surface. A similar site was also observed by Kunhi Mohamed[33] in the C-S-H interlayer, who carried out a density functional theory study of the favorable calcium sites and reported this site as the energetically most favorable. The second inner sphere adsorption site (figure S6c) is due to only one silicate oxygen entering the first coordination shell of Ca^{2+}. The upper silanol group was identified as highly acidic (pKa = 6.15) [34], where the solvent contribution for deprotonation is high. Further, Androniuk and Kalinichev carried out a metadynamics adsorption study [35], where they identified this second site as energetically preferential for Ca^{2+} adsorption.

The typical environment for outer sphere adsorption is shown in figure S6 with a triangle. Due to the structural characteristics of the tobermorite structure each next silicate chain is shifted in the b-axis direction by one silicate. Therefore, looking in the a-axis direction a Q^{2p}-Q^{2p} dimer is neighboring a Q^{2b} silicate. The upper deprotonated silanol groups of the Q^{2b} silicates (corners of the triangle in figure S6) seem to be equally attractive to the calcium ion, positioning it approximately in the geometrical center of them. There are two distinguished heights of adsorption, as seen in figure S7a and the number density along z-axis direction in figure S5. The lower height is approximately at the same height as the upper deprotonated silanol group.
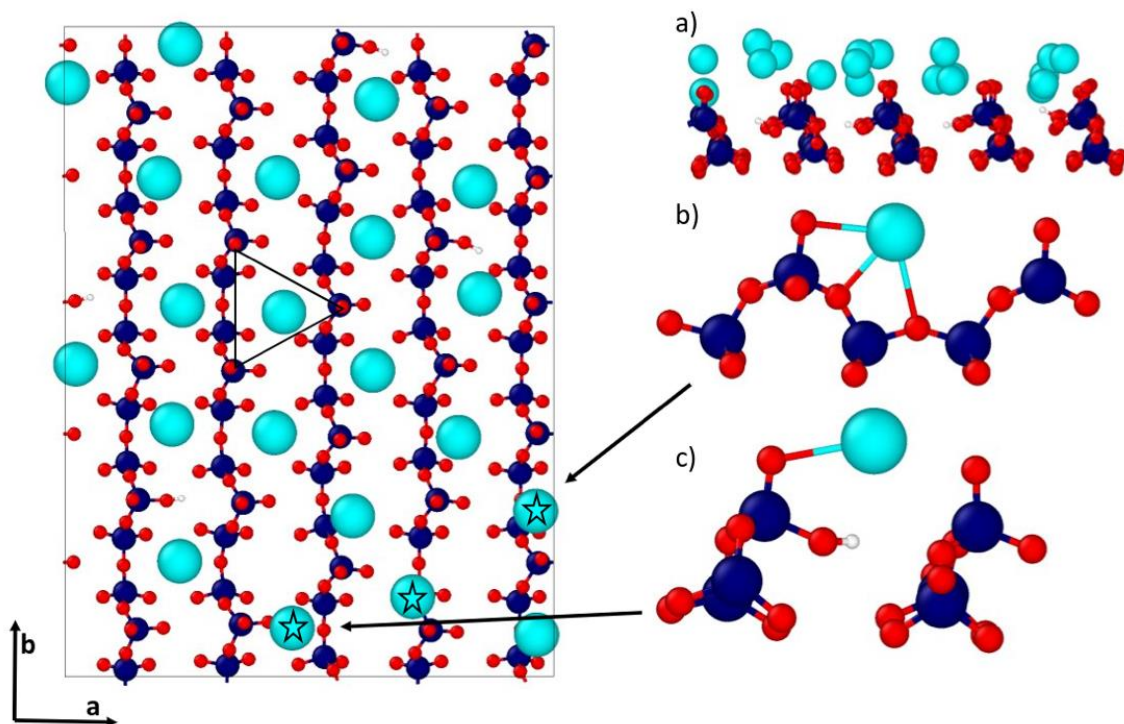
Figure S6. Location of inner (star) and outer (triangle) sphere adsorbed Ca^{2+}. Everything beside the silicates and surface calcium is hidden for clarity. First shell coordination is shown with a bond. Color code: Ca-cyan, Si-blue, O-red, H-white.

Labbez et al. [9] predicted a surface charge of 4.5 e/nm², for this type of surface at 90% deprotonation (pH 13) in contact with 2mM CaX_2 solution (X being any monovalent anion). Accounting for all inner and outer sphere adsorbed Ca^{2+} (below 53 Å in figure S5) the resulting surface charge of the surface equals –1.2 e/nm².

A5-7   Calcium-Hydroxide Surface Network

The calcium-hydroxide network of the C-S-H (001) surface was investigated for the Ca/Si = 1.7 system, as described in the main text. To exclude possible effects of the initial configuration, two separate simulations with different initial configurations were carried out. The difference was in the initial placement of Ca^{2+} and OH^- next to the surface (see figure S7). The first (1) initial configuration had the calcium placed according to the adsorption sites in the literature [12, 33, 35]. As explained in the previous section, those sites are Ca^{2+} on top of the Q^{2p}-Q^{2p} (Q^1-Q^1) dimer and on top of the Q^{2b} silicate. The OH^- were placed in the proximity of the Individual calcium ions. The second (2) configuration had the same Mixed-Surface with Ca_B and Q^{2b} termination, although the required Ca^{2+} and OH^- were randomly placed in the 30 Å

slab next to the surface. The ions, as well as the water molecules were inserted using Packmol [25].

In both cases a similar calcium-hydroxide networks formed on the surface (figure S9). Both networks started to form in a similar manner, therefore only the first (1) initial configuration will be examined in the following discussion. The final configuration data files for both simulations are provided as part of the SI.
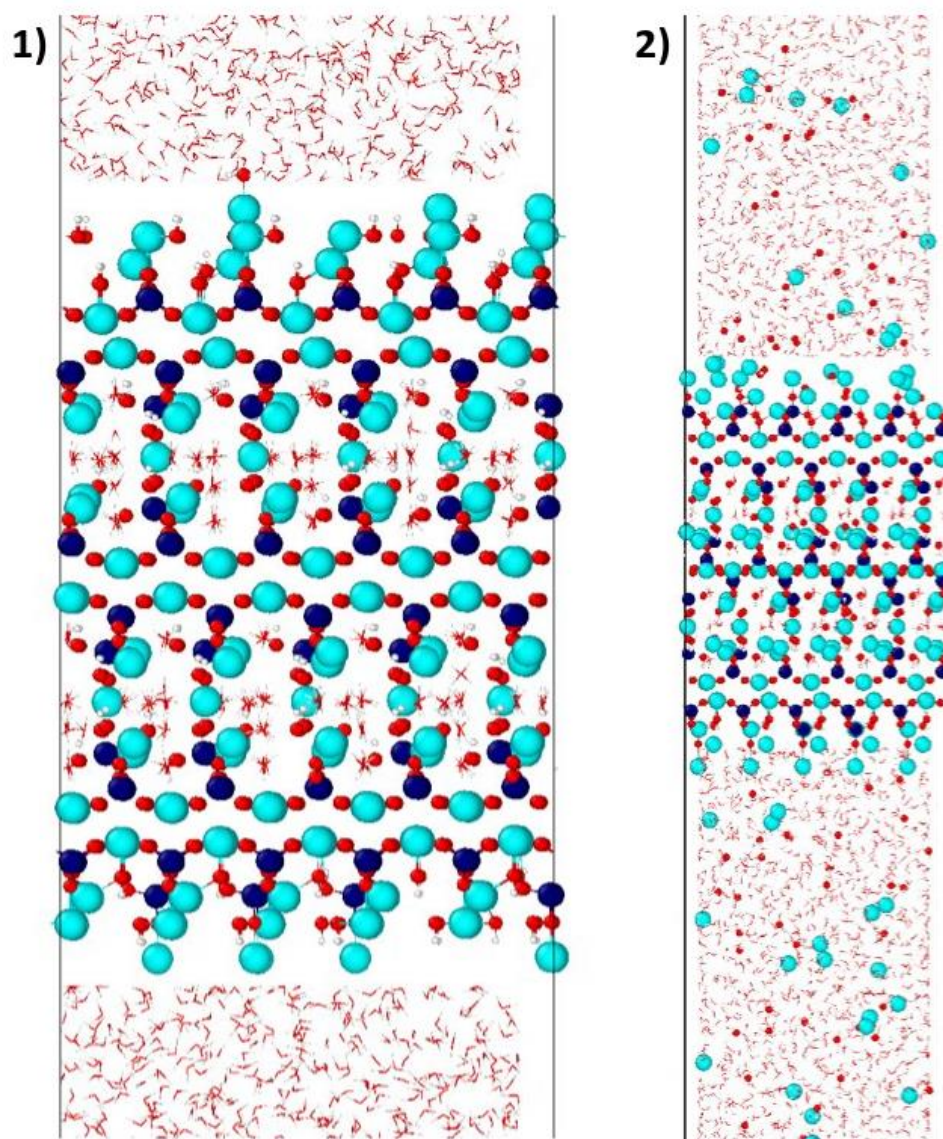

Figure S7. Initial configuration of the C-S-H nanofoil: 1) Ca^{2+} located at the dimer and Q^{2b} adsorption sites and 2) Ca^{2+} located on top of the deprotonated silanol groups, the remaining Ca^{2+} and OH^- are randomly inserted next to the surface. Color code: Ca-cyan, Si-blue, O-red, H-white.

As seen in figure S8, The Ca-O radial distribution function (rdf) shows the affinity of Ca^{2+} for inner sphere adsorption to the deprotonated silanol groups (O). The high intensity peak for the Mixed-Surface with Ca^{2+} and OH^- adsorption, at approximately 2.3 Å, clearly points to a preferred inner sphere adsorption in comparison to the Si-Surface 2 with Ca^{2+} adsorption. The higher packing density of Ca^{2+} next to the surface is further confirmed with the Ca-Ca rdf. The Ca-OH network of the Mixed-Surface results in Ca-Ca distance of around 4 Å, while the pure Ca^{2+} adsorption on the Si-Surface results in Ca-Ca distances of roughly 7 Å.
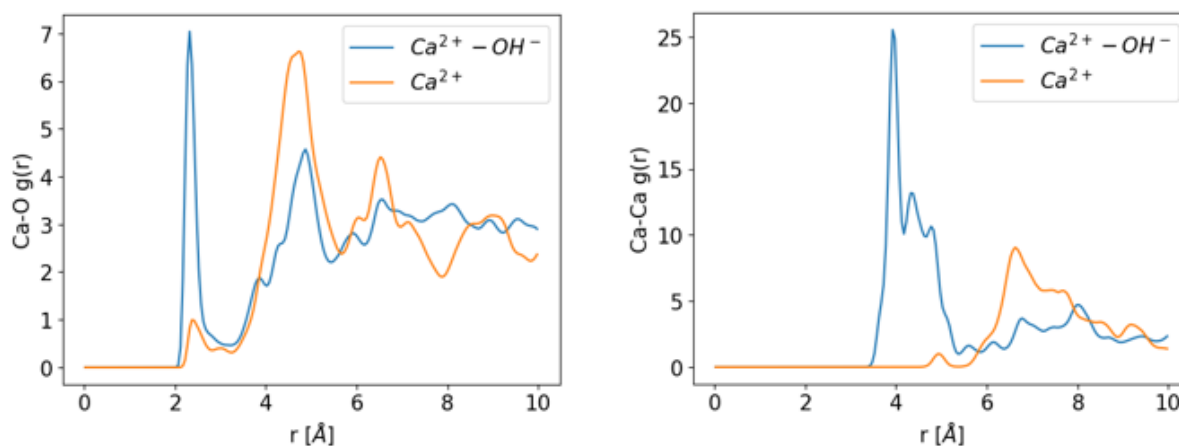

Figure S8. Comparison of Ca-O and Ca-Ca radial distribution functions for the Si-Surface 2 with Ca^{2+} adsorption (orange) and the Mixed-Surface with Ca^{2+} and OH^- adsorption (blue).

Excluding Ca_B (calcium in the bridging site) 30% of the Ca^{2+} are inner sphere adsorbed. Again, here we refer to inner sphere adsorption if a Ca^{2+} is less than 3.15 Å away from a silicate oxygen (first shell coordination). Including Ca_B roughly 60 % of calcium at the surface is inner sphere adsorbed. As can be seen in figures S10 and S11, the inner sphere adsorption is exclusively associated with the adsorption on top of the Q^1-Q^1 (Q^{2p}-Q^{2p}) dimer, which was previously observed by Kalinichev et al. [12] The adsorption at the dimer site is further favored when the neighboring silicate chain carries the Q^{2b} species. However, in 50 % of the inner sphere adsorptions (Ca_B excluded) a hydroxide (OH^-) is acting additionally as a bridge between the adsorbed Ca^{2+} and the main layer calcium (figure S11, black arrow).
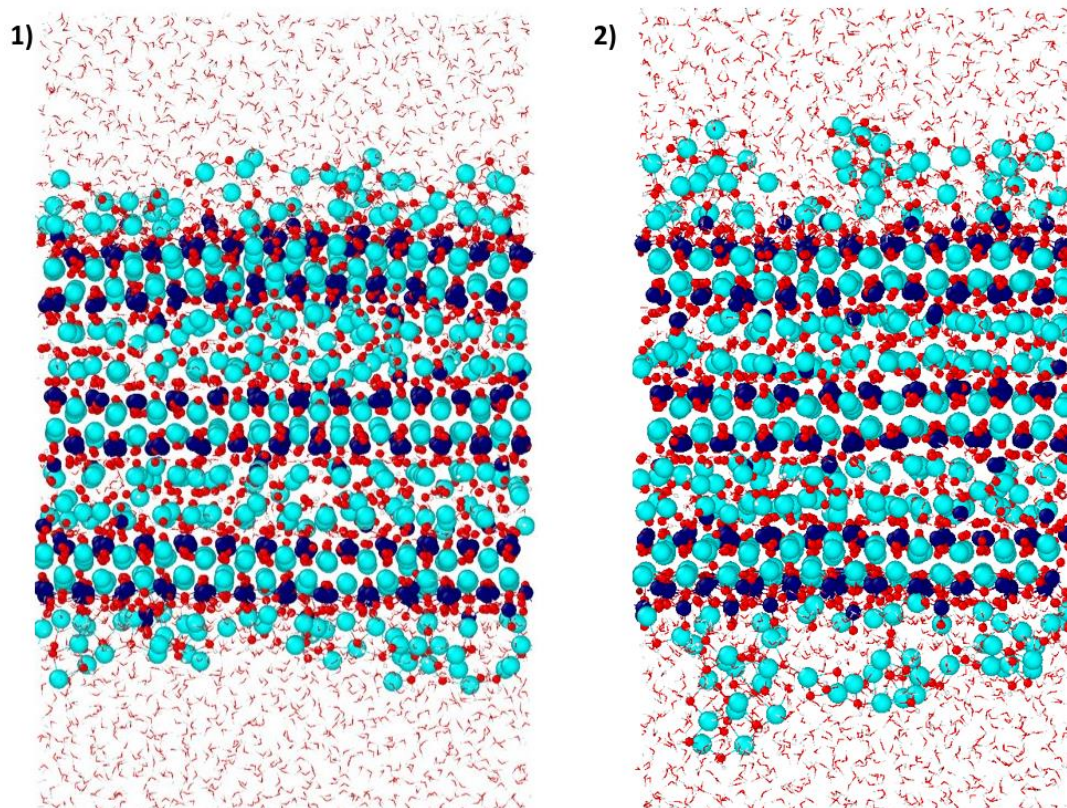
Figure S9. Final configuration of the C-S-H nanofoil shown in figure S6. Color code: Ca-cyan, Si-blue, O-red, H-white.
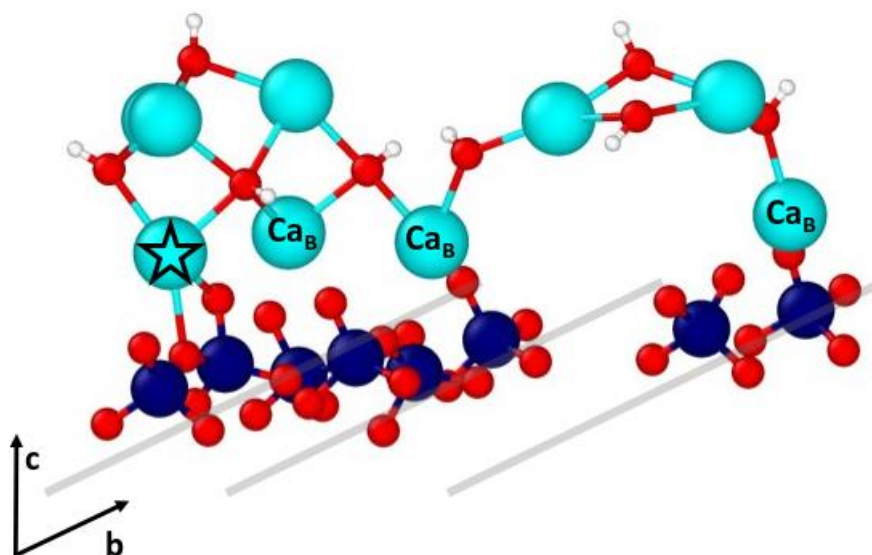

Figure S10. Formation of the calcium-hydroxide network. Ca$_B$ corresponds to the calcium in the bridging site. The star marks the inner sphere adsorbed calcium. Gray lines show the direction of the silicate chains (b-axis). Color code: Ca-cyan, Si-blue, O-red, H-white.
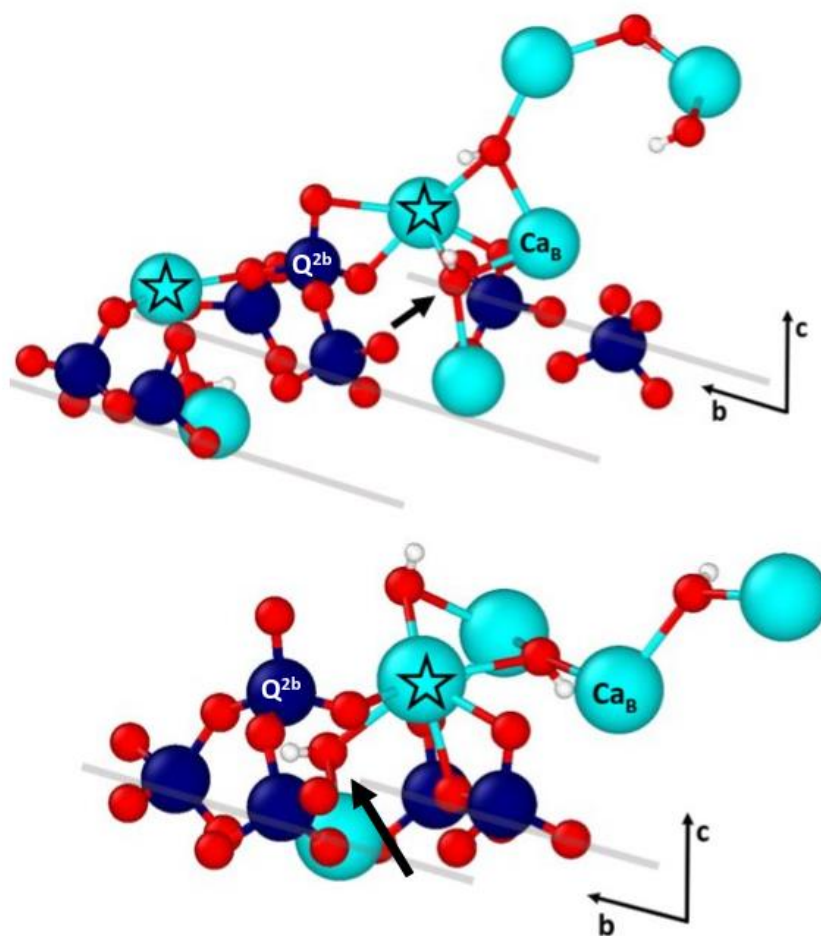
Figure S11. Typical inner sphere adsorption of calcium ions and the start of the calcium-hydroxide network. The star marks the inner sphere adsorbed calcium, Ca$_B$ is calcium in the bridging site (linking dimers), and the arrow points to the hydroxide on the main layer calcium chains, which acts as a bridge for calcium adsorption. Gray lines show the direction of the silicate chains (b-axis). Color code: Ca-cyan, Si-blue, O-red, H-white.

References

[1]   Kunhi Mohamed, A.; Parker, S. C.; Bowen, P.; Galmarini, S. An Atomistic Building Block Description of C-S-H - Towards a Realistic C-S-H Model. *Cem Concr Res* **2018**, *107* (March), 221–235. https://doi.org/10.1016/j.cemconres.2018.01.007.

[2]   Předota, M.; Machesky, M. L.; Wesolowski, D. J. Molecular Origins of the Zeta Potential. *Langmuir* **2016**, *32* (40), 10189–10198. https://doi.org/10.1021/acs.langmuir.6b02493.

[3]   Masoumi, S.; Zare, S.; Valipour, H.; Abdolhosseini Qomi, M. J. Effective Interactions between Calcium-Silicate-Hydrate Nanolayers. *Journal of Physical Chemistry C* **2019**, *123* (8), 4755–4766. https://doi.org/10.1021/acs.jpcc.8b08146.

[4]   Heinz, O.; Heinz, H. Cement Interfaces: Current Understanding, Challenges, and Opportunities.   *Langmuir*   **2021**,   *37*   (21),   6347–6356. https://doi.org/10.1021/acs.langmuir.1c00617.

[5]   Shishehbor, M.; Sakaniwa, D.; Stefaniuk, D.; Krakowiak, K. J.; Abdolhosseini Qomi, M. J. On the Significance of Interfacial Chemistry on the Strength of Fly Ash-Cement Composites.   *Cem   Concr   Res*   **2022**,   *151*   (October   2021),   106619. https://doi.org/10.1016/j.cemconres.2021.106619.

[6]   Deng, H.; He, Z. Interactions of Sodium Chloride Solution and Calcium Silicate Hydrate with Different Calcium to Silicon Ratios: A Molecular Dynamics Study. *Constr Build Mater* **2021**, *268*, 121067. https://doi.org/10.1016/j.conbuildmat.2020.121067.

[7]   Hong, S. Y.; Glasser, F. P. Alkali Binding in Cement Pastes: Part I. The C-S-H Phase. *Cem Concr Res* **1999**, *29* (12), 1893–1903. https://doi.org/10.1016/S0008-8846(99)00187-8.

[8]   Glasser, F. P. Characterisation of the Barrier Performance of Cements. In *Materials Research Society Symposium - Proceedings*; Materials Research Society, 2002; Vol. 713, pp 721–732. https://doi.org/10.1557/proc-713-jj9.1.

[9]   Labbez, C.; Jönsson, B.; Pochard, I.; Nonat, A.; Cabane, B. Surface Charge Density and Electrokinetic Potential of Highly Charged Minerals: Experiments and Monte Carlo Simulations on Calcium Silicate Hydrate. *Journal of Physical Chemistry B* **2006**, *110* (18), 9219–9230. https://doi.org/10.1021/jp057096+.

([0]   Yoshida, S.; Elakneswaren, Y.; Nawa, T. Electrostatic Properties of C-S-H and C-A-S-H for Predicting Calcium and Chloride Adsorption. *Cem Concr Compos* **2021**, *121* (104109).

[11]   Marry, V.; Rotenberg, B.; Turq, P. Structure and Dynamics of Water at a Clay Surface from Molecular Dynamics Simulation. *Physical Chemistry Chemical Physics* **2008**, *10* (32), 4676–4677. https://doi.org/10.1039/b812223g.

[12]   Kalinichev, A. G.; Wang, J.; Kirkpatrick, R. J. Molecular Dynamics Modeling of the Structure, Dynamics and Energetics of Mineral–Water Interfaces: Application to Cement Materials. **2007**, *37*, 337–347. https://doi.org/10.1016/j.cemconres.2006.07.004.

[13]   Duque-Redondo, E.; Bonnaud, P. A.; Manzano, H. A Comprehensive Review of C-S-H Empirical and Computational Models, Their Applications, and Practical Aspects. *Cem Concr Res* **2022**, *156*, 106784. https://doi.org/10.1016/j.cemconres.2022.106784.

[14]   Kumar, A.; Walder, B. J.; Kunhi Mohamed, A.; Hofstetter, A.; Srinivasan, B.; Rossini, A. J.; Scrivener, K.; Emsley, L.; Bowen, P. The Atomic-Level Structure of Cementitious Calcium Silicate Hydrate. *The Journal of Physical Chemistry C* **2017**, *121* (32), 17188–17196. https://doi.org/10.1021/acs.jpcc.7b02439.

[15]   Chen, J. J.; Thomas, J. J.; Taylor, H. F. W.; Jennings, H. M. Solubility and Structure of Calcium Silicate Hydrate. *Cem Concr Res* **2004**, *34* (9), 1499–1519. https://doi.org/10.1016/j.cemconres.2004.04.034.

[16]   Abdolhosseini Qomi, M. J.; Krakowiak, K. J.; Bauchy, M.; Stewart, K. L.; Shahsavari, R.; Jagannathan, D.; Brommer, D. B.; Baronnet, A.; Buehler, M. J.; Yip, S.; Ulm, F. J.; Van Vliet, K. J.; Pellenq, R. J. M. Combinatorial Molecular Optimization of Cement Hydrates. *Nat Commun* **2014**, *5*, 1–10. https://doi.org/10.1038/ncomms5960.

[17]   Maddalena, R.; Li, K.; Chater, P. A.; Michalik, S.; Hamilton, A. Direct Synthesis of a Solid Calcium-Silicate-Hydrate (C-S-H). *Constr Build Mater* **2019**, *223*, 554–565. https://doi.org/10.1016/j.conbuildmat.2019.06.024.

[18]   Yan, Y.; Yang, S.-Y.; Miron, G. D.; Collings, I. E.; L'Hôpital, E.; Skibsted, J.; Winnefeld, F.; Scrivener, K.; Lothenbach, B. Effect of Alkali Hydroxide on Calcium Silicate Hydrate (C-S-H). *Cem Concr Res* **2022**, *151*, 106636. https://doi.org/10.1016/j.cemconres.2021.106636.

[19]   Cong, X.; Kirkpatrick, R. J. 17O MAS NMR Investigation of the Structure of Calcium Silicate Hydrate Gel. *Journal of the American Ceramic Society* **1996**, *79* (6), 1585–1592. https://doi.org/10.1111/j.1151-2916.1996.tb08768.x.

[20]   Yu, P.; Kirkpatrick, R. J.; Poe, B.; McMillan, P. F.; Cong, X. Structure of Calcium Silicate Hydrate (C-S-H): Near-, Mid-, and Far-Infrared Spectroscopy. *Journal of the American Ceramic Society* **2004**, *82* (3), 742–748. https://doi.org/10.1111/j.1151-2916.1999.tb01826.x.

[21]   Cong, X.; James Kirkpatrick, R. 29Si MAS NMR Study of the Structure of Calcium Silicate Hydrate. *Advanced Cement Based Materials* **1996**, *3* (3–4), 144–156. https://doi.org/10.1016/s1065-7355(96)90046-2.

[22]   Thomas, J. J.; Chen, J. J.; Jennings, H. M.; Neumann, D. A. Ca-OH Bonding in the C-S-H Gel Phase of Tricalcium Silicate and White Portland Cement Pastes Measured by Inelastic Neutron Scattering. *Chemistry of Materials* **2003**, *15* (20), 3813–3817. https://doi.org/10.1021/cm034227f.

[23]   Morales-Melgares, A.; Casar, Z.; Moutzouri, P.; Venkatesh, A.; Cordova, M.; Kunhi Mohamed, A.; L. Scrivener, K.; Bowen, P.; Emsley, L. Atomic-Level Structure of Zinc-Modified Cementitious Calcium Silicate Hydrate. *J Am Chem Soc* **2022**, *144* (50), 22915–22924. https://doi.org/10.1021/jacs.2c06749.

[24]   Momma, K.; Izumi, F. VESTA: A Three-Dimensional Visualization System for Electronic and Structural Analysis. *J Appl Crystallogr* **2008**, *41* (3), 653–658. https://doi.org/10.1107/S0021889808012016.

[25]   Martinez, L.; Andrade, R.; Birgin, E. G.; Martínez, J. M. PACKMOL: A Package for Building Initial Configurations for Molecular Dynamics Simulations. *J Comput Chem* **2009**, *30* (13), 2157–2164. https://doi.org/10.1002/jcc.21224.

[26]   Valavi, M.; Casar, Z.; Kunhi, A.; Bowen, P.; Galmarini, S. Molecular Dynamic Simulations of Cementitious Systems Using a Newly Developed Force Field Suite ERICA FF. *Cem Concr Res* **2022**, *154*, 106712. https://doi.org/10.1016/j.cemconres.2022.106712.

[27]   Kunhi Mohamed, A.; Moutzouri, P.; Berruyer, P.; Walder, B. J.; Siramanont, J.; Harris, M.; Negroni, M.; Galmarini, S. C.; Parker, S. C.; Scrivener, K. L.; Emsley, L.; Bowen, P. The Atomic-Level Structure of Cementitious Calcium Aluminate Silicate Hydrate. *J Am Chem Soc* **2020**, *142* (25), 11060–11071. https://doi.org/10.1021/jacs.0c02988.

[28]   Mishra, R. K.; Mohamed, A. K.; Geissbühler, D.; Manzano, H.; Jamil, T.; Shahsavari, R.; Kalinichev, A. G.; Galmarini, S.; Tao, L.; Heinz, H.; Pellenq, R.; van Duin, A. C. T.; Parker, S. C.; Flatt, R. J.; Bowen, P. Cemff: A Force Field Database for Cementitious Materials Including Validations, Applications and Opportunities. *Cem Concr Res* **2017**, *102*, 68–89. https://doi.org/10.1016/j.cemconres.2017.09.003.

[29]   Abascal, J. L. F.; Vega, C. A General Purpose Model for the Condensed Phases of Water: TIP4P/2005. *Journal of Chemical Physics* **2005**, *123* (23). https://doi.org/10.1063/1.2121687.

[30]   Thompson, A. P.; Aktulga, H. M.; Berger, R.; Bolintineanu, D. S.; Brown, W. M.; Crozier, P. S.; in 't Veld, P. J.; Kohlmeyer, A.; Moore, S. G.; Nguyen, T. D.; Shan, R.; Stevens, M. J.; Tranchida, J.; Trott, C.; Plimpton, S. J. LAMMPS - a Flexible Simulation Tool for Particle-Based Materials Modeling at the Atomic, Meso, and Continuum Scales. *Comput Phys Commun* **2022**, *271*, 108171. https://doi.org/10.1016/j.cpc.2021.108171.

[31]   Mitchell, P. J.; Fincham, D. Shell Model Simulations by Adiabatic Dynamics. *Journal of Physics: Condensed Matter* **1993**, *5*, 1031–1038. https://doi.org/10.1088/0953-8984/5/8/006.

[32]   Bischoff, M.; Biriukov, D.; Předota, M.; Marchioro, A. Second Harmonic Scattering Reveals Ion-Specific Effects at the SiO2 and TiO2 Nanoparticle/Aqueous Interface. *Journal of Physical Chemistry C* **2021**, *125* (45), 25261–25274. https://doi.org/10.1021/acs.jpcc.1c07191.

[33]   Kunhi Mohamed, A. Atomistic Simulations of The Structure of Calcium Silicate Hydrates: Interlayer Positions, Water Content and a General Structural Brick Model, EPFL, 2018, Vol. TH 8840. https://doi.org/10.5075/EPFL-THESIS-8840.

[34]   Churakov, S. v.; Labbez, C.; Pegado, L.; Sulpizi, M. Intrinsic Acidity of Surface Sites in Calcium Silicate Hydrates and Its Implication to Their Electrokinetic Properties. *Journal of Physical Chemistry C* **2014**, *118* (22), 11752–11762. https://doi.org/10.1021/jp502514a.

[35]   Androniuk, I.; Kalinichev, A. G. Molecular Dynamics Simulation of the Interaction of Uranium (VI) with the C–S–H Phase of Cement in the Presence of Gluconate. *Applied Geochemistry* **2020**, *113* (July 2019), 104496. https://doi.org/10.1016/j.apgeochem.2019.104496.

Curriculum Vitae

Ziga Casar

Mail home	casar.ziga@outlook.com
Mail work	ziga.casar@epfl.ch

Education

2019 – 2023 PhD in Material Science
Laboratory of Construction Materials, EPFL, Switzerland
Thesis: Atomistic modeling of C-S-H: bulk and surface
Advisors: Prof Karen Scrivener, Dr Aslam Kunhi Mohamed,
          Prof Paul Bowen

2016 – 2019 MEng in Mechanical Engineering
Faculty of Mechanical Engineering University of Maribor, Slovenia
Thesis: Numerical analysis of fluid flow in a vial
Advisors: Prof Matjaz Hribersek, Asst Prof Matej Zadravec

2013 – 2016 BEng in Mechanical Engineering
Faculty of Mechanical Engineering University of Maribor, Slovenia
Thesis: Numerical analysis of mixing with radial-axial ABT stirrer for
          gas-liquid dispersion
Advisors: Prof Matjaz Hribersek, Asst Prof Matej Zadravec

Experiences

08/2019 – 08/2023 Doctoral Assistant:
Teaching: MSE-326 Ceramics and Colloids – TP3 Density, Sintering and Microstructures; LC3 Doctoral School: SEM
Supervising BSc semester projects: Jérémie Bonvin, Tecla Bottinelli, Lucca Ferro, Zoë Evans
Supervising MSc semester projects: Laura Mismetti
Laboratory of Construction Materials, EPFL, Lausanne, Switzerland

03/2018 – 07/2019 Research student: Numerical simulation of freeze-drying
Institute for Power, Process and Environmental Engineering, University of Maribor, Maribor, Slovenia

10/2016 – 07/2019 Tutor for Power, process and environmental engineering
Faculty of Mechanical Engineering University of Maribor, Maribor, Slovenia

02/2019 – 07/2019 Research student: Tracer permeability in a porous medium
Computational Statistical and Biological Physics, Department of Mathematics and Computer Science, Freie Universität Berlin, Berlin, Germany

07/2018 – 09/2018	Research Student: Influence of porosity, hydrogenation, and nitrogen doping on thermal conductivity of nanoporous amorphous carbon Pilon's Lab, UCLA Henry Samueli School of Engineering and Applied Science, Los Angeles, USA
10/2017 – 03/2018	Research Student: Two-phase flow in microchannels Kumamoto University, Graduate School of Science and Technology, Fluids Engineering Laboratory, Kumamoto, Japan
07/2017 – 08/2017	Research Student: Force and torque interaction between rigid bodies and fluid flow Friedrich-Alexander-University of Erlangen-Nuremberg, Chair of Applied Mechanics, Erlangen, Germany
04/2016 – 06/2016	Internship: Remote vessel inspection and handling Max-Planck-Institute for Plasma Physics, Garching bei München, Germany

Selected Awards

2009	Silver Stefan Prize in Physics, Slovenia
2009	Silver Pregel Prize in Chemistry, Slovenia
2010	Bronze Stefan Prize in Physics, Slovenia
2011	Bronze Stefan Prize in Physics, Slovenia
2011	Bronze Prize for Young Researchers in Slovenia in the Field of Informatics and Computer Science, Slovenia
2013	Silver Astra Prize from Prva Gimnazija Maribor for Outstanding Performance, Slovenia
2009 – 2013	Zois Scholarship for Talented Students, Slovenia
2017 – 2018	Maribor City Scholarship for Talented Students, Slovenia
2018	Award for best contribution among young researchers at the conference Kuhljevi dnevi 2018, Lasko, Slovenia
2022	School of Engineering Teaching Assistant Award, EPFL

Publications

A. Kunhi Mohamed, A. Bouibes, M. Bauchy, **Z. Casar**. Molecular modeling of cementitious materials: current progress and benefits, RILEM Technical Letters, 2022, 7: 209-219

A. Morales-Melgares & Z. Casar, P Moutzouri, A. Venkatesh, M. Cordova, A. Kunhi Mohamed, K. L. Scrivener, P. Bowen, L. Emsley. Atomic-Level Structure of Zinc Modified Cementitious Calcium Silicate Hydrate, Journal of the American Chemical Society, 144, 50, 2022
** AMM & ZC contributed equally

M. Valavi, **Z. Casar**, A. Kunhi Mohamed, P. Bowen, S. Galmarini. Molecular dynamic simulations of cementitious systems using a newly developed force field suite ERICA FF, Cement and Concrete Research, 154, 2022

M. Zadravec, **Z. Casar**, J. Ravnik, M. Hribersek: CFD Based Determination of Sublimation Mass Flux for Lyophilization Inside a Vial. International Journal of Computational Methods and Experimental Measurements, 8, 2020.

Conference contributions

M. Frajnkovic, A. Kermiche, **Z. Casar**, A. Fujii, I. Catton and L. Pilon, Vpliv vključkov vodika in dušika v matrici na toplotno prevodnost amorfnega nanoporoznega ogljika = Influence of Hydrogenation and Nitrogenation on Thermal Conductivity of Amorphous Nanoporous Carbon. In: Kuhljevi dnevi 2018 [conference], Zbornik del. Ljubljana: Slovensko društvo za mehaniko. 2018

Z. Casar, M. Hriberšek and M. Zadravec, Numerična analiza tokovnih razmer v viali = Numerical analysis of fluid flow in a vial. In: Kuhljevi dnevi 2018 [conference], Zbornik del. Ljubljana: Slovensko društvo za mehaniko. 2018

M. Hribersek, M. Zadravec, **Z. Casar**, J. Ravnik. The influence of the vial stopper on the flow and mass transfer conditions inside a vial. V: HERNÁNDEZ, Santiago (ur.), ŠKERGET, Leopold (ur.), RAVNIK, Jure (ur.). AFM 18, Twelfth International Conference on Advances in Fluid Mechanics, AFM 18 [Ljubljana, Slovenia], (WIT transactions on engineering sciences (Online), ISSN 1743-3533, vol. 120). Southampton: WIT Press. 2018, pp.193-200.

Z. Casar, M. Hriberšek, M. Ramšak and M. Zadravec. Numerična analiza mešanja pri razprševanju plina v kapljevino = Numerical analysis of mixing for gas - liquid dispersion. In: Kuhljevi dnevi 2017 [conference], Zbornik del. Ljubljana: Slovensko društvo za mehaniko. 2017

Language Skills

Slovenian	Native proficiency
English	Professional working proficiency
German	Professional working proficiency
Italian	Beginner

Free time

Besides scientific activities, ZC enjoys reading (history and geopolitics), cooking and making chocolates (when the experiment fails, you can still eat it), wine (does not know how to say no to a Riesling), running (through the Lavaux vineyards), and volleyball.